Studies of Polar Molecules and Spinor Gases with an Ultracold Mixture of Na and Rb Atoms

超冷鈉銣混合物中的極性分子和自旋氣體

ZHU, Bing

朱兵

A Thesis Submitted in Partial Fulfilment

of the Requirements for the Degree of

Doctor of Philosophy

in

Physics

The Chinese University of Hong Kong

September 2016

Thesis Assessment Committee

Professor LAW, Chi Kwong (Chair)
Professor WANG, Dajun (Thesis Supervisor)
Professor GOH, Swee Kuan (Committee Member)
Professor YAN, Bo (External Examiner)

Abstract

Quantum gas nowadays is one of the hottest research frontiers in physics. ^{23}Na and ^{87}Rb, the first two Bose-condensed atomic species, have been both intensively studied. Their ultracold mixture, which has been investigated a lot theoretically, is studied experimentally for the first time in our lab. In this thesis, I would like to present two distinct experimental projects with this mixture.

In the first part, the successful creation of an ultracold sample of absolute ground-state polar ^{23}Na^{87}Rb molecules are described. Pure samples of weakly bound ^{23}Na^{87}Rb molecules are obtained from an atomic mixture with the help of a s-wave Feshbach resonance. Starting from them, we have explored the excited-state molecular structures, which are one of the main results in this thesis. We also demonstrated the transfer from the Feshbach state to the absolute ground state via a stimulated Raman adiabatic passage (STIRAP) and then we characterized those interesting molecules.

The second project concerns the first investigation of the coherent nature of spin-exchange collisions in a heteronuclear spin system. Specifically, we have observed the coherent heteronuclear spin-mixing dynamics with a mixture of a ^{23}Na condensate and a ^{87}Rb thermal gas. We have measured the magnetic-field dependence of this dynamics and identified a resonant feature. To understand the observed phenomenon, we have developed a theory based on the Gross-Pitaevskii equation (GPE) for the condensate and a Boltzmann transport equation for the thermal gas. We have also demonstrated a unique tool to tune the dynamics in the spinor mixture with species- and state-dependent light shifts.

摘要

量子氣體是代物理學中最熱門的研究前沿領域之一。^{23}Na 和^{87}Rb 作為最早實現波色愛因斯坦凝聚的兩種原子，已經被深入地探索過。雖然他們的超冷混合物在理論上有過很多地討論，但是我們實驗室是率先在實驗上進行研究的。在本論文中我將介紹用鈉銣混合物進行的兩個截然不同的實驗項目。

我會在第一部分描述由處於絕對基態的極性^{23}Na^{87}Rb 分子組成的超冷樣品的成功製備。在s 波的Feshbach 共振的幫助下，我們可以從原子的混合物中得到純弱束縛分子的樣品。作為本論文的主要結果之一，我們研究了^{23}Na^{87}Rb 分子的激發態分子結構。我們通過受激絶熱拉曼路徑將這些弱束縛的分子轉移到了絶對基態并對他們進行了表征。

第二個部分主要展現對於異核自旋系統中自旋交換碰撞的相干性的研究。特別地，我們利用^{23}Na的波色凝聚體和^{87}Rb的熱原子氣體觀察到了異核間的相干自旋混合動力學過程。我們測量了該動力學過程對於外界磁場的依耐性並且發現了一種共振現象。為了理解這些觀測到的實驗結果，我們發展了一套基於用於凝聚體的Gross-Pitaevskii方程和用於熱原子氣體的Boltzmann輸運方程的理論。我們還演示了一種利用矢量光頻移在自旋氣體混合物中調節自旋動力學的特殊實驗手段。

Acknowledgement

It was an amazing life during these past four years I spent in CUHK. Lots of people should be acknowledged for the work described in this thesis.

First of all, I would give the most respect to my thesis advisor, Prof. WANG Dajun. He is a learned professor and he could help whenever I got stuck in any technique or physical problems. He is also a patient elder in my daily life and I always got insightful suggestions from him when I had some inner struggles. The BEC team in CUHK is a big warm family for me. The first postdoc I met, Dr. Xiong Dezhi, together with two senior PhD students, Li Xiaoke and Wang Fudong, introduced me into the quantum gas lab. They taught me from running the whole experiments to aligning a mirror on the optical table. Xiaoke is also a nice person and we had many conversations from physics to life. Chen Jun is a master student who joined the lab at the same year as me and he helped me a lot on the technique problems. The second postdoc, Dr. He Xiaodong, taught me how to design and optimize optical setups. I am thankful to Xiaoke and Xiaodong for the work on spinor gases. Junior student Guo Mingyang is intelligent and hardworking and I thank him for the nice work on the molecular project. The third postdoc working with us on this project is Dr. Lu Bo and he is nice and patient. Another junior student Ye Xin is smart and lively and I think his collaboration with Mingyang would result in a prosperous future for the molecular experiment. The spinor lab is now taken over by the junior student Li Lintao and our new postdoc Dr. Yu Shi.

Besides the BEC team, I am also grateful to other professors and supporting staffs in the department of Physics for their help during my PhD. I want to thank Prof. Law Chi Kwong and Prof. Goh Swee Kuan for being the member of my thesis assessment committee. Prof. Law also taught me quantum optics. Prof. Zhou Qi taught me quantum mechanics and I respect him a lot for his thinking mode.

Mr. Andrew S. K. LI and Mr. YEUNG Man Hau helped a lot in the use of public instruments. Mr. Edward W. K. CHAO and Ms. SUN Lan Fong provided supports in purchasing experimental instruments. Lots of the administrative problems were settled by Mrs. WONG LEE Yeuk Lan, Ms. Mandy S. Y. TANG and Ms. HO Pui Yee. It is impossible to list all of the staffs in CUHK who have helped me these years and I just want to give my best wishes to all of them here.

Outside CUHK, I would like to give my thanks to several professors for their support and collaboration. Prof. Yan Bo is the external examiner for my thesis and he is a very nice person to talk to. I appreciate a lot for the collaboration with the Theomol team in France on the molecular experiments, especially Dr. Olivier Dulieu, Dr. Goulven Quéméner, Dr. Nadia Bouloufa and Dr. Romain Vexiau. I also want to thank Dr. Wang Gaoren for the discussion on the Feshbach resonance. We collaborated with Prof. Xu Zhifang and Prof. Zhang Shizhong on the spinor project. We also have many discussions with a lot of people from all over the world on our experiments and I want to thank them.

From my personal side, I gained a lot from my friends and family members and I feel deeply indebted to them. My high school classmates, Wang Yang, Liu Qingyuan, Wang Fei, Bao Chengzhou, Zhou Panpan and so on, will be my good brothers forever. I would never forget the helps from my college friends, Jin Zhenyu, Ding Wen, Tong Bo, Zhou Zhenghua and Bian Yuhui. Special thanks should be given to my wife Tian Tian for her continuous encouragement and love. I appreciate the support and love from my parents and my wife's parents. They are always behind us when we need them. The birth of my little girl gives me the most power and I love her so much.

This work is dedicated to my wife Tian Tian (田添).

Contents

List of Figures

List of Tables

Chapter 1

Introduction

Bose-Einstein Condensation, a macroscopic quantum phenomenon predicted in 1925 by Albert Einstein, was first realized with the ultracold dilute atomic gases in 1995 [1–3]. These landmark experiments led to the Nobel Prize in physics shared by Wolfgang Ketterle, Eric A. Cornell and Carl Wieman in 2001. Since the birth of the Bose-Einstein condensate (BEC), the field of quantum gas has been explosively developed and it makes connections with many other areas of physics. Quantum simulations of fundamental models and concepts in condensed matter and high energy physics have been extensively reviewed in Ref. [4] and Ref. [5] respectively. So far with quantum gases, quite a few experiments have been carried out, such as the synthetic spin-orbit coupling reviewed in Refs. [6–8], Bose-Hubbard model [9, 10], Fermi-Hubbard model [11] and even the topological Haldane model [12] which is impossible in condensed matter systems. Linking between cold atom physics and astrophysics has been discussed in [13]. Beyond understanding the fundamental problems, quantum gases are also excellent platforms to achieve the high-precision quantum metrology [14]. With their long coherence time and high controllability, cold atoms have been widely used to perform precision measurements beyond the classic limit, for example using atom interferometers to measure the fundamental physical constants like the gravitational constant [15] and fine structure constant [16].

These exciting progresses are only possible with the rapid developments of several essential techniques. The basic technique is the standard laser cooling

and trapping method which makes the Nobel prize in physics awarded to Steven Chu, Claude Cohen-Tonnoudji and William D. Phillips in 1997. It brings the temperature of atomic clouds from the room temperature to the ultracold regime lower than tens of microkelvin (uK). In this regime, the collisions between two atoms are dominated by the lowest partial waves, typically s-wave for bosons or distinguishable atoms and p-wave for fermions. Furthermore, we can tune the two-body interactions at arbitrary strengths with the help of Feshbach resonances [17–19], which I think may be the most influential technique. This unique tool, which cannot be found in other physical systems, makes the extensive applications of the quantum gases possible [20]. Another important technique is the optical lattice which is a periodic trap potential formed by standing waves of laser light [21]. The atoms or molecules loaded into optical lattices can mimic the electrons in solid crystal lattices and due to the well-controlled degrees of freedoms they are ideal for simulating the condensed-matter systems [4], discovering exotic quantum states [22], realizing the quantum computing [23–26] and so on. These essential techniques, together with other helpful ones, give us the opportunity to explore the quantum physics with dilute ultracold gases.

Among the numerous things we could do with quantum gases, exploring the mixtures of atoms interests us most. Naturally we expect that mixtures would give us the possibility to study new physics which is not present in the single-component quantum gases. Actually, it has been thought long before in the liquid-helium systems [27, 28] and now it is revolutionized with atomic quantum gases. The mixture of two spin-1 bosons, which is one of the main topics in this thesis, is served as a nice example. In the section 1.1 we would simply mention the various applications of atomic mixtures.

One the other hand, instead of working with multi-component atomic gases, we are also interested in quantum gases of molecules regarding their more complex constituents. In this thesis I would limit my discussions within the case of diatomic molecules, with which already lots of new physics could be investigated. If molecules are composed of two heteronuclear atoms, they would be more attractive than the homonuclear ones. The reason is that they belong to the so-called polar molcules, where permanent dipole moments allow them to be polarized by an external electric field. This helps us play with tunable long-range and anisotropic interactions, which will be one of the protagonists at the frontier of quantum gas research for many years. Stimulated by the various possibilities with ultracold po-

lar molecules, we have created an ultracold sample of absolute ground-state polar $^{23}Na^{87}Rb$ molecules, which is the most import result presented in this thesis.

1.1 Atomic Quantum Gas Mixture

Liquid helium systems were the only macroscopic examples of mixtures of matters exhibiting quantum effects for a long time. In He3-He4 mixtures the strong interactions between helium isotopes limit the maximum fraction of ^{3}He and make the theoretical analysis challenging [29]. The situation was renewed by the first demonstration of a quantum-gas mixture with two hyperfine states of ^{87}Rb atoms [30]. Such mixtures are quickly extended to systems covering Fermi-Fermi (FF) [31,32], Bose-Fermi (BF) [33–36] and Bose-Bose (BB) [37–42] mixtures of different isotopes of the same element, or of two different elements.

FF mixtures of two different hyperfine states can be mapped to the spin-1/2 systems which play a crucial rule in condensed matter physics. They are ideal systems to study topics such as the BCS-BEC crossover [43–47], superfluidity with population imbalance [48] and new exotic quantum states like the Fulde-Ferrell-Larkin-Ovchinnikov (FFLO) state [49, 50]. On the other hand, FF mixtures of different atomic species provide unique analogies to several many-body systems for the existing of the mass difference, for examples see Ref. [51].

BF mixtures are interesting mainly because of the presence of both Bose-Einstein and Fermi-Dirac statistics. Unlike the mixtures of ^{3}He and ^{4}He, such mixtures with dilute atomic gases provide simple but intriguing scenarios to explore the BCS-like fermionic superfludity [52], phase separation [53,54] and Bose or Fermi polarons [55,56]. Loaded into an optical lattice, BF mixtures are promising for the observation of the exotic supersolid state [57–59]. Recently, the spinor BF mixtures are proposed to realize spontaneous quantum Hall effect [60] and control non-abelian emergent gauge potentials [61].

We are most interested in BB mixtures for their unique properties and rich applications. The first paper concerning the binary BECs predicted that they have a great variety of possible ground states and excitations by only varying the particle numbers [62]. The spatial distribution of the ground state of a trapped binary BEC could be miscible or immiscible due to the competition between the inter- and intra-component interactions [63]. A quantum phase transition between

these two phases has been studied a lot both theoretically [64–67] and experimentally [39, 42, 68, 69]. However, it is still of experimental challenging to realize many theoretical proposals with trapped binary BECs, for example, measuring the collective modes [70, 71], observing the turbulence in the hydrodynamic regime [72] and quantitatively testing the Kibble-Zurek scaling [67]. BB mixtures are also important to investigate the impurities immersed in a bosonic environment, another example of Bose polarons [73]. Mixtures of bosonic spinor gases may find applications in creating two entangled BECs [74], simulating complicated spin systems and realizing the bosonic Kondo model. Besides the above applications in the bulk samples, the loading of BB mixtures into optical lattices has opened the door of studying the multi-component Bose-Hubbard model [75, 76], multiparticle entanglement [77, 78], super-exchange interactions [79], and spin-gradient thermometry [80].

All of above applications focus on the interplay between different components of the mixtures. The possibility that we can produce an ultracold molecular gas from the ultracold atomic mixtures is another driving force of the more and more explorations of them.

1.2 Ultracold Polar Molecule

Interactions play the most important role in the understanding of nature, from the elementary particles in the Standard Model to stars in the universe. This is also true in quantum gases and engineering the interactions is the most powerful tool in our community. The contact interactions encountered most in atomic gases are short-range and isotropic and other types of interactions have been pursued intensively in last two decades. Dipole-dipole interaction (DDI) (see Appendix A.1 for detailed introduction), which is one of the most promising candidates, is long-range and anisotropic. The physics with dipolar quantum gases has been reviewed in [81–83], which can be realized with magnetic atoms, Rydberg atoms and ultracold polar molecules (UPMs).

With quantum gases of highly magnetic atoms, the efforts of experimentalists have led to observations of the anisotropic expansion [84] and directional stability [85] of a BEC, Fermi surface deformation [86], nonequilibrium quantum magnetism [87], and chaotic scattering [88]. Although stunning influences of DDI in

magnetic atoms have been observed, they are typically smaller, or at most the same order as the contact interactions. Due to the much stronger electrical DDI, it can dominate with highly excited Rydberg atoms and UPMs. Resonant dipolar interactions between Rydberg atoms have been demonstrated experimentally in cold Rydberg gases [89, 90]. The dipole blockade, caused by the DDI-induced energy shifts, is the suppression of Rydberg excitations neighbouring an existing Rydberg atom. Experiments have been carried out with two independently trapped atoms to observe this effect [91,92]. However, the lifetime of a dense Rydberg gas is quite short due to the avalanche ionization [93].

The advantages of relative large DDIs and long lifetimes with quantum gases of UPMs, combined with other unique properties and some necessary techniques, make their extensive applications possible. The various aspects of cold and ultracold molecules have been reviewed in Ref. [94]. Roughly new physics with the studying on UPMs can be divided into three fields: ultracold chemistry, precision measurement and the many-body physics.

The rates of inelastic processes and chemical reactions are dramatically modified by the particle statistics, the inter-particle interactions and the dimensionality. The Bose-enhanced chemistry has been investigated theoretically in Ref. [95]. The study of molecular loss rates with different particle statistics has been realized by controlling the quantum state of a $^{40}K^{87}Rb$ molecular gas [96]. With DC or AC electromagnetic (EM) fields we can study the controlled chemistry, which has been described in detail in Ref. [97]. The DC electric fields are utilized to induce the DDI among polar molecules which would change the various collision processes significantly. For example the dipolar collisions between two $^{40}K^{87}Rb$ molecules have been studied in Ref. [98]. AC EM fields could be used to control the dimensionality which has been proven to be a power knob to tune the inelastic rates in Ref. [99].The combination of both the DC and AC EM fields are also quite interesting [100].

The UPM prepared in a single quantum state may provide the most accurate measurements where the shot-noise limit is decreased due to the increased occupation number and coherence time [94]. The complex molecular structures could be utilized to set the frequency benchmarks ranging from the microwave domain to the visible one. It is also useful in testing possible time variations of some fundamental constants [101].

The applications in many-body physics could be discussed separately accord-

ing to the trap potentials. Most of the existing literatures exploring quantum gases of polar molecules focus on the dramatic effects induced by the DDI, especially the understanding of the dipolar Bose gas [81]. The possibility that tuning the BEC from the contact interaction dominated regime to the strongly dipolar regime stimulates many theoretical and experimental efforts [94]. Beyond the harmonically trapped bulk samples, the UPMs in optical lattices also attract lots of attentions. A minimal model describing quantum lattice physics is the Hubbard model. Within this model, the phase digram of a dipolar Bose gas is predicted to be the same as that of the extended Bose Hubbard model [102], where Mott insulator, checkerboard insulator, superfluid, supersolid and collapse phase could be observed. The simplest Hamiltonian for lattice-confined polar molecules has been derived in Ref. [103] where the dynamical phase transitions are also included.

1.3 Spinor Gas

The study of the interplay between superfluidity and magnetic ordering has a long history in condensed matter system, especially in superconductors. In the conventional superconductors explained by the Bardeen-Schrieffer-Cooper (BCS) theory, very low concentration of a magnetic impurity could suppress the superconducting state [104]. For the high-transition temperature (high-T_c) superconductors like copper oxides and iron-based superconductors, the antiferromagnetic order maybe play a important role in accounting for the high-T_c [105,106]. Quantum gases with their internal degrees of freedom liberated, are ideal platforms to study the physics simultaneously associated with superfluidity and magnetism.

1.3.1 Single-species Spinor Gas

One profound system is the bosonic spinor gas realized in optical dipole traps [107–109], where different sub-levels of a hyperfine manifold experience a common external trapping potential. Spin domains, spin-mixing dynamics and spin textures are there most interesting phenomena proposed theoretically and observed experimentally with bosonic spinor gases, which have been intensively reviewed in Refs. [110, 111]. Spin mixing has also been demonstrated with fermionic atoms recently [112].

The phase diagram as well as the dynamical properties are mainly determined by the spin-dependent binary interactions. In a spin-1 BEC, it is well-known that the only spin-dependent term has the form of $c\mathbf{f}_1 \cdot \mathbf{f}_2$ [108], where $\mathbf{f}_i (i = 1, 2)$ are the hyperfine spins of two colliding atoms. It is obvious that the interaction energy is lowered when the two spins are parallel (anti-parallel) for $c < 0$ ($c > 0$), which is called a ferromagnetic (antiferromagnetic) interaction. In the absence of external magnetic fields, the ground state is the ferromagnetic (antiferromagnetic) phase for the ferromagnetic (antiferromagnetic) interaction with which the system reaches the maximum (minimum) value of its spin density [108]. We have a large degeneracy of the ground state due to the SU(2) symmetry of spin-1 objects. When an external magnetic field is applied, the Zeeman interaction would break the SU(2) symmetry and only a axisymmetry about the quantization axis is left. Furthermore, the Zeeman energy could compete with the spin-dependent interaction energy and the ground state becomes more complex [107].

Besides the ground-state structures, the spin-mixing processes, where two colliding atoms exchange their magnetic quantum numbers, play a important role in determining the magnetic nature of spinor gases [113–116]. They are also utilized to study the quantum coherence [112,116–120], nonequilibrium dynamics [121,122], spin-squeezing and entanglement [123, 124], quantum phase transitions [121, 125], and so on.

The workhorses for the bosonic spinor gases are the ground-state ^{23}Na and ^{87}Rb atoms. The coefficient c for ^{23}Na spin-1 gases is positive while it is negative for ^{87}Rb spin-1 gases. The phase diagram of a spin-2 gas is much richer due to more spin-dependent interaction terms. For the ^{87}Rb spin-2 BEC the ground state is not clear even at a zero magnetic field, although most likely it is ferromagnetic [114].

1.3.2 Mixture of Spin-1 Gases

Although the spinor gas of single-species atoms has been extensively studied, their mixtures are rarely investigated, especially in experiments. The situation that magnetic impurities interact with a magnetic host would provide us many interesting settings.

In bulk samples, the mean field phase diagram of a binary spin-1 mixture has been studied theoretically in Refs. [126, 127], where various new phases are

predicted due to the competition between intra-species and inter-species spin-dependent interactions. The quantum ground state has also been studied by theorists in Refs. [128,129]. The possibility of generating two entangled BECs has been discussed in Ref. [74]. The heteronuclear spin-mixing dynamics was investigated in Ref. [130].

By loading a binary spin-1 gas into an optical lattice, we could mimic the quantum magnetism in crystal structures. For example, we could make a ^{87}Rb Mott insulator and a ^{23}Na superfluid and possibly study the indirect interactions between localized ^{87}Rb spins or the influence of the localized impurities on the spin-mixing dynamics of the host. Although the magnetic excitations in an optical lattice has already been studied with single-species atoms in Ref. [131], it is still interesting to explore them with a binary mixture where the mass difference may play a role.

1.4 Thesis Outline

The main part of this thesis would be divided into three chapters. The first chapter concerns with the experimental setups and their corresponding working mechanism. Logically we follow the constructions of different experimental apparatuses and the experimental time sequence. In the second chapter, we focus on the molecular part where every steps from atoms to molecules are discussed in detail. The last chapter would describe the spinor work including the study of the heteronuclear mixtures of two spin-1 atoms and the ^{87}Rb thermal spinor gases.

Chapter 2

Experimental Setups

The cooling and trapping of atoms are standard techniques in today's quantum gas lab. Nevertheless, every system has its own peculiarities and I would like to describe our unique setups to create the quantum degenerate mixtures of ^{23}Na and ^{87}Rb in this chapter.

The basic components in our lab include the following six parts. (1) A ultra-high vacuum (UHV) system. It is needed to isolate the atomic samples from the environment. (2) Lasers. They could be used to cool and trap the atoms, like in a magneto-optical trap (MOT) and far-off-resonance optical dipole trap (FORT). We also utilize them to control the quantum state of atoms or molecules via many coherent processes, such as the STIRAP. (3) Imaging system. This is constructed to gain information from the samples by taking pictures of them with a complementary metal-oxide-semiconductor (CMOS) camera. (4) The DC external fields. A magnetic gradient field is needed for the MOT and the magnetic trap. We use a uniform magnetic field to induce the Feshbach resonances. We also play with a uniform electric field to manipulate the ground-state polar molecules. (5) The microwave (MW) and radio-frequency (RF) fields. They are used to control the internal states of atoms or molecules. (6) Experimental control system. With this system, we can engineer the experimental time sequence with a time resolution of one millisecond. I will introduce these six parts in this order.

2.1 UHV System

The UHV system, with which the works in the thesis were carried out, was constructed and finished before I joined the lab in 2012. However, during my PhD time I had the opportunity to participate in the construction of a new experimental setup from the very beginning. Here I still want to focus on our old setup.

The opening of a quantum gas lab usually starts with the design and preparation of a UHV system. Our main vacuum chamber was designed to have a height of 30 cm. Enough spaces should be left to provide good optical accesses, especially for a single chamber system where they are severely limited by the presence of magnetic coils, electrodes, RF coils and MW horns.

There are some standard procedures to be followed [132] to build up the UHV. Here I briefly summary the steps we have taken to achieve the UHV in Table 2.1. Details of totally 7 steps can be found as well as some remarks and tips for each step.

Table 2.1: Steps to reach UHV. Here DI water and TSP refers to deionized water and Titanium sublimation pump respectively.

STEP	DETAIL	REMARKS and TIPs
Cleaning	Most of the metal and ceramic components should be washed in ultrasonic bath of soap, DI water, acetone and methanol in $1 \sim 2$ hour in the order.	Except the angle valve, feedthrough and pumps.
First bake-out	Bake all the components in 300∼400 °C for several hours and wrap up them in Al-foil after cooling down naturally.	Different parts will have different temperature ratings and we need to bake them in different ovens.

Assembly	Design a proper assembly order, roughly speaking, the main metal part and its support, the glass cell and its protector, the dispenser and feedthrough, the ion pump, TSP and the turbo pump.	a) Wire dust-free gloves and gauze masks all the time and change them regularly. b) Wipe the knife edges and copper gaskets with methanol before using them. c) Watch out for the glass cell all the time. d) Use the spot welding to connect dispensers and feedthrough.
Pump down and leak check	Pump the vacuum down to the order of 10^{-7} Torr and check the leakage by applying nitrogen or helium gas to the whole system and methanol to the joints.	This is a very rough testing process by just monitoring the pressure after applying the gas and liquid. Actually we can qualitatively determine the leakage rate by closing the ion pump and measuring the pressure rise curves after the second baking.
Check dispensers and outgas TSP	Dispensers should be checked by seeing the fluorescence of ^{23}Na and ^{87}Rb. If there is no problem we then outgas the TSP by applying a slowly rising current for $\sim$10 min.	During applying the current to the dispensers, we first use a small current for several minutes to outgas them. Then the temperature is raised to melt the indium sealing and at last the alkali metal starts to be evaporated. The outgasing of TSP should be operated below the sublimation temperature of Titanium for several times.

Second bake-out	Wrap the heat tapes in good contact with surfaces evenly and place the thermocouples to the cell protector, glass-to-metal joint, angle valve, ion pump and feedthrough. Then wrap the fiberglass cloth and fasten all the heat tapes and cloth with Kapton tapes. Start to rise the temperature slowly to 250 °C (5 $\sim$ 6h) and maintain for several days. Heat the dispensers and TSP by applying currents to avoid possible condensation of contaminants.	Make sure the temperature gradient on the glass cell small by keeping suitable ratio of heat tapes wrapped on the cell protector. Never overlap the heat tapes. The temperature difference between different parts should not exceed 30 °C during the whole baking process. Record all the readings: time, temperature, pressure and applied voltage to the heat tape.
Cool down and turn on ion pump and TSP	The system should also be cooled down slowly to $\sim$40 °C (6$\sim$8h), especially the ion pump. Then turn on the ion pump and close the angle valve and turbo pump. The last step is to turn on the TSP with full current for several minutes to reach further UHV.	The ion pump can be turned on at temperature below 85 °C and baked for one or two days until the pressure reach 10^{-8} Torr. Monitor the pressure drop when the temperature is lowered.

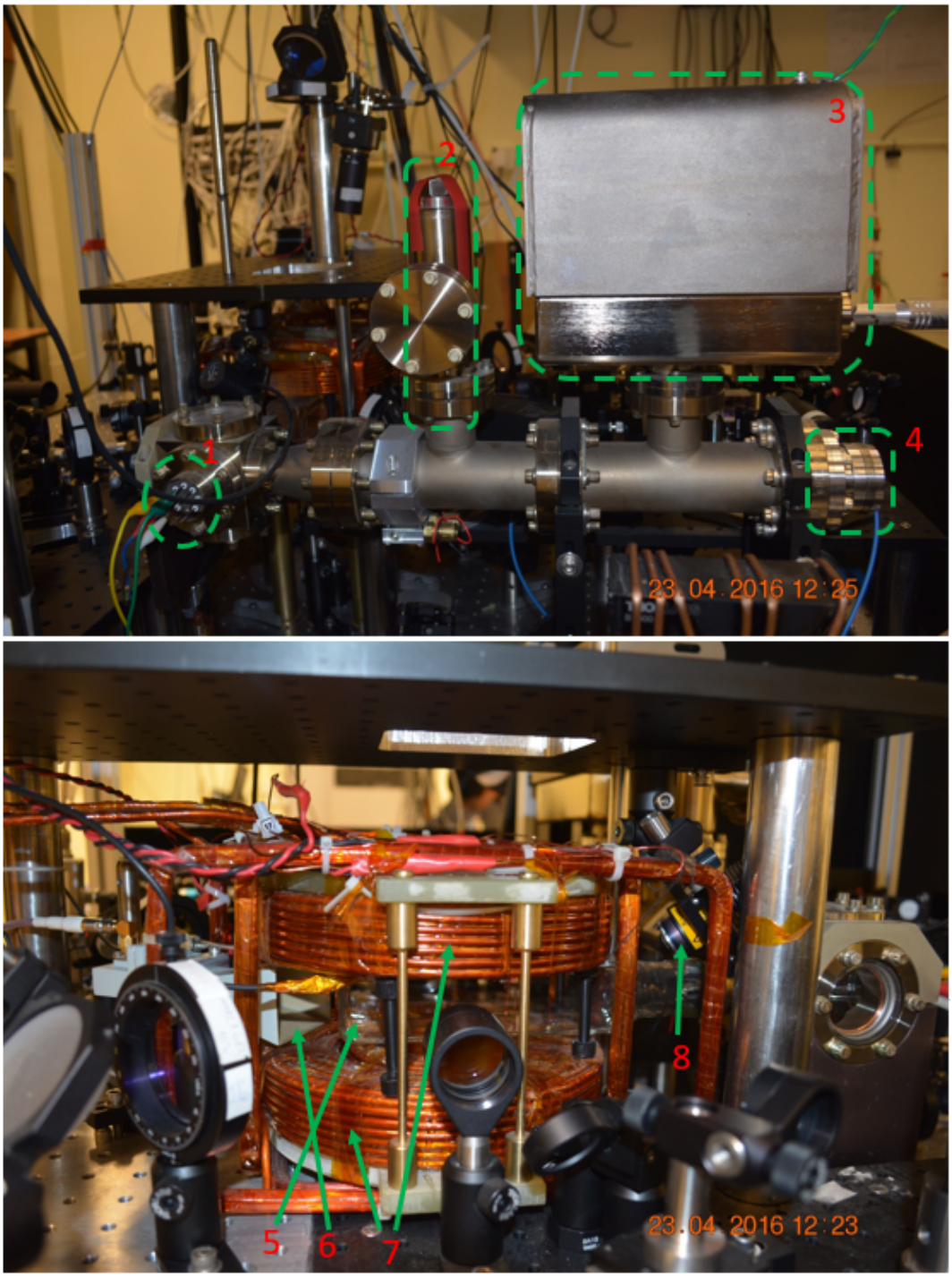

Figure 2.1: Photograph of our experimental apparatus. 1-Feedthrough, 2-Angle valve, 3-Ion pump, 4-TSP, 5-Glass cell, 6-Microwave horn, 7-Coils producing magnetic fields, 8-UV LED.

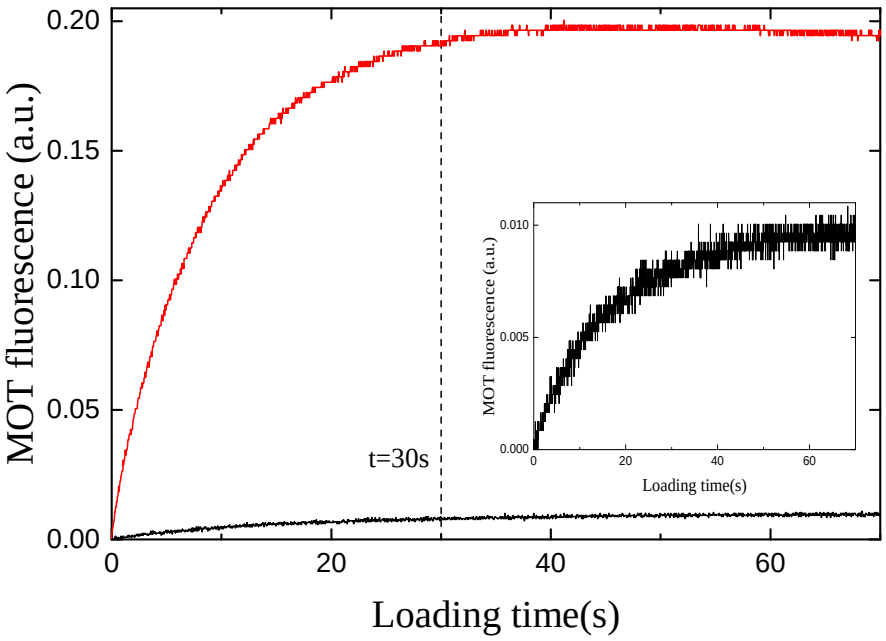

Figure 2.2: Fluorescences of ^{87}Rb during the MOT loading. The red and black curves are corresponding to the presence and absence of the UV light, respectively. The dashed vertical line indicates the MOT loading time in our daily experiments. The inset shows the black curve with a rescaled vertical axis.

As seen in the photograph in Fig. 2.1, our vacuum system is a single-chamber setup where the pressure of $\sim 1.4 \times 10^{-11}$ Torr is maintained by the ion pump (Gamma Vacuum 45s). The single chamber is a glass cell (pyrex glass) with outer sizes of 40 mm×40 mm×132 mm and a wall thickness of 3 mm. The cell is not anti-reflection coated as we work with several quite different colors. It is connected to a standard stainless six-way cross though a $2\frac{3}{4}''$ CF flange. The atomic sources (dispensers) are on the opposite side of the cross, which are about 12 cm away from the cell center and connected through an electrical feedthrough. The other sides of the cross are closed with viewports except the side linked to a reducing cross through a conical reducer. The angle valve, ion pump and TSP are installed to the down, up and back flanges of that reducing cross respectively.

Dispensers are commonly used for ^{87}Rb, while Zeeman slowers for ^{23}Na due to its lower vapor pressure at the room temperature. However, we use the former for both species and this could be a limit for our ^{23}Na atom number. On the

other hand, the UHV in our single chamber is below the vapor pressure for both species. To solve these disadvantages for the MOT loading, the light-induced atomic desorption (LIAD) effect [133] is utilized to temporarily increase the atomic vapor pressure by turning on a 365 nm ultraviolet (UV) light-emitting diode (LED) [134]. The LED (Thorlabs M365L2) is mounted near the glass-to-metal transition part and has a maximum output power of 200 mW. A comparison between the MOT loading curves of ^{87}Rb with and without the UV light is shown in Fig. 2.2. It is apparent that the UV light increases the saturation value of the fluorescence by ~ 200 times and reduces the loading time constant by 50%. The fluorescence of ^{23}Na is too small to be separated from the noise. However, we can confirm the great effect of the UV light on ^{23}Na by checking its atom number at latter stages. For daily operations, we set the MOT loading time to be 30 s. To make the LIAD technique stable over a whole day we need heat our dispensers with constant currents.

2.2 Laser System

Lasers are essential elements in a quantum gas lab. In our lab, we have setup three different laser systems for different purposes, namely the ^{87}Rb and ^{23}Na MOT lasers, the FORT laser, and the Raman lasers for STIRAP. I would like to begin with an overview of the atomic structures of ^{23}Na and ^{87}Rb followed by the introduction to the fundamental light-matter interactions. At last we focus on the laser setups.

2.2.1 Atomic Structures of ^{23}Na and ^{87}Rb

In a neutral atom the electronic states are labeled with the term symbols $^{2S+1}L_J$, where S, L, and J are quantum numbers representing the spin, orbital, and total angular momentum of electrons, respectively. L is designated as $S, P, D, \cdots$ for the value $0, 1, 2, \cdots$. The simple alkali atoms have only one outermost valence electron, while all other electrons are wise-paired to give a zero contribution to the angular momentum. The lowest three electronic levels are $^2S_{1/2}$, $^2P_{1/2}$ and $^2P_{3/2}$. In Fig. 2.3 we show these levels for both ^{23}Na and ^{87}Rb atoms.

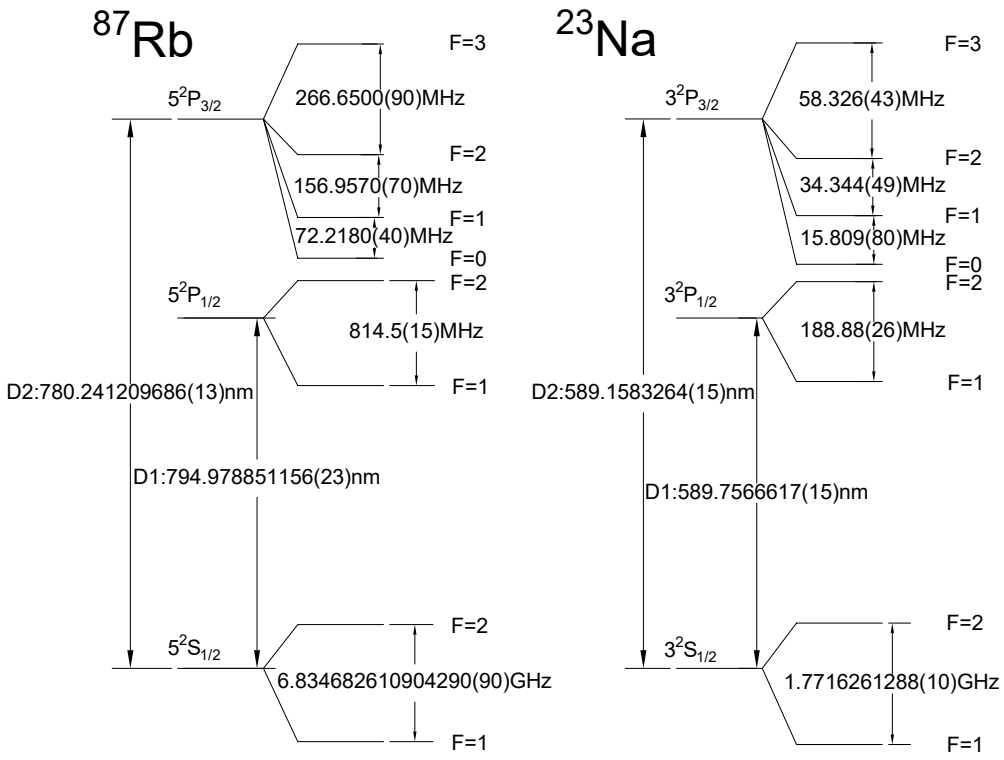

Figure 2.3: Atomic structures of ^{23}Na and ^{87}Rb. The electronic ground state ($^2S_{1/2}$) and the first two excited states ($^2P_{1/2}$ and $^2P_{3/2}$) are shown. Due to their same nuclear spin of $I = 3/2$, the hyperfine structures of ^{23}Na and ^{87}Rb are similar, which are also presented here. All of the numerical values are from Ref. [135, 136]

Beyond the electronic structures, the interactions between electrons and nucleus give rise to the hyperfine structures, are also presented in the figure. The Hamiltonian for hyperfine interactions is easy to be found in any atomic physics textbooks and reads

$$H_{\rm hf} = A_{\rm hf}\mathbf{I}\cdot\mathbf{J} + B_{\rm hf}\frac{3(\mathbf{I}\cdot\mathbf{J})^2 + \frac{3}{2}\mathbf{I}\cdot\mathbf{J} - I(I+1)(J+1)}{2I(2I-1)(2J-1)}, \tag{2.1}$$

where $A_{\rm hf}$ and $B_{\rm hf}$ are two constants and $\mathbf{I}$ is the nuclear spin with quantum number I. The first term is the magnetic dipole term and the second is the electric quadrupole term which is vanished for $J = 1/2$ states. Based on this Hamiltonian, the good quantum numbers are I, J, F and m_F, where $\mathbf{F} = \mathbf{I} + \mathbf{J}$

and m_F its projection along the quantization axis. Each F state has a degeneracy of $2F+1$ and this degeneracy can be lifted by an external magnetic field. Due to their same nuclear spin quantum number of $I = 3/2$, the hyperfine structures of ^{23}Na and ^{87}Rb are quite similar. The influence of the external magnetic field would be presented in the subsection 2.4.1, especially for their electronic ground states.

2.2.2 Two-level Atoms in a Monochromatic Light Field

The light-matter interaction is one of the fundamental topics in modern quantum physics. Before the advent of a full quantum description, the most well-known attempt to solving this problem is the Lorentz oscillator model [137] based on Maxwell's equations by Hendrik Lorentz. That model assumed that electrons are bound to the nucleus through forces obeying the Hook's law. The electric field of the applied radiation interacts with the electron's charge where the situation is like a driven oscillator. The model succeed in explaining the normal Zeeman effect [137] and some optical properties of materials, such as the complex refractive index and frequency response of metals. Although it is a classical model, the driven oscillator picture is still useful today for it is convenient to get the quantum result starting from this model.

The full quantum description of light-matter interaction deals with both quantized atoms and quantized radiations. However, the treatment with quantized atoms and classical radiations is enough for our purpose. We start our discussion with a two-level atom interacting with a monochromatic light field which is sketched in Fig. 2.4**a**. With an oscillating electric field $\mathbf{E}\cos\omega t$, the Hamiltonian under the rotating wave approximation (RWA) reads

$$H = \hbar \begin{pmatrix} \omega_0 - \frac{i}{2}\Gamma & \frac{\Omega}{2}e^{-i\omega t} \\ \frac{\Omega}{2}e^{i\omega t} & \frac{i}{2}\Gamma \end{pmatrix}, \tag{2.2}$$

where ω_0 is the energy spacing between the ground state $|g\rangle$ and the excited state $|e\rangle$, Γ is the decay rate of $|e\rangle$ and it is the reciprocal of the lifetime τ, ω is the angular frequency of the light and Ω is the Rabi frequency defined as $\Omega \equiv |q\mathbf{E}\cdot\langle e|\,\mathbf{r}\,|g\rangle|/\hbar$. With an unitary transformation $H \to UHU^\dagger - i\hbar U\partial_t U^\dagger$, the Hamiltonian can be

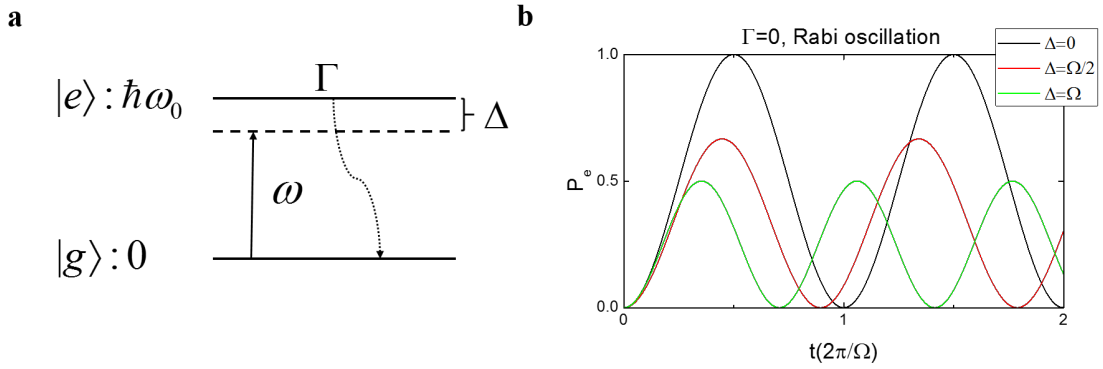

Figure 2.4: **a**, An two-level atom in a monochrome light field. The ground and excited states are represented by $|g\rangle$ and $|e\rangle$ respectively. ω_0 is the energy spacing between $|g\rangle$ and $|e\rangle$ and Γ is the decay rate of $|e\rangle$ to $|g\rangle$. The two-level atom is driven by a light field with an angular frequency ω and Δ is the detuning. **b**, The Rabi oscillation of a two-level atom. Assuming $\Gamma = 0$, three cases with $\Delta = 0, \Omega/2$ and Ω are plotted here.

rewritten as

$$H = \hbar \begin{pmatrix} -\Delta - \frac{i}{2}\Gamma & \frac{\Omega}{2} \\ \frac{\Omega}{2} & \frac{i}{2}\Gamma \end{pmatrix}, \tag{2.3}$$

here the detuning $\Delta \equiv \omega - \omega_0$ and U reads

$$U = \begin{pmatrix} e^{i\omega t} & 0 \\ 0 & 1 \end{pmatrix}. \tag{2.4}$$

The Schrödinger equation $i\hbar\partial_t |\Psi(t)\rangle = H |\Psi(t)\rangle$ with $|\Psi(t)\rangle = c_g(t) |g\rangle + c_e(t) |e\rangle$ gives two coupled differential equations

$$\begin{aligned} i\dot{c_e} &= (-\Delta - \frac{i}{2}\Gamma)c_e + \frac{\Omega}{2}c_g, \\ i\dot{c_g} &= \frac{\Omega}{2}c_e + \frac{i}{2}\Gamma c_g. \end{aligned} \tag{2.5}$$

The initial state is usually prepared at the ground state: $|\Psi(0)\rangle = |g\rangle$. We first assume $\Gamma = 0$ and the solution reads

$$|\Psi(t)\rangle = -i\frac{\Omega}{\Omega'}e^{i\Delta t/2}\sin\theta\,|e\rangle + e^{i\Delta t/2}(\cos\theta - i\frac{\Delta}{\Omega'}\sin\theta)\,|g\rangle\,, \tag{2.6}$$

where $\Omega' = \sqrt{\Omega^2 + \Delta^2}$ and $\theta = \Omega' t/2$. The probability of finding atoms at their excited states can be expressed as $P_e(t) = |c_e|^2 = \frac{\Omega^2}{\Omega'^2}\sin^2\theta$. As shown in Fig. 2.4**b**, $P_e(t)$ oscillates periodically which is referred to as the Rabi oscillation. From the expression of P_e, the on-resonance case ($\Delta = 0$) gives the maximum of the oscillation amplitude and period. In this case, a radiation pulse with a length of $\pi/(2\Omega)$ (π/Ω) is called $\pi/2$ (π)-pulse where $P_e = 0.5$ (1).

The finite lifetime of $|e\rangle$ ($\Gamma \neq 0$) gives rise to the decoherence effect and the amplitude of the Rabi oscillation approaches 0 for a sufficient long driving time ($t \gg \Gamma^{-1}$). This corresponds to the steady state where the population of $|e\rangle$ reads

$$\begin{aligned} \lim_{t\to+\infty} P_e(t) &= \frac{\Omega^2}{2\Omega^2 + 4\Delta^2 + \Gamma^2} \\ &= \frac{1}{2}\frac{I/I_{sat}}{1 + I/I_{sat} + 4\Delta^2/\Gamma^2}, \end{aligned} \tag{2.7}$$

where the saturation intensity is defined by $I/I_{sat} = 2\Omega^2/\Gamma^2$. From this expression we know that a strong driving field ($I \to \infty$) tends to equalize the population between $|g\rangle$ and $|e\rangle$. A derivation of this result using the optical Bloch equations can be found in Ref. [138].

Let us consider the net absorption of a radiation by a sample with N two-level atoms.The steady state is a dynamic equilibrium, where the rate of the absorption is equal to the rate of emission. Three basic processes are involved: stimulated absorption, stimulated emission and spontaneous emission (SE). The first two processes have the same rates for a single atom and the last one gives the dissipation of the radiation field. Supposing the light propagates along z-direction, we can write down the attenuation of the intensity according to Beer's law as

$$\frac{dI(z)}{dz} = -(N_g - N_e)\sigma I(z), \tag{2.8}$$

where $N_i = NP_i$ is the population of $|i\rangle$ ($i = e$ or g) and σ is a parameter called cross section characterizing the rate of the stimulated absorption or emission of a single atom. Considering the energy conversation we have

$$\begin{aligned} &(N_g - N_e)\sigma I = N_e A_{21}\hbar\omega_0, \\ \Longrightarrow\ &\sigma = \frac{P_e A_{21}\hbar\omega_0}{(1 - 2P_e)I} \\ &= \frac{1}{2}\frac{A_{21}\hbar\omega_0}{I_{sat}}\frac{1}{1 + 4\Delta^2 + \Gamma^2}. \end{aligned} \tag{2.9}$$

Here the Einstein coefficient A_{21} is related to the saturation intensity I_{sat} by $A_{21}\hbar\omega_0 = 2\sigma_0 I_{sat}$ with $\sigma_0 = 3\lambda_0^2/2\pi$ [138]. So the cross section reads

$$\sigma(\omega) = \frac{\sigma_0}{1 + 4\Delta^2 + \Gamma^2}. \tag{2.10}$$

This result is important for the understanding of the absorption imaging discussed in section 2.3.

Next I will switch to the discussion of how this simple two-level model can be used to understand the laser cooling and trapping.

2.2.3 The Radiative Forces

The ability of slowing down and trapping the atoms by light can be understood in the context of mechanical effects arose by the so-called radiative forces. There are two kinds of such forces, namely the scattering force and the dipole force. Although they can be treated in a unified manner [139], here we discuss them separately to emphasis their different mechanisms and applications.

Scattering Force

The idea that light has certain momentum and energy dates back to Maxwell in the 19th century. The modern version of this point is coined photon, an elementary particle representing the quantum of all kinds of radiation fields. A photon has definite momentum and energy: $\mathbf{p}_{ph} = \hbar\mathbf{k}, E_{ph} = \hbar\omega$. We already see that the scattering (net absorption) of near-resonance photons by two-level atoms has the same rate as the SE, which is ΓP_e, the inverse of the lifetime of the excited state. The mean momentum of the scattered photons is zero due to the isotropic nature of SE. In this way the momentum, similar to the energy, is transfered from the light field to the atom and we can define a related force as

$$\mathbf{F} = d\mathbf{p}/dt = \mathbf{p}_{ph}\Gamma P_e = \hbar\mathbf{k}\frac{\Gamma}{2}\frac{I/I_{sat}}{1 + I/I_{sat} + 4\Delta^2/\Gamma^2}. \tag{2.11}$$

Here the steady state solution in eq. 2.7 is used. This force is called the scattering force, which has important applications in both optical molasses and MOT.

Dipole Force

Another kind of force is caused by the interaction between the electric field gradient of a laser field and the induced dipole of the atom. Let us consider the case that a two-level atom is driven by a far-off-resonance light field ($\Delta \gg \Gamma, \Omega$). Although the scattering force could be neglected due to the large detuning, the energy levels of the atom are shifted by the light. For a two-level atom, these shifts can be calculated by diagonalizing the Hamiltonian in Eq. 2.3, where the eigenvalues read

$$\begin{aligned} E_{\pm} &= \hbar \frac{-\Delta \pm \sqrt{\Delta^2 + \Omega^2}}{2} \\ &\approx \hbar \frac{-\Delta \pm \Delta(1 + \frac{\Omega^2}{2\Delta^2})}{2}. \end{aligned} \tag{2.12}$$

The energy shift of the ground state is given by $U = E_+ = \frac{\hbar\Omega^2}{4\Delta} = \frac{\hbar\Gamma^2}{8\Delta I_{sat}} I$. This is called AC stark shift and the saturation intensity $I_{sat} = \frac{\hbar\Gamma\omega_0^3}{12\pi c^2}$ [140] can be substituted into the expression to give $U = \frac{3\pi c^2}{2\omega_0^3}\frac{\Gamma}{\Delta} I$. The light intensity typically has a nonuniform spatial distribution and thus the nonuniform energy shift gives rise to a conservative force

$$\begin{aligned} \mathbf{F}(\mathbf{r}) &= -\nabla U(\mathbf{r}) \\ &= -\frac{3\pi c^2}{2\omega_0^3}\frac{\Gamma}{\Delta}\nabla I(\mathbf{r}). \end{aligned} \tag{2.13}$$

This force tends to trap the atom in the lowest (highest) intensity regime for a blue (red) detuning. Although real atoms or molecules have very complex internal structures, this simple picture is a good approximation in many cases [141]. By engineering the intensity distributions, we can create various trapping potentials like harmonic potentials, box potentials, [142] and periodic potentials for atoms or molecules.

For ^{23}Na and ^{87}Rb atoms in our FORT, we have a convenient expression for the trap potential which reads [141]

$$U(\mathbf{r}) = -\frac{3\pi c^2\Gamma}{2\omega_0^3} I(\mathbf{r})\left(\frac{1}{\omega_0 - \omega} + \frac{1}{\omega_0 + \omega}\right), \tag{2.14}$$

where $\omega_0 = \frac{2}{3}\omega_2 + \frac{1}{3}\omega_1$ is the center of D-line doublet with $\omega_{1(2)}$ for the D1 (2) transition frequency.

2.2.4 Optical Molasses and MOT

Optical Molasses

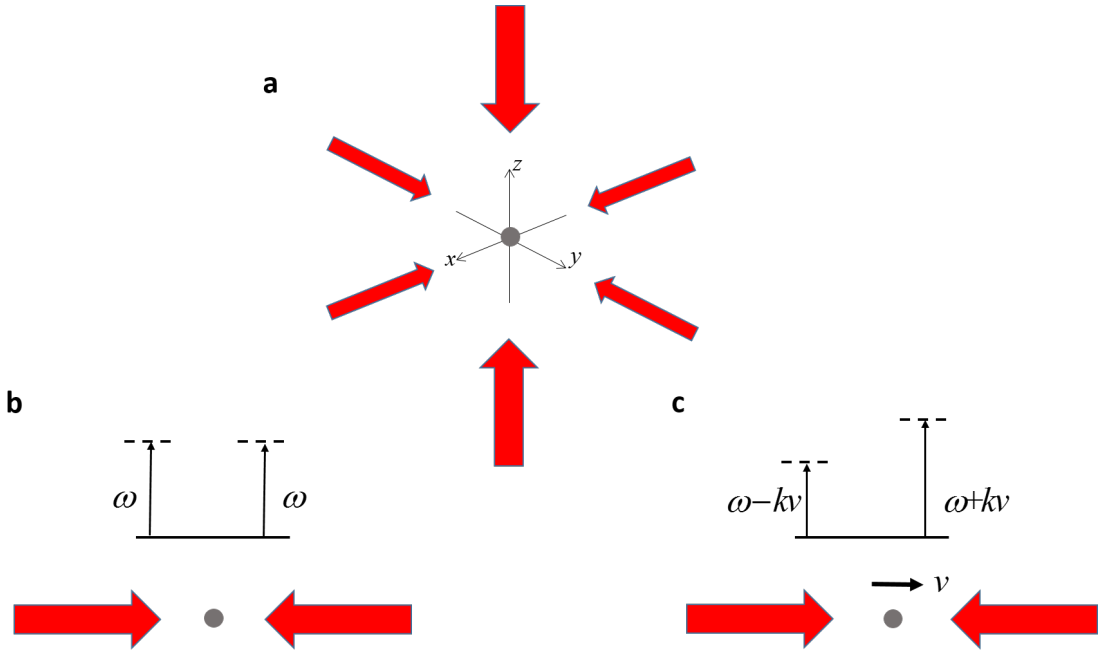

Figure 2.5: 3D optical molasses. **a**, The laser cooling technique that uses the configuration of three pairs of counter-propagating beams is given the name ″optical molasses″. **b**, A stationary atom radiated by a pair of counter-propagating beams. The scattering forces of these two beams cancel each other in this case. **c**, A moving atom radiated by a pair of counter-propagating beams. Now the Doppler effect would give rise to a force imbalance which is the working mechanism of optical molasses.

As shown in Fig. 2.5**a**, a 3D optical molasses is composed of three pairs of counter-propagating laser beams along there orthogonal directions. At the first glance, this configuration is useless as it seems that the scattering forces exerted on the atom by the two counter-propagating beams cancel each other (Fig. 2.5**b**). However, it is not the case for a moving atom with a finite velocity **v**. It experiences a force imbalance due to the Doppler effect, as illustrated in Fig. 2.5**c**. The net force

exerted on the atom reads

$$\begin{aligned} F_{net} &= \hbar k \frac{\Gamma}{2}[\frac{I/I_{sat}}{1+I/I_{sat}+4(\omega-kv-\omega_0)^2/\Gamma^2} - \frac{I/I_{sat}}{1+I/I_{sat}+4(\omega+kv-\omega_0)^2/\Gamma^2}] \\ &\approx 4\hbar k^2 \frac{I}{I_{sat}} \frac{2\Delta/\Gamma}{(1+4\Delta^2/\Gamma^2)^2} v \\ &= -\alpha v, \end{aligned} \tag{2.15}$$

with $\alpha = -4\hbar k^2 \frac{I}{I_{sat}} \frac{2\Delta/\Gamma}{(1+4\Delta^2/\Gamma^2)^2}$. Here we have assumed that the atom moves with a low velocity $kv \ll \Gamma$ and the radiation has a low intensity $I/I_{sat} \ll 1$. This is a dissipative force when the detuning is red (negative) and the kinetic energy of the atom would be reduced in this case:

$$\frac{dE}{dt} = F_{net} v = -\frac{2\alpha E}{M}. \tag{2.16}$$

From this equation we may conclude that the atom could come to an absolute stop by this cooling force. However, it is wrong for here we have neglected any possible heatings coming along with the cooling process. A proper model to explain the heatings assume that the random transfer of the linear momentum causes a random walk of the atomic momentum. The mean square of the momentum $\langle \hbar^2 k^2 \rangle$, hence the mean kinetic energy, would increase in a random-walk model. According to that model, the rate of increasing $\langle \hbar^2 k^2 \rangle$ is $\Gamma P_e \hbar^2 k^2$ and the heating rate is $\Gamma P_e \frac{\hbar^2 k^2}{2M}$. The minimum temperature is reached when the cooling and heating balance each other. At that point we have the temperature $T = \frac{\hbar\Gamma}{4k_b}(\frac{\Gamma}{\Delta} + \frac{4\Delta}{\Gamma})$. So the lowest achievable temperature, called the Doppler cooling limit T_{D}, is achieved when $\Delta = \Gamma/2$ and $T_{\mathrm{D}} = \hbar\Gamma/2k_b$. For ^{23}Na and ^{87}Rb the Doppler limit are 470 µK and 300 µK, respectively.

MOT

The configuration of MOT is shown in Fig. 2.6**a**. It is composed of an optical molasses together with an anti-Helmholtz pair of coils. Each pair of laser beams consists of light with orthogonal circular polarizations. The center of the anti-Helmholtz coils is placed inside the overlap area of the light beams and they produce a magnetic field gradient in the 3D space (see section 2.4.1).

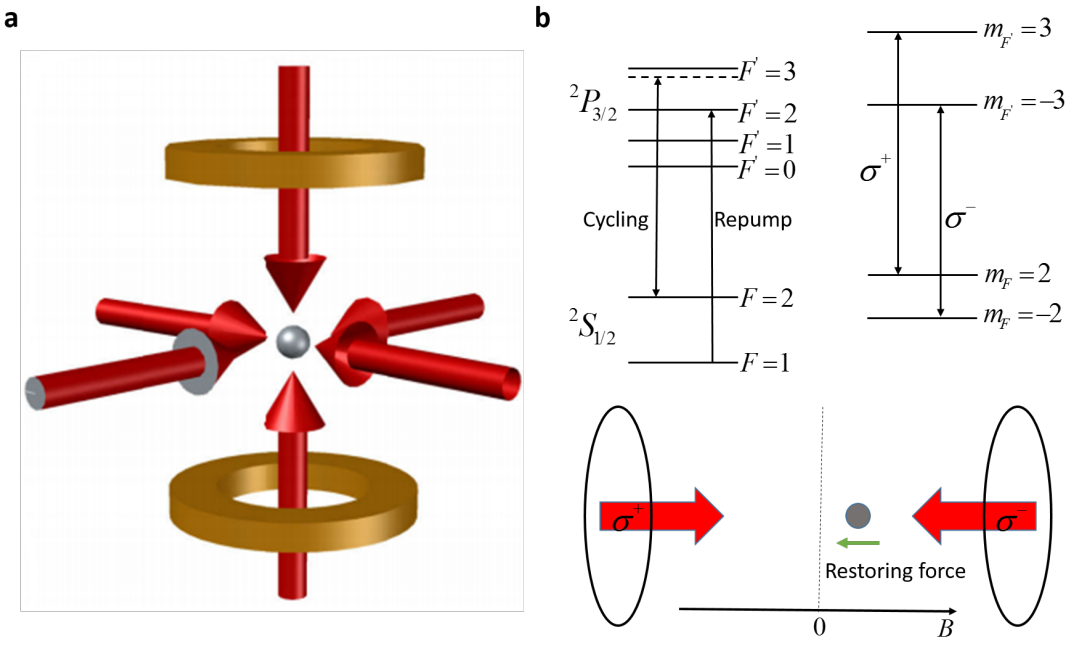

Figure 2.6: The configuration of MOT. **a**, Three orthogonal pairs of laser beams are crossed at the center of an anti-Helmholtz coil placed along the z axis. The atoms are cooled and accumulated around this center. **b**, Each pair is composed of two counter-propagating beams with orthogonal circular polarizations. Atom away from the magnetic field minimum (center) experiences a restoring force due to the presence of the magnetic field gradient in this configuration.

Hundreds of thousands times of scattering are necessary to cool a room-temperature atom down to the sub-millikelvin regime. So the cooling is only possible with the existence of a cycling transition where a nearly closed two-level system is formed. Due to the similar atomic structure of ^{23}Na and ^{87}Rb atom, both their cycling transitions are occurred between the state $\left|^2S_{1/2}, F = 2\right\rangle$ and the state $\left|^2P_{3/2}, F' = 3\right\rangle$, as illustrated in Fig. 2.6b. However, the atoms can still be excited to the $F' < 3$ states which would decay back to the ground $F = 1$ state. Then those atoms are invisible to the cycling light. To save them, another light, named repump light, is added to drive the transition between $F = 1$ and $F' = 2$ states. The combination of the cycling and the repump light is sufficient to cool the atoms down to the

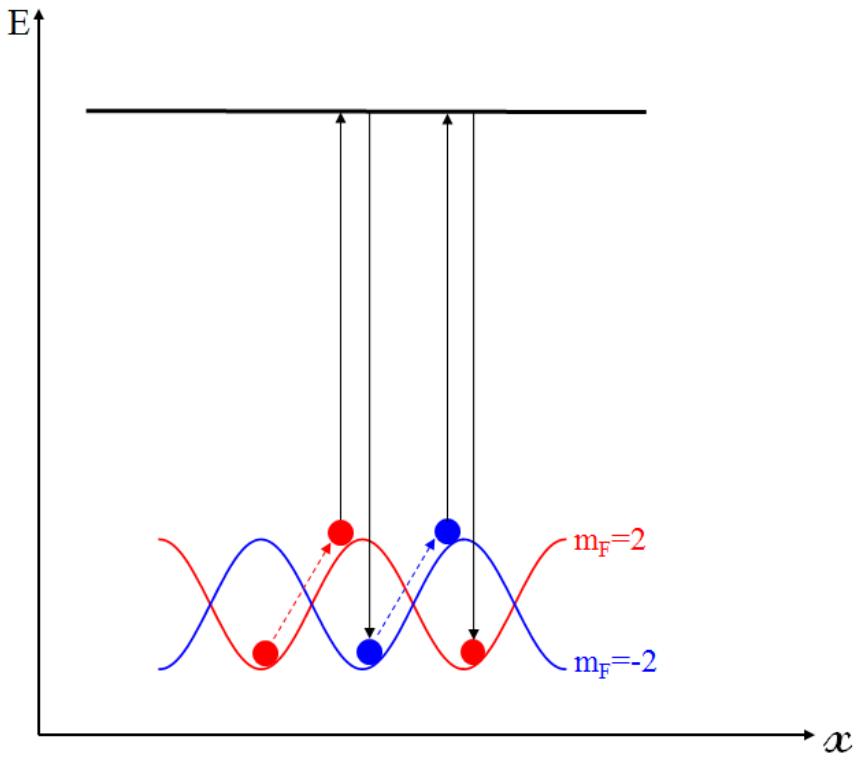

Figure 2.7: The working principle of Sisyphus cooling. The counter-propagating light beams create different potential landscapes for different magnetic sublevels. With the help of optical pumping, the atoms would continuously climb the potential mountains by losing their kinetic energies. The achievable temperature with this cooling process is well below the Doppler cooling limit.

Doppler limit.

To explain the trapping mechanism in a MOT, let us consider that a rest atom sits at some small positive magnetic field away from the center of the coils, as shown on the bottom of Fig. 2.6**b**. Compared to the zero-field case where the cycling transition is red-detuned, at this positive field the detuning of the σ^+ and σ^- cycling transitions become larger and smaller, respectively. Thus based on the discussion of the scattering force in previous subsection, the atom would scatter more σ^- photons and experience a restoring force pointing to the center. The similar argument can be made when the direction of the magnetic field is reversed if we note that the roles of the two beams exchange in that case.

In real experiments the achieved lowest temperature in a MOT or an optical molasses is well below the Doppler cooling limit thanks to the so-called Sisyphus cooling or polarization gradient cooling. The working principle of this sub-Doppler cooling method is illustrated in Fig. 2.7. The counter-propagating beam pair creates a standing wave with an alternating polarization with the order: σ^+, π, σ^- and π. This polarization gradient gives different potential landscapes for different magnetic sublevels. When an atom moves toward the local potential maximum, its kinetic energy is transfered to the potential energy. Near the maximum, the atom is then optically pumped to the local potential minimum of another sublevel. In this way it is continuously cooled by climbing the potential mountains, like Sisyphus in Greek mythology. With this cooling method the lowest temperature achieved in our lab is about 50 µK for ^{23}Na and 20 µK for ^{87}Rb.

2.2.5 Laser Setup For Two-species Vapor Cell MOT

To work with two kinds of atoms, a two-species vapor cell MOT is constructed on our vacuum optical table. As already seen in Fig. 2.1, an homemade anti-Helmholtz pair is placed outside the glass cell which is common for both species. For each of them, six beams forming three orthogonal pairs compose a 3D optical molasses and every corresponding beam of ^{23}Na and ^{87}Rb are overlapped using a polarizing beamsplitter (PBS) cube. However, with this configuration the ^{23}Na and ^{87}Rb clouds would suffer from huge heteronuclear collisional losses due to their perfect spatial overlap and it is especially heavy for the minor ^{23}Na atoms. To avoid such losses, a nearly on-resonance beam for the ^{87}Rb cycling transition is turned on during the MOT loading process, which could push the ^{87}Rb cloud away from the ^{23}Na cloud. This beam, called pushing beam by us, is essential for the successful loading of ^{23}Na MOT.

For ^{87}Rb, we use three home-made lasers working near 780 nm (^{87}Rb D2 line) to generate the MOT beams, as well as the pushing, optical pumping and imaging beams (see explanation latter). The cycling light comes from a diode laser with a maximum output power of 300 mW which is injection-locked by a master laser. Both this master laser and the repump laser generating the repump light are tunable external cavity diode lasers (ECDLs). The longitudinal modes of them are locked to the proper atomic transitions by the standard saturated absorption

spectroscopy. The pushing beam, which is also used as the imaging beam, is delivered from the cycling master laser. Meanwhile, the optical pumping light comes from the repump laser.

The D2 transition for ^{23}Na atoms locates near 589 nm and the light source is a Raman fiber amplifier (RFA) laser. Previously a dye laser (DYE-SF-077) was used and we suffered a lot from the long-term drifting of the output power and direction. The description of it can be found in the thesis of Xiaoke Li [143], one of our former group members. The new RFA laser is much stable with a maximum output power of 1.5 W. It operates with a seed laser at 1178 nm which is a commercial ECDL (LYNX-S3-1180-100). The seed light is coupled into the RFA with an optical fiber and then amplified by the RFA. The output of the RFA is frequency-doubled to 589 nm by a PPLN crystal. The seed power is typically about 20 mW and we lock the final yellow light to one of the ^{23}Na atomic transitions using the modulation transfer spectroscopy.

ECDL

A bare diode laser has the drawbacks of wide linewidth and poor tunability. By providing a frequency-dependent optical feedback to the diode we can overcome these drawbacks. The ECDL, a common example, is to form an external cavity between the diode and a grating which functions as the frequency selective element. With a Littrow configuration, the first-order diffraction from a reflective grating is coupled back into the diode and the directly reflected light is guided out as the output. Two important parameters, the grating constant N and the diffraction efficiency η, are carefully considered to choose a proper grating. The grating equation reads

$$\frac{1}{N}(\sin\theta_i + \sin\theta_m) = m\lambda, \tag{2.17}$$

where m, θ_i, θ_m and λ is the diffraction order, the incident angle, the m-order diffraction angle and the light wavelength, respectively. To get a enough output power with stable performance, η is often chosen to be among the range of $10 \sim 30\%$.

Our homemade ECDL is based on the design in Ref. [144]. For us, $m = 1, \theta_i = \theta_m = 45^\circ$ and $\lambda = 780$ nm. These give that $N \approx$1800/mm. We choose one of the gratings from Thorlabs (GH13-18U) with N =1800 lines/mm and $\eta \approx 28\%$ for our purpose. A photograph of our ECDL is shown in Fig. 2.8, where all the essential

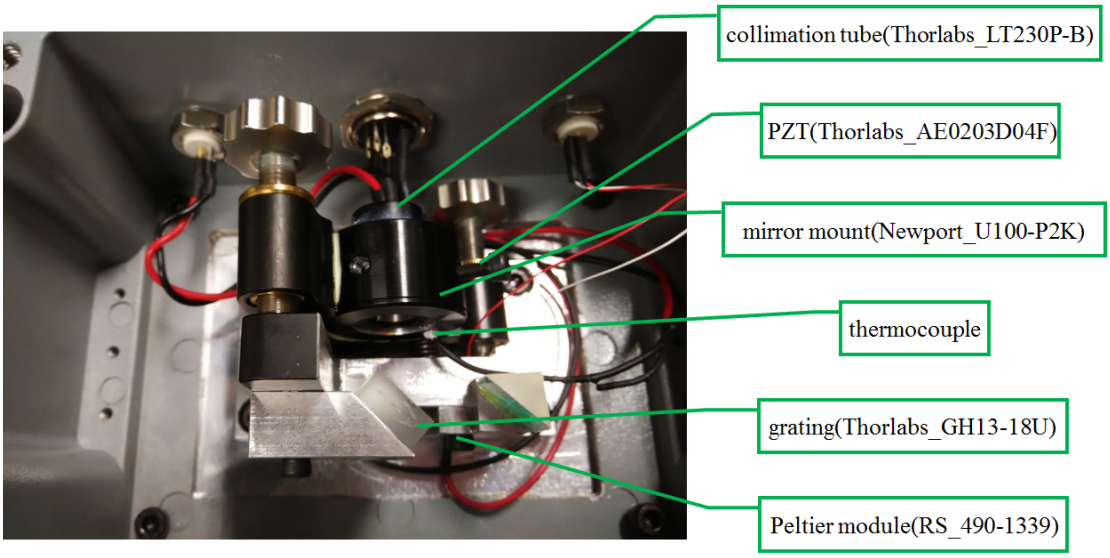

Figure 2.8: Photograph of our homemade ECDL. It is in a Littrow configuration and the tuning of the laser frequency is finished with a PZT stack. The direction of the output beam is kept almost fixed with the help of a mirror parallel to the grating. See text for detailed description.

components are mounted on a modified mirror mount (Newport_U100-P2K). The grating and a parallel mirror are fixed to the front plate of the mount. This mirror helps keep the beam direction of the output light almost fixed. The laser diode and an aspheric lens are mounted into a collimation tube (Thorlabs_LT230P-B) to provide a well collimated light beam which is important for the optical feedback. The temperature of the system is sensed with a thermocouple and actively controlled by a Peltier module installed between the mirror mount and an Aluminum block. This block serves as the heating sink. The grating-mirror pivot arm can be adjusted manually with the tuning screw to couple back the diffracted light and tune the laser frequency. We also use a piezoelectric transducer (PZT) stack to drive it. With a total length of about 20 mm between the grating and the diode, we can reduce the laser linewidth down to 1 MHz.

Besides the aforementioned two ECDLs, we have several other ones. For example, the Raman lasers used to do the STIRAP transfer and the seed laser for the RFA are all commercial ECDLs. Other kinds of diode lasers, like the distributed feedback laser (DFBL), are also commonly used in our lab. One profound exam-

ple is that we have used a DFBL to do the absorption imaging of ^{87}Rb at a high magnetic field.

Saturated Absorption Spectroscopy

The saturated absorption spectroscopy is a basic technique in experimental atomic physics to resolve the atomic transitions below the Doppler-broadened linewidth at room temperature. A pump-probe scheme is adopted in this technique to realize the Doppler-free spectroscopy, as shown in Fig. 2.9**a**. A relatively high intensity beam, referred to as the pump beam, is sent to the atomic vapor. Another counter-propagating probe beam with the same frequency but a lower intensity is overlapping with the pump beam. The absorption of the probe beam is recorded versus the light frequency.

Due to the Doppler effect, the two beams are absorbed by the same amount of atoms only when the frequency is on-resonance with one of the atomic transitions or it is tuned to one of the crossovers of two transitions. For simplicity, we deal with the former case and the latter one is easy to get by extending the formalism here.

Assuming a single excited state, the pump beam would equalize the population between the excited state and ground state among those atoms. With the Maxwell-Boltzmann distribution of atomic velocities $f(v) = \sqrt{\frac{M}{2\pi k_b T}} e^{-\frac{Mv^2}{2k_b T}}$ and the absorption cross section $\sigma(\omega) = \sigma_0 \frac{\Gamma^2/4}{(\omega-\omega_0)^2+\frac{1}{4}\Gamma^2(1+I/I_{sat})}$, the absorption coefficient of the probe beam can be written as

$$\begin{aligned} a(\omega) &= n \int f(v)[\rho_1(v) - \rho_2(v)]\sigma(\omega - kv)dv \\ &= n \int f(v)[1 - 2P_e(\omega + kv)]\sigma(\omega - kv)dv \\ &= n \int f(v)\frac{\sigma_0}{2}\frac{1 + 4(\Delta + kv)^2/\Gamma^2}{[1 + I/I_{sat} + 4(\Delta + kv)^2/\Gamma^2][1 + I/I_{sat} + 4(\Delta - kv)^2/\Gamma^2]}dv \end{aligned} \tag{2.18}$$

Here n is the atomic density, $\rho_i(v)$ is the steady state population of the ground (excited) state with atomic velocities v for $i = 1(2)$ and $\Delta = \omega - \omega_0$. In the integrand both $P_e(\omega + kv)$ and $\sigma(\omega - kv)$ act like delta functions and when $\Delta = 0$, $a(\omega)$ gets a local minimum.

The absorption coefficient versus the detuning is plotted in Fig. 2.9**b** and we can see that a small hole is burnt into a Gaussian background which is known as

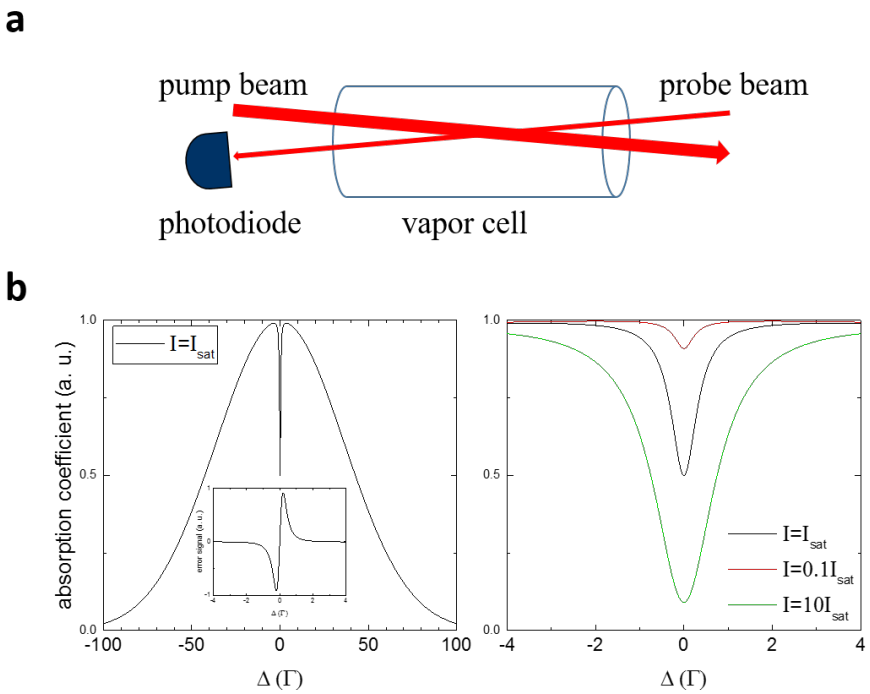

Figure 2.9: The saturated absorption spectroscopy. **a**, A pump-probe scheme is adapted to realize the Doppler-free spectroscopy. See text for the description. **b**, The absorption coefficient of the probe beam versus the laser detuning. Left: A hole is burnt in a wide Gaussian background and the inset shows the differential curve of this absorption line shape. Right: The burnt holes at three different pump powers are compared (see text).

hole burning. The full width at half maximum (FWHM) of the hole is on the order of the nature linewidth of the excited state. When increasing the pump power, the FWHM of the hole will be broadened and its depth is increased, as seen in the right plot of Fig. 2.9**b**. For multilevel atoms, if we have two atomic resonances with frequencies ω_1 and ω_2, both beams could also interact with the atoms around the velocity $v = \frac{|\omega_1 - \omega_2|}{k}$ and a hole is burnt at the frequency of $\frac{\omega_1 + \omega_2}{2}$.

This technique is used to lock the laser frequency to one of the burnt holes. We utilize the slope of the absorption line shape around the hole as the error signal which is fed back to the current and the PZT controller to stabilize the frequency. The error signal, shown in the inset of Fig. 2.9**b**, is got by the dither technique.

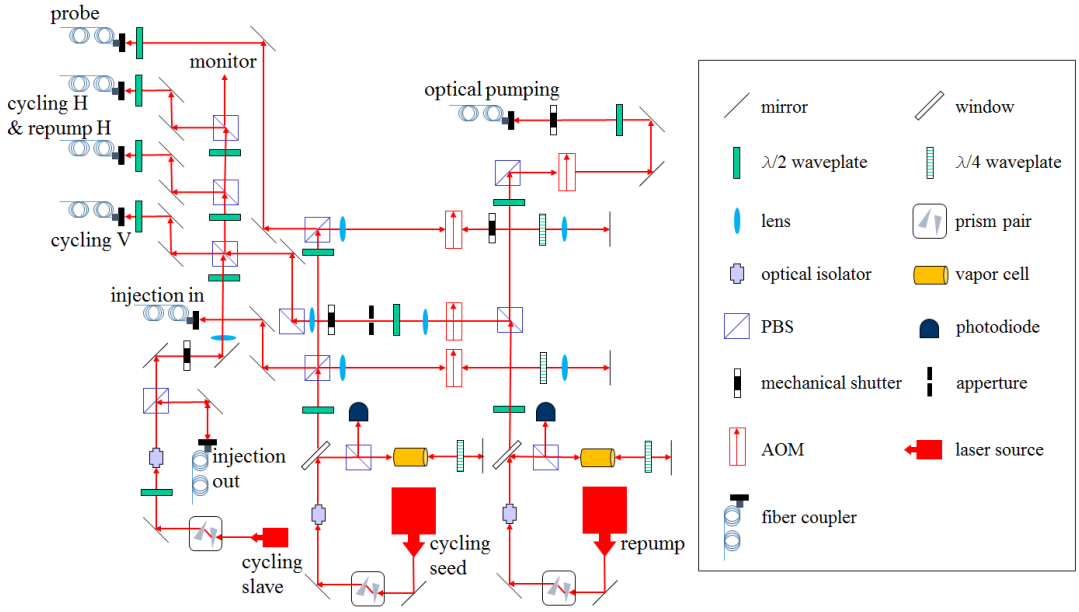

Figure 2.10: Optical layout on the ^{87}Rb optical table. Totally three homemade diode lasers are used to generate six MOT beams, one imaging (pushing) beam and one optical pumping beam all of which are delivered to the vacuum table using PM single mode fibers. See text for the locking of the lasers.

For the ECDLs, we modulate the current with a small amplitude 50 kHz sinusoid which is a frequency modulation and then the absorption signal is differentiated using a frequency mixer to give the error signal. For the 589 nm fiber laser the modulation is added to the pump beam by an acousto-optic modulator (AOM) where both the frequency and amplitude are modulated. This modulation would be transfered to the absorption signal and then it is processed almost the same as that in the ECDL case.

Optical Layout

The real laser setups for the MOT operation in our lab are sketched in Fig. 2.10 and 2.11 for ^{87}Rb and ^{23}Na respectively.

For ^{87}Rb, the cycling master laser is locked to the crossover of $\left|^2S_{1/2}, F = 2\right\rangle \rightarrow \left|^2P_{3/2}, F' = 1, 3\right\rangle$ transitions at 384.227 903 THz. A portion of 20 mW light is sent to double pass a +96 MHz AOM and then coupled into a fiber as the injection

for locking the slave laser. Thus the slave laser receives a injection of ∼2 mW and works at 384.228 095 THz. This corresponds to a detuning of -20 MHz to the cycling transition. Another small portion of the master laser light is used as the imaging (pushing) light after double passing a +106 MHz AOM. The repump laser, locked to the crossover of $\left|^2S_{1/2}, F=1\right\rangle \rightarrow \left|^2P_{3/2}, F'=1,2\right\rangle$ transitions at 384.234 605 THz, provides the repump and optical pumping light with frequency shifts of +79 MHz and -67 MHz respectively.

The ^{23}Na fiber laser frequency is transfered by an double-pass AOM and then locked to the $\left|^2S_{1/2}, F=2\right\rangle \rightarrow \left|^2P_{3/2}, F'=3\right\rangle$ transition (508.848 094 THz). The transfer AOM works at +139.9 MHz and thus the output light of our fiber laser has a frequency of 508.848 234 THz. About 500 mW light is enough for our experiments. A portion of this power passes a -80.7 MHz AOM twice which gives a detuning of -21.5 MHz to the cycling transition. Another portion of the output light is send to pass an AOM for four times and most of its power is used as the repump light with a +391.4 MHz driving frequency. The optical pumping light is got when this four-pass AOM works at 385.1 MHz. The imaging light works nearly on-resonance with the cycling transition after a double-pass -69.9 MHz AOM.

2.2.6 FORT

Our FORT is composed of two crossed 1070 nm Gaussian beams at an angle of 61° in the horizontal plane, as shown in Fig. 2.12. The intensity distribution of a Gaussian beam is expressed as

$$I(x,y,z) = \frac{2P}{\pi w(z)^2} \exp\left[-\frac{2r^2}{w(z)^2}\right], \tag{2.19}$$

where $r = \sqrt{x^2+y^2}$ is the radial distance from the central axis, z is the axial position starting from the beam focus, P is the laser power and $w(z)$ is the transverse size at z. The transverse size at the focus $w(0)$ is denoted as w_0 and referred to as the beam waist. The explicit expression for the beam size is $w(z) = w_0\sqrt{1+(\frac{z\lambda}{\pi w_0^2})^2}$. The Rayleigh range, $z_R = \frac{\pi w_0^2}{\lambda}$, represents the distance where the transverse size is increased by a fact of $\sqrt{2}$.

With the limit of $r \ll w_0$ and $z \ll z_R$, the intensity can be approximated by

$$I(x,y,z) = \frac{2P}{\pi w_0^4}(-2r^2 - z^2\frac{w_0^2}{z_R^2} + w_0^2). \tag{2.20}$$

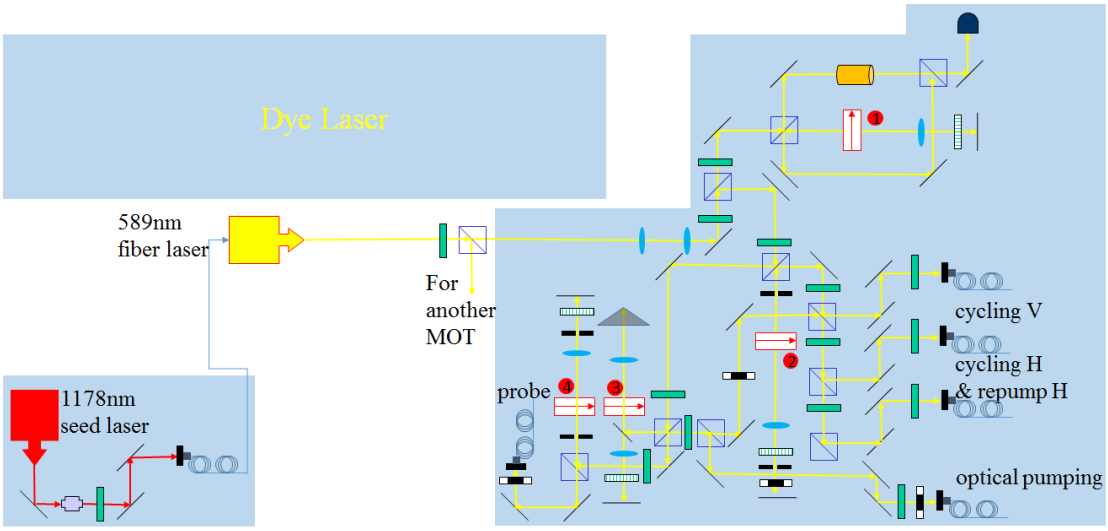

Figure 2.11: Optical layout on the ^{23}Na optical table. The working frequencies for the labeled four AOMs are: 1. +139.9 MHz for the modulation transfer spectroscopy 2. -80.7 MHz for the cycling light 3. +391.4 MHz for the repump light and +385.1 MHz for the optical pumping light 4. -69.9 MHz for the imaging light.

The trap potential associated with this intensity distribution reads

$$U(x,y,z) = -\frac{3\pi c^2\Gamma}{2\omega_0^3}\left(\frac{1}{\omega_0-\omega}+\frac{1}{\omega_0+\omega}\right)\frac{2P}{\pi w_0^4}\left(-2r^2-\frac{\lambda^2}{\pi^2 w_0^2}z^2+w_0^2\right). \quad (2.21)$$

This is a harmonic potential which can be written as $U(x,y,z) = \frac{1}{2}M\omega_x^2x^2 + \frac{1}{2}M\omega_y^2y^2+\frac{1}{2}M\omega_z^2z^2$ with the angular frequency $\omega_i = \sqrt{\partial_i^2 U/M}|_{x,y,z=0}$ for $i = x, y, z$. Typically the radial confinement is much stronger than the axial confinement ($\omega_{x,y} \ll \omega_z$) due to the fact that $\lambda \ll \omega_0$. The trap depth U_0 is defined as the minimum energy for a stationary particle to escape from the trap and here $U_0 = \frac{3\pi c^2\Gamma}{2\omega_0^3}\left(\frac{1}{\omega_0-\omega}+\frac{1}{\omega_0+\omega}\right)\frac{2P}{\pi w_0^2}$.

FORT Parameter

With the configuration described above, we can calculate out the trap parameters, namely the trap depth and the trap frequency, for atoms and molecules.

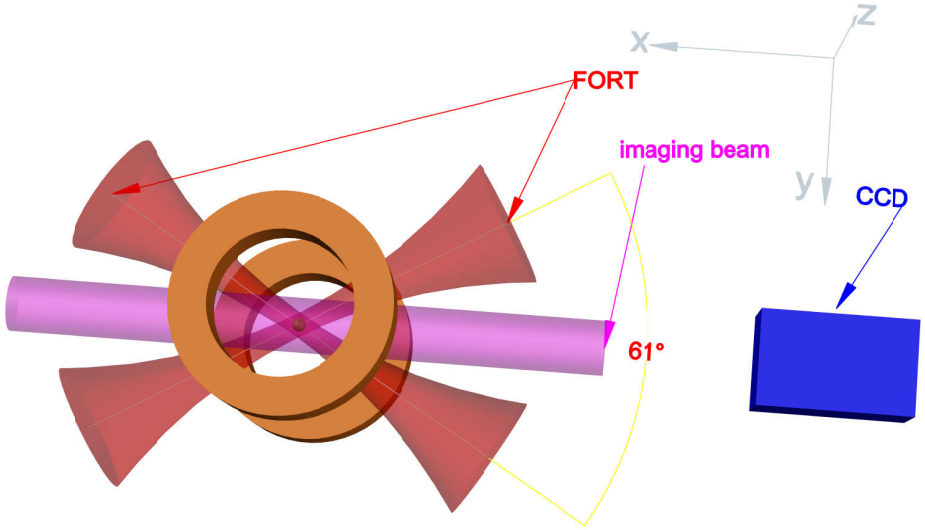

Figure 2.12: Crossed FORT. Two 1070 nm Gaussian beams cross at an angle of 61° in the horizontal plane with their focuses coincided. The coordinate system is also indicated with the origin at the beam focuses. See text for the calculation of the trap potential.

The trap potential for either ^{23}Na or ^{87}Rb atoms can be expressed in the following formula including the gravitational potential

$$\begin{aligned}
U(x,y,z) = &-\frac{3\pi c^2\Gamma}{2\omega_0^3}\left(\frac{1}{\omega_0-\omega}+\frac{1}{\omega_0+\omega}\right)\left[I_1\left(x\sin\frac{\theta}{2}+y\cos\frac{\theta}{2}, z, x\cos\frac{\theta}{2}-y\sin\frac{\theta}{2}\right)\right.\\
&\left.+I_2\left(-x\sin\frac{\theta}{2}+y\cos\frac{\theta}{2}, z, x\cos\frac{\theta}{2}+y\sin\frac{\theta}{2}\right)\right]+M_a g z\\
\approx &-\frac{3\pi c^2\Gamma}{2\omega_0^3}\left(\frac{1}{\omega_0-\omega}+\frac{1}{\omega_0+\omega}\right)\left\{\frac{2P_1}{\pi w_1^4}\left[-2\left(x\sin\frac{\theta}{2}+y\cos\frac{\theta}{2}\right)^2-2z^2\right.\right.\\
&\left.-\frac{\lambda^2}{\pi^2 w_1^2}\left(x\cos\frac{\theta}{2}-y\sin\frac{\theta}{2}\right)^2+w_1^2\right]+\frac{2P_2}{\pi w_2^4}\left[-2\left(-x\sin\frac{\theta}{2}+y\cos\frac{\theta}{2}\right)^2-2z^2\right)\\
&\left.-\frac{\lambda^2}{\pi^2 w_2^2}\left(x\cos\frac{\theta}{2}+y\sin\frac{\theta}{2}\right)^2+w_2^2\right]\right\}+M_a g z,
\end{aligned} \tag{2.22}$$

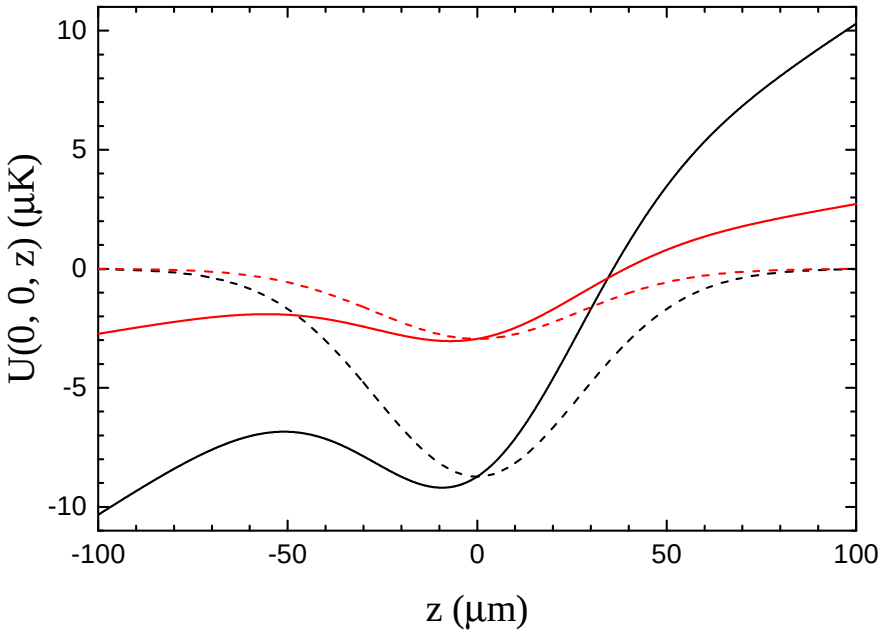

Figure 2.13: The gravitational effect on the FORT. We plot the trap potential along the vertical axis for both species with and without the gravitational potential. The presence of gravitation would cause a gravitational sag and lower the trap depth. Comparing the potential between different species in our trap, we know that the ^{23}Na atom have a smaller trap depth and a larger trap frequency thus a smaller the gravitational sag.

here θ is the acute angle between two beams, M_a is the atomic mass, g is the gravitational acceleration and the harmonic approximation is adapted. Based on this expression we can get the trap frequencies $\omega_i (i = x, y, z)$ by diagonalizing the Hessian matrix of the potential $U(x, y, z)$. Then the potential is rewritten as

$$\begin{aligned} U(x,y,z) &= U_0 + \frac{1}{2}M_a\omega_x^2 x^2 + \frac{1}{2}M_a\omega_y^2 y^2 + \frac{1}{2}M_a\omega_z^2 z^2 + M_a g z \\ &= U_0 - \frac{M_a g^2}{2\omega_z^2} + \frac{1}{2}M_a\omega_x^2 x^2 + \frac{1}{2}M_a\omega_y^2 y^2 + \frac{1}{2}M_a\omega_z^2 (z + \frac{g}{\omega_z^2})^2, \end{aligned} \tag{2.23}$$

with $U_0 = \frac{3\pi c^2 \Gamma}{2\omega_0^3}(\frac{1}{\omega_0 - \omega} + \frac{1}{\omega_0 + \omega})\frac{\pi}{2}(\frac{P_1}{w_1^2} + \frac{P_2}{w_2^2})$. From the above equation, we can see that the potential minimum is shifted vertically by g/ω_z^2 due to the gravitation and this shift is called the gravitational sag. It also affects the trap depth in the vertical direction, especially when the trap power is low. An example is given in

Fig. 2.13 where the $U(0,0,z)$ versus z is plotted. From the figure, it is quite clear that the trap depth is lowered due to the gravitation. Also we see that the trap depth of ^{23}Na atom is smaller than that of ^{87}Rb atom in a 1070 nm trap. The ratio of the trap frequencies for different species is given by

$$\omega_i^{Na}/\omega_i^{Rb} = \sqrt{\frac{M_{Rb}}{M_{Na}} \frac{\frac{1}{\omega_{0Na}-\omega} + \frac{1}{\omega_{0Na}+\omega}}{\frac{1}{\omega_{0Rb}-\omega} + \frac{1}{\omega_{0Rb}+\omega}} \frac{\omega_{0Rb}^3}{\omega_{0Na}^3} \frac{\Gamma_{Na}}{\Gamma_{Rb}}} \approx 1.13. \tag{2.24}$$

Thus the larger trap frequency in the vertical direction would give rise to a smaller gravitational sag for ^{23}Na.

For the molecular states the calculation of the trap potential starting from the molecular structures is too complex to be completed by ourselves. Our theoretical collaborators from France provide us the data of the polarizability α for the Feshbach and ground molecular states of ^{23}Na^{87}Rb in the 1070 nm light. In this case the potential can be calculated by $U(x,y,z) = -\frac{1}{2\varepsilon_0 c}\,\mathrm{Re}(\alpha)[I_1(x\sin\frac{\theta}{2} + y\cos\frac{\theta}{2}, z, x\cos\frac{\theta}{2} - y\sin\frac{\theta}{2}) + I_2(-x\sin\frac{\theta}{2} + y\cos\frac{\theta}{2}, z, x\cos\frac{\theta}{2} + y\sin\frac{\theta}{2})] + M_m g z$ and then we follow the same steps as that of atoms to get the trap depth and trap frequencies.

2.3 Imaging System

The imaging system is important for almost all the quantum gas experiments. Any reliable and necessary information is obtained by the optical imaging based on the light-matter interaction. As already discussed in the previous section, a two-level atom shed by a monochromatic light could undergo the absorption, emission and phase shift, where the last one corresponds to the AC stark shift. By monitoring the affected light field with a CMOS camera we could gain the information about the atomic samples.

The fluorescence imaging, done by shining a near-resonance light and collecting the spontaneously emitted photons, typically has a low signal-to-noise ration (SNR) due to the fact that only a small portion of the isotropically distributed photons reaches the detector (proportional to the solid angle expanded by the imaging lens). The absorption imaging has a much larger SNR, recording the light field after it passes the atomic cloud which is a effective record of all the scattered

photons. However, this method is difficult to be applied for a very dense sample where the complete absorption of the light would happen. To overcome this difficulty the cloud is released from the trap and allowed to expand for certain times to reduce the density to a acceptable level. This is called time-of-flight (TOF).

Both methods above are destructive of the samples because of the heating caused by the photon recoils. Other methods, based on the phase shift with a far-off-resonance light, affect the samples less and they are used to obtain the in-situ images. The dark-ground or phase contrast imaging detect the interference of the scattered light with the forward scattered light or unscattered light respectively. However, both ones are not commonly used due to the much complexer setup compared to the fluorescence and absorption imaging.

Following I will describe our imaging system in detail and discuss the diagnosis of harmonically trapped Bose gases.

2.3.1 A Weakly Interacting Bose Gas in Harmonic Traps

The main purpose of imaging is to provide the density distribution of the atomic gases, from which their properties are inferred. This is done by comparing the detected density distributions with some theoretical models. I will present several models for the Bose gases trapped in harmonic traps in this subsection.

Thermal or Near Degenerate Gases

For a weakly interacting thermal or near degenerate gas, the interaction can be neglect if the diluteness $na^3 \ll 1$ is satisfied, where n is the average density and a is the s-wave scattering length. So let us consider a ideal gas with temperature T higher than the Bose-Einstein condensation transition temperature T_c confined in a harmonic trap with a trap potential

$$V(\mathbf{r}) = \frac{1}{2}M\omega_x^2 x^2 + \frac{1}{2}M\omega_y^2 y^2 + \frac{1}{2}M\omega_z^2 z^2. \tag{2.25}$$

In the limit $k_b T \gg \hbar\omega_{x,y,z}$ we can use the semi-classical approximation to deduce the density distribution [145]

$$\begin{aligned} n(\mathbf{r}) &= \frac{1}{(2\pi\hbar)^3}\int d\mathbf{p} f_{BE}(\varepsilon) \\ &= \frac{1}{(2\pi\hbar)^3}\int d\mathbf{p}\frac{1}{e^{(\varepsilon-\mu)/k_bT}-1}, \end{aligned} \tag{2.26}$$

where $f_{BE}(\varepsilon)$ is the Bose-Einstein distribution, μ is the chemical potential and $\varepsilon = \mathbf{p}^2/2M + V(\mathbf{r})$ is the single particle energy. By introducing the quantity $z(\mathbf{r}) = e^{(\mu - V(\mathbf{r}))/k_bT}$ and substituting the energy expression we can rewrite the density as

$$\begin{aligned} n(\mathbf{r}) &= \frac{1}{(2\pi\hbar)^3}\int_0^{2\pi} d\phi \int_0^{\pi} \sin(\theta) d\theta \int_0^{+\infty} \frac{p^2}{z(\mathbf{r})^{-1}e^{p^2/2Mk_bT} - 1} dp \\ &= \frac{2}{\sqrt{\pi}\lambda_T^3}\int_0^{+\infty} \frac{\sqrt{s}}{z(\mathbf{r})^{-1}e^s - 1} ds \\ &= \frac{g_{3/2}(z(\mathbf{r}))}{\lambda_T^3}, \end{aligned} \tag{2.27}$$

where $\lambda_T = \sqrt{\frac{2\pi\hbar^2}{Mk_bT}}$ is the thermal de Brogile wavelength and

$$g_l(x) = \sum_{n=1}^{+\infty} \frac{x^n}{n^l}$$

is called the Bose function. For $V(\mathbf{r}) = 0$ the quantity $z(\mathbf{r})$ reduces to the fugacity. The chemical potential is determined by the total atom number

$$\begin{aligned} N &= \int d\mathbf{r} n(\mathbf{r}) \\ &= \frac{1}{\lambda_T^3}\int g_{3/2}(z(\mathbf{r})) d\mathbf{r} \\ &= \frac{1}{\lambda_T^3}\sum_{n=1}^{+\infty} \frac{z(0)^n}{n^{3/2}} \int e^{-nV(\mathbf{r})/k_bT} d\mathbf{r} \\ &= (\frac{k_bT}{\hbar\bar{\omega}})^3 \sum_{n=1}^{+\infty} \frac{z(0)^n}{n^3} \\ &= (\frac{k_bT}{\hbar\bar{\omega}})^3 g_3(z(0)) \end{aligned} \tag{2.28}$$

with $\bar{\omega} = (\omega_x\omega_y\omega_z)^{1/3}$. The Bose function accounts for the quantum effect in the density distribution of a thermal Bose gas. If only the lowest order contribution is kept we have $z(0) = N(\frac{\hbar\bar{\omega}}{k_bT})^3$ and

$$\begin{aligned} n(\mathbf{r}) &= N\bar{\omega}^3(\frac{M}{2\pi k_bT})^{3/2} e^{-V(\mathbf{r})/k_bT} \\ &= n_{\text{peak}} e^{-\frac{x^2}{2\sigma_x^2} - \frac{y^2}{2\sigma_y^2} - \frac{z^2}{2\sigma_z^2}}, \end{aligned} \tag{2.29}$$

where $\sigma_i = \sqrt{\frac{k_bT}{M\omega_i^2}} (i = x, y, z)$ and $n_{\text{peak}} = N\bar{\omega}^3(\frac{M}{2\pi k_bT})^{3/2} = \frac{N}{(2\pi)^{3/2}\sigma_x\sigma_y\sigma_z}$. This is a Gaussian distribution which coincides with the result of the classical Maxwell-Boltzmann distribution. From the relation $n_{\text{peak}}\lambda_T = g_{3/2}(e^{\mu/k_bT})$ we know that the

chemical potential is negative when the atom number is small or the temperature is high, namely the phase-space-density (PSD) $n_{\text{peak}}\lambda_T \ll 1$. If the PSD approaches the order of 1, the chemical potential will approach zero which means we cannot add extra atoms to the finite-momentum states. The zero chemical potential marks the BEC transition point: $n_{\text{peak}}\lambda_T = g_{3/2}(1) \approx 2.612$ or $N(\frac{\hbar\bar{\omega}}{k_bT})^3 = g_3(1) \approx 1.202$. So the critical temperature is $T_c \approx 0.94\hbar\bar{\omega}N^{1/3}/k_b$.

This semi-classical method can also be used to obtain the density distribution of a thermal gas in a time-of-flight during which it is ballistically expanding. At the expansion time t, the position $\mathbf{r}(t)$ of a particle with initial position $\mathbf{r}_0$ and momentum $\mathbf{p}_0$ can be expressed as $\mathbf{r}(t) = \mathbf{r}_0 + \mathbf{p}_0 t/M$ where the origin is set to the center of mass. The density is given by

$$\begin{aligned}
n_{\text{tof}}(\mathbf{r},t) &= \frac{1}{(2\pi\hbar)^3}\int d\mathbf{r}_0 d\mathbf{p}_0 f_{BE}(\varepsilon)\delta(\frac{\mathbf{p}_0 t}{M} - \mathbf{r} + \mathbf{r}_0) \\
&= \frac{1}{(2\pi\hbar)^3}\int d\mathbf{r}_0 \frac{1}{\exp\{[\frac{\mathbf{p}_0^2}{2M} + V(\mathbf{r} - \frac{\mathbf{p}_0 t}{M}) - \mu]/k_bT\} - 1} \\
&= \frac{1}{(2\pi\hbar)^3}\int d\mathbf{p}_0 \frac{1}{y(\mathbf{r},t)^{-1}\exp\left[\frac{1}{2Mk_bT}\sum_i(1+\omega_i^2t^2)p_{0i}^2\right] - 1} \\
&= \frac{1}{(2\pi\hbar)^3}(2Mk_bT)^{3/2}\prod_i(1+\omega_i^2t^2)^{-1/2}\int d\mathbf{s}\frac{1}{y(\mathbf{r},t)^{-1}e^{\mathbf{s}^2} - 1} \\
&= (\frac{1}{\pi\lambda_T^2})^{3/2}\prod_i(1+\omega_i^2t^2)^{-1/2}\int_0^{2\pi}d\phi\int_0^{\pi}\sin(\theta)d\theta\int_0^{\infty}\frac{\sqrt{s}}{2y(\mathbf{r},t)^{-1}e^s - 1}ds \\
&= \frac{2}{\sqrt{\pi}\lambda_T^3}\prod_i(1+\omega_i^2t^2)^{-1/2}\int_0^{\infty}\frac{\sqrt{s}}{y(\mathbf{r},t)^{-1}e^s - 1}ds \\
&= \prod_i(1+\omega_i^2t^2)^{-1/2}\frac{g_{3/2}(y(\mathbf{r},t))}{\lambda_T^3}
\end{aligned} \tag{2.30}$$

with

$$y(\mathbf{r},t) = \exp\left[(\mu - \sum_i\frac{1}{2}M\frac{\omega_i^2}{1+\omega_i^2t^2}i^2)/k_bT\right](i = x,y,z).$$

For a long expansion time ($t \gg 1/\omega_{x,y,z}$) we have

$$n_{\text{tof}}(\mathbf{r},t) = \frac{g_{3/2}(\exp\left[(\mu - \frac{M\mathbf{r}^2}{2t^2})/k_bT\right])}{\lambda_T^3}. \tag{2.31}$$

Thus, the density distribution of a long expanded gas is isotropic and has the same form as that of a trapped gas..

Bose-Einstein Condensates

The above semi-classical method is inapplicable to a pure condensate where all the particles occupy the lowest-energy state. Eugene P. Gross [146] and Lev P. Pitaevskii [147] have independently derived a equation using the Hartree-Fock approximation and the pseudopotential interaction model to quantitatively describe a weakly interacting BEC. This equation named after them is called G-P equation and reads

$$i\hbar\frac{\partial\Psi}{\partial t} = (-\frac{\hbar^2}{2M}\nabla^2 + V(\mathbf{r}) + U_0\left|\Psi\right|^2)\Psi, \tag{2.32}$$

where $\Psi = \Psi(\mathbf{r}, t)$ is the macroscopic wavefunction of the condensate and $U_0 = \frac{4\pi\hbar^2}{M}a$ is the contact interaction. The three terms on the right-hand side of the equation come from the kinetic energy, trap potential and the interaction energy respectively. The wavefunction can be expressed as $\Psi(\mathbf{r}, t) = \sqrt{n(\mathbf{r}, t)}e^{i\phi(\mathbf{r},t)}$ with the condensate density $n(\mathbf{r}, t)$ and phase $\phi(\mathbf{r}, t)$. The stationary states of this equation $\Psi(\mathbf{r}, t) = \psi(\mathbf{r})e^{-i\mu t/\hbar}$ is given by

$$\mu\psi(\mathbf{r}) = (-\frac{\hbar^2}{2M}\nabla^2 + V(\mathbf{r}) + U_0\left|\psi(\mathbf{r})\right|^2)\psi(\mathbf{r}), \tag{2.33}$$

here μ is the chemical potential. Supposing the spatial extent of the BEC is R, the ground state can be obtained by balancing the competing energies: the kinetic, trap and interaction energy scale as $\frac{\hbar^2}{2MR^2}$, $\frac{1}{2}M\bar{\omega}^2R^2$ and $U_0N/(\frac{4}{3}\pi R^3)$ respectively. For the ideal gas limit ($\left|U_0\right| n \ll \hbar\bar{\omega}$), the balancing of the kinetic and trap energy gives the R on the order of $a_{ho} = \sqrt{\hbar/M\bar{\omega}}$. The ground state wavefunction is the well-known one of the harmonic oscillator ground state and the density has a Gaussian distribution. For a attractive interaction case ($g < 0$), R tends to become smaller and smaller to balance the interaction energy and kinetic energy as the atom number is increased or the interaction becomes stronger. However, due to the very narrow width of the momentum distribution of a BEC the spatial extent has a minimum value according to the uncertainty principle and there exists a critical value of gN where the BEC collapses [148–150]. On the other hand, BEC with a repulsive interaction ($g > 0$) is always stable. The repulsive interaction makes R larger than a_{ho} and there is a limit case where the kinetic energy is negligible compared to the other two energies. This so-called Thomas-Fermi limit is valid when $\frac{Na}{a_{ho}} \gg 1$ and at this limit the stationary G-P equation becomes

$$\mu\psi(\mathbf{r}) = (V(\mathbf{r}) + g\left|\psi(\mathbf{r})\right|^2)\psi(\mathbf{r}). \tag{2.34}$$

The density is obtained by

$$n(\mathbf{r}) = |\psi(\mathbf{r})|^2 = \max\{\frac{\mu - V(\mathbf{r})}{g}, 0\} \tag{2.35}$$

The total atom number N determines the chemical potential μ:

$$N = \int n(\mathbf{r})d\mathbf{r} = \int_{V(\mathbf{r})\leq\mu} \frac{\mu - V(\mathbf{r})}{g} d\mathbf{r} = \frac{1}{15}(\frac{2\mu}{\hbar\bar{\omega}})^{5/2}\frac{a_{ho}}{a}. \tag{2.36}$$

By solving this equation we obtain $\mu = \frac{1}{2}\hbar\bar{\omega}(\frac{15Na}{a_{ho}})^{2/5}$ and the density can be rewritten as

$$n(\mathbf{r}) = \max\{n_{\text{peak}}(1 - \frac{x^2}{R_x^2} - \frac{y^2}{R_y^2} - \frac{z^2}{R_z^2}), 0\} \tag{2.37}$$

where $R_i = \sqrt{\frac{2\mu}{M\omega_i^2}} = a_{ho}\frac{\bar{\omega}}{\omega_i}(\frac{15Na}{a_{ho}})^{1/5}(i = x, y, z)$ are the Thomas-Fermi radii and $n_{\text{peak}} = \mu/g = \frac{15N}{8\pi a_{ho}^3}(\frac{a_{ho}}{Na})^{3/5} = \frac{15N}{8\pi R_x R_y R_z}$ is the peak density. This is a parabolic profile with the zero-value boundary determined by the interaction energy and the trap potential.

The free expansion of the condensate of a idea gas is same as that of a thermal cloud, say becoming isotropic after a long expansion time. However, the expansion is quite different in the Thomas-Fermi region where the nonlinear effect is important. It has been shown that the parabolic profile is kept with a scaled radii $R_i(t)$: $R_i(t) = b_i(t)R_i(0)$. The time-dependent scaling factors satisfy the coupled ordinary different equations:

$$\ddot{b_i} - \frac{\omega_i^2}{b_i b_x b_y b_z} = 0. \tag{2.38}$$

In between the near degenerate gas and the pure condensate is the partially condensed gas where both are present. In equilibrium the thermal and condensed part are respectively described by the semi-classical equations and the G-P equation. The density distribution is the sum of the thermal and condensed component for a trapped or released gas reads

$$n(\mathbf{r}) = n_{\text{th}}e^{-\frac{x^2}{2\sigma_x^2} - \frac{y^2}{2\sigma_y^2} - \frac{z^2}{2\sigma_z^2}} + \max\{n_{\text{BEC}}(1 - \frac{x^2}{R_x^2} - \frac{y^2}{R_y^2} - \frac{z^2}{R_z^2}), 0\}. \tag{2.39}$$

2.3.2 Imaging System Setup

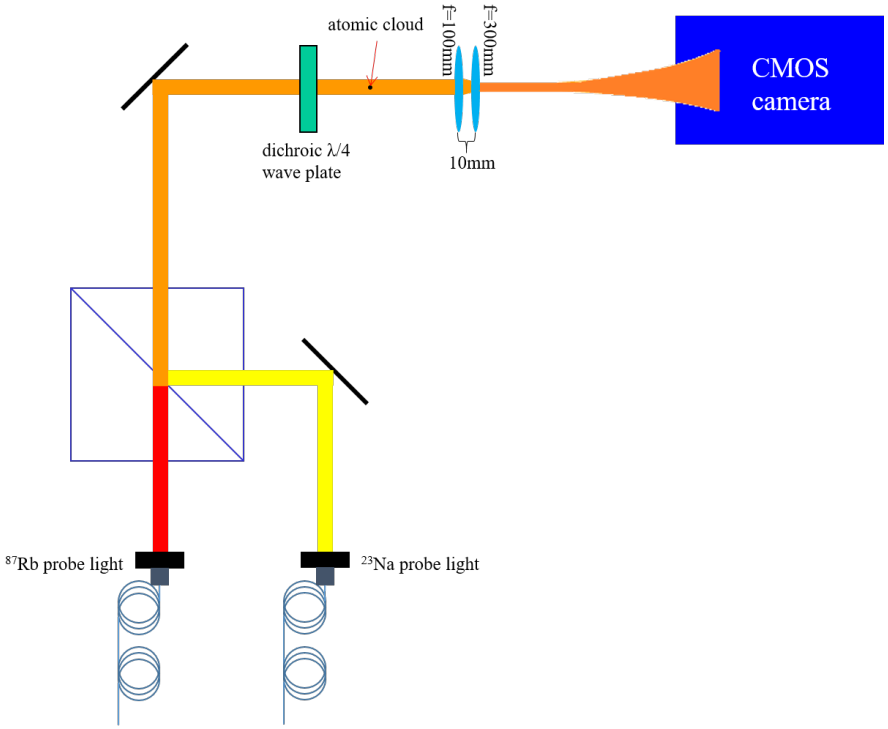

Figure 2.14: Setup of the imaging system. The two probe beams are combined using a PBS cube and then they pass a dichroic $\lambda/4$ wave plate before shining the atoms. The imaging lenses are composed of two convex lenses with f=100 mm and f=300 mm respectively. The atomic cloud is put at the front focus point of the f=100 mm lens and the distance between the two lenses is 10 mm. The CMOS sensor of our camera is at the back focus point of the second lens.

Due to the simplicity and high SNR with the absorption imaging, we have setup such a system to simultaneously image ^{23}Na and ^{87}Rb atoms in our lab, which is shown in Fig. 2.14. Using a PBS cube we combine the two probe lights with orthogonal linear polarizations. Then they pass a dichroic $\lambda/4$ wave plate which change both their polarizations to σ^+. Two achromatic lenses with respective 100 mm and 300 mm focus lengths are placed outside the vacuum cell as the imaging lenses. The atoms are located at the front focal point of the f=100 mm lens while the CMOS sensor is placed at the back focal point of the f=300 mm lens.

The distance between these two lenses is 10 mm. During the early time of my PhD a frame-transfer camera (Apogee Alta U1) was used for imaging. However, it was inefficient for a mixture setup as we were allowed to image only one atomic species for each experimental shot due to the low data transfer rate. Soon after my joining into the group it was replaced by a new one (PCO.Pixelfly USB) which has a interline transfer architecture where each pixel contains both a photodiode and an associated temporary storage region. This design enables the fast transfer of the previous accumulated electrons from the photodiode to the storage region and a second picture can be taken with only several microseconds delay. This new camera helps us image the two species in one experimental run almost simultaneously and makes the data-taking process much more efficient.

2.3.3 Absorption Imaging

The idea of the absorption imaging bases on the Beer's law: The attenuation of the intensity of a radiation by medium obeys the equation

$$\frac{dI}{dx} = -n(x,y,z)a(\omega,I)I, \tag{2.40}$$

here $n(x,y,z)$ is the local density of the medium, the radiation propagates along x-direction and $a(\omega,I)$ is the single atom absorption coefficient. This yields $I = I_{-\infty}e^{-a(\omega,I)\int_{-\infty}^{x} n(x,y,z)dx} = I_{-\infty}e^{-\int_{-\infty}^{x}\mathrm{OD}(x,y,z)dx}$, where the optical density OD is defined as

$$\mathrm{OD}(x,y,z) = a(\omega,I)n(x,y,z). \tag{2.41}$$

The absorption coefficient $a(\omega,I)$ equals to $(P_g - P_e)\sigma(\omega)$ in a two-level model and the expressions for $P_i(i = e,g)$ and $\sigma(\omega)$ have been deduced in section 2.2.2. Substitute these equations into above formula

$$\mathrm{OD}(x,y,z) = n(x,y,z)\frac{\sigma_0}{1 + 4\Delta^2/\Gamma^2 + I/I_{sat}}. \tag{2.42}$$

To calculate the distribution of the OD we have to know the intensity distribution of the radiation before and after its interacting with the sample which can be

recorded by our camera. So we have

$$\begin{aligned}\tilde{\mathrm{OD}}(y,z) &= \int_{-\infty}^{+\infty} \mathrm{OD}(x,y,z) \\ &= -\ln\left(\frac{I_{+\infty}(y,z)}{I_{-\infty}(y,z)}\right) \\ &= \ln\left(\frac{I_i(y,z)-I_b(y,z)}{I_f(y,z)-I_b(y,z)}\right),\end{aligned} \tag{2.43}$$

here I_i, I_f and I_b are the intensity distributions of the three pictures taken with the presence of only probe light, both probe light and atoms and neither probe light nor atoms. $I_{+\infty,-\infty} = I_{i,f} - I_b$, removing the background contribution. One can immediately get the atomic density distribution in the y-z plane

$$\begin{aligned}\tilde{n}(y,z) &= \int_{-\infty}^{+\infty} n(x,y,z)dx \\ &= \frac{\tilde{\mathrm{OD}}(y,z)\sigma_0}{1+4\Delta^2/\Gamma^2+I/I_{sat}}.\end{aligned} \tag{2.44}$$

In previous section we have derived the 3D density distribution for a thermal, partially condensed and fully condensed gas. However, what we detect is the column density which should be compared with the theoretical models with integrated distribution along the probe direction, say x-direction here:

$$\begin{aligned}\tilde{n}_{th}(y,z) &= \int_{-\infty}^{\infty} \frac{N}{(2\pi)^{3/2}\sigma_x\sigma_y\sigma_z} e^{-\frac{x^2}{2\sigma_x^2}-\frac{y^2}{2\sigma_y^2}-\frac{z^2}{2\sigma_z^2}}dx \\ &= \frac{N}{2\pi\sigma_y\sigma_z} e^{-\frac{y^2}{2\sigma_y^2}-\frac{z^2}{2\sigma_z^2}}\end{aligned} \tag{2.45}$$

for a thermal gas,

$$\begin{aligned}\tilde{n}_{BEC}(y,z) &= \int_{-\infty}^{\infty} \max\{\frac{15N}{8\pi R_x R_y R_z}(1-\frac{x^2}{R_x^2}--\frac{y^2}{R_y^2}-\frac{z^2}{R_z^2},0\}dx \\ &= \frac{5N}{2\pi R_y R_z}\max\{(1-\frac{y^2}{R_y^2}-\frac{z^2}{R_z^2},0\}^{3/2}\end{aligned} \tag{2.46}$$

for a pure condensate and

$$\tilde{n}_{partial}(y,z) = \frac{N_{th}}{2\pi\sigma_y\sigma_z} e^{-\frac{y^2}{2\sigma_y^2}-\frac{z^2}{2\sigma_z^2}} + \frac{5N_{BEC}}{2\pi R_y R_z}\max\{(1-\frac{y^2}{R_y^2}-\frac{z^2}{R_z^2},0\}^{3/2} \tag{2.47}$$

for a partially condensed gas.

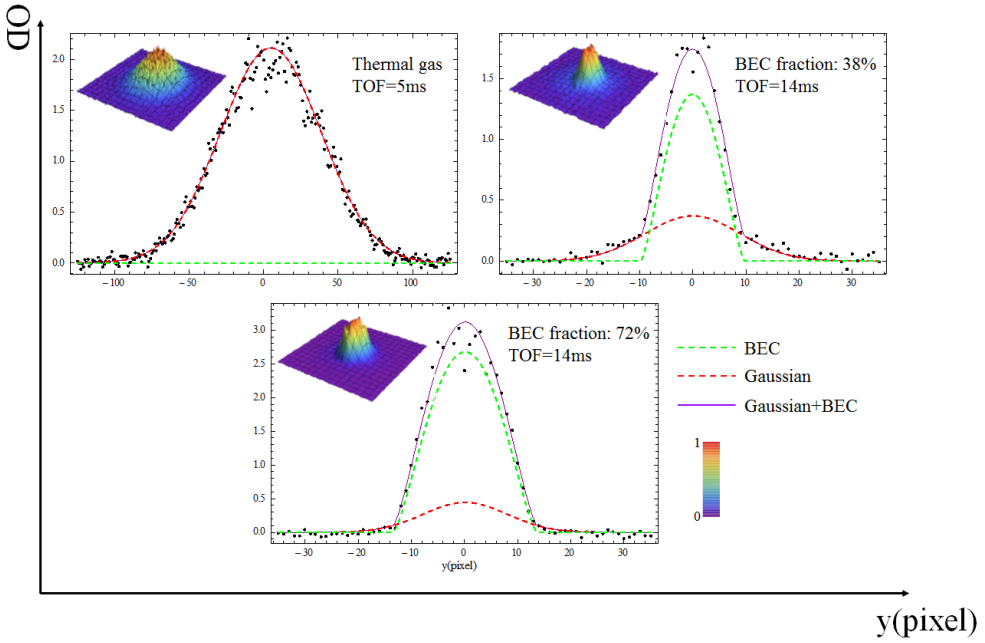

Figure 2.15: Examples of the absorption images. Three line ODs along the vertical direction passing through the trap center versus the vertical coordinate are plotted with the BEC fraction of $0\%, 38\%$ and 72%. The solid violet curves are fits with a bimodal function and the BEC (thermal) parts are indicated with the dashed green (red) curves. The inset in each plot is the density plot of the 2D distribution of the OD.

Several examples are presented in Fig. 2.15. The insets show the density plots of the column density where the difference of the distributions for a thermal and condensed gas is already seen. To quantify them further, we fit all the images with the distribution function of a partially condensed gas. The intersections along the vertical direction (y axis here) of the images as well as the fitting results are shown in the figure. Also the thermal and BEC parts determined from the fits are indicated. We could see that the fits agree with the data very well in all the three cases, which suggest that we can get reliable densities from our images.

2.3.4 Measuring The Physical Quantities

Atom Number

The most important information we could get is the total atom number: $N = N_{\text{th}} + N_{\text{BEC}} = 2\pi n_{\text{th0}}\sigma_y\sigma_z + \frac{2\pi}{5}n_{\text{BEC0}}R_yR_z$. Of course the BEC fraction is also got: $f_{\text{BEC}} = \frac{N_{\text{BEC}}}{N} \times 100\%$. Here the real sizes of the cloud are determined by the pixel size of the camera sensor (d_0), the magnification factor of the imaging system (Mag) and the binning of the image (bin). The real size unit is given by $d = \frac{d_0}{\text{Mag}} \times \text{bin}$, where d_0=6.45 µm, Mag≈ 3.1 and bin= 2.

Temperature

The temperature of the system is measured by the relation between the size of the thermal cloud and the expansion time, according to Eq. 2.31 which reads

$$\sigma_i(t) = \sqrt{\frac{k_bT}{M}(t^2 + \frac{1}{\omega_i^2})}. \tag{2.48}$$

By fitting the sizes at different expansion time with this equation we can get the temperature of the gas and an example is shown in Fig. 2.16.

Atomic Density

For a thermal gas, we can reconstruct the density distribution from the total atom number, the trap frequencies and the temperature according to eqn. (2.31). For a BEC the density distribution is also accessable in the weak and Thomas-Fermi limit with the atom number and trap frequencies via eqn. (2.39). The average density can be obtained by the reconstructed density distribution $\langle n\rangle = \frac{1}{N}\int n^2(\mathbf{r})d\mathbf{r}$. So the trap frequencies are important for the determination of the density which can be calculated using the equations in section 2.2.6 or measured by the parametric heating method [151].

Calibration of Atom Numbers

The above calculation of the atomic density (hence the atom number) is based on some idea conditions like on-resonance, weak probe light intensity, perfect alignment of the light in terms of polarization and exact two-level atomic structure.

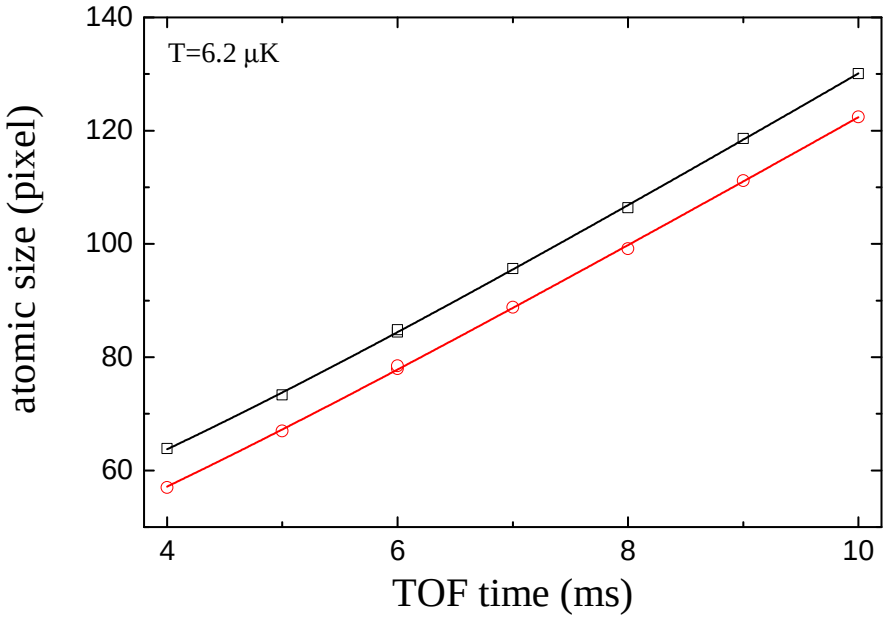

Figure 2.16: An example for the temperature measurement. The black squares and the red circles are corresponding to the atomic sizes along the horizontal and vertical direction, respectively. Solid lines are fits to Eq. 2.48, from which the temperature of the sample is determined to be 6.2 μK.

However imperfections are unavoidable in experiments, such as saturation effect of the probe light, misaligned polarization and optical pumping effect. Taking these into consideration by introducing an effective probe intensity [152, 153] we obtain the following equation:

$$\frac{dI}{dx} = -n\sigma_0 \frac{I_{eff}}{1 + I_{eff}/I_{sat}} = -n\sigma_0 \frac{I/\alpha}{1 + I/(\alpha I_{sat})}. \tag{2.49}$$

Integrating this equation we have

$$\alpha \int \ln \frac{I_i - I_b}{I_f - I_b} dydz + \int \frac{I_i - I_f}{I_{sat}} dydz = \sigma_0 \int \tilde{n}(y,z) dydz = \sigma_0 N. \tag{2.50}$$

The right-hand side of the above equation is a constant when we only change the probe intensity. So if we plot the quantity $B = \frac{I_i - I_f}{I_{sat}}$ as a function of $A = \ln \frac{I_i - I_b}{I_f - I_b}$ we expect a line with a slope of α. Based on this understanding, we implement different probe intensities and get the correct factor α shown in Fig. 2.17 for ^{87}Rb with $\alpha = 2.0(2)$. This factor for ^{23}Na is found to be equal to 1 in our system

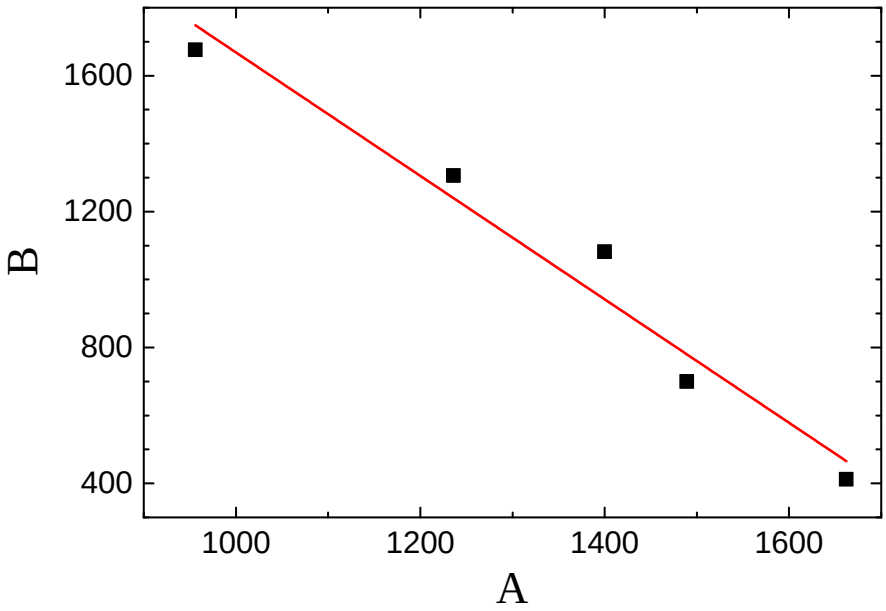

Figure 2.17: Calibration for the ^{87}Rb atom number. See text for the explanations of A and B. The solid red line is a linear fit.

using the same method. The calibration of the atom number is important for us especially in the spinor experiments where the spin-dependent mean-field energy strongly depends on the atomic density, and hence the atom number.

2.4 DC Magnetic Fields and Electric Fields

Atoms and molecules can interact with DC external fields and their internal structures are perturbed by these fields. For DC electric fields they can only interact with a neutral particle possessing a nonzero permanent dipole moment, namely the ground-state ^{23}Na^{87}Rb polar molecule in our case. The external DC magnetic fields interact with particles having nonzero magnetic dipole moments. Here I will focus on the atoms in the magnetic fields and molecules in the electric fields for this section. Both the theoretical treatments and the experimental implementations will be presented.

2.4.1 DC Magnetic Fields

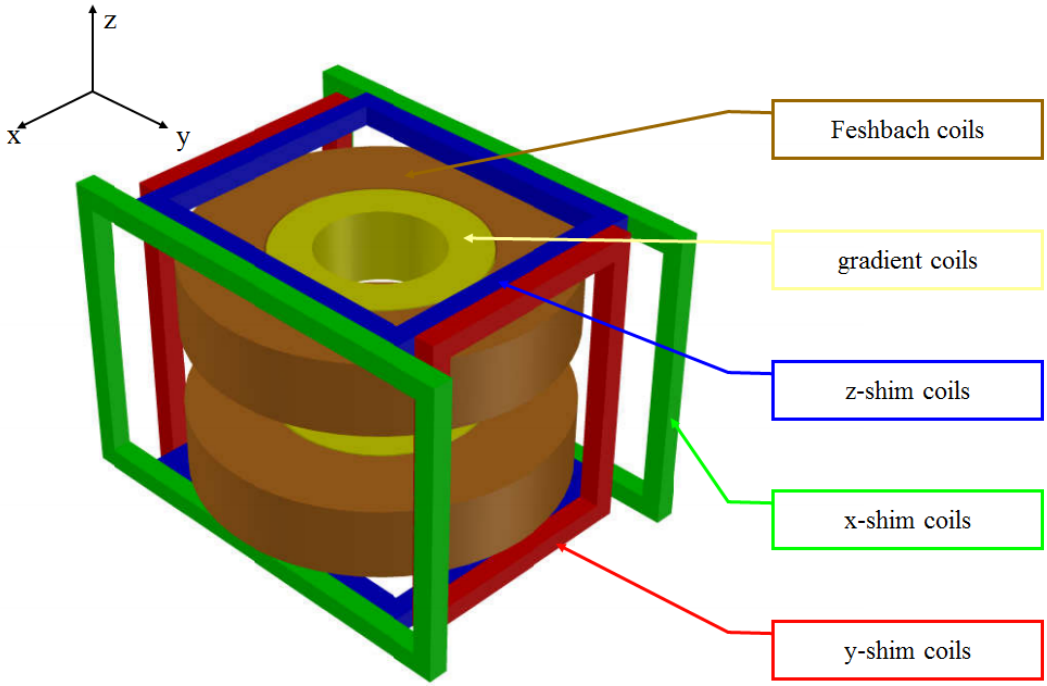

Figure 2.18: The configuration of our magnetic coils to generate various magnetic field. Totally there are five pairs of coils around our vacuum cell. The innermost one is an anti-Helmholtz to generate the gradient field, shown by the hollow yellow cylinders. Next to them are the Feshbach coils used to provide the Feshbach magnetic field (hollow brown cylinders). Another three pairs of rectangular coils are positioned along the three cartesian axes to cancel the background field and produce small magnetic fields from several milligauss to about 3 G.

As mentioned in section 2.2.1, the external magnetic fields would lift the degeneracy of the hyperfine states which is termed Zeeman effect. This well-known effect was first observed by the Dutch physicist Pieter Zeeman and named after him. With several pairs of copper coils, we can generate various types of magnetic fields to create the MOT and magnetic traps for atoms, induce Feshbach resonances between atoms and tune the spin dynamics based on the Zeeman effect. The

configuration of the coils is shown in Fig. 2.18, where the coordinate system is consistent with that in Fig. 2.12. I would like to discuss these coils respectively in following subsections. However, let me revisit the influences of magnetic fields on the atomic structures first.

Hyperfine Structure of ^{23}Na and ^{87}Rb in a Static Magnetic Field

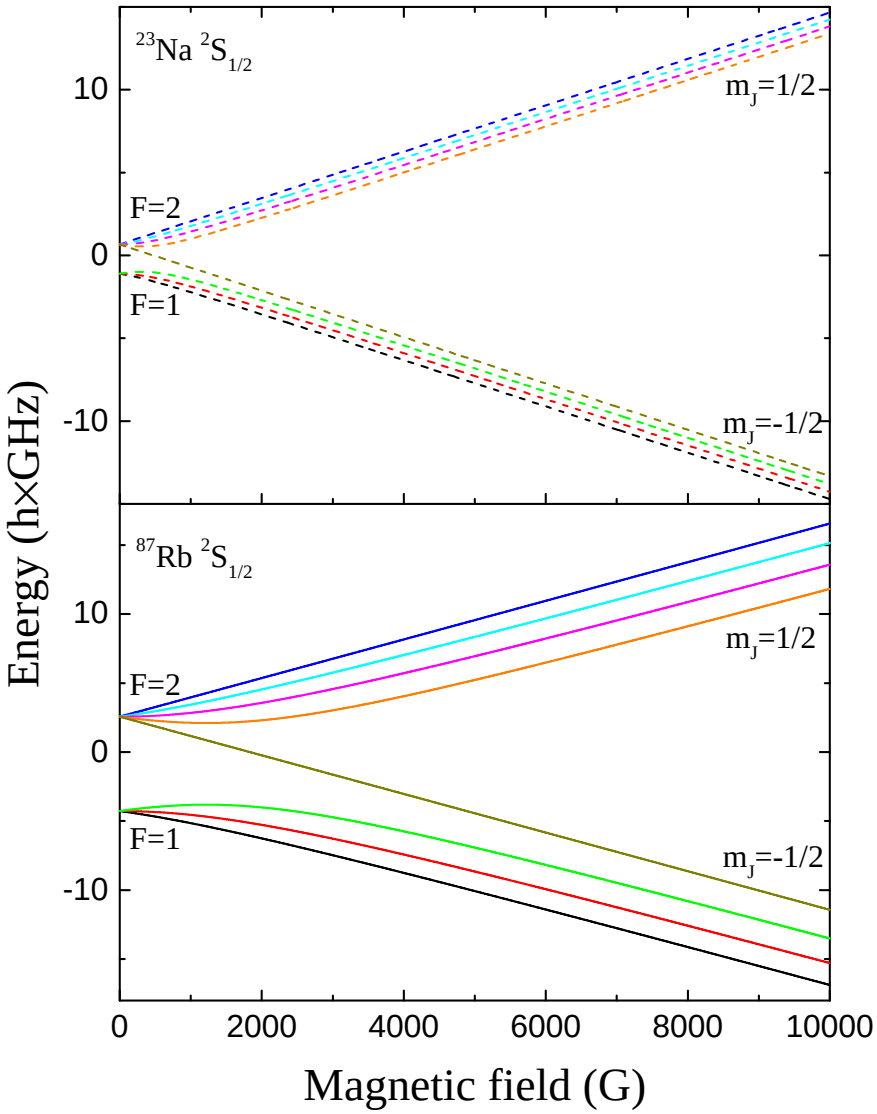

Figure 2.19: ^{23}Na and ^{87}Rb $^2S_{1/2}$ state hyperfine structure in a static magnetic field

I start with a consideration of the atomic hyperfine structure in a static magnetic field. The Hamiltonian is written as

$$\begin{aligned} H &= H_{hf} + H_Z \\ &= H_{hf} + \mu_B(g_J \mathbf{J}\cdot\mathbf{B} + g_I \mathbf{I}\cdot\mathbf{B}), \end{aligned} \tag{2.51}$$

where H_{hf} has the form as that in eqn. (2.1), μ_B is the Bohr magneton, g_J is the fine Landé g-factor and g_J is the nucleus g-factor. The hyperfine state labeled by F, quantum number of the total angular momentum of the atom, has a $(2F+1)$-fold degeneracy. When the magnetic field is turned on, this degeneracy is destroyed and we can identify two limited cases where either the Zeeman interaction or the hyperfine interaction can be treated as a perturbation. For the weak field limit ($g_J\mu_B B \ll A, B_{hf}$) F remains a good quantum number and the perturbation H_Z becomes

$$H_Z = g_F \mu_B \mathbf{F}\cdot\mathbf{B}, \tag{2.52}$$

here $g_F = g_J \frac{F(F+1)-I(I+1)+J(J+1)}{2F(F+1)} + g_I \frac{F(F+1)+I(I+1)-J(J+1)}{2F(F+1)}$ is the hyperfine g-factor. The eigenstate is denoted by $|F, m_F\rangle$ where m_F is the projection of $\mathbf{F}$ along $\mathbf{B}$. In the strong field limit ($g_I\mu_B B \gg A, B_{hf}$), the good quantum numbers are m_I and m_J, the projection of $\mathbf{I}$ and $\mathbf{J}$ on the $\mathbf{B}$, and the hyperfine interaction is the perturbation term. In between these two limits, it is difficult to obtain the energy levels and we need to numerically diagonalize the Hamiltonian H.

However, we can have a exception for a simple case in which $J = 1/2$. The B_{hf} term of the hyperfine interaction vanishes in this case and the Hamiltonian can be organized as

$$\begin{aligned} H &= A\mathbf{I}\cdot\mathbf{J} + \mu_B(g_J \mathbf{J}\cdot\mathbf{B} + g_I \mathbf{I}\cdot\mathbf{B}) \\ &= A\mathbf{I}\cdot\mathbf{J} + \mu_B(g_J B I_z + g_I B J_z) \\ &= \frac{A}{2}(I_+ J_- + I_- J_+) + A I_z J_z + \mu_B(g_J B I_z + g_I B J_z), \end{aligned} \tag{2.53}$$

where the static magnetic field $\mathbf{B}$ is along the z-axis with a magnitude B and $I_\pm = I_x \pm i I_y$ and $J_\pm = J_x \pm i J_y$ are the ladder operators. With $|1\rangle = |m_I, \pm 1/2\rangle$ and $|2\rangle = |m_I \pm 1, \mp 1/2\rangle$ we can construct an eigenstate of H by doing the following

algebra:

$$
\begin{aligned}
&H(|1\rangle + l_\pm |2\rangle) \\
&= \frac{A}{2}\sqrt{(I \mp m_I)(I \pm m_I + 1)}\,|2\rangle + [Am_J m_I + \mu_B(g_J m_J B + g_I m_I B)]\,|1\rangle \\
&+ l_\pm\{\frac{A}{2}\sqrt{(I \mp m_I)(I \pm m_I + 1)}\,|1\rangle + [-Am_J(m_I \pm 1) + \mu_B(-g_J m_J B + g_I(m_I \pm 1)B)]\,|2\rangle\} \\
&= E_{m_I \pm 1/2}(|1\rangle + l_\pm |2\rangle), \\
&\Longrightarrow E_{m_I \pm 1/2} = -\frac{1}{4}A + g_I(m_I \pm 1/2)\mu_B B \pm \frac{A(I+1/2)}{2}\sqrt{1 + \frac{4(m_I \pm 1/2)}{2I+1}x + x^2}.
\end{aligned}
\tag{2.54}
$$

Here $x = \frac{\mu_B(g_J - g_I)B}{A(I+1/2)}$ and the expression of the energy is called Breit-Rabi formula [154] which is applicable to the $^2S_{1/2}$ and $^2P_{1/2}$ states of alkali atoms. The energy shifts of the ground states of ^{23}Na and ^{87}Rb are shown in Fig. 2.19 where the crossover from the weak field regime to the strong field regime is clearly demonstrated.

Magnetic Gradient Fields in MOT and Magnetic Quadrupole Traps

In the weak field limit, the lowest order perturbation theory gives the energy shift of $|F, m_F\rangle$ as

$$\Delta E_{F,m_F} = \mu_B g_F m_F B. \tag{2.55}$$

If a magnetic field gradient is applied, the atoms will experience a spatial-dependent energy shift which has been used to cause the restorative imbalance of the scattering force in the MOT. However, this shift itself can provide a conservative force which is also restorative for some atomic states:

$$
\begin{aligned}
\mathbf{F} &= -\nabla\{\Delta E_{F,m_F}\} \\
&= -\mu_B g_F m_F \nabla B(\mathbf{r}) \\
&= -\mu_B g_F m_F B'_z \hat{z},
\end{aligned}
\tag{2.56}
$$

where $B'_z = \partial_z B$ are the gradients along the z axis. If $g_F m_F B'_z > 0$ atoms at the state $|F, m_F\rangle$ will be trapped to the local minimum of the magnetic field in the z-direction.

The axis of a pair of anti-Helmholtz coils (gradient coils in Fig. 2.18) is aligned along the z-direction. With opposite direction currents, the magnetic field around the center is approximated by $\mathbf{B} = B'(\frac{x}{2}\hat{x} + \frac{y}{2}\hat{x} - z\hat{z})$ with $0 \leq B' \leq 218\,\mathrm{G/cm}$.

The potential created by this field configuration is written as

$$U_{QT}(x, y, z) = \mu_B g_F m_F B' \sqrt{\frac{x^2}{4} + \frac{y^2}{4} + z^2}. \tag{2.57}$$

For the electronic ground states of both ^{23}Na and ^{87}Rb, $g_1 < 0$ and $g_2 > 0$, hence the trappable states are $|1, -1\rangle$, $|2, 1\rangle$ and $|2, 2\rangle$. Since only the mixtures of ^{23}Na and ^{87}Rb $F = 1$ states are stable enough for a long time ($\sim$10 s) evaporation cooling, we use $|1, -1\rangle$ state for both species in our experiments.

Feshbach Coils

Another pair of coils placed in the same horizontal plane with larger sizes is operated with same direction currents and labeled with Feshbach coils in Fig. 2.18. With its center coincided with that of the gradient coils, this pair generates a uniform magnetic field up to 1000 G around the center. We use the Feshbach coils to induce the interspecies Feshbach resonances between ^{23}Na and ^{87}Rb atoms. Especially, one of the s-wave resonances located at 347.7 G is selected to create the Feshbach molecules.

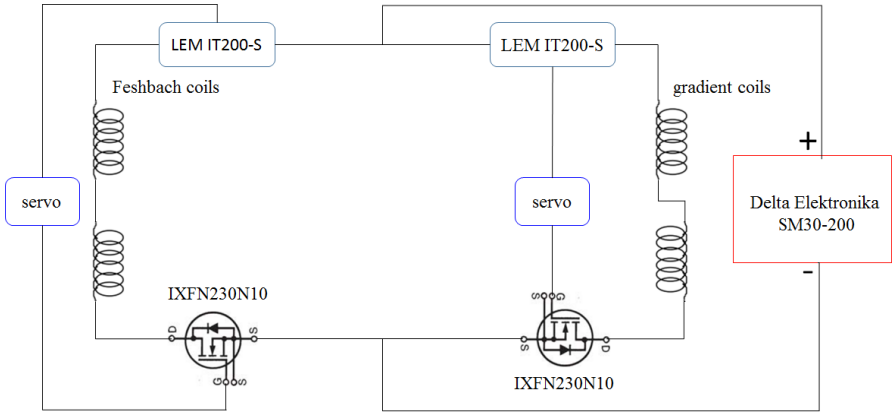

Figure 2.20: Schematic for the control of the gradient and Feshbach coils

Both the gradient and Feshbach coils are constructed with hollow copper tubes and driven by a common power supply (Delta Elektronika SM30-200) with a parallel relation, as illustrated in Fig. 2.20. The currents flowing the two pairs are separately stabilized with two active control systems. In each system, we use a Hall transducer (LEM IT200-S) to precisely sense the current and a MOSFET (IXFN230N10) as the controller. As a result, we can have a relative stability of

3×10^{-5} for the Feshbach fields. The stability of the gradient fields is not tested. A more detailed description of the coil constructions, magnetic field modelings and servo circuit as well as its performance can be found in the thesis of our senior PhD Fudong Wang.

Shim Coils

As seen in Fig. 2.1 and Fig. 2.18, three mutually perpendicular pairs of rectangular shape coils are winded at the edges of the mount of the gradient and Feshbach coils. These pairs, called shim coils, are used to compensate the background magnetic field and also provide a small uniform field. Two of them (y-shim and z-shim) are driven by low ripple and noise DC power supplies (ISO-TECH IPS 303DD) and a 4A extremely low noise current controller (LDC240C) is used to drive the left one (x-shim).

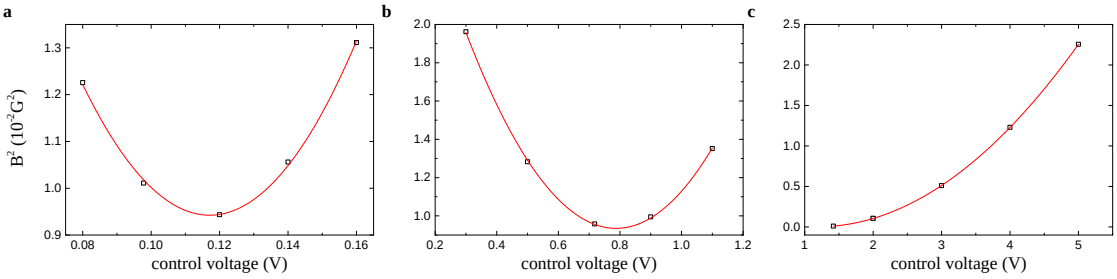

Figure 2.21: Compensation of the background magnetic field with the shim coils

The compensation of the background magnetic field is important for the Sisyphus cooling, absorption imaging and spinor experiments. In a zero magnetic field, the Sisyphus cooling bunches the atoms near the zero velocity region with a narrow distribution. However, a finite magnetic field would bunch the atoms around a finite velocity determined by the Larmor frequency. Experimentally this gives rise to a unwanted multimodal distribution of the atomic velocity [155]. Typically we use a magnetic field smaller than 50 mG which is enough for the successful operation of the Sisyphus cooling. For the absorption imaging we need a finite magnetic field to determine the quantization axis. The alignment of the probe light along this axis will be much easier if we have a good knowledge of the magnetic field. In the spinor experiment an crucial point is the light vector shift which strongly depends on the magnetic field direction. Taking these into consideration,

we employ a simple and effective method to compensate the background magnetic filed. It is based on the fact that the three shim coils can independently control the magnetic field along the three Cartesian axes. The magnitude of the field is written in the form of

$$\begin{aligned} B &= \sqrt{B_x^2 + B_y^2 + B_y^2} \\ &= \sqrt{(a_x I_x + b_x)^2 + (a_y I_y + b_y)^2 + (a_z I_z + b_z)^2}, \end{aligned} \tag{2.58}$$

where the field B_i is linearly determined by the current I_i with the slope a_i and the intercept b_i for $i = x, y$ and z. By tuning one of the currents while keeping the other two constant and calibrating the magnetic field with the microwave transition of ^{87}Rb, we can get a set of data (I, B^2) and fit it with a parabolic function. The vertex of the parabola gives us the compensation value of the selected current. The results for all the three currents are shown in Fig. 2.21. Since the outputs of either the power supplies or the current controller are linearly controlled using the DC voltages that come from a digital-analog converter (DAC), we use the voltage instead of current in the plot which is more convenient for us. With this method, we can compensate the background DC magnetic field below 10 mG confirmed by the microwave transition. We can also precisely create a magnetic field with a magnitude up to 10 G in an arbitrary direction with these three shim coils.

2.4.2 DC Electric Fields

A DC electric field affects the electronic ground states of both ^{23}Na and ^{87}Rb atoms little while it may strongly interact with the ground state polar molecules. I will left the discussion of this point to chapter 3 and here I want to focus on the setup and model of the electric fields.

Two parallel plate-electrodes have been installed outside our vacuum cell with their normal axes along the vertical direction. They are made of conductive and transparent ITO (Indium-Tin-Oxide) glasses. The transmissions of the 780 nm and 589 nm lights are both around 80% for the normal incidences. Each plate is a cylinder with a radius of 24 mm and a height of 1.1 mm. The distance between the two plates is 5.37 cm and they are both very close to the glass cell (<1 mm). They are held by two home-designed mounts which are adapted into the central hole of the gradient coils.

Typically we need an electric field up to 1 ∼2 kV/cm and this requires a voltage difference of 10 kV between the two plates from the roughest estimation. The experience in JILA on ^{40}K^{87}Rb experiments [156] tells us that the balanced configuration of the voltage difference gives the smallest electric field gradient which is unexpected for our purpose. To this end, we use two commercial high voltage amplifiers (AMT-5B20) with an output range of ±5 kV. These high-speed amplifiers have a voltage slew rate of 170 V/µs in our setup.

The real electric fields experienced by the molecules are hard to measure and we use theoretical values instead. Assuming a ±1 kV voltage applied on the two plates respectively and including the presence of the glass cell, we can estimate the electric field between the plates to be

$$\begin{aligned} E &\approx \frac{\Delta V}{5.37\,\mathrm{cm} + (\varepsilon_r - 1) \times 2 \times 3\,\mathrm{mm}} \\ &\approx 0.264\,\mathrm{kV/cm}, \end{aligned} \tag{2.59}$$

where ε_r is the relative permittivity of the Pyrex and the wall thickness of the cell is 3 mm. However, this estimation is quite accurate when the electrodes is much larger than the glass cell which is the case here. Also the influences of surrounding metal components cannot be ignored. For a better knowledge of our electric fields, we use the software platform COMSOL MULTIPHYSICS® to model them based on the finite element method. The simulating result to the above problem is presented in Fig. 2.22, where the contour plot of the electric field distribution in the horizontal plane containing the molecular cloud is shown. It gives a electric field of 0.18 kV/cm at the molecular position which is well below the previous estimation.

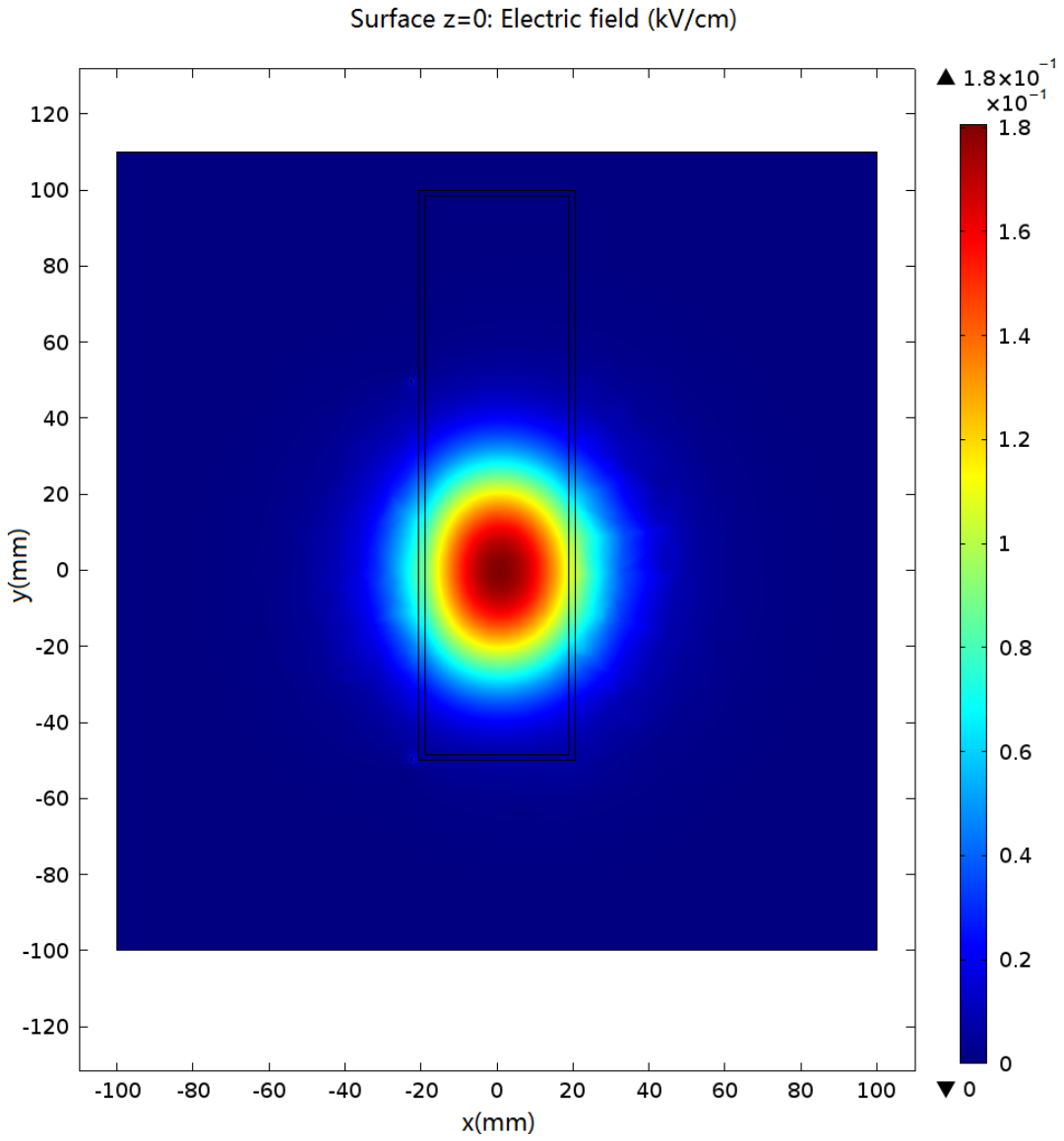

Figure 2.22: Modeling of the electric field

Also this simulation is not accurate due to the uncertainties of the input parameters and important ones are the distance between plates (5%), the size of the plates (2%), the thickness of the cell's wall, the relative permittivity of the Pyrex (10%), the positions of the gradient and Feshbach coils (5%) and the inner radius of the gradient coils (5%). Here the uncertainties of the parameters are given inside the parentheses and combining all of them give rise to a overall uncertainty of 10% for the electric field.

2.5 Microwave and Radio-frequency Transitions and Their Implementations

For the atomic ground states of ^{23}Na and ^{87}Rb, the transitions among the same or different hyperfine manifolds correspond to radio-frequency (RF) or microwave (MW) transitions respectively. Also the transition frequencies between adjacent rotational states of our ground state molecules lie at the MW regime. Our group employs the MW transitions of ^{87}Rb $^2S_{1/2}$ $F = 1 \leftrightarrow F = 2$ around 6.8 GHz to do the evaporative cooling in the magnetic or hybrid trap, calibrate the uniform magnetic field, manipulate the internal states for the study of $F = 2$ spinor gas and control the heteronuclear spin dynamics. The same transitions of ^{23}Na are rarely used and the MW devices for driving transitions between molecular rotational levels are in preparation in our lab. The RF transitions are useful in preparing the mixtures with different state combinations to study the Feshbach spectroscopy and produce the Feshbach molecules and also initializing the special superposition states for coherent spin dynamics.

2.5.1 ^{87}Rb MW Device

A schematic of the setup of the MW device for ^{87}Rb is shown in Fig. 2.23. A MW signal coming from the signal generator (SG386) is sent into an amplifier (ZVE-3W-183+) after passing a high-speed electronic switch (RFSP2TA0218G). The gain of the amplifier is typically 35 dB with a maximum output power of 3 W. The transmission loss of the system from the source to the input of the amplifier is about 9 dB and we would have a saturated output for a source output power >9 dBm. The amplified signal is transmitted to a pyramidal horn antenna (OLB-112-10) whose output is guided to the atomic position. With this setup, we can get Rabi-frequencies up to $2\pi\times10$ kHz for the ^{87}Rb hyperfine transitions. As an example, the on-resonance Rabi oscillation between $|1,1\rangle$ and $|2,2\rangle$ states at 1 G magnetic field is also plotted in the lower right corner of Fig. 2.23.

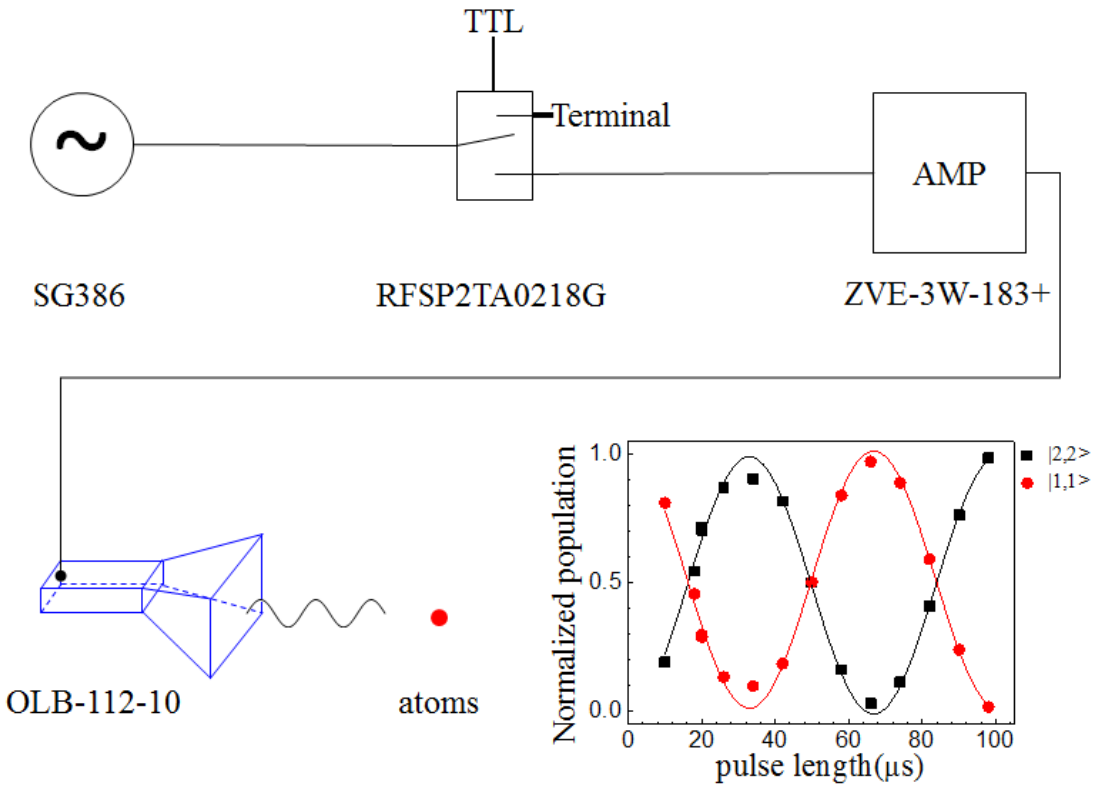

Figure 2.23: The simple schematic of the ^{87}Rb MW device

2.5.2 Spin Rotations and RF Devices

Spin Rotations

At a small magnetic field B_0 along z-direction, we can apply an oscillating transverse magnetic field with a small amplitude to drive transitions between different Zeeman sublevels among the same hyperfine manifold. The Hamiltonian can be written as

$$\begin{aligned} H &= H_0 + H_{RF} \\ &\approx E_0 + g_F \mu_B F_z B_0 + \frac{g_F^2 \mu_B^2 B_0^2}{(2I+1)A} F_z^2 + g_F \mu_B F_y b \cos(\omega t). \end{aligned} \tag{2.60}$$

Here E_0 is the a constant, $F_i (i = x, y, z)$ are the spin-F cartesian operators, b is the magnitude of the oscillating field and ω is its frequency. For $F = 1$, we use the basis $|1, m\rangle = (1, 0, 0)^T, (0, 1, 0)^T$ and $(0, 0, 1)^T$ for $m = 1, 0$ and -1 respectively.

Then the matrix representation of the three spin operators reads

$$F_x = \frac{1}{\sqrt{2}}\begin{pmatrix} 0 & 1 & 0 \\ 1 & 0 & 1 \\ 0 & 1 & 0 \end{pmatrix}, F_y = \frac{1}{\sqrt{2}i}\begin{pmatrix} 0 & 1 & 0 \\ -1 & 0 & 1 \\ 0 & -1 & 0 \end{pmatrix}, F_z = \begin{pmatrix} 1 & 0 & 0 \\ 0 & 0 & 0 \\ 0 & 0 & -1 \end{pmatrix}. \quad (2.61)$$

With $p = g_F\mu_B B_0/\hbar < 0$, $q = \frac{\hbar p^2}{A(2I+1)} > 0$ and $\Omega = g_F\mu_B b/2\hbar$, the Hamiltonian in the matrix form is

$$\begin{aligned} H &= \hbar \begin{pmatrix} p+q & -i\sqrt{2}\Omega\cos(\omega t) & 0 \\ i\sqrt{2}\Omega\cos(\omega t) & 0 & -i\sqrt{2}\Omega\cos(\omega t) \\ 0 & i\sqrt{2}\Omega\cos(\omega t) & -p+q \end{pmatrix} \\ &\to \hbar \begin{pmatrix} \delta+q & -i\frac{\Omega}{\sqrt{2}} & 0 \\ i\frac{\Omega}{\sqrt{2}} & 0 & -i\frac{\Omega}{\sqrt{2}} \\ 0 & i\frac{\Omega}{\sqrt{2}} & -\delta+q \end{pmatrix}, \end{aligned} \quad (2.62)$$

where $\delta = \omega - |p|$, the RWA is applied ($|p| + \omega \gg |\delta|$), and $p(q)$ is often referred to as the linear (quadratic) Zeeman energy. Starting from the initial state $|1,1\rangle$ and supposing the on-resonance ($\delta = 0$) driving as well as negligible quadratic Zeeman energy ($\Omega \gg |q|$), the state at any time t is $(\cos^2(t\Omega/2), \frac{\sin(t\Omega)}{\sqrt{2}}, \sin^2(t\Omega/2))^T$. For another initial state $|1,0\rangle$ it is $(-\frac{\sin(t\Omega)}{\sqrt{2}}, \cos(t\Omega), \frac{\sin(t\Omega)}{\sqrt{2}})^T$.

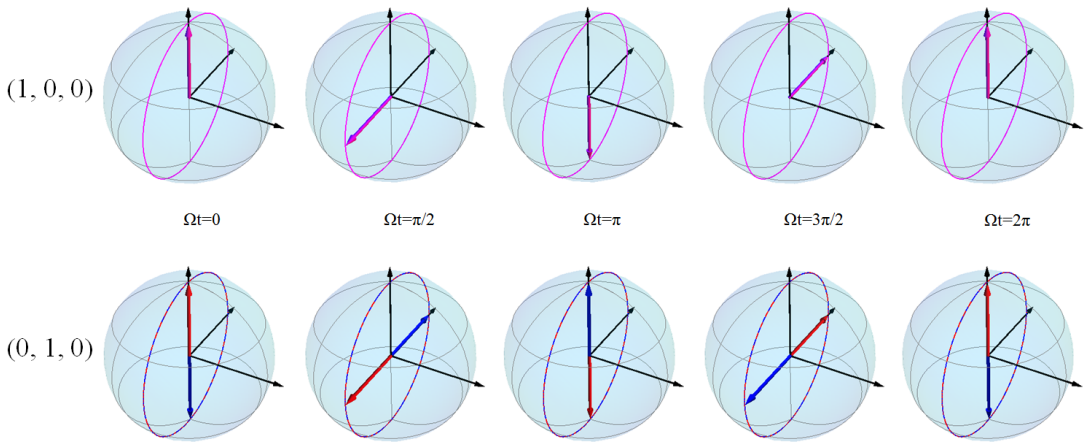

Figure 2.24: Majorana representation of the spin rotation

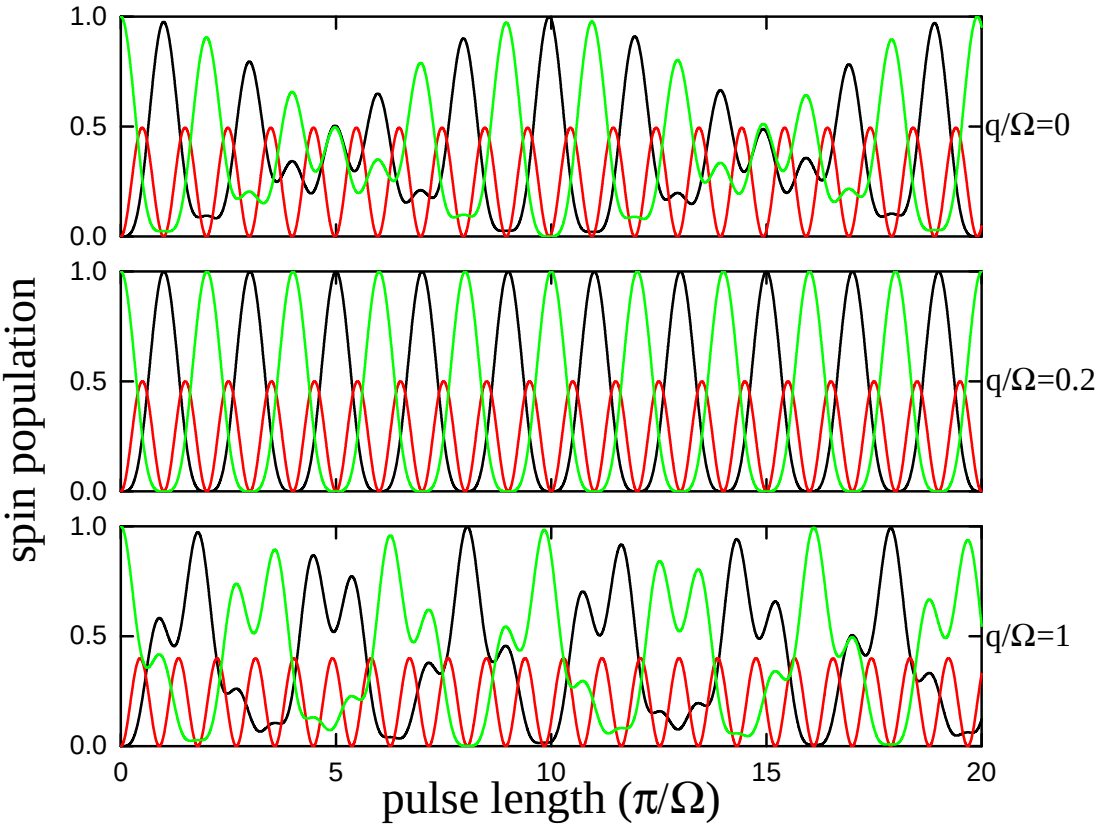

Figure 2.25: Population dynamics of the spin rotation

Here in both cases the spin state rotates periodically in the spin space with a period $2\pi/\Omega$ which is driven by the RF field. To illustrate it explicitly, in Fig. 2.24 we use the Majorana representation of a spin-F object where it is mapped to a set of $2F$ points on an unit sphere. In $F = 1$ cases, two points are needed and they oscillate with same frequency on the unit sphere. For the populations of different sublevels they also oscillate periodically, but maybe with different frequencies. This phenomenon is also termed Rabi oscillation which occurs in a two-level system in the original sense. However, as $|q|$ becomes non-negligible the rotation of the two points have different frequencies and the state experiences a very complex trajectory in the spin space. This can be seen from the beat signal of the population dynamics, shown in Fig. 2.25.

RF Devices

We use homemade small loop antennas with rectangular shapes to meet this purpose where they are small in the sense that the wavelengths of the RF fields (λ) are much larger than the characteristic sizes of the antennas (l). Since the radiation resistance of a loop antenna is proportional to $(l/\lambda)^2$ which is quite small in our case, we can get the maximum radiation power by simply making the power stored by the antenna largest. When there are no extra impedance matching components the loop antenna together with the transmission lines behaves like a LC circuit for RF frequencies >100 kHz. The typical output resistance of an amplifier is 50 Ω and the impedance of an antenna is composed of a resistive one R and a reactive one $i\omega L$ with R its static resistance and L its inductance. However, it is very different of the impedance matching at lower frequencies (<1 MHz) and higher frequencies (>1 MHz) $\cdots$

2.6 Experimental Sequence and Its Control

With all of the previous sections I have introduced many essential equipments working for producing ultracold mixtures of ^{23}Na and ^{87}Rb. A nature question is that how they cooperate in a controlled manner to achieve our purpose. This is realized thanks to the well-developed communication and information technologies. In our lab, the on-off states of lasers, DC and AC external fields and CCD are controlled using TTL gates (DIO64) and their parameters are fine tuned with the DAC outputs (PCI 6713 & 6733). These TTLs and DACs are time-controlled using the computer clock where the resolution of 1 µs is set by the update rate of the DAC cards. A Labview program is utilized to set and change the time sequence with a friendly interface. Also another independent VB.Net program is developed to control the CCD, calculate the OD images and fit them with certain distribution functions.

Our main experimental time sequence could be divided into three parts roughly and next I would go through them one by one.

2.6.1 MOT, Compressed MOT and Optical Molasses

Almost all the quantum gas experiments start with a MOT where millions or billions high-temperature atoms are cooled and accumulated at the center of it. For us we operate with a double-MOT using the LIAD technique and they are spatially separated to avoid possible collision losses by pushing the ^{87}Rb MOT away from the ^{23}Na one with the ^{87}Rb probe light. After a loading time of about 29 s we turn off the UV light and the push beam. Then the atomic mixture is compressed to a higher density with only a minute loss of the atom number but a little increase of the temperature. This is called a compressed MOT which is accomplished by increasing the cycling laser detuning and reducing the repump power. Following a compression of about 20 ms the magnetic gradient field is abruptly turned off and the cycling laser frequency is further detuned. In this way the temperature of the sample is lowered by the Sisyphus cooling with about 6 msand now it is ready to be loaded into the hybrid trap.

2.6.2 Hybrid Trap

Optical Pumping and The Hybrid Trap Loading

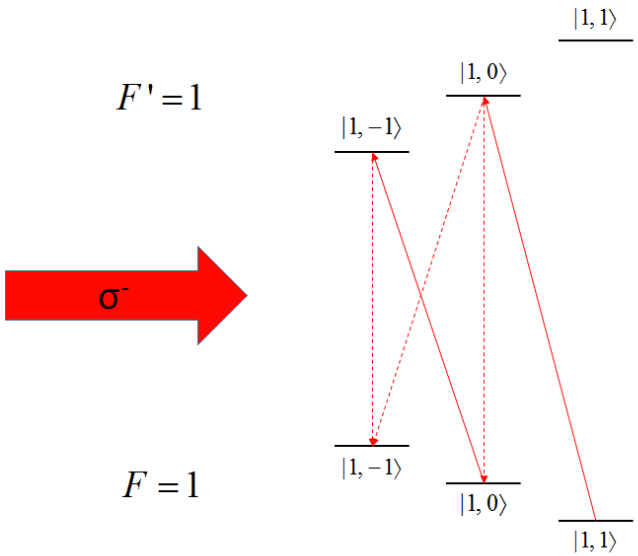

Figure 2.26: The scheme of optical pumping to $|1, -1\rangle$ state

After optically pumping the atoms to $|1,-1\rangle$ states of both species we load our cold mixture into a hybrid trap composed of the quadrupole magnetic trap and a single beam 1070 nm FORT. In Fig. 2.26 we show the scheme of optical pumping. Just before the optical pumping the repump light is turned off and the cycling light is tuned to on-resonance with $^2S_{1/2}\ F=2 \leftrightarrow\ ^2P_{3/2}\ F'=2$ transition which can act as a repump light for the optical pumping process. Then a σ^- light near-resonance with the transition $^2S_{1/2}\ F=1 \leftrightarrow\ ^2P_{3/2}\ F'=1$ is applied where the magnetic field is provided by the shim coils. Almost all the atoms accumulate on the dark state $|1,-1\rangle$ within 500 µs. At this stage we can keep the atom number and PSD from the molasses.

To capture the atoms with a minimum number and PSD loss we first turn on the magnetic gradient to 85 G/cm within 10 ms and then linearly ramp it to 160 G/cm using 250 ms after a holding of 40 ms. After a delay of 200 ms the power of the FORT laser is also linearly ramped to about 2.5 W with 300 ms. An advantage of the hybrid trap over the pure quadrupole magnetic trap is that the former can suppress the Majorana loss which is the major limit of the achievable PSD in the later trap [157]. The spin-flip rate from the trappable state to non-trappable states near the zero-point of the magnetic field is severely enhanced for a cold or ultracold sample and thus both the lifetime and further cooling are limited. Our hybrid trap solves this problem by horizontally shifting the magnetic gradient center about 70 µm away from the optical trap center in a direction perpendicular to the probe light. Supposing the optical trap along the x-direction, its center is the origin and the vertical axis is z, the resultant hybrid trap potential reads

$$U_{hy}(x,y,z) = -\frac{U_0}{1+x^2/x_R^2}\exp\left[-\frac{2(y^2+z^2)}{w_0^2(1+x^2/x_R^2)}\right] + \frac{1}{2}\mu_B B'\sqrt{\frac{(x-x_0)^2}{4}+\frac{(y-y_0)^2}{4}+z^2} + Mgz, \tag{2.63}$$

where w_0 =48 µm, $U_0 = k_b\times 96$ µK for ^{87}Rb and $k_b\times 32$ µK for ^{23}Na, x_R =6.9 mm, x_0 =−36 µm and y_0 =60 µm. For $x \ll x_R$ the optical potential is almost a constant along the x-direction and the potential curve is solely determined by the magnetic quadrupole trap. This point makes the efficient MW or RF evaporative cooling possible. Numerical calculation helps us find the local minimums of the hybrid trap potential and the potential curves along y-direction are plotted in Fig. 2.27 for both species. Typically there are two local minimums present: one corresponds to the optical potential and another is close to the magnetic trap center. When the atoms

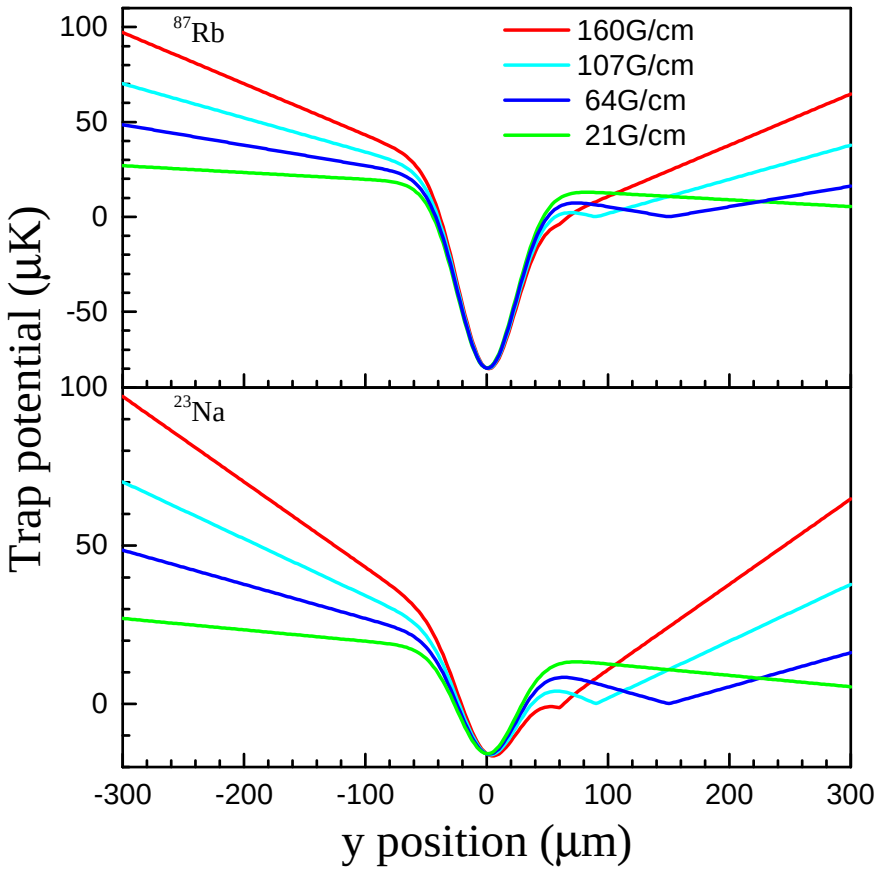

Figure 2.27: Trap potentials of hybrid trap with different magnetic gradient values

are loaded into the hybrid trap, we expect them to locate at the fist minimum to avoid the Majorana loss and the distance between these two minimums is increased when we ramp down the magnetic field gradient. The potential difference between the two minimums is about $k_b \times 76\,\mu\text{K}$ for ^{87}Rb and $k_b \times 15\,\mu\text{K}$ for ^{23}Na. Compared to the temperature of the sample, these values suggest that the Majorana loss is well suppressed for ^{87}Rb while it is not for ^{23}Na.

Evaporative and Sympathetic Cooling in The Hybrid Trap

For us we use the MW evaporative cooling for ^{87}Rb in the hybrid trap. With a MW field, the Doppler shift is negligible and the resonance condition is determined by the local magnetic field where the $|1,-1\rangle$ atoms are transfered to the non-trappable states $|2,m\rangle$ $(m = 0,-1,-2)$. As already mentioned, only along the x-direction the potential curve is severely affected by this MW field which is illustrated in

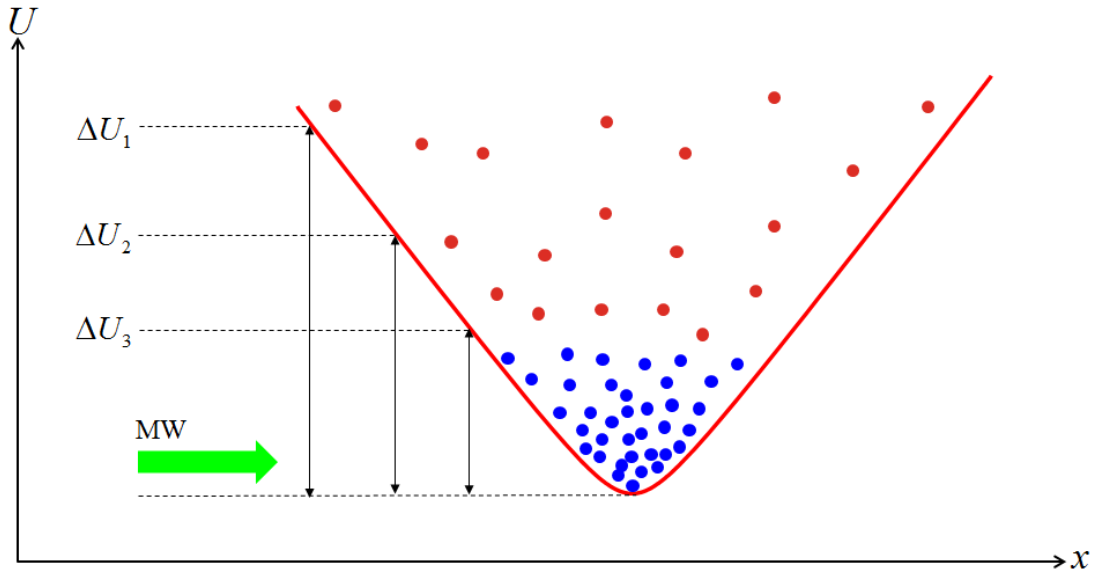

Figure 2.28: MW evaporative cooling of ^{87}Rb in the hybrid trap

Fig. 2.28. The MW frequency determines the resonant magnetic field, hence the x-coordinate, and the nearby atoms is ejected from the trap. As we know the high-velocity atoms would like to stay near the top of the potential curve, we will selectively remove the high-velocity atoms from the trap if we swap the MW frequency in a way that the corresponding resonance point is swept from the top toward the bottom of the potential curve.

The ^{23}Na atoms are sympathetically cooled through the thermalization process with the cold ^{87}Rb cloud. The sympathetic cooling efficiency depends on the relative rate of the elastic and inelastic collisions. The elastic collision rate is determined by the elastic scattering cross section, the density overlap and the temperature of the gas which reads $\Gamma_{\text{elastic}} = \sigma_{\text{elastic}}\langle n\rangle\sqrt{\frac{16k_bT}{\mu\pi}}$. Here $\sigma_{\text{elastic}} = 4\pi a^2$ for the far-from-resonance scattering and μ is the reduced mass. The inelastic collisions typically cause the trap losses and we have three kinds of inelastic collisions: 1) Background collisions. It is unavoidable for the collisions between trapped atoms and room temperature background atoms. This process limits the achievable lifetime for any traps. 2) Two-body dipolar relaxation. These collisions result from the magnetic DDI or the spin-orbit coupling which transfers the orbital angular momentum to the spin one and thus scatters the spin state into non-trappable spin states. 3) Three-body recombination. When three atoms collide, it is possible that two of them form a molecular state and the left atom helps conserve the energy

and linear momentum. The released energy is converted into the kinetic energy which is usually much larger than the trap depth, hence all the three atoms are lost from the trap. The background collision rate is low if the UHV is well-maintained. This is also true for the two-body process where both the magnetic DDI and spin-orbit interaction are quite weak for ^{87}Rb and ^{23}Na. The three-body loss will be a problem only when the density is high enough or the scattering length becomes extraordinarily large. So the sympathetic cooling works efficiently between ^{87}Rb and ^{23}Na in the usual case.

In our experiments, we start from 6794 MHz which corresponds to x =3.6 mm and the sweeping slope of the frequency is optimized to achieve the highest cooling efficiency. Down to 6832 MHz, where the Majorana loss becomes severe for ^{23}Na, we ramp down the magnetic field gradient from 160 G/cm to 64 G/cm using 300 ms to push away the zero-point of the magnetic field. Finally we stop at a frequency ranging from 6833.5 MHz to 6834 MHz and transfer the atoms to the crossed FORT. With different ending frequencies we can control the relative number of ^{23}Na and ^{87}Rb from 0 to ∞.

2.6.3 Crossed FORT

The crossed FORT is formed by slowly ramping up another 1070nm beam to 0.7 W and simultaneously ramping down the magnetic field gradient to 6 G/cm at the end of the MW evaporative cooling. The power of the initially present beam is also ramped down to 0.7 W. After a holding of 10 ms the gradient is turned off and a 2 G uniform magnetic field is turned on to align the spin. Actually the atoms are evaporatively cooled during the loading of the crossed FORT where the final power of the beams are optimized to achieve the highest PSD. The atoms are further cooled by lowering the trap laser power. This is also called evaporative cooling since the basic picture is the same as that of the MW one. The trap potential has been derived in section 2.2.6 and it is shown there the trap depth of ^{23}Na is smaller than that of ^{87}Rb. This results in the evaporative cooling of ^{23}Na firstly and the sympathetic cooling of ^{87}Rb by the ^{23}Na gas. Since the ^{23}Na number is limited and we have tried to add another 660 nm beam to tune the relative trap depth of them. This helps us improve the mixture number and the detail could be found in our previous group member Jun Chen's thesis [158]. Due

to the fact that the alignment of this 660 nm beam changes frequently and most of the time we are satisfied with the crossed 1070 nm trap, it is rarely used. After the forced evaporative cooling in the crossed FORT we end up with an ultracold mixture of ^{23}Na and ^{87}Rb and the total atom number is about $1.5 \sim 2 \times 10^5$ at a temperature around 300 nK.

With this compact setup our lab has already achieved several scientific results before I joined it: 1) The production of a double Bose-Einstein condensate with tunable interspecies interactions [42]. 2) The Feshbach spectroscopy between ^{23}Na and ^{87}Rb [159]. Based on these results, from next chapter I begin to present you the new achievements I have contributed to.

Chapter 3

From Weakly Bound State to Absolute Ground State

Heteronuclear diatomic molecules at their rovibrational ground states, the simplest forms of the polar molecules, have attracted the most interests in the quantum gas community. Although there are continuous efforts and significant progresses in the direct cooling of various ground-state diatomic molecules [], the most successful method to produce an ultracold sample is still associating the ultracold atoms into weakly bound molecules followed by transferring these molecules into the ground state via the STIRAP.

Our $^{23}Na^{87}Rb$ molecule, possessing a permanent dipole moment of 3.2 Debye at its ground state, is an idea candidate for the realization of the DDI-dominated system and chemically stable against the $^{23}Na^{87}Rb + {}^{23}Na^{87}Rb$ to $^{23}Na_2 + {}^{87}Rb_2$ reaction where the energy barrier is about $47\,cm^{-1}$ [160]. From the historical point of view, the $^{23}Na^{87}Rb$ molecule was well-studied using the traditional spectroscopy method [161–164]. The molecular structures of the first several electronic states will be presented in section 3.1.

The first step toward the ground-state molecules is the association of free atoms into bound states. This requires moderate couping between them and it is possible with the laser field or magnetic field which induce Feshbach resonances. Near resonant lasers are need in the former case which would limit the lifetime of the

ultracold sample and the achievable PSD is low. Our group utilizes an s-wave magnetic Feshbach resonance to realize the free to bound transition and the production of the Feshbach molecules is going to be discussed in section 3.2.

The next step is to find a suitable intermediate state involved in the STIRAP. This state is required to have strong enough coupling with both the Feshbach molecular state and the ground state. Its hyperfine structures are need to be well-resolved to achieve a high-efficiency population transfer. The lifetime of this state is long enough to set acceptable requirements for the state couping and laser coherence. For ^{23}Na^{87}Rb, the candidates are the states belong to the admixture of $A^1\Sigma^+$ and $b^3\Pi$ or $B^1\Pi$ and $c^3\Sigma^+$ state. To locate the interested regions we have performed spectroscopy study of the excited states around the proposed positions in Ref. [162] for the former case and near the dissociation limits ^{23}Na $3^2S_{1/2}$ + ^{87}Rb $5^2P_{1/2}$ and $5^2P_{3/2}$ for the later. We successfully classified the long-range states just below the ^{87}Rb D2 line and a few more deeply bound states are considered to be promising for the STIRAP. During our planning of this scheme, we surprisingly identified a suitable pathway with the $A^1\Sigma^+/b^3\Pi$ admixture through which our existing lasers work very well. In section 3.3 and 3.4 I will present you the details of our spectroscopy studies.

The following section is devoted to the creation and characterization of the ground-state molecules. The transfer process was well understood using a phenomenological master equation. The ground-state hyperfine structure was fine resolved and we confirmed the occupation of the pure lowest energy level. The dipolar nature of our molecules was characterized by the stark spectroscopy where we measured the stark shifts of the rovibrational ground state. The effective dipole moment over 1 Debye, the largest value achieved with ultracold molecules, was induced. The lifetime of the ground-state molecules was also studied and extensively discussed.

At the end of this chapter, I would like to briefly summarize it and mention the perspectives with our ^{23}Na^{87}Rb molecule.

3.1 Structures of Diatomic Molecules: ^{23}Na^{87}Rb as an Example

Diatomic molecules have much more complex internal structures than the atoms, mainly resulting from the relative motion of the two nuclei as well as its interplay with the electronic motion. It was proposed by Born and Oppenheimer [165] that the motion of the nuclei and electrons can be separated in a molecule due to the dramatic mass difference between them. In this so-called Born-Oppenheimer (BO) approximation, we first fix the internuclear distance $\mathbf{R}$ and solve the electronic Schrödinger equation: $H_e(\mathbf{r};\mathbf{R})\psi(\mathbf{r};\mathbf{R}) = E_e\psi(\mathbf{r};\mathbf{R})$ where $\mathbf{R}$ is a parameter. By varying $\mathbf{R}$ in very small steps and repeatedly solving the previous equation we can construct the potential energy surface (PES) $E_e(\mathbf{R})$. As long as the PES is well isolated from others, we can solve the nuclei motion by treating $E_e(\mathbf{R})$ as an effective potential and thus the vibrational and rotational structures are obtained. The BO PESs are represented by $^{2S+1}\Lambda_\Omega$ where the meaning of the symbols will be explained below.

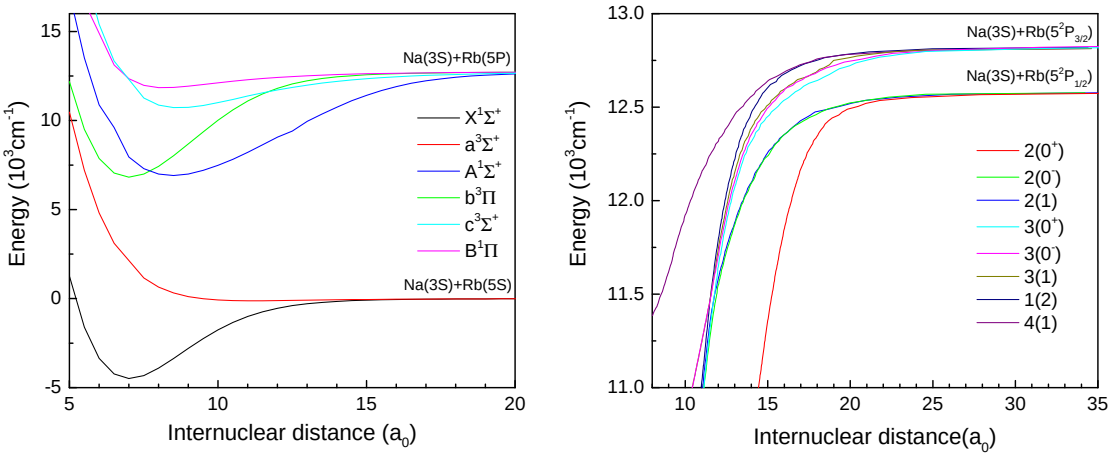

Figure 3.1: The PESs of the lowest six electronic states of the ^{23}Na^{87}Rb molecule: The BO PECs at small internuclear distance R and the long-rang spin-orbit potential.

The BO approximation neglects the possible coupling between the electronic and nuclear motions which breaks down in some cases. Including those coupling

we are interested in how the angular momenta in a molecule are coupled which is important for us to specify the transition selection rules. The angular momenta considered are the total electronic orbital angular momentum **L**, the total electronic spin angular momentum **S** and the nuclear rotational angular momentum **N**. In a diatomic molecule **L** processes very fast about the molecular axis and only its project M_L along this axis is well defined. The states with $\pm M_L$ are degenerate and we use $\Lambda = |M_L|$ to classify the energy levels. If $\Lambda \neq 0$, the total electronic spin would interact with the magnetic field produced by the orbital motion of the electrons which is called spin-orbit coupling. This causes **S** to process about the molecular axis and its projection Σ. The resultant total electronic angular momentum $\mathbf{J}_e$ is obtained by adding **L** and **S** and its component along the molecular axis $\Omega = |\Lambda + \Sigma|$. The above problem was first systematically studied by Hund giving rise to the five Hund's coupling cases. **Case (a):** Both the electronic orbital and spin angular momenta are strongly coupled to the molecular axis and the resultant Ω couples with **N** to form the total angular momentum **J**. The good quantum numbers are Λ, S, Σ, J and Ω. **Case (b):** The electronic spin is decoupled from the molecular axis and Ω is not defined. This can happen when $\Lambda = 0$ or the spin-orbit coupling is very weak. Then Λ is first coupled to **N** to form **K** which is coupled to **S** to give **J**. The good quantum numbers are Λ, N, S and J. **Case (c):** There are some cases where the spin-orbit coupling is stronger than the coupling to the molecular axis and Λ and Σ are not well defined. **L** and **S** first couple to give $\mathbf{J}_e$ which processes about the molecular axis. Then Ω couples with **N** to form **J**. In case (c) the good quantum numbers are J_e, Ω and J. **Case (d):** The coupling between **L** and **N** is the strongest one and the resultant **K** couples with **S** to give **J**. The good quantum numbers are L, N, K, S and J. **Case (e):** The coupling of **L** and **S** to the molecular axis is so weak that $\mathbf{J}_e$ couples with **N** directly. The resultant good quantum numbers are J_e, N and J. Only the first three coupling cases are important for us and the coupling in a diatomic molecule in certain electronic state may change with the internuclear distance R. For ^{23}Na^{87}Rb molecule, the lowest six levels at a short internuclear distance belongs to Hund's case (a) or (b) and their long-range parts are corresponding to Hund's case (b) or (c), which are illustrated in Fig. 3.1. So PESs are labeled by $^{2S+1}\Lambda_\Omega^{+/-}$ for short-range states while the long-range states are designated with $n(\Omega^{+/-})$. Here $+/-$ represents the reflection symmetry about a plane containing the molecular axis and n counts the same Ω states beginning from the lowest one.

The vibrational levels for a well-isolated electronic state form a regular progression that is represented by the anharmonic oscillator with the vibrational energy:

$$G(v) = \omega_e(v+1/2) - \omega_e x_e(v+1/2)^2 + \omega_e y_e(v+1/2)^3 + \cdots , \tag{3.1}$$

where v is the vibrational quantum number beginning from the lowest vibrational state with $v = 0$ and $\omega_e \gg \omega_e x_e \gg \omega_e y_e \gg \cdots$ are constants determined by the PES. However, the regular progression of the vibrational states can be disturbed by the presence of other neighboring electronic states locally via the spin-orbit coupling. In this situation we must solve the problem including the off-diagonal elements between the different electronic states. Apart from the vibrational motion, the rotational motion of the two nuclei would give us another energy scale in the molecule dynamics. It could be approximately modeled as a rigid rotor as the vibrational motion is much faster than the rotational one. Of course the rigorous solution is also available with the rotational energy:

$$F(J) = B_v J(J+1) - D_v[J(J+1)]^2 + H_v[J(J+1)]^3 + \cdots , \tag{3.2}$$

where J is the rotational quantum number and the coefficients $B_v \gg D_v \gg H_v \gg \cdots$ depend on the vibrational quantum number v and the PES. Usually these coefficients also form regular progressions in a well-isolated PES like $B_v = B_e - \alpha_e(v+1/2) + \gamma_e(v+1/2)^2 + \cdots$. These progressions becomes irregular as well for mixed electronic states. Alternatively we can experimentally determine them by analyzing the observed rotational spectrum.

Hyperfine interactions are also present in molecules and their structures would be perturbed by the external magnetic fields as that for atomic ones. The hyperfine structures result from the fact that the nuclei possess nonzero magnetic dipole and electric quadrupole moments which can interact with the magnetic and electric fields produced by the electrons. It is rather completed to fully understand the hyperfine structures in a diatomic molecule and the situation becomes even more difficult in a external magnetic field. So I will discuss some specific cases when we need them.

3.2 Creation of Feshbach Molecules

In this section I will present our work on the creation of the $^{23}Na^{87}Rb$ Feshbach molecule and also its characterizations.

3.2.1 Feshbach Resonance

From the quantum mechanics textbook we know the scattering amplitude of lth partial wave can be written as

$$f_l(k) = \frac{1}{k \cot \delta_l - ik}, \tag{3.3}$$

where k is determined by the scattering energy as $E = \frac{\hbar^2 k^2}{2M}$ and δ_l is the phase shift. When a bound state energy comes close to and crosses the scattering energy the phase shift crosses through $\pi/2$ and the scattering cross section rises through its maximum value $4\pi/k^2$. Physically this means the scattered wave is retarded by the bound state which has a finite lifetime. A Feshbach resonance refers to the resonant scattering when the bound state is provided by another channel which is called close channel. The scattering channel is designated as the entrance channel or open channel which is labeled by the quantum numbers of the two colliding atoms and their relative angular momentum. The phase shift picks up a resonant part δ_l^{res} depending on the closed channel and its coupling to open channel, apart from the background value δ_l^{bg} determined by the open channel. In the low-energy limit ($k \to 0$) only s-wave scattering contributes and the s-wave scattering length will also pick up a resonance feature. Due to the different magnetic moments of the scattering atoms and the bound states, the differential energies between the bound states and the scattering state can be tuned with a magnetic field. There are cases that those differential energies are tuned close to zero and Feshbach resonances occur. The explicit form of the s-wave scattering length for a magnetic Feshbach resonance is expressed as [**?**]

$$a = a_{bg} - a_{bg} \frac{\Delta}{B - B_0}, \tag{3.4}$$

where a_{bg} is the background scattering length related to the open channel, Δ is the resonance width and B_0 is the resonance position. By tuning the magnetic field we can continuously tune the scattering length from $-\infty$ to $+\infty$.

The above picture is based on a two-channel model and in practice a multi-channel model is need to determine the widths and positions of the different resonances. By comparing the theoretical and experimental results we can refine the PESs between the atoms and gain insights into the various spin couplings in a molecule. For us, the knowledge of the collision properties between ^{23}Na and ^{87}Rb atoms with different spin combinations is important for both the molecule and spinor experiments. Our group has measured the Feshbach resonances between ^{23}Na and ^{87}Rb both at their $F = 1$ states with different combinations of sublevels by monitoring the heating and loss of the atoms in the FORT. The experimental details and theoretical modelings can be found in [159]. We also extend this work to include more spin combinations and the data will be shown in the appendix.

3.2.2 Magneto-association

To specify the Feshbach resonances we have utilized to create the Feshbach molecules, the open channel is labeled with $|m_{Na}, m_{Rb}\rangle$ and the closed channel is labeled with $|\eta, v, m_F, N, m_N\rangle$. Here we have assumed the s-wave scattering at their lowest hyperfine manifolds. The symbols η, v, m_F, N and m_N represent the electronic state, the vibrational quantum number, the projection of the total angular momentum ignoring the molecular rotation along the magnetic field, the rotational quantum number and its projection respectively. Typically people classify the resonances according to N where $N = 0, 1, 2, \cdots$ is termed $s, p, d, \cdots$ wave resonance. To conserve the angular momentum we have $m_{Na} + m_{Rb} = m_F + m_N$. The Feshbach resonance we is located at 347.7 G with the open channel $|1, 1\rangle$ and closed channel $|a^3\Sigma^+, 21, 2, 0, 0\rangle$. The width of this resonance is predicted to be 4.89 G using the coupled channel calculation.

The association of the molecules can be understood from the dressed-state picture of a two-channel model which is illustrated in Fig. 3.2**a**, where the energies of the open channel (red dashed line), the closed channel (green dashed line) and the dressed states(black curve) are shown. If we start at a magnetic field above the resonance and adiabatically tune the magnetic field across the resonance we will end up with the population transfer from the free atoms to bound molecules. The ramping of the magnetic field in our experiments is presented in Fig. 3.2**b**. We prepare a ultracold mixture of ^{23}Na and ^{87}Rb at B =360 G with a typical atomic

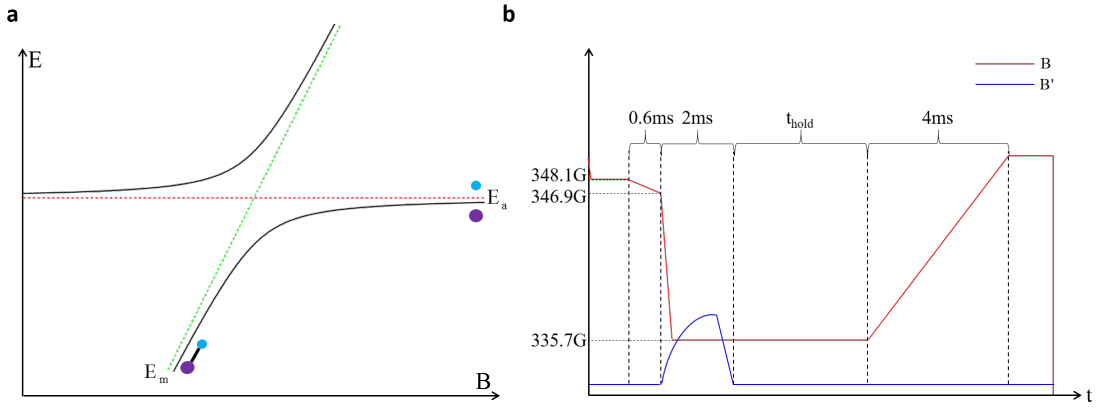

Figure 3.2: Magneto-association of the Feshbach molecules. **a**, The dressed state picture of the magneto-association. The dashed red (green) line is the bare energy of the entrance (closed) channel and the solid curves are the energies of the dressed states. **b**, Time sequence of the magneto-association. The red and blue curves represent the bias field and the gradient field, respectively.

number of 7×10^4 for both species and a temperature of 400 nK. The calculated peak density and PSD for ^{23}Na (^{87}Rb) are about $4 \times 10^{12}\text{cm}^{-3}$ ($3 \times 10^{13}\text{cm}^{-3}$) and 1.0 (0.84) respectively. To perform the magnetic association, we firstly ramp down the magnetic field near but still ∼0.4 G above the resonance and then across it with a ramp speed of 5.2 G/ms. We stop at about 346.9 G and further decrease the magnetic field to 335.7 G in 0.2 ms. Meanwhile, a magnetic field gradient pulse is imposed immediately after the association and the pulse shape is also shown in the figure with a duration of ∼2 ms and a maximum amplitude of 150 G/cm. This gradient pulse is used to remove the remaining atoms while the Feshbach molecules are little affected due to their near zero magnetic moments at the final field. After this step the pure molecular samples are held in the trap for certain times and then the magnetic field is ramped back crossing the resonance with a speed of 3.9 G/ms to dissociate the molecules to atoms for detection. With these procedures we can create about 1800 molecules, only 2.5% of the atomic number. A detailed study suggests an atom-molecule conversion efficiency of more than 10% [166]. We believe that this discrepancy is due to the fast molecular loss during the removing of the free atoms which will be illustrated later.

3.2.3 Lifetime Measurement

A long-lived sample of the Feshbach molecules is needed for further investigations like molecular spectroscopy and STIRAP. The most possible loss mechanism is the two-body process: A Feshbach molecule relaxes into deeper bound vibrational states via collisions with another particle (atom or molecule) and the released energy ejects both particles from the trap. Due to the high density of the atomic clouds, the molecule-atom collisional loss dominates when the atoms are present. To clarify this point we have performed the lifetime measurements with the atoms present or removed. For a direct comparison we fit both data points with an fist-

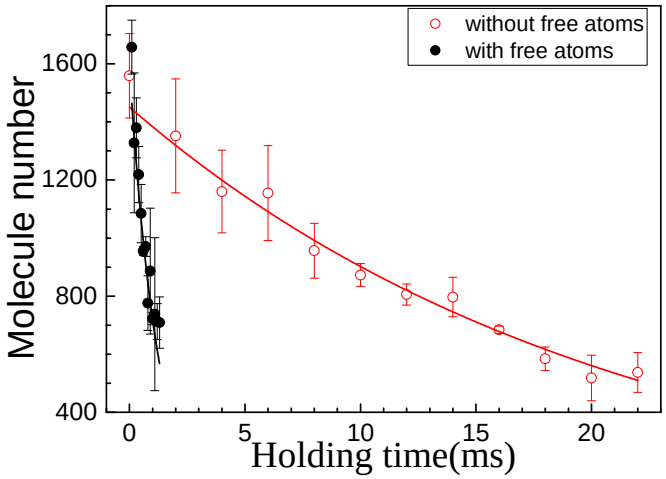

Figure 3.3: The lifetime measurement of the Feshbach molecules.

order exponential decay, shown in Fig. 3.3. We get a lifetime of 1.3(1) ms with the free atoms and 21(1) ms without the free atoms. The gradient pulse helps improve the molecular lifetime by a factor of about 16. However, we estimate that 1 ms is still needed for a complete spatial separation of the molecular and atomic clouds which is long enough to account for the aforementioned discrepancy.

The lifetime of 21(1) ms for pure molecular samples is long enough for the spectroscopic study and STIRAP. Our data in a pure molecular sample suggests a one-body loss dominated process which may come from the one-photon excitation of the molecules by our broadband trap light. Further increase of the lifetime can be done by using a single-frequency trap and a lattice potential can even make the lifetime only limited by the off-resonant scattering of the trap light.

3.2.4 Binding Energy of The Feshbach Molecule

To further characterize the Feshbach molecule as well as the Feshbach resonance, we have also measured the binding energy of the molecule using the oscillating magnetic field method [167]. Pairs of free atoms decay into the bound molecular state by stimulated emission with the help of the applied radio-frequency field when its frequency matches the binding energy of the molecules. This field is delivered by a small loop coil driven by a 1 W amplifier (ZHL-32A-S+) where it is coaxial with the Feshbach coil. As such a coil has a rather narrow bandwidth it is difficult to maintain a constant field strength when scanning the frequency. Instead we sweep the magnetic field with a frequency-fixed RF field and the molecular state will manifest itself as a narrow dip showing up in a wide background of the loss spectrum. An example of 1 MHz is shown in Fig. 3.4 and the data points are fitted with a Gaussian function for the background loss feature plus another Gaussian function convolved with a Maxwell distribution of the atomic kinetic energy for the narrow dip. The width and asymmetry of the dip is determined by the finite temperature of the atomic clouds and the resonant magnetic field from the fit is shifted from the maximum loss point.

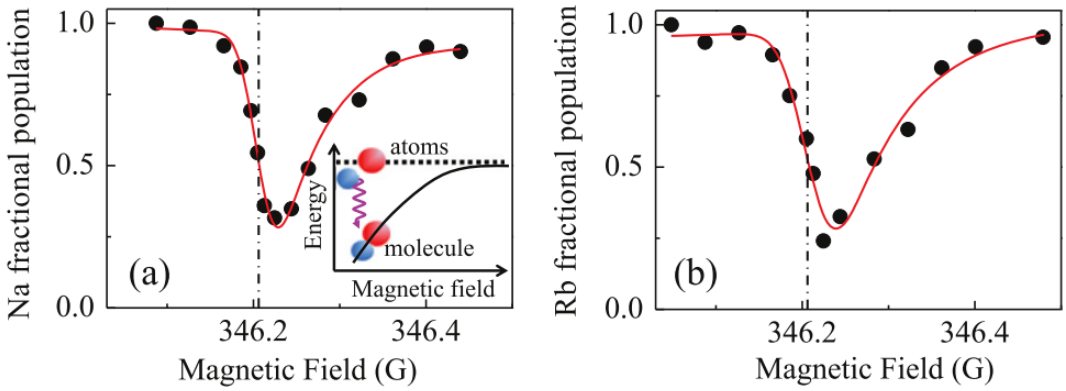

Figure 3.4: The binding energy measurement of the Feshbach molecule by the oscillating magnetic field method.

We systematically perform the measurements with the RF frequency varying from 0.1 MHz to 3.5 MHz. Due to the reduce of the free-bound Frank-Condon factor beyond 3.5 MHz, the coupling between atoms and molecules becomes so weak that we cannot obtain any reliable data. The results are summarized in

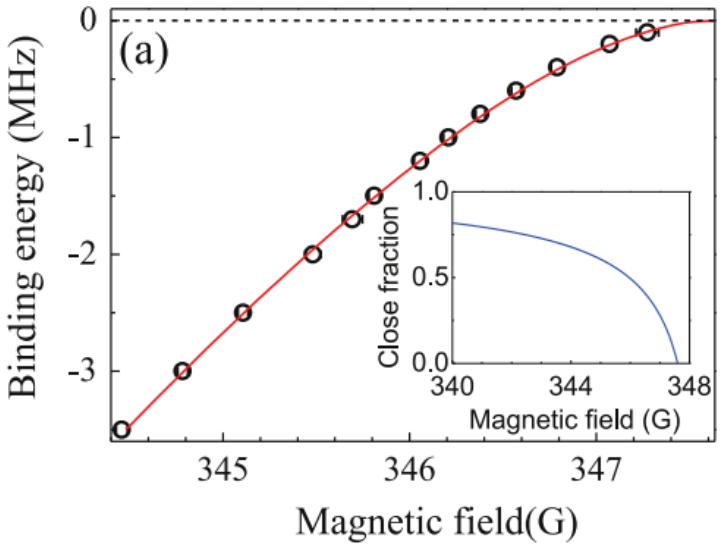

Figure 3.5: Binding energy versus the magnetic field. The solid red curve is a fit to the square well model [].

Fig. 3.5 where the data is fitted with the square model developed by Lange *et al* [168]. According to that model, the binding energy $E_b = \frac{\hbar k^2}{2m}$ is determined by the magnetic moment difference $\delta\mu$ between the open and closed channel and the Feshbach coupling strength Γ as

$$k = \frac{1}{a_{bg} - \bar{a}} + \frac{\Gamma/2}{\bar{a}(E_b + \delta\mu(B - B_c))}, \tag{3.5}$$

where $a_{bg} = 66.77 a_B$ [159], $\bar{a}$ is the mean scattering length calculated from the van der Walls C_6 coefficient by $\bar{a} \approx 0.478(2mC_6/\hbar^2)^{1/4}$ and B_c is the magnetic field where the molecular state is degenerate with the open channel threshold. The solid red curve in Fig. 3.5 is the fitting result with $\Gamma, \delta\mu$ and B_c as the free parameters. The Feshbach resonance width Δ and position B_0 can be calculated from these parameters by $\Delta = \frac{1}{\delta\mu}\frac{(a_{bg}-\bar{a})^2}{a_{bg}\bar{a}}\frac{\Gamma}{2}$ and $B_0 = B_c - \frac{a_{bg}}{a_{bg}-\bar{a}}\Delta$ and they are compared with the coupled-channel calculation in Table 3.1. These two models are consistent on the resonance position and they have different results for the width. Also I want to mention that the binding energies given by the coupled channel calculation have some disagreements with our measurement. We hope to resolve these problems by adding more data points to the Feshbach spectroscopy to refine the models.

	B_0(G)	Δ(G)	$\delta\mu(\mu$B)
Square well	347.64(3)	5.20(0.27)	2.66(29)
Coupled channel	347.75	4.89	-

Table 3.1: Parameters obtained from the square well model fit of the binding energy data.

3.2.5 Summary

In this section I have described the formation of Feshbach molecules by magneto-association as well as the characterization of their lifetime and the binding energy. We could produce a pure sample of ∼1800 molecules with a typical temperature of 500 nK and we are ready for the next step toward the ground state molecules with a lifetime of 21 ms in our current FORT. The work presented in this section is part of the publication of Ref. [166] for which I am the fourth author. I have contributed to the data acquisition and manuscript discussion for this paper.

3.3 One-photon Spectroscopic Study of The Molecular Excited States

Starting from the weakly bound Feshbach molecules we want to realize the population transfer to the rovibrational ground state. With a binding energy of 21 MHz at 335.7 G the Feshbach molecule is dominated by the closed channel which is of spin-triplet and designated as $|1\rangle$. The rovibrational ground state is of spin-singlet and labeled with $|3\rangle$. Since the electric dipole transition is semi-forbidden between triplet and single states, we need another intermediate state $|2\rangle$ which is able to simultaneously couple with the Feshbach and rovibrational ground states. (Even with a spin-singlet Feshbach dominated Feshbach state we still need an intermediate state for the quite poor Franck-Condon (FC) overlap.) So significant singlet-triplet mixing is expected for $|2\rangle$ and strong enough couplings with both $|1\rangle$ and $|3\rangle$ are required. These three states form a Λ-type system which is illustrated

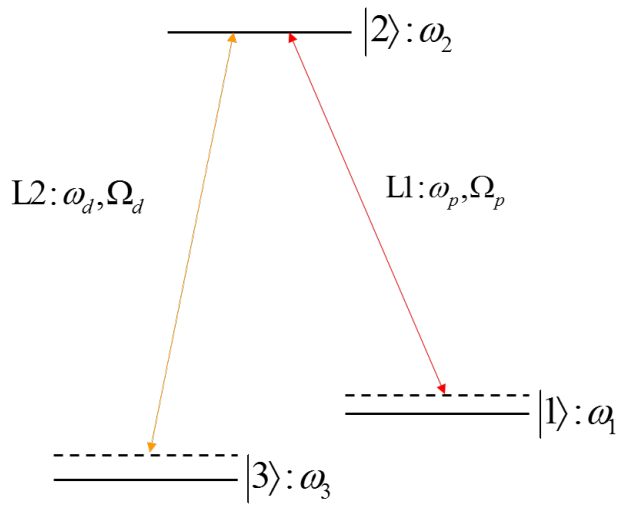

Figure 3.6: The Λ-type three-level system.

in Fig. 3.6, where $\hbar\omega_i$ are the energies for the state $|i\rangle$ (i =1, 2, 3), $|1\rangle$ and $|2\rangle$ are coupled by the pump light $L1$ (the angular frequency ω_p) with a Rabi frequency Ω_p and the dump transition between $|2\rangle$ and $|3\rangle$ are driven by the dump light $L2$ (the angular frequency ω_d) with a Rabi frequency Ω_d. Apart from the above requirements on $|2\rangle$ we also expect it to be well isolated from other states, namely a large hyperfine splitting, and have a long lifetime. These two requirements will

be discussed in detail in the next section.

In this section I would like to focus on the spectroscopic study of the excited states of the ^{23}Na^{87}Rb molecule to locate a suitable intermediate state. Apart from this purpose, the molecular structures themselves are also quite interesting to be investigated with an ultracold sample of Feshbach molecules. It is easy to get high-resolution spectra and here the bound-bound transitions are much stronger than the free-bound transitions in the photoassociation spectra [169]. However, the study is performed at a relative high magnetic field (335.7 G) and the molecular structures become much complexer due to the Zeeman effect. The measurements are performed with a horizontally propagating light with tunable linear polarizations which is exactly the laser $L1$ with a beam waist around 45 µm. Typically we impose a rectangular light pulse with a maximum power ranging from 1 µW to 20 mW and a pulse length of 1 µs∼4 ms and the excited molecular states will manifest as the loss of the Feshbach molecules. The laser frequency is measured by a commercial wavelength meter (HighFinesse WS7) with an absolute accuracy of 60 MHz. I want to list here several selection rules for the pump transition $|\mathrm{a}^3\Sigma^+, J=1, N=0, M=2\rangle \rightarrow |\mathrm{n}(\Omega'), J', M'\rangle$:

- $\Delta J = 0, \pm 1 : J' = 0, 1, 2;$
- $\Delta M = 0, \pm 1 : M' = 1, 2, 3 \begin{cases} M' = 2 & \text{for } \pi \text{ polarized light} \\ M' = 1, 3 & \text{for } \sigma \text{ polarized light} \end{cases};$
- Parity consideration:

$$\begin{cases} \text{Hund' s case (a):} & \mathrm{b}^3\Pi \text{ and } \mathrm{B}^1\Pi \ J' = 0, 1, 2 \\ \text{Hund' s case (b):} & \begin{cases} \mathrm{A}^1\Sigma & J' = 1 \\ \mathrm{c}^3\Sigma & J' = 0, 1, 2; N' = 1, J' = 2; N' = 3 \end{cases} \\ \text{Hund' s case (c):} & \begin{cases} \Omega' = 0^+ & J' = 1 \\ \Omega' = 0^- & J' = 0, 2 \\ \Omega' = 1 & J' = 1, 2 \\ \Omega' = 2 & J' = 2 \end{cases} \end{cases}.$$

The first two rules are easy to understand for a electric dipole transition and the third one is valid for approximately idea Hund' s cases. Also the possible J' values are based on the fact that we start with a positive parity state $|1\rangle$ and the electric dipole couples states with different parities. So only excited states with negative parities are addressed. For pure $\mathrm{b}^3\Pi$ and $\mathrm{B}^1\Pi$ states the rotational levels contain

both positive and negative parity parts due to the degeneracy of $\pm\Lambda$ states. The same argument is held for the Hund' s case (c) with $\Omega' \neq 0$. For pure $A^1\Sigma$ and $c^3\Sigma^+$ states the parity is determined only by the molecular rotation $(-1)^{N'}$. For Hund' s case (c) with $\Omega' = 0^+$ the electronic parity is positive. Only odd J' level can have negative total parity, so only $J' = 1$ can be accessed. While for the 0^- state, the electronic parity is negative; thus both $J' = 0$ and 2 can be reached.

This section will be divided into three parts. The first part presents the search for the states belonging to the $b^3\Pi_1$-$B^1\Pi$-$c^3\Sigma^+$ admixture near the dissociation asymptote ^{23}Na $(3^2S_{1/2})$+^{87}Rb $(5^2P_{1/2})$. We have observed quite complicated structures there and even the identification of different vibrational series is still lacking. However, we have found several vibrational levels which are very promising for the STIRAP. To better understand the molecular structures we explored the vibrational states just below the ^{87}Rb D2 line where a simpler case is expected and we have successfully identified five vibrational series. This is the second part. The third part deals with the $A^1\Sigma^+_{\Omega'}$-$b^3\Pi_{\Omega'}(\Omega' = 0, 1)$ admixture where a suitable intermediate state is located and finally used to conduct the STIRAP transfer.

Here I want to thank our theoretical collaborators (Theomol Group in CNRS) for providing all the calculations of the transition energies, singlet (triplet) fractions and transition dipole moments (TDMs).

3.3.1 Excited States Near The ^{87}Rb D1 Line

The study of the excited states just below the ^{87}Rb D1 line is stimulated by two reasons. One is that singlet-triplet mixing has been observed in the traditional spectroscopic investigations around this frequency region [163,164]. It was justified that the strong perturbations of $B^1\Pi(v' = 7 \sim 30)$ states come from the $c^3\Sigma^+$ or $b^3\Pi_1$ states through the spin-orbit interactions. However, significant broadening of the states slightly above the ^{87}Rb D1 line has been observed in [164] and we also confirmed this phenomenon in our experiments. The other reason is related to the FC principle where the coupling between two vibrational levels of different electronic states is propotional to the vibrational wavefunctions overlap. For the dump transition, supposing that the internuclear distance is unchanged during the electronic transition it happens more likely when the equilibrium distance R_e^X of the ground state coincides with one of the classical turning points of the excited

states. In the $B^1\Pi$ case it corresponds to the region close to the dissociation asymptote ^{23}Na $3^2S_{1/2}$+^{87}Rb $5^2P_{1/2}$. In Fig. 3.7 I present the theoretical results for the TDMs between the perturbed excited states and both the Feshbach and rovibrational ground state, namely $b^3\Pi/a^3\Sigma^+(v = 22)$, $c^3\Sigma^+/a^3\Sigma^+(v = 22)$ and $B^1\Pi/X^1\Sigma^+(v'' = 0)$. The inset shows you the single fractions of the excited states

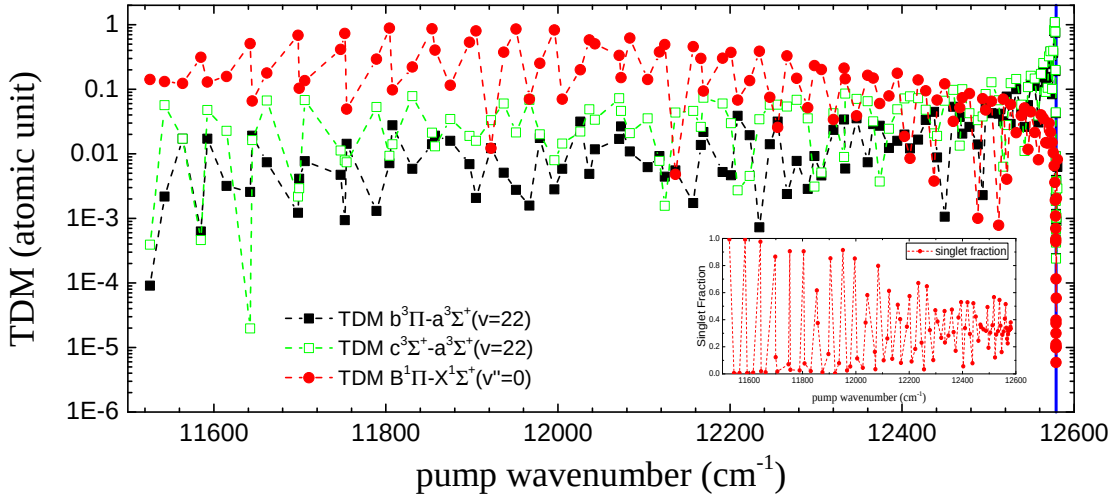

Figure 3.7: The transition dipole moments between the excited states below the ^{87}Rb D1 line and both the Feshbach and rovibrational ground state.

and we can see that it is more likely to find a strongly perturbed state not far away from the ^{87}Rb D1 line (blue solid line in the figure). In the pump wavenumber window [12 400 cm^{-1}, 12 550 cm^{-1}] we can have TDMs on the order of 0.1 ea$_B$ for both pump and dump transitions. So the states inside this window may be ideal for STIRAP.

To locate a suitable intermediate state in this frequency region as well as understand the molecular structures, we have scanned the $L1$ wavenumber from 12 579.1 cm^{-1} to 12 544 cm^{-1} with a step of 0.002 cm^{-1}. We have also selectively scanned the wavenumber around 12 523 cm^{-1}, 12 498 cm^{-1} and 12 449 cm^{-1} where we have greater possibilities to observe strong singlet-triplet mixing. The spectrum is summarized in Fig. 3.8 and the ^{87}Rb D1 line at 335.7 G is also indicated with a green mark. For states dissociated to the ^{87}Rb D1 line, it is more reasonable to work with Hund' s (c) case where they are labeled by $n(\Omega')$. We have $2(0^{\pm})$ and $2(1)$ correlated to the ^{87}Rb D1 line; $3(0^{\pm}), 3(1), 4(1)$ and $1(2)$ correlated to ^{87}Rb D2 line are used for a consistent label. For the former three states, it is useful to

analyze the vibrational series with the LeRoy-Bernstein (LB) formula [170,171]. It expresses the binding energies E_v of a potential $V(R)$ having an asymptotic form as $-C_n/R^n$ versus the vibrational quantum number v by

$$v_D - v = (\frac{E_v}{E_n})^{\frac{n-2}{2n}} \text{ with } E_n = [\sqrt{\frac{\pi}{2\mu}} \frac{\hbar(n-2)}{C_n^{1/n}} \frac{\Gamma(1+\frac{1}{n})}{\Gamma(\frac{1}{2}+\frac{1}{n})}]^{\frac{2n}{n-2}}, \tag{3.6}$$

where v_D is the effective vibrational quantum number at dissociation and E_n is a parameter determined by the reduced mass μ and the asymptotic form of $V(R)$. Here for van der Walls potentials with $n = 6$ the energy spacings between adjacent vibrational states scale as $E_6(v_D - v)^3$. However this analysis may not work well here if many vibrational states are strongly perturbed by the other five vibrational series and the spacings become irregular. We cannot classify all the observed levels into different vibrational series of 100% confidence.

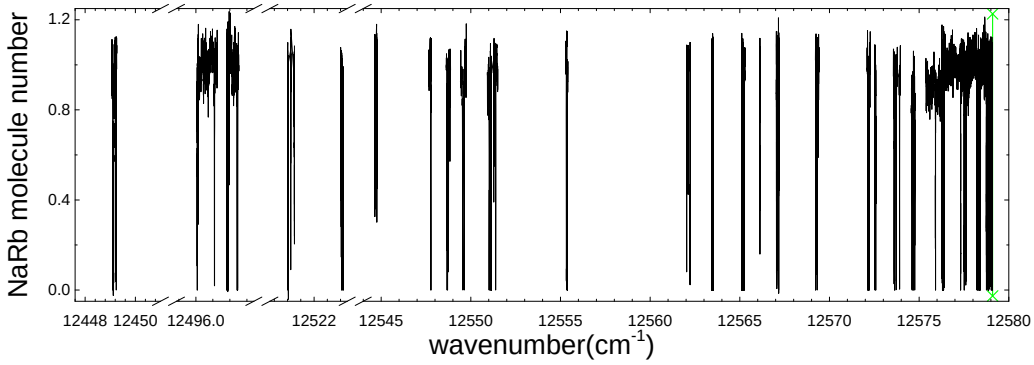

Figure 3.8: The excited states near the Rb D1 line.

Although the assignment of the vibrational states is lacking, we can characterize the pump TDMs and the lifetimes of the excited states. This is done based on a master-equation treatment of a two-level system with a dissipative excited state [172]. It is equivalent to the non-Hermitian Hamiltonian method [173] where an imaginary part is added to the energy of $|2\rangle$ to account for the dissipative nature of $|2\rangle$. Here we present the master-equation approach and the non-Hermitian Hamiltonian method is used to illustrate the insight into the strong decay regime in the next subsection. In the master equation, the Hamiltonian can be written as

$$H = \hbar \begin{pmatrix} -\Delta & \frac{\Omega}{2} \\ \frac{\Omega}{2} & 0 \end{pmatrix}. \tag{3.7}$$

Here Δ and Ω are the detuning and the Rabi frequency, respectively. The finite lifetime of the excited state is taken into consideration by introducing a phenomenological decay matrix [172]:

$$\frac{d\rho}{dt} = -\frac{i}{\hbar}[H,\rho] - \frac{1}{2}\{\Gamma,\rho\}, \tag{3.8}$$

where $\Gamma = \mathrm{diag}(\gamma, 0)$ with the excited state natural width γ. With the initial state occupying the ground state, we have $\rho(0) = \left(\begin{smallmatrix} 0 & 0 \\ 0 & 1 \end{smallmatrix}\right)$. Solving the master equation gives the time-dependent $\rho_{22}(t)$, namely the population of the ground state. We fit the spectrum to this result using Ω, Γ and the line shape center as the free parameters. Furthermore, this treatment is quite easy to be extended to cases with $n(n = 1, 2, 3, \cdots)$ excited states, where the corresponding Hamiltonian and decay matrix read:

$$H_n = \hbar \begin{pmatrix} -\Delta_n & 0 & \cdots & 0 & \frac{\Omega_n}{2} \\ 0 & -\Delta_{n-1} & \cdots & 0 & \frac{\Omega_{n-1}}{2} \\ \vdots & \vdots & \ddots & \vdots & \vdots \\ 0 & 0 & \cdots & -\Delta_1 & \frac{\Omega_1}{2} \\ \frac{\Omega_n}{2} & \frac{\Omega_{n-1}}{2} & \cdots & \frac{\Omega_1}{2} & 0 \end{pmatrix}, \tag{3.9}$$

$$\Gamma_n = \mathrm{diag}(\gamma_n, \gamma_{n-1}, \cdots, \gamma_1, 0).$$

We have selectively done the calibration for several lines which are most likely to fulfill our requirements. With the fitted Rabi frequency Ω, laser power P and beam waist w_0 we can obtain the TDM by the equation: TDM$= \hbar\Omega\frac{w_0}{2}\sqrt{\frac{\pi c\epsilon_0(1+e)}{P}}$. Here c is the light velocity, ϵ_0 is the vacuum permittivity and e is a parameter accounting for the laser polarization. ($e = 0$ (1) for π (σ) transitions.) The fitted curves are shown in Fig. 3.9 and the obtained parameters are listed in Table 3.2. For the $n > 1$ cases here, we have assumed the same nature linewidth which is reasonable for resolvable substructures belonging to a same rotational level.

The typical lifetimes of the excited states are on the order of 30 ns. The fitted pump TDMs are typically 3∼5 times smaller than the calculated values in Fig. 3.7, which don't include the Hönl-London (HL) factor concerning the hyperfine structure. We will present a detailed analysis of the 12449.1 level below. The results suggest that the pump TDM is increasing as the state approaches the ^{87}Rb D1 line. However, we still focus on the more deeply bound states , namely the 12449.1 level, due to its expected much larger dump TDM. I would like to leave the calibration of this value to next section. With a maximum laser power of

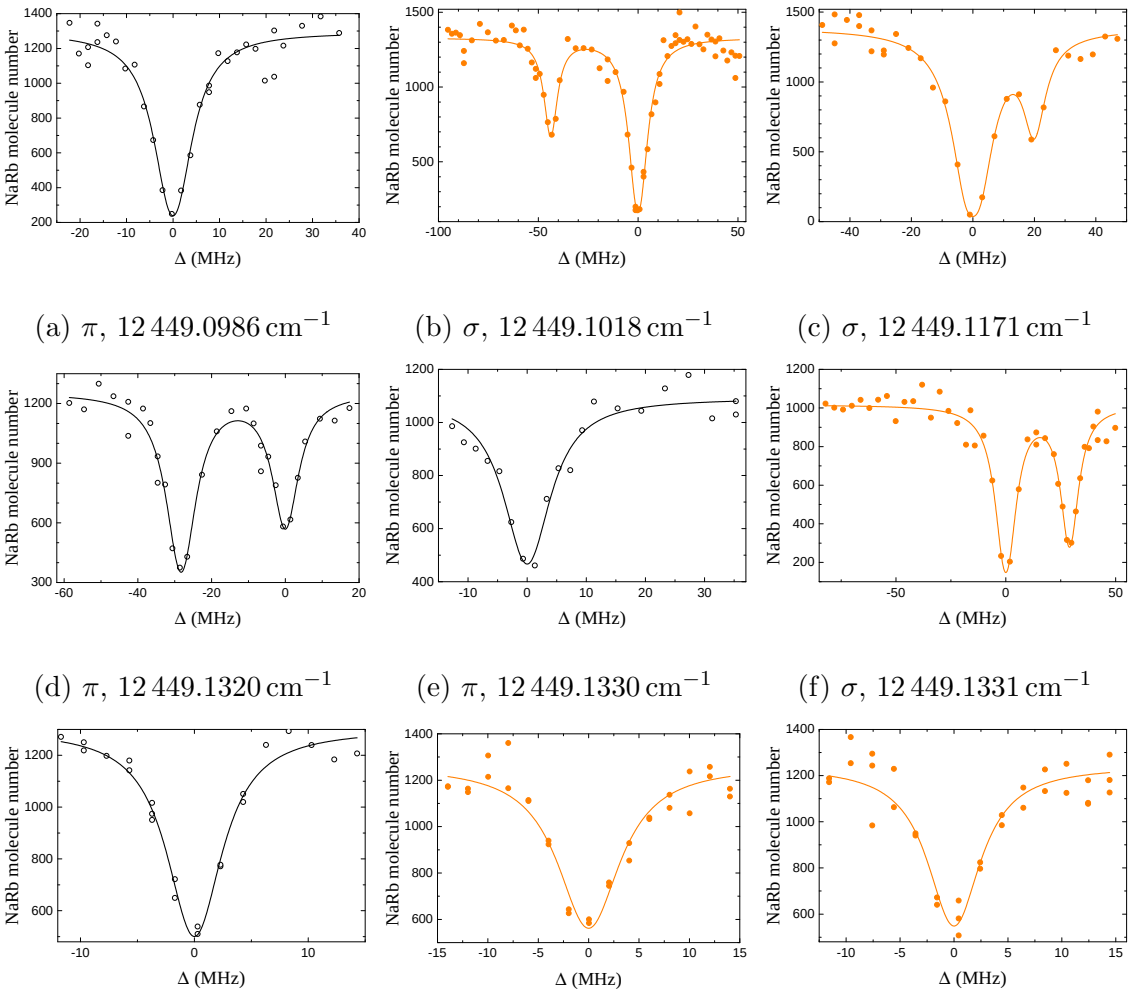

(a) π, 12 449.0986 cm^{-1} (b) σ, 12 449.1018 cm^{-1} (c) σ, 12 449.1171 cm^{-1}

(d) π, 12 449.1320 cm^{-1} (e) π, 12 449.1330 cm^{-1} (f) σ, 12 449.1331 cm^{-1}

(g) π, 12 499.2226 cm^{-1} (h) σ, 12 548.6562 cm^{-1} (i) σ, 12 548.7012 cm^{-1}

Figure 3.9: Calibration of the pump transition dipole moments and the lifetimes of the excited states for several lines slightly below the ^{87}Rb D1 line.

30 mW and a beam waist of 45 µm, the maximum Rabi frequency available for the strongest transition around 12 449.1 cm^{-1} is up to $2\pi\times400$ MHz.

In Fig. 3.10 we show all the observed lines near 12 449.1 cm^{-1} and we have identified the $J' = 1$ and $J' = 2$ states. So we confirm that this state is mainly of $\Omega' = 1$ character from the selection rules. The understanding of the hyperfine structures is not thoroughly finished at this point and we still need both theoretical and experimental efforts. Here I want to present our preliminary analysis based on a asymptotic model described in Ref. [174]. Neglecting the interaction between

f_c (cm^{-1})	P	τ (ns)	TDM (ea_B)	f_c (cm^{-1})	P	τ (ns)	TDM (ea_B)
12449.0986	π	24	0.004	12449.1330	π	22	0.006
12449.1004	σ	23	0.008	12449.1331	σ	22	0.013
12449.1018	σ	23	0.014	12449.1341	σ	22	0.011
12449.1171	σ	22	0.010	12499.2226	π	34	0.018
12449.1177	σ	22	0.005	12548.6562	σ	26	0.021
12449.1310	π	22	0.012	12548.7012	σ	33	0.048
12449.1320	π	22	0.010	-	-	-	-

Table 3.2: Calibrated parameters for the excited states slightly below the ^{87}Rb D1 line.

the molecular rotation and the nuclear spin, the Hamiltonian for the hyperfine structure at a magnetic field can be written as

$$\begin{aligned} H/\hbar &= H_{hfs} + H_Z, \\ H_{hfs} &= (A_{Na}\mathbf{I}_{Na} + A_{Rb}\mathbf{I}_{Rb}) \cdot \mathbf{\Omega}' + K_{Na}\mathbf{I}_{Na} \cdot \mathbf{\Sigma}, \\ H_Z &= -g_{Na}M_{Na}B - g_{Rb}M_{Rb}B - g_{J'}M_{J'}B. \end{aligned} \tag{3.10}$$

Here A_{Na} (A_{Rb}) term accounts for the coupling between the molecular axis and the ^{23}Na (^{87}Rb) nuclear spin, K_{Na} term is the atomic Fermi contact interaction between the electronic wavefunction and the ^{23}Na nuclear spin (It is negligible for a P state atom.), and g_{Na}, g_{Rb} and g_J terms are Zeeman energies of the Na nuclear, Rb nuclear and electrons. From our theoretical collaborators the values of A_{Na}, A_{Rb} and K_{Na} within the asymptotic model are estimated to be 13 MHz, 130 MHz and 399 MHz respectively. The Zeeman energy of the nuclear spin is on the order of 0.5 MHz which is negligible here. With the π and σ polarized light, we can access totally 18 basis states $|M_{J'}, M_{Na}, M_{Rb}\rangle$ starting from $M = 2$ for the initial state: 9 $M' = 1$ states, 6 $M' = 2$ states and 3 $M' = 3$ states. In principle, we can represent the Hamiltonian by a 18×18 matrix and diagonalizing the matrix will give all the observable energy levels. Then we can adjust the

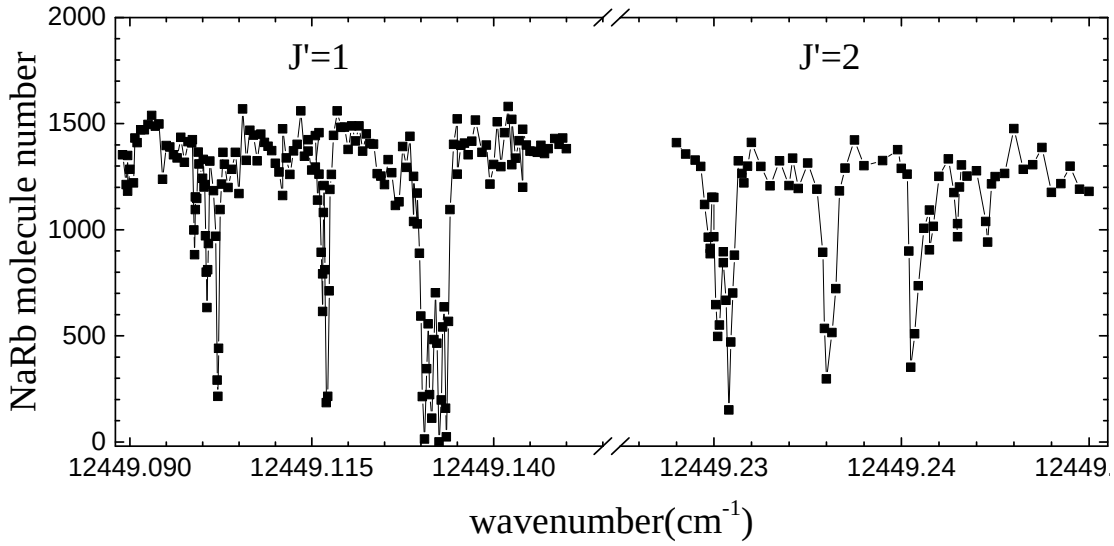

Figure 3.10: The one-photon spectrum of the vibrational state near 12 449.1 cm^{-1}.

interaction parameters to match the calculated levels to the observed spectra. In this way we can interpret the observed loss features within the basis.

The coupled-channel calculation of the vibrational levels reveal that this level is a strongly mixed state of $b^3\Pi$, $B^1\Pi$ and $c^3\Sigma^+$ potentials and thus it cannot be represented by any pure Hund' s case (a) or (c). However, we can still write down the Hamiltonian as that in Eq. 3.10 for the form of the Hamiltonian is the same for the three BO states. Now the interaction parameters are mixed and we cannot have any initial value for them. For example, the Zeeman energy parameter of the electrons for the $J' = 1$ level, $g_1 B$, is a mixing of these three values: $g_1 B(\mathrm{B}^1\Pi)$=$g_1 B(\mathrm{b}^3\Pi)$=235 MHz and $g_1 B(\mathrm{c}^3\Sigma^+)$=470 MHz at B =335.7 G. It is similar for Σ: $\Sigma(\mathrm{B}^1\Pi)$=$\Sigma(\mathrm{b}^3\Pi)$=0 and $\Sigma(\mathrm{c}^3\Sigma^+)$=1. We diagonalize the resultant Hamiltonian and adjust the interaction parameters to match the eigenvalues to the spectrum. With this step we can only figure out the component of $c^3\Sigma^+$ to be around 58% to our best estimation, which is close to the value obtained from the coupled-channel calculation. The detailed assignments would be presented in the future publications of our group. For the $J' = 2$ level the Zeeman interaction parameter will become smaller, roughly one half of that for the $J' = 1$ level. Although five groups of substructures are expected, only three are observed maybe due to the small TDMs. (Missing lines are $M_{J'} = \pm 2$ from our calculation.) We can also obtain the rotational constant B_v from the data by the spacing between different J' states: $B_v = \frac{\Delta E}{2(2+1)-1(1+1)} = h \times 0.003\,\mathrm{cm}^{-1}$ where ΔE is the spacing

between $M_{J'} = 0$ states.

With one of the lines near 12 449.1 cm^{-1} as the intermediate state, the dump wavenumber is around 17 427 cm^{-1} (574 nm). The available laser in our lab for this wavelength is the dye laser with a maximum output power of 600 mW and a short-term linewidth <100 kHz. For our purpose, we need to reduce the this value down to the order of 1 kHz by either the internal modulation, like inserting a electric-optical modulator (EOM) into the laser cavity [175], or the external modulation [176] and some special efforts are needed in all cases.

3.3.2 Excited States Near The ^{87}Rb D2 Line

As the understanding of the spectrum just below the ^{87}Rb D1 line is difficult due to the strong perturbation among various states, the excited states just below the ^{87}Rb D2 line are free of perturbations and the study of them may help us partially solve the previous difficulty. Besides this purpose, it is also important for understanding fundamental molecular dynamics at the long-range parts of the potential which are not covered well by the conventional molecular spectroscopy.

We obtain the spectrum by tuning the spectroscopic laser from 12816.5 to 12 806 cm^{-1} with typical steps of 50 MHz. We would present our results detuned to the ^{87}Rb D2 transition, namely the transition from the ground-state hyperfine asymptote $^{23}\mathrm{Na}(3^2S_{1/2},\ |F=1, m_F=1\rangle)+\ ^{87}\mathrm{Rb}(5^2S_{1/2},\ |F=1, m_F=1\rangle)$ to the center of gravity of the $^{23}\mathrm{Na}(3^2S_{1/2})+^{87}\mathrm{Rb}(5^2P_{3/2})$ asymptote. After taking the Zeeman shifts at 335.7 G into account, the excited-state asymptotic limit is taken as 12 816.724 cm^{-1}. The small binding energy of the Feshbach molecules is neglected.

In Fig. 3.11 we show the whole spectrum near the $^{23}\mathrm{Na}(3^2S_{1/2})+^{87}\mathrm{Rb}(5^2P_{3/2})$ asymptote. Levels with detuning less than $-1.2\,\mathrm{cm}^{-1}$ are not resolved, probably due to the very dense and strong resonances near this region, as well as predissociation-induced broadening which we will discuss below. At a first glance the spectrum seems rather complex and similar to that below ^{87}Rb D1 line, reflecting the fact that there are five attractive long-range potentials, $3(0^+), 3(0^-), 3(1), 4(1)$ and $1(2)$, associated with this asymptote. Here we are using the Hund's case (c) notation, already discussed in previous section.

Scrutinizing the line shape patterns and level spacings, we have picked out four vibrational series from the spectrum and listed them in Table 3.3. One key to

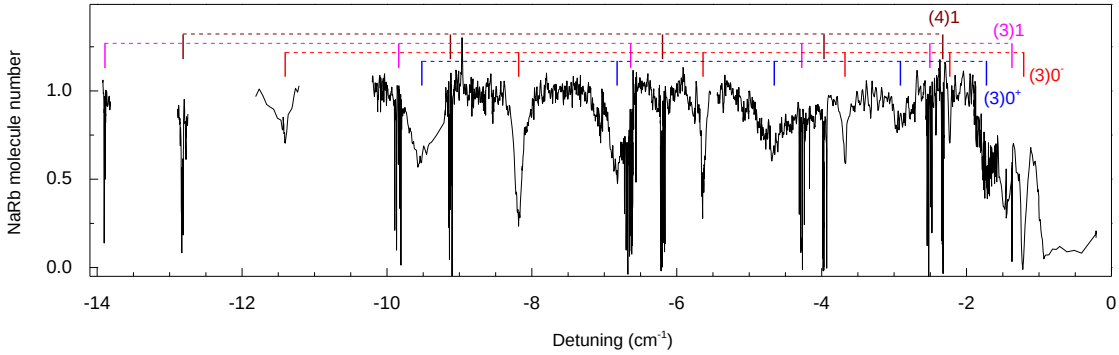

Figure 3.11: The excited states near the Rb D2 line. Four vibrational series are distinguished from each other by their very different line shapes and distributions. Each series contains five to six levels. Our assignments are depicted by four sets of vertically displaced solid bars. The bottom dashed line correlates with both 3(1) and $3(0^-)$.

achieve sensible assignments is the well resolved hyperfine and Zeeman structures for $\Omega' > 0$ states. As shown in Figs. 3.12 (a) and 3.12**b**, vibrational levels in two of the identified series have sharp substructures. To tell which state they belong to, we compare our spectrum to calculated vibrational levels based on the Rydberg-Klein-Rees (RKR) potential of the $B^1\Pi$ state given in [164]. The 4(1) state is correlated to the $B^1\Pi$ state at long range. Good matching to the series including the level in Fig. 3.12**a** is found by an overall $-0.15\,\mathrm{cm}^{-1}$ shift of the calculated vibrational levels. This series is thus assigned to the 4(1) state.

Another key for the assignment is the predissociation caused by coupling with long-range states correlated to the lower $^{23}\mathrm{Na}(3^2S_{1/2})+^{87}\mathrm{Rb}(5^2P_{1/2})$ asymptote. A similar mechanism, which typically results in significant linewidth broadening, has been observed in several other alkali dimers [177]. It affects the $3(0^+), 3(0^-)$ and 3(1) states, as can be seen from the long-range potential in the right column of Fig. 3.1. The 4(1) and 1(2) states, on the other hand, are free from predissociation. Thus the vibrational series including the level in Fig. 3.12**b** can only come from the 1(2) state, as the well resolved substructures with sharp peaks indicate no sign of predissociation. Detailed assignment of these substructures is still lacking at this point.

Table 3.3: Summary of the observed long-range vibrational levels near the $^{23}\mathrm{Na}(3^2S_{1/2})+^{87}\mathrm{Rb}(5^2P_{3/2})$ asymptote. The v index is deduced from a LeRoy-Bernstein fit (see text). Note that $v = -1$ represents the highest vibrational level. The linewidths of levels with predissociation are also listed.

State	E_v (cm^{-1})	v	Linewidth (GHz)	State	E_v (cm^{-1})	v	Linewidth (GHz)
	12814.3843	-6	-		12814.9872	-6	9.4
	12812.7455	-7	-		12813.8007	-7	8
4(1)	12810.5167	-8	-	$3(1,0^-)$	12812.0585	-8	10
	12807.5884	-9	-		12809.8893	-9	10
	12803.8984	-10	-		12807.194	-10	-
	12815.3403	-5	-		12815.5017	-5	3
	12814.2063	-6	-		12814.4814	-6	3.4
	12812.4381	-7	-		12813.0347	-7	1.8
1(2)				$3(0^+)$			
	12810.0764	-8	-		12811.0757	-8	1.7
	12806.8752	-9	-		12808.5312	-9	1
	12802.8207	-10	-		12805.3087	-10	1.9

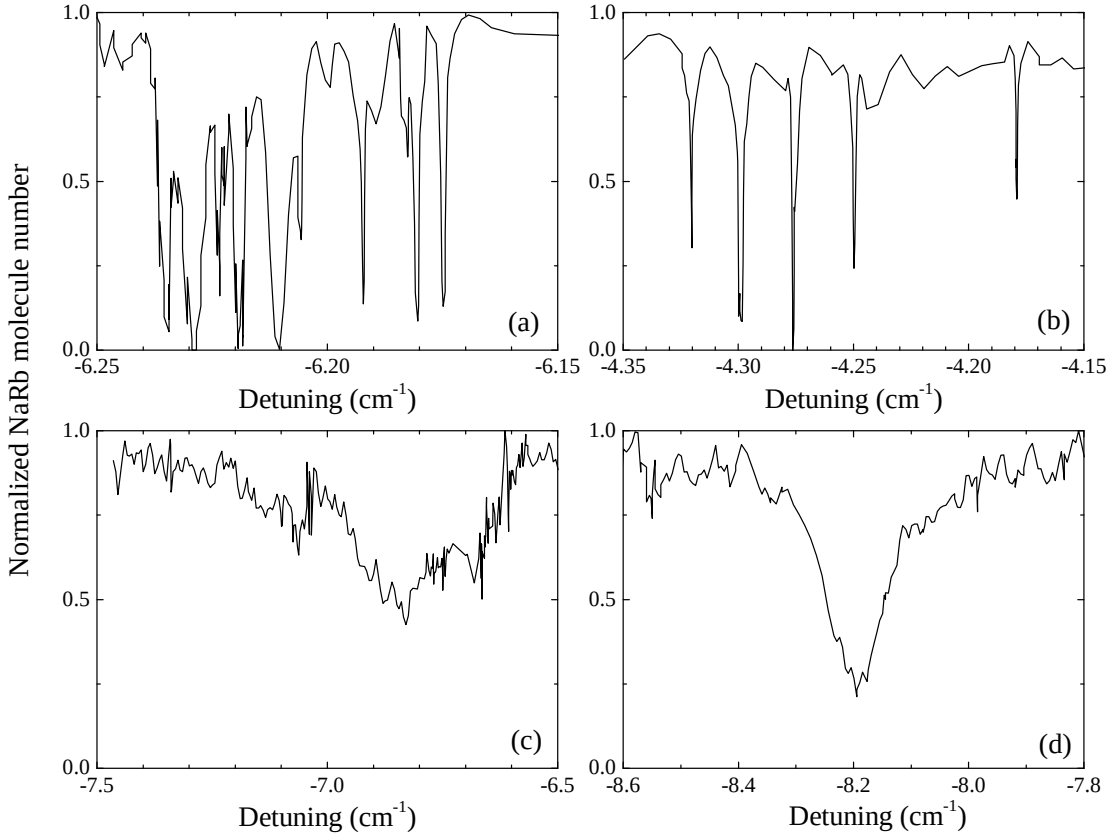

Figure 3.12: High resolution spectrum of different states below ^{87}Rb D2 line. (a), (b), (c) and (d) are typical line shapes of 4(1), 1(2), 3(1,0$^-$) and 3(0$^+$) states, respectively. The sharp structures in 4(1) and 1(2) levels are from hyperfine and Zeeman interactions. The very broad linewidths in 3(1,0$^-$) and 3(0$^+$) levels are due to fast predissociation. See text for details.

According the selection rules listed at the beginning of this chapter, for 3(1) and 4(1) states we can access $J' = 1$ and 2, while for the 1(2) state, only $J' = 2$ is possible. For the 0^+ state, only $J' = 1$ can be accessed. While for the 0^- state both $J' = 0$ and 2 can be reached. The predissociation observed in the other three states, however, obscures all rotational structures. We could treat the excitation to these vibrational levels as two-level problems with strongly dissipative excited states. We have mentioned in previous subsection that the non-Hermitian Hamiltonian method could give a simple understanding of the observed line shapes

where the Hamiltonian reads

$$H = \hbar \begin{pmatrix} -\Delta - i\Gamma/2 & \frac{\Omega}{2} \\ \frac{\Omega}{2} & 0 \end{pmatrix}. \tag{3.11}$$

In the limit of $\Gamma \gg \Omega$, the excited state is well-isolated from the ground state and the excitation probability reduces as Γ is increased. The loss line shapes in Figs. 3.12 (c) and 3.12 (d) have large widths but small depths which indicate strongly dissipative excited states. We can fit the line shapes to the solution of the Schrödinger equation and extract Γ. As can be seen in Table 3.3, for the series including Fig. 3.12 (c), the extracted linewidths are on the order of 10 GHz, while the other series have typical linewidths of 1 to 3 GHz. Typical rotational spacings for these near dissociation levels are estimated to be about 1 GHz, comparable or smaller than the observed linewidths. All of these values are much larger than the radiative lifetime limited linewidths, which are on the order of several MHz. We have verified experimentally that the contribution from the power broadening is negligible. We note that even for the 4(1) state without predissociation, rotational levels are still hard to identify due to the comparable splittings from hyperfine and Zeeman interactions.

To make the final assignment we resort to the detailed study of the predissociation processes. The $3(0^+)$ state results from the spin-orbit coupling between the $A^1\Sigma^+$ and the $b^3\Pi$ states with a crossing at internuclear distance of about $7.7\,a_0$. The $3(0^-)$ and the main characters of the 3(1) states are from the spin-orbit coupling between the $c^3\Sigma^+$ and the $b^3\Pi$ states with a crossing at around $11.8\,a_0$. The linewidth can be estimated with a Landau-Zener model which takes into account the spin-orbit coupling strength between the adiabatic potential curves and the difference between their slopes at their crossing point. With this model we obtain linewidth upper bounds of $2\pi\times$ 2.7, 9.4 and 12.3 GHz for the $3(0^+)$, 3(1) and $3(0^-)$ states, respectively. Thus most probably, the series including Fig. 3.12 (d) is from the $3(0^+)$ state. We attribute the series including Fig. 3.12 (c) to both 3(1) and $3(0^-)$, as those two states have very similar long-range dispersion coefficients and are expected to have closely spaced vibrational levels. With the very large predissociation linewidth, it becomes hard to resolve them individually.

With the assignment decided, the C_6 coefficients can be obtained by fitting the measured vibrational binding energies of each series to the LB formula described in previous subsection. However, here we take v_D to be a number between 1

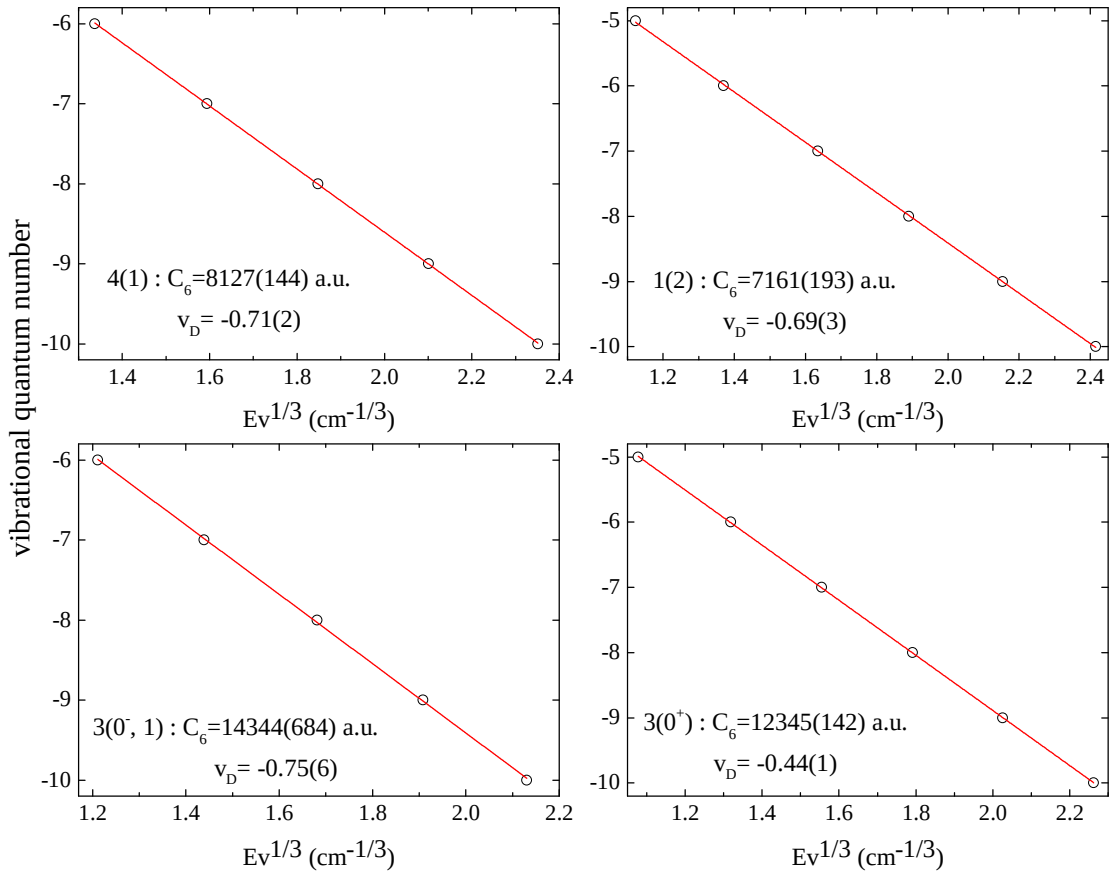

Figure 3.13: Plot of the the relative vibrational quantum number v vs. 1/3 power of the vibrational binding energy E_v. The states in (a), (b), (c) and (d) are in the same order as Fig. 3.12. The C_6 coefficients can be obtained from the slopes of the linear fits.

and 0 as the last bound level is designed as $v = -1$. Figure 3.13 shows the fits of the $E_v^{1/3}$ versus v for all the observed vibrational series. For each series, the C6 coefficients are extracted from the fit and listed in Table 3.4, together with the C_6 values from two previous calculations [178, 179]. The C_6 values of columns (a) and (b) in Table 3.4 are deduced from the van der Waals coefficients for Hund's case (a) states calculated in Ref. [178] and [179], respectively, using the analytical formulas of Ref. [180] which are exactly solvable with the exchange energy neglected. The agreement between our results and the values deduced from Ref. [178] is quite reasonable, with less than 10% discrepancies for most of

Table 3.4: C_6 coefficients from the LB fits and their comparison with several theoretical works. (a) and (b) from Refs. [178] and [179], respectively, using the analytical formula of Ref. [180]. (c) From Ref. [179].

States	LB fit (a.u.)	(a)(a.u.)	(b)(a.u.)	(c)(a.u.)
4(1)	-8238	-7484.5	-9351	-9437
1(2)	-7236	-7484.5	-9351	-9428
3(1)	-14509	-14909	-17702	-18261
$3(0^-)$	-14509	-14909	-17702	-18276
$3(0^+)$	-12498	-14909	-17702	-18252

the states. The only exception is the $3(0^+)$ state, which shows a 16% difference. On the other hand, we observe a disagreement larger than 20% for most states with the values analytically deduced from Ref. [179]. Such differences originate in those observed in the Hund's case (a) C_6 values between Refs. [178] and [179], related to the details of the computed atomic wave functions. For completeness, we also display in column (c) of Table 3.4 the C_6 values reported in Ref. [179], where the authors fitted their numerical calculations.

The uncertainties of our results for the C_6 coefficients can be discussed by estimating the contribution of the next term in the multipolar expansion of the long-range interaction energy, i.e., C_8/R^8. At the internuclear distance of $30\,a_0$ already reached by several of the observed vibrational levels, and using C_8 values from Ref. [178], this term amounts for a noticeable fraction of about 11% of the van der Waals energy. However, a fit using an improved LB formula [181] including both C_6/R^6 and C_8/R^8 contributions does not give satisfactory results as there are too many free parameters compared to the number of observed lines. We believe that scanning for deeper bound levels will not help to improve the results, as we are already close to the internuclear distance where exchange potential and higher order terms in the multipolar expansion should play a role. Thus we will have uncertainties on our C_6 values because we are at the limit of what we can do with

the LB formula.

We also note that the LB formula should be applied to molecules in zero magnetic field only, while our spectra are taken at 335.7 G. The Zeeman and hyperfine interactions result in complicated structures corresponding to successive series converging in principle toward different hyperfine Zeeman dissociation limits, such that application of the LB formula, strictly speaking, is impossible. Here we define a center of gravity for each structured line assuming equal weighting of all observed substructures, and the detuning (binding energy) corresponding to this center of gravity is determined with respect to the single dissociation limit as defined before. Although both the Zeeman shift and the overall substructure width are much smaller than the vibrational level spaces, the C_6 values extracted could still be slightly distorted.

In short summary, we have investigated the near dissociation levels of the ^{23}Na^{87}Rb molecule correlated with the ^{23}Na$(3^2S_{1/2})$+^{87}Rb$(5^2P_{3/2})$ asymptote and observed the five long-range states with attractive potentials. We have extracted the C6 coefficients with the LB model and found reasonable agreements with previous theoretical calculations. The work presented here was published in [182] and I was the first author.

3.3.3 Excited States of The $A^1\Sigma^+$-$b^3\Pi$ Admixture

For ^{23}Na^{87}Rb molecule, besides the $b^3\Pi_1$-$B^1\Pi$-$c^3\Sigma^+$ admixture, strong mixing has been reported between the $A^1\Sigma^+$ and the $b^3\Pi$ state near there crossing at a internuclear distance of about 7.7 a_0. This is also from the spin-orbit coupling and several lines have been proposed for the STIRAP in Ref. [162]. The authors there also provided the deperturbated potentials and the spin-orbital interaction matrix which we have adapted to calculate out all the mixed vibrational levels as well as the TDMs. The TDM versus the pump wavenumber is plotted in Fig. 3.14. The range of the vibrational levels, hence the pump wavenumber, we explore is chosen such that both the pump and the dump TDMs are rather large and the required lasers are easy to get. Among this range, namely from $v' = 53$ to $v' = 79$, the calculation tells us that there are a few states where the pump and the dump TDMs are on the order of $5 \times 10^{-3} ea_B$ and $0.5\, ea_B$, respectively. These states actually are $\Omega' = 0^+$ states where the hyperfine splittings are expected to be small.

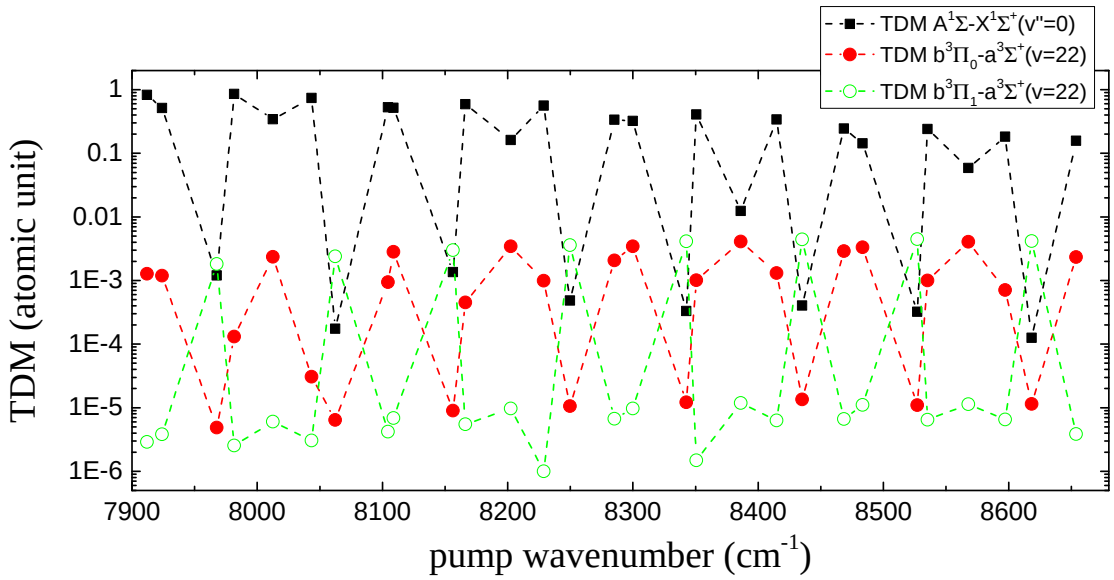

Figure 3.14: The transition dipole moments between the excited states of the $A^1\Sigma^+$-$b^3\Pi$ admixture and both the Feshbach and rovibrational ground state.

Although $\Omega' = 1$ states may have resolvable hyperfine structures and comparable pump TDMs, the dump TDMs are much smaller (on the order of $1 \times 10^{-3} ea_B$). On the other hand, they are expected to have longer lifetimes due to the weak coupling to the X state. So the goal is to find a $\Omega' = 0$ state with resolvable hyperfine structures or a $\Omega' = 1$ state with a large enough dump TDM.

An overview scan of this range is presented in Fig. 3.15, where the blue and red bars indicate the calculated $\Omega' = 0$ and $\Omega' = 1$ levels and the black curve is the observed data. Totally we have recorded 16 vibrational levels and the overall deviation between the observed and calculated results is about $0.04\,\mathrm{cm}^{-1}$. Among them, there are eleven $\Omega' = 0$ states and five $\Omega' = 1$ states. In the later case, we have observed both $J' = 1$ and $J' = 2$ levels and thus the rotational constants were obtained. For the $\Omega' = 0^+$ states only $J' = 1$ is observed except the one located near $8300\,\mathrm{cm}^{-1}$. There we find two rotational structures separated by $\sim 0.5\,\mathrm{cm}^{-1}$. This value is too large to be the spacing between $J' = 1$ and $J' = 2$ levels and we suspect that the level with resolvable substructures is from a $\Omega' = 0^-$ state. All of these results are summarized in Table 3.5. Here the pump wavenumber is determined by assuming uniform weights for substructures of each rotational level in case of lacking assignments of these substructures. So the obtained $B_{v'}$ for

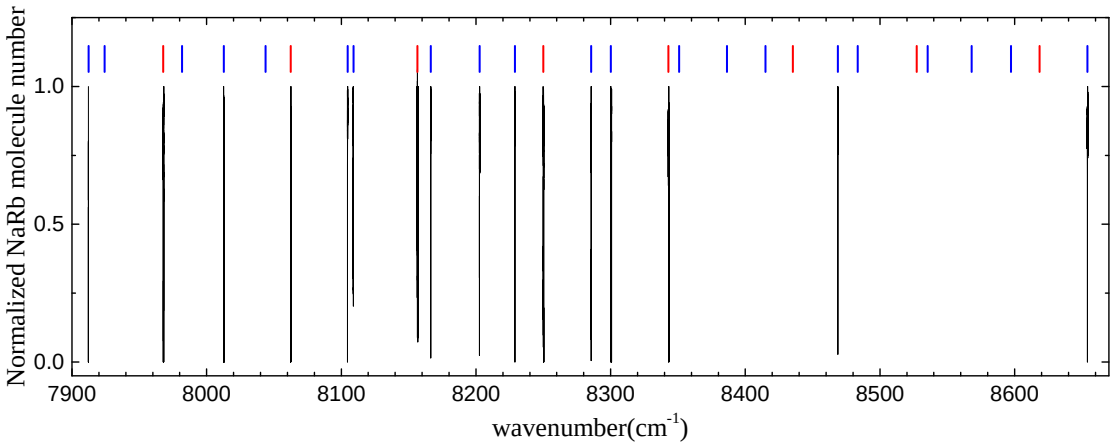

Figure 3.15: An overview scan of the $A^1\Sigma^+$-$b^3\Pi$ admixture with the pump wavenumber from 7910 cm^{-1} to 8660 cm^{-1}.

the $\Omega' = 1$ states are only accurate to second decimal places while the calculated values are close to 0.065 cm^{-1}.

As done for the $b^3\Pi$-$B^1\Pi$-$c^3\Sigma^+$ admixture, we calibrate the pump TDMs and the excited states lifetimes for $J' = 1$ states of several vibrational levels. Although $\Omega' = 0$ levels with small hyperfine splittings are not favorable for STIRAP, it is convenient to use them to observe the ground state. We have chosen $v' = 59$ near 8108.997 cm^{-1} to perform the two-photon spectrum to first precisely locate the ground state. For the STIRAP, previously we hoped that one of the $\Omega' = 1$ levels works and we have tried the $v' = 60$ level near 8156.541 cm^{-1}.

Table 3.5: Summary for all the observed excited states of the $A^1\Sigma^+$-$b^3\Pi$ admixture.

$\Omega' = 1$				$\Omega' = 0$		
v'	J'	pump wavenumber (cm^{-1})	$B_{v'}$ (cm^{-1})	v'	J'	pump wavenumber (cm^{-1})
53	1	7967.840	0.067	51	1	7912.254
	2	7968.108		55	1	8012.716
57	1	8062.469	0.06475	58	1	8104.6515
	2	8062.728		59	1	8108.997
60	1	8156.541	0.06475	61	1	8166.416
	2	8156.800		62	1	8202.634
64	1	8250.052	0.06325	63	1	8228.923
	2	8250.305		65	1	8285.496
67	1	8342.008	0.06375	66	1	8300.150
	2	8342.263		?	?	8300.650
				72	1	8468.760
				79	1	8653.989

Figure 3.16: Calibration of the pump TDMs and the lifetimes of the excited states for several lines belonging to $A^1\Sigma^+$-$b^3\Pi$ admixture: $v' = 59$ and $v' = 60$. Here the line shapes taken with either σ polarized (solid orange circles) or π polarized (open black circles) light are fitted with the loss model (see text).

(a) v'=59 of mainly $\Omega' = 0^+$ character

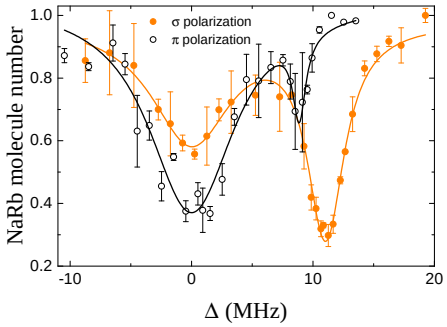

(b) $v' = 60$ of mainly $\Omega' = 1$ character

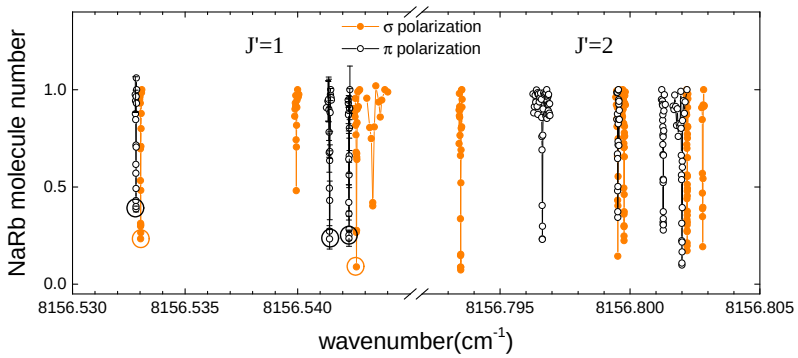

(c) Five substructures from $J' = 1$ of $v' = 60$

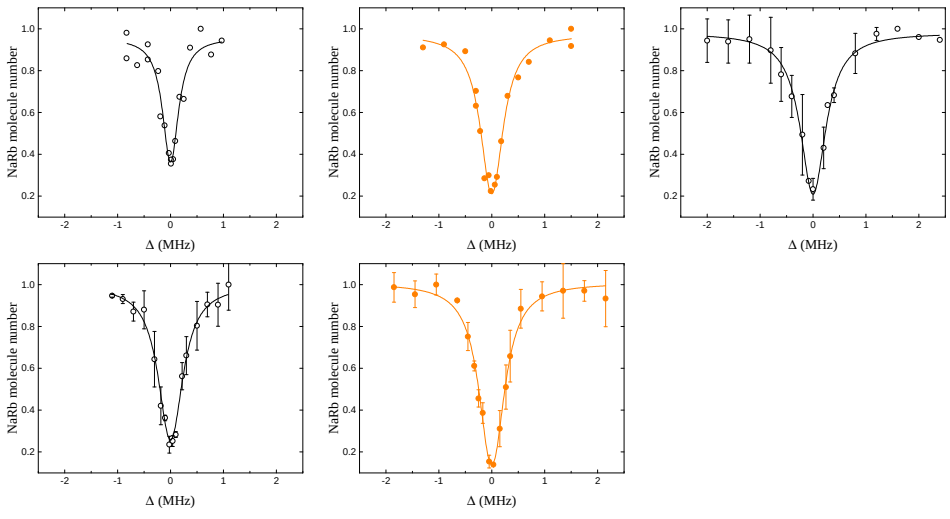

	f_c (cm^{-1})	polarization	τ (ns)	pump TDM (ea_B)
$v' = 59$ ($\Omega' = 0^+$)	8108.9968	π	24	1.51×10^{-3}
	8108.9971	π	135	3.7×10^{-4}
	8108.9968	σ	22	1.65×10^{-3}
	8108.9972	σ	58	1.59×10^{-3}
$v' = 60$ ($\Omega' = 1$)	8156.5328	π	553	3.3×10^{-4}
	8156.5330	σ	445	1.19×10^{-3}
	8156.5414	π	398	1.57×10^{-3}
	8156.5423	π	368	4.8×10^{-4}
	8156.5426	σ	439	1.22×10^{-3}

Table 3.6: Calibrated parameters for $v' = 59$ and $v' = 60$ of the $A^1\Sigma^+$-$b^3\Pi$ admixture.

The spectrum as well as the calibration curves of these two levels are shown in Fig. 3.16 and the fitted parameters are listed in Table 3.6. In Fig. 3.16**a**, two loss features are observed for the $v' = 59$ state (mainly of $\Omega' = 0^+$ character) with either the π or the σ polarized pump light. We fit the line shapes with the loss model of two excited states and assume different lifetimes for those two loss features as we have observed different FWHMs. With the π (σ) polarization, the spacing between two loss features is 8.86 MHz (11.04 MHz). The FWHMs obtained from a Lorentzian fit are mainly contributed by the nature widths which are on the order of several MHz. The pump TDMs from the fit are $1.51 \times 10^{-3} ea_B$ and $3.7 \times 10^{-4} ea_B$ for π polarization, and $1.65 \times 10^{-3} ea_B$ and $1.59 \times 10^{-3} ea_B$ for σ polarization. The calculated value for the $v' = 59$ state is about $2.8 \times 10^{-3} ea_B$ where the Hönl-London factor [183] is not included. Detailed study of the hyperfine structures of the $J' = 1$ level, which are unresolvable here, may be necessary to solve this discrepancy. Due to the unresolvable hyperfine structures, this level is

not suitable for the STIRAP transfer.

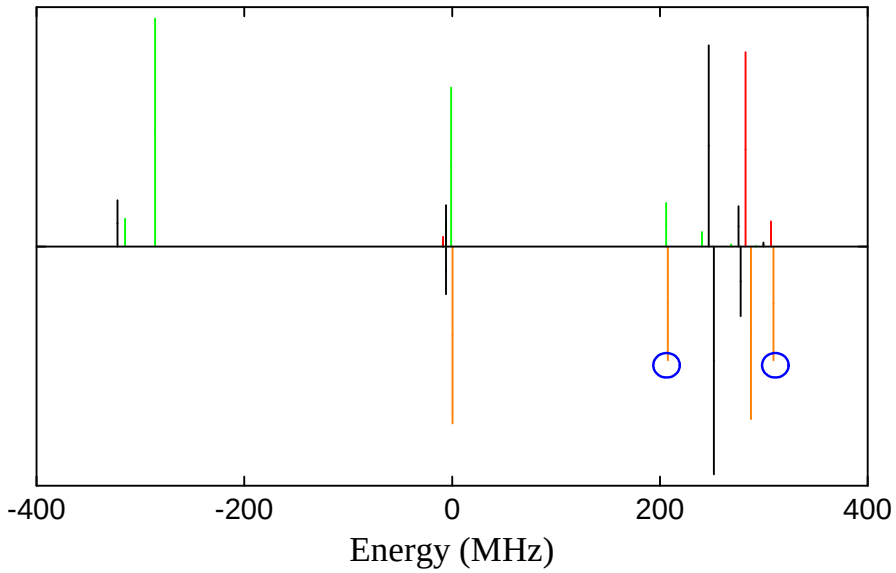

Figure 3.17: Comparison between the modeled spectrum and the observed spectrum for the $v' = 60; J' = 1$ state. Top panel: modeled result where green, black and red lines represent $M' = 1$, 2 and 3 states. The length of the line is proportional to the TDM including the HF factor. Bottom panel: experimental spectrum where the black and orange lines label the loss features observed with π and σ polarization respectively. Also the length of the line is proportional to the measured TDM except the two lines marked by the blue circles which are not calibrated.

For the $J' = 1$ rotational level of the $v' = 60$ state (mainly of $\Omega' = 1$ character from $b^3\Pi$), we totally have observed seven confirmed loss features and another uncertain one, as seen in Fig. 3.16**b**. Three of the confirmed features are from the π polarized light and the other four are detected with the σ polarization. Within the same polarization, the smallest spacing between the observed features are about 20 MHz and the FWHMs are on the order of 0.5 MHz. From these we are sure that we have well resolved the different hyperfine levels. We pick up five stronger transitions to calibrate the pump TDMs and the lifetimes. The typical value of the latter is around 400 ns, which are much longer than that of the $v' = 59$ state. The calculated pump TDM for the $J' = 1$ level is $3.0 \times 10^{-3} ea_B$ and the

different between this value and our measurements can be accounted for by taking the HL factors into consideration. Based on the Hamiltonian in Eq. 3.10 and the fact that $\Sigma = 0$ and $g_1 B$=235 MHz for $b^3\Pi$ state, we can find a well agreement between the model and the observation with A_{Na} =15 MHz, A_{Rb} =80 MHz, as shown in Fig. 3.17. Both the positions and the relative TDMs match with each other very well. Also we can have confirmed the lines around −300 MHz suggested by the model. Then the apparently the levels form three groups which correspond to three magnetic sublevels of $J' = 1$: $M_{J'} = 0, \pm 1$. We have done the same analysis for the $J' = 2$ level while the results are not presented here.

Unfortunately, the coupling between the selected $v' = 60$ state and the ground state may be not strong enough and thus even the observation of the latter was missing with this intermediate level. We also suspect that the dump TDMs with other $\Omega' = 1$ states nearby may be on the same order as that of $v' = 60$. This can also be inferred from the coarse scan of the spectrum already seen in Fig. 3.15. So we begin to look at the various $\Omega' = 0$ states the coarse scan of which is also included in Fig. 3.15. Accidentally, we have found that the $v' = 55$ state, of $\Omega' = 0^+$ character from the calculation, displays resolvable hyperfine structures as shown in Fig. 3.18**a**. Roughly three groups of substructures are observed and our detailed scan reveals that the most left group with four loss features has the largest spacings between them (> 60 MHz) while the FWHMs of the lines are on the order of 1 MHz. We calibrate two features observed with different polarizations and the fitted curves are shown in Fig. 3.18**b**. Not only the line shapes are fitted to the model described in Eq. 3.7, but also the molecular number versus the pulse length obtained when $\Delta = 0$ is included to give a more reliable estimation of the lifetime. The pump TDMs and lifetimes are summarized in Table 3.7. Both these two parameters are modest compared to those of $v' = 59$ and $v' = 60$.

f_c (cm^{-1})	polarization	τ (ns)	pump TDM (ea_B)
8012.6967	π	235	7.3×10^{-4}
8012.6989	σ	218	5.4×10^{-4}

Table 3.7: Calibrated parameters for $v' = 55$ of the $A^1\Sigma^+$-$b^3\Pi$ admixture.

Figure 3.18: Excited states of $v' = 55$. **a**, The one-photon spectrum recorded with $v' = 55; J' = 1$ level of $\Omega' = 0$ character which displays resolvable hyperfine structures. The black and orange circles mark the strongest π and σ transitions, respectively. **b**, The calibration of the strongest π and σ transitions.

(a) $v' = 55; J' = 1$ of $\Omega' = 1$ character: resolvable hyperfine structures

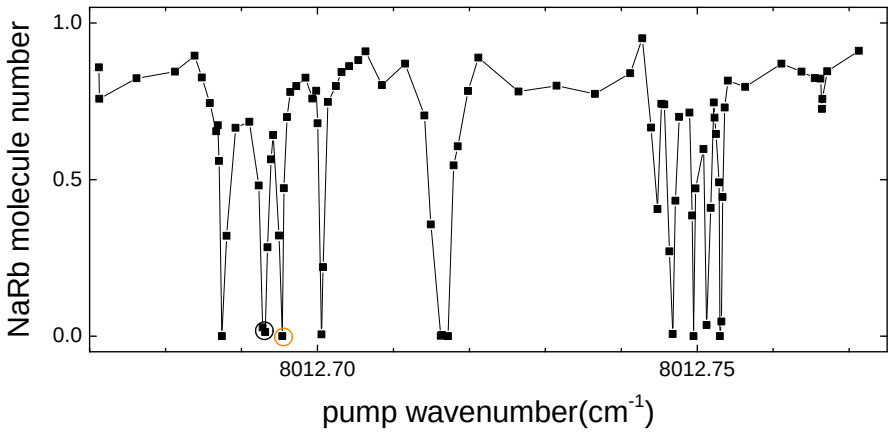

(b) Calibration of the strongest π and σ transitions respectively: black for π and orange for σ.

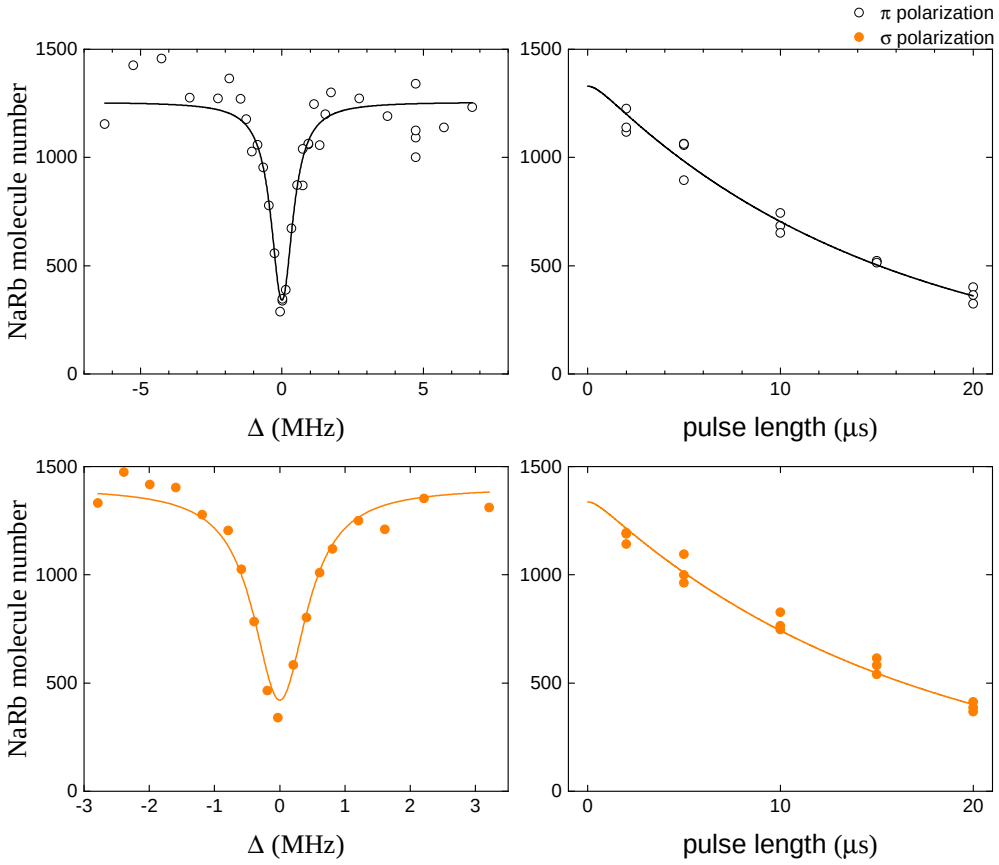

Such a large hyperfine splitting is abnormal according to the asymptotic model [174] and the previous study of the $^{87}Rb^{133}Cs$ molecule [183]. We suspect that it is due to an accidental resonance which occurs between the 0^+ and some 0^- vibrational state. Actually in Rb_2 it has been shown that the couping between 0^+ and 0^- state can result in unusually large hyperfine splittings []. Considering the $\Omega' = 0$ states of main $b^3\Pi$ character in NaRb, pairs of $2(0^\pm)$ vibrational states are degenerate without the spin-orbital interactions. At the internuclear distance we are interested in, the $2(0^-)$ states are weakly perturbed by the coupling to $c^3\Sigma^+$ potential and the vibrational progression is still regular. However, the $2(0^+)$ vibrational progression becomes irregular due to the strong spin-orbital coupling between $A^1\Sigma^+$ and $b^3\Pi$ potential. We are still exploring this possibility both theoretically and experimentally.

3.4 Two-photon Spectroscopic Study of The $X^1\Sigma^+$ state

Let us recall the three-level problem illustrated in Fig. 3.6. In the previous section, we have studied the excited state $|2\rangle$ with one-photon spectra where ω_p was scanned. In this section, I would like to present our exploration of $|3\rangle$ with two-photon spectra. We have located the $v'' = 0; J'' = 0, 2$ levels of the $X^1\Sigma^+$ state as well as the first excited vibrational level $v'' = 1; J'' = 0$. The hyperfine structure of the rovibrational ground state was also resolved. Based a phenomenological master equation, we have calibrated the dump TDM by simulating the two-photon line shape.

A non-Hermitian Hamiltonian [173] under the rotating wave approximation reads

$$H = \hbar \begin{pmatrix} -i\gamma_1/2 & \frac{\Omega_p}{2}e^{i\omega_p t} & 0 \\ \frac{\Omega_p}{2}e^{-i\omega_p t} & \omega_{21} - i\gamma_2/2 & \frac{\Omega_d}{2}e^{-i\omega_d t} \\ 0 & \frac{\Omega_d}{2}e^{i\omega_d t} & \omega_{31} - i\gamma_3/2 \end{pmatrix}. \tag{3.12}$$

Here $\omega_{ij} = \omega_i - \omega_j$ is the energy spacing between $|i\rangle$ and $|j\rangle$ and γ_i is the decay rate of $|i\rangle$ $(i, j \in \{1, 2, 3\})$. By doing a unitary transformation $H \to UHU^\dagger - i\hbar U\partial_t U^\dagger$

with

$$U = \begin{pmatrix} 1 & 0 & 0 \\ 0 & e^{i\omega_p t/\hbar} & 0 \\ 0 & 0 & e^{-i(\omega_d-\omega_p)t/\hbar} \end{pmatrix}, \tag{3.13}$$

the Hamiltonian is rewritten as

$$\tilde{H} = \hbar \begin{pmatrix} -i\gamma_1/2 & \frac{\Omega_p}{2} & 0 \\ \frac{\Omega_p}{2} & -\Delta - i\gamma_2/2 & \frac{\Omega_d}{2} \\ 0 & \frac{\Omega_d}{2} & \delta - i\gamma_3/2 \end{pmatrix}. \tag{3.14}$$

We have defined the two-photon detuning as $\delta \equiv (\omega_d - \omega_p) + \omega_{31}$ and the one-photon detuning as $\Delta \equiv \omega_p - \omega_{21}$. In the master equation, we would also take the finite laser coherence into consideration. Since the two-photon transition is insensitive to the one-photon detuning, we only include the relative linewidth of the two Raman lasers which affects the two-photon detuning. The equation reads

$$\frac{d\rho}{dt} = -\frac{i}{\hbar}(H\rho - \rho H^\dagger) + \frac{\eta}{2}(2s_{33}\rho s_{33}^\dagger - \rho s_{33}^\dagger s_{33} - s_{33}^\dagger s_{33}\rho), \tag{3.15}$$

where the relative linewidth η is included in the Lindblad form with $s_{33} = \mathrm{diag}(0, 0, 1)$.

In our two-photon spectroscopic study here, we always kept the $L1$ on-resonance ($\Delta = 0$) and scanned the $L2$ frequency, hence the two-photon detuning δ. The typical pulse shapes are shown in Fig. 3.19. Two rectangular pulses of $L1$ and $L2$ are imposed to the Feshbach molecules where the pump pulse is contained in the dump pulse. The location of $|3\rangle$ manifests itself as the recovery of the molecular number. There are two different situations for the two-photon spectra depending on the laser conditions of $L2$. In the first case, only $L1$ is locked to the ULE cavity and $\Omega_d \gg \Omega_p$. From the well-known dressed-state picture of a two-level system, we can intuitively think that the pump transition is off-resonance due to the AC stark shift caused by the strong dump light. Here $L1$ and $L2$ are completely uncorrelated and the relative linewidth is the sum of the quadratic individual linewidth. In the second case, the two lasers are locked to the ULE cavity simultaneously. The recovery of the molecular number is related to the dark resonance of the three-level system in this situation and the relative linewidth can be estimated from the locking properties. We would revisit this point in next section. Then I want to briefly mention the selection rules for the two-photon transition:

- $\Delta J = 0, \pm 1, \pm 2 : J'' = 0, 1, 2, 3$

- $\Delta M = 0, \pm 1, \pm 2 : M'' = 0, 1, 2, 3$
- Parity consideration: only even J'' are accessible.

So we can only access the $J'' = 0$ and 2 levels starting from our initial Feshbach state with $J = 1$.

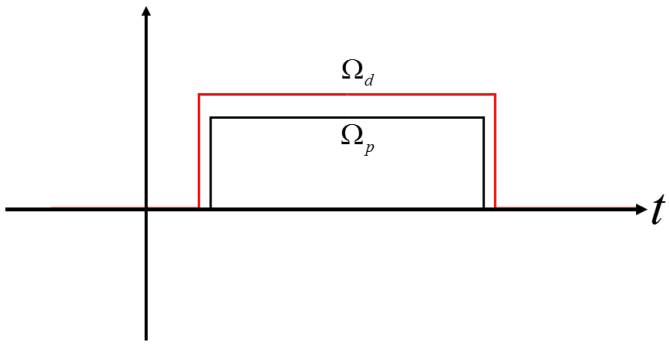

Figure 3.19: The typical pulse shape for the two-photon spectra: A rectangular $L2$ pulse with a height of Ω_d is imposed and a similar $L1$ pulse with Ω_p is contained in the $L2$ pulse.

3.4.1 Locating Different Rovibrational Levels of X State

Although the first signal of the rovibrational ground state were seen with $v' = 59; J' = 1$ of the $A^1\Sigma^+$-$b^3\Pi$ admixture, here I present the location of different vibrational levels of $X^1\Sigma^+$ utilizing the excited state with a pump wavenumber of $12\,449.1018\,\mathrm{cm}^{-1}$. The pump transition here is a σ transition with a pulse length of $10\,\mu\mathrm{s}$ and $2\pi\times0.49\,\mathrm{MHz}$ Rabi frequency. The pump laser $L1$ was the free-running dye laser for this measurement. So the relative linewidth is mainly determined by the linewidth of the dye laser on the order of $100\,\mathrm{kHz}$ while the pump laser has a linewidth of a few kHz to our best estimation. On the other hand, the lifetimes of the Feshbach molecules and the ground-state molecules are both on the order of tens of milliseconds which is negligible compared to the pulse lengths.

The two-photon spectrum data is shown in Fig. 3.20**a** where the solid orange lines are fits with Gaussian to extract the center and hence the location of $|3\rangle$. The orange color here indicates that the dump transition is of σ type. The spacing between $v'' = 0$ and $v'' = 1$ is $105.833(3)\,\mathrm{cm}^{-1}$ and the uncertainty comes from

the absolute accuracy of our wavelength meter. This number is quite close to the value 105.839 cm^{-1} calculated from the experimental potential in Ref. [161]. Using parameters, $\Delta = 0$, $\gamma_1 = \gamma_3 = 0$, $\Omega_p = 2\pi\times0.49\,\mathrm{MHz}$, $\gamma_2 = 2\pi\times6.92\,\mathrm{MHz}$ and $\eta = 2\pi\times0.1\,\mathrm{MHz}$, we can roughly estimate the dump TDM to be $0.03\,\mathrm{ea}_B$ and $0.074\,\mathrm{ea}_B$ for the $v'' = 0$ and 1 respectively.

Different vibrational levels of the $X^1\Sigma^+$ state are promising to study the ultracold collisions of chemically stable UPMs as well as chemically unstable ones within the same setup. As mentioned at the beginning of this chapter, the rovibrational ground state of our $^{23}Na^{87}Rb$ molecule is stable against the chemical reactions. At the same time, it is already reactive at its first vibrational excited state ($v'' = 1$) from the comparison between the measured vibrational spacing and the calculated 47 cm^{-1} energy barrier for the chemical reaction.

Besides the control of the vibrational quantum number, we can also choose different rotational levels to be reached by the two-photon process. Here with the $v' = 55$ state of the $A^1\Sigma^+$-$b^3\Pi$ admixture, we have precisely determined the positions of $J'' = 0$ and 2 rotational states of the lowest vibrational level using the two locked Raman lasers. The pump transition is the π transition listed in Table 3.7. The spectrum is shown in Fig. 3.20**b** where the solid lines have the same meaning as those in (a). The spacing between these two observed rotational levels is 12.5366(7) GHz. Recall that the rotational energy of a diatomic molecule can be expressed as $\hbar B_v J(J+1)$ for the small rotational quantum number J and B_v is the rotational constant. So the energy spacing between $J'' = 0$ and $J'' = 2$ is $6\hbar B_v$ and thus $B_v = 2\pi\times2.0894(1)\,\mathrm{GHz}$. Here the uncertainty is mainly from the fitting error of the line center. This value also agrees very well with the calculated one, $2\pi\times2.0897\,\mathrm{GHz}$, based on the potential in Ref. [161]. Another important spectroscopic constant we can directly get is the dissociation energy of the $v'' = 0; J'' = 0$ level which is just the energy difference between the pump and dump transitions: D_0^X =4977.308(2) cm^{-1}. This value is 0.121 cm^{-1} larger than that reported in Ref. [161] and 0.018 cm^{-1} less than our previous result in Ref. [159]. The uncertainty is coming from the absolute frequency measurement accuracy.

Figure 3.20: Two-photon spectrum to locate different rovibrational levels of $X^1\Sigma^+$ state. The solid orange lines are Gaussian fits to extract the line center and the orange is used to indicate that the dump transition is a σ one.

(a) Two-photon spectrum to locate the $v'' = 0, 1; J'' = 0$ levels of $X^1\Sigma^+$: The intermediate state is belonging to the $b^3\Pi$-$B^1\Pi$-$c^3\Sigma^+$ admixture.

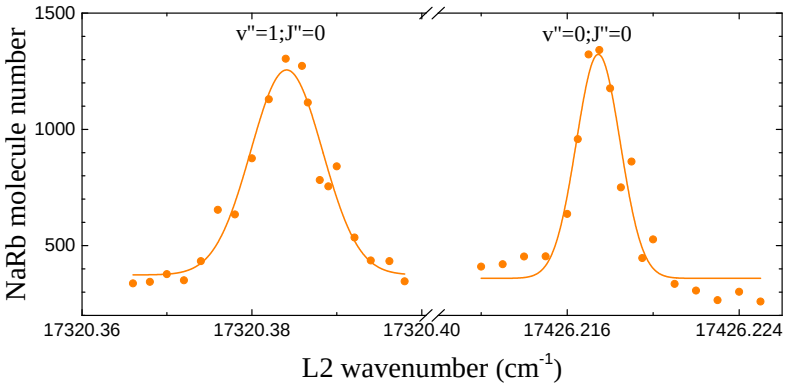

(b) Two-photon spectrum to locate the $v'' = 0; J'' = 0, 2$ levels of $X^1\Sigma^+$: The intermediate state is belonging to the $A^1\Sigma^+$-$b^3\Pi$ admixture.

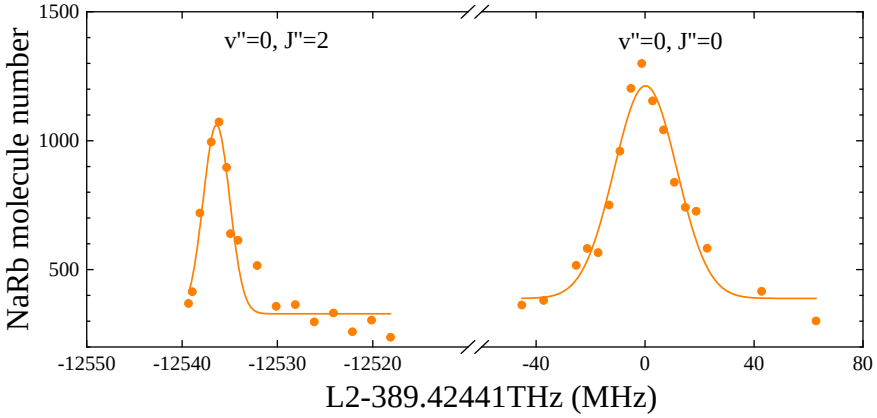

The two-photon line shapes are of course modeled to estimate the dump TDM. For both the pump and the dump lasers are locked to the cavity the relative linewidth is best estimated to be 5 kHz. Other parameters are listed here: $\Delta = 0$, $\gamma_1 = \gamma_3 = 0$, $\gamma_2 = 2\pi \times 0.68$ MHz and Ω_p is experimentally calibrated. The dump TDMs obtained using these parameters are $0.033\, ea_B$ and $0.096\, ea_B$ for the $J'' = 0$ and 2 respectively. However, this estimation is not accurate due to the fact that we may couple different hyperfine Zeeman states with such strong dump light.

3.4.2 The Hyperfine Zeeman Structures of The Rovibrational Ground State

In previous subsection the two-photon spectrum is done in the condition of $\Omega_d \gg \Omega_p$ and thus the resultant FWHM of the line shape is on the order of tens of MHz. On the other hand, the hyperfine Zeeman splitting of the rovibrational ground state is tiny due to the zero electronic angular momentum. According to the study in Ref. [184], it is smaller than 1 MHz. So previous spectra may involve many hyperfine Zeeman states in the single wide peak and all of the modelings of the line shapes are inaccurate. In this section I would like to present well-resolved hyperfine Zeeman levels of the rovibrational ground state with the two-photon dark-resonance spectrum.

For the rovibrational ground-state molecule, the interactions between the nuclear spins and the magnetic fields produced by the electronic motion are almost vanished. The only terms causing the hyperfine structure are the nuclear electric quadrupole interactions, the spin-rotation couplings and the spin-spin interactions between nuclei. Including the Zeeman interactions, the Hamiltonian can be written as

$$H = H_{\text{rot}} + H_{\text{hfs}} + H_{\text{Z}}, \tag{3.16}$$

where $H_{\text{rot}} = B_v \mathbf{N}^2$, $H_{\text{hfs}} = \sum_i [\mathbf{V}_i \cdot \mathbf{Q}_i + c_i \mathbf{N} \cdot \mathbf{I}_i] + c_3 \mathbf{I}_1 \cdot \mathbf{I}_2 + c_4 \mathrm{T}(\mathbf{I}_1, \mathbf{I}_2)$ and $H_Z = -\sum_i \boldsymbol{\mu}_i \cdot \mathbf{B}$. H_{rot} and H_{Z} are easy to understand. The first term in H_{hfs} describes the coupling between the electric field gradient at the nucleus i and its electric quadrupole moment $\mathbf{Q}_i$. The explicit form is $\frac{(eqQ)_i[(3/8)C(C+1)-(1/2)\mathbf{I}_i^2\mathbf{N}^2]}{I(2I-1)(2N-1)(2N-1)(2N+3)}$ and $C = 2\mathbf{I}_i \cdot \mathbf{N}$. Here $(eqQ)_i$ is the coupling constant. The second term represents the interaction between the nuclear spin $\mathbf{I}_i$ and the molecular rotation. The third and

fourth term are the scalar and tensor spin-spin interactions respectively. Based on this Hamiltonian and the calculated couping constants, our theoretical collaborators have modeled the hyperfine structure of the rovibrational ground state by taking $N = 0 \sim 3$ into consideration.

The two-photon dark-resonance spectrum relies on the existence of the so-called dark state, $|\text{Dark}\rangle = \Omega_d/\Omega\,|1\rangle - \Omega_p/\Omega\,|2\rangle$ ($\Omega = \sqrt{\Omega_p^2 + \Omega_d^2}$), which is one of the instantaneous eigenstates of the Hamiltonian in Eq. 3.14 which doesn't involve the short-lived excited state $|2\rangle$. It only happens when the two-photon resonance is fulfilled ($\delta = 0$). With the pulse shapes shown in Fig. 3.19, the sudden shinning of $L1$ projects the initial state to the three instantaneous eigenstates and only the dark state survives the following evolution. Then the sudden switch-off of $L1$ projects the dark state back to the initial state. So the remaining Feshbach molecule number is proportional to $(\Omega_d/\Omega)^2$ from this simple picture. However, we also need to consider the decoherence effect during the pulse duration which would cause the observed molecule number decreased as the pulse length is increased. The measurement of this effect would give us the knowledge of in what extent the two-photon resonance is maintained in our system. Due to the requirement of two-photon resonance, this dark-resonance spectrum is expected to be of high resolution and precision, and hence resolving the hyperfine Zeeman structures.

In Fig. 3.21, I show our spectrum data as well as the modeled hyperfine Zeeman structures of the rovibration ground state. It was performed with the same intermediate state as that in Fig. 3.20**b** with a π pump transition. By changing the polarization of $L2$ we could couple the rovibrational ground state with $M'' = 1, 2$ and 3, if we recall that $M = 2$ for the initial Feshbach molecules. In the basis of $|m_{\text{Na}}, m_{\text{Rb}}\rangle$, we totally have $(2I_{\text{Na}} + 1)(2I_{\text{Rb}} + 1)$ different energy levels, namely 16 states. Here m_{Na} and m_{Rb} are the projection of the ^{23}Na nuclear spin $I_{\text{Na}}(= 3/2)$ and the ^{87}Rb nuclear spin $I_{\text{Rb}}(= 3/2)$ along the external field, respectively. At 335.7 G, the nuclear Zeeman energy of the state $|m_{\text{Na}}, m_{\text{Rb}}\rangle$ is -$\hbar \times 2\pi \times (0.37805 m_{\text{Na}} + 0.46757 m_{\text{Rb}})$MHz. Actually the Zeeman term dominates the Hamiltonian at such a high magnetic field, which can be seen from the inset of Fig. 3.21**a**. The energy differences between the full model calculation and the Zeeman term are not larger than $\hbar \times 2\pi \times 20$ kHz and thus m_{Na} and m_{Rb} are still regarded as good quantum numbers. With the polarization configuration of π pump + σ dump, we could access one $M'' = 3$ and three $M'' = 1$ levels. With the polarization configuration of π pump + π dump, two $M'' = 2$ levels were

observed. All of these 6 levels were well-resolved in Fig. 3.21**b** and the line centers were extracted by Lorentzian fits. We could find an excellent agreement between the observed centers and the modeled results.

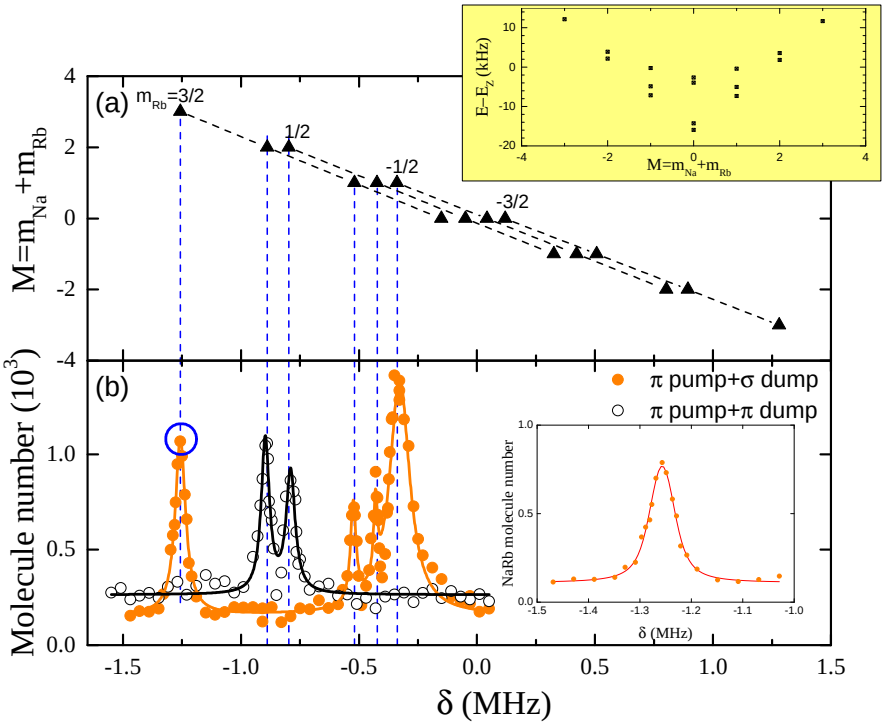

Figure 3.21: The hyperfine Zeeman structures of the rovibrational ground state. **a**, The modeled results are clarified according to the total magnetic quantum number $M = m_{\mathrm{Rb}} + m_{\mathrm{Na}}$. Points connected by dashed lines have the same value of m_{Rb}. The inset shows the energy differences between these full-model result and the pure Zeeman term. **b**, The dark-resonance spectrum shows well-resolved hyperfine Zeeman structures with both π pump $+\,\sigma$ dump (solid orange circles) and π pump $+\,\pi$ dump (open black circles) polarization configurations. Solid lines are fittings to the Lorentzian functions. The lowest energy level is marked with a blue circle and the modeling of the line shape with the master equation is shown in the inset.

The line shapes of the two-photon dark-resonance spectra can be also modeled with the master equation (Eq. 3.15) and the dump TDM could be calibrated. However, only the lowest energy state is calibrated with this method for other states are not well-isolated. The result is shown in the inset of Fig. 3.21**b** and the dump TDM is $0.021(1)\,\mathrm{ea}_B$ from the calibration. Also other line shapes can be modeled, and hence the calibration of dump TDM for other states, if we extend the three-level master equation to the four- or five- level case which is straightforward.

3.5 Absolute Ground-State Molecules: Creation and Characterization

With the intermediate state of the selected $v' = 55; J' = 1$ level, both the pump and dump TDM as well as the excited-state lifetime are calibrated to be $7.3 \times 10^{-4}\mathrm{ea}_B$, $0.021(1)\,\mathrm{ea}_B$ and 235 ns respectively in previous two sections. These conditions give us a good starting point to create the absolute ground-state polar molecules via the STIRAP. This process not only strongly depends on the dark state $|\mathrm{Dark}\rangle$, but also requires a special design of the pulse shapes of the Raman lasers. Since only the latter is different from the dark-resonance spectrum, we can also model the STIRAP transfer with Eq. 3.15. The details of the STIRAP would be presented in the first part of this section.

In the next two parts the characterization of the absolute ground-state molecules are described which includes the measurements of the permanent dipole moment and the lifetime of the samples.

3.5.1 STIRAP

The STIRAP technique has been a standard method to realize the almost lossless population transfer in a three-level system for more than 25 years [185]. The basic idea relies on the dark state only existing when the two-photon detuning is set to zero. In that case the eigenvalues and eigenstates of the Hamiltonian in Eq. 3.14

($\gamma_1 = \gamma_2 = 0$ and $\gamma_2 \equiv \gamma$) read

$$\begin{aligned}
&E_0 = 0, && |\text{Dark}\rangle = \tfrac{\Omega_d}{\Omega}|1\rangle - \tfrac{\Omega_p}{\Omega}|3\rangle\,; \\
&E_+ = \tfrac{1}{2}(-\Delta - i\gamma/2 + \sqrt{(-\Delta - i\gamma/2)^2 + \Omega^2}), && |+\rangle = \frac{\Omega_p|1\rangle + (-\Delta - i\gamma/2 + \sqrt{(-\Delta - i\gamma/2)^2+\Omega^2})|2\rangle + \Omega_d|3\rangle}{\sqrt{\Omega^2 + \left|-\Delta - i\gamma/2 + \sqrt{(-\Delta - i\gamma/2)^2+\Omega^2}\right|^2}}; \\
&E_- = \tfrac{1}{2}(-\Delta - i\gamma/2 - \sqrt{(-\Delta - i\gamma/2)^2 + \Omega^2}), && |-\rangle = \frac{\Omega_p|1\rangle + (-\Delta - i\gamma/2 - \sqrt{(-\Delta - i\gamma/2)^2+\Omega^2})|2\rangle + \Omega_d|3\rangle}{\sqrt{\Omega^2 + \left|-\Delta - i\gamma/2 - \sqrt{(-\Delta - i\gamma/2)^2+\Omega^2}\right|^2}}.
\end{aligned} \tag{3.17}$$

The first eigenstate, named dark state, doesn't involve the strongly dissipative state $|2\rangle$. Assuming that initially all the particles occupy $|1\rangle$, we start with zero Ω_p and finite Ω_d and then the Rabi frequencies are adiabatically ramped to finite Ω_p and zero Ω_d. In this way it is possible to have near unit transfer efficiency between $|1\rangle$ and $|3\rangle$ and the pulse sequence is counterintuitive. For simplicity we also have $\Delta = 0$. The adiabatic condition is fulfilled when the couping between $|\text{Dark}\rangle$ and $|\pm\rangle$ is much smaller than the energy spacing between them: $\left|\langle\pm|\,\frac{d}{dt}\,|\text{Dark}\rangle\right| \ll |E_\pm - E_0|$. In the limit of $\gamma \gg \Omega$, this criterion gives that $\Omega^2 T \gg \pi\gamma$ for nearly equal pump and dump Rabi frequency. It becomes $\Omega T \gg \sqrt{2}\pi$ when $\Omega \gg \gamma$ or $\Omega \sim \gamma$. Here T is the pulse length. For a high-efficiency transfer we typically need $\Omega T > 10\pi$.

In real experiments, maintaining a perfect adiabaticity is impossible and some molecules would loss from the three-level system due to the visit to the dissipative excited state $|2\rangle$. Intuitively we expect that the transfer efficiency η would decay monotonically with the increasing γ and it was shown that besides the non-adiabaticity, another loss mechanism called quantum overdamping would contribute severely in the strong-decay regime ($\gamma \gg \Omega$) [173]. However, Ref. [186] has asserted that there exists a minimum value of η versus the change of γ, which is out of the scope of our phenomenological model. For us, the available laser power of $L1$ are about 26 mW corresponding to $\Omega_p = 2\pi\times 0.73$ MHz, meanwhile $\gamma = 2\pi\times 0.68$ MHz. This means that we are in the regime of $\Omega \sim \gamma$ and for the decay of $|2\rangle$ we only need to consider the adiabatic criterion, i.e. $\Omega T \gg \sqrt{2}\pi$. The fast fluctuations of the Rabi frequencies are expected to be negligible and we don't consider it here.

Another factor affecting η is the decoherence effect caused by various phase noises. These noises enter the problem by changing both the one-photon and two-photon detuning, especially η is extremely sensitive to the latter parameter. The contributions mainly come from the phase fluctuations of the laser fields and

the noise of the external DC magnetic and electric fields. The electric field is almost zero in this case and the fluctuations can also be neglected. Our magnetic field suffers from a RMS noise of 10 mG. However, our Feshbach state has almost zero magnetic dipole moment and the energy of the absolute ground state would fluctuate on the order of 40 Hz. The noise of the two-photon detuning due to these fluctuations is also negligible. So the only source of the noise comes from the fluctuations of the Raman lasers which is estimated to be on the order of 5 kHz.

The STIRAP transfer was performed using the pulse sequence shown in Fig. 3.22**b**. The figure was obtained based on the measured pump and dump powers by two photodiodes. Through previous calibrated TDMs they were translated into the Rabi frequencies and the maximum value of Ω_p (Ω_d) is $2\pi\times0.7$ MHz ($2\pi\times1.1$ MHz). The pulse can be divided into four parts: (1) Ω_d is slowly ramped to its maximum value in 15 µs while Ω_p is kept zero. (2) In 15 µs, Ω_d is decreased to zero and Ω_p is increased to its maximum. This is the STIRAP sequence and here $\Omega_{\mathrm{RMS}}T = 11.4\pi$ where T =15 µs. (3) In another 15 µs, Ω_d is again increased to its maximum and Ω_p is deceased to zero. This is a reversed STIRAP sequence. (4) Ω_d is slowly ramped down to zero in 15 µs and meanwhile Ω_p is kept zero. It is not necessary to make the part (3) immediately following the part (2) and actually the lifetime of the absolute ground-state molecules was measured by varying the holding time between these two parts. The parts (1) and (4) are not relevant to our main results.

In Fig. 3.22**a** the time evolution of the number of the Feshbach molecules are presented. The data points were taken based on the pulse sequence shown in 3.22**b**. We begin with about 1.55×10^3 Feshbach molecules and their number is not changed during the above-mentioned part (1). Comparing the configuration of the Rabi frequencies in this part to the three eigenstates in Eq. 3.17, we could identify that $|1\rangle$ coincides with the dark state $|\mathrm{Dark}\rangle$. During part (2) the Rabi frequencies are adiabatically changed and ideally the quantum state of the three-level system would follow the dark state. In the end of (2), the dark state coincides with $|3\rangle$, the absolute ground state. However, due to the non-adiabaticity and the decoherence only a portion of η of the Feshbach molecules are transferred to their absolute ground state. The other molecules visit the dissipative $|2\rangle$ followed by spontaneously decaying to many unknown molecular levels. These molecules are irreversibly lost from our system. Within our detection limit, zero Feshbach molecules are observed after part (2). In part (3) a reverse pulse sequence of that in part (2) is applied and the absolute ground state molecules are transferred

back to the Feshbach state $|1\rangle$ assuming a same transfer efficiency η. The number revival of the Feshbach molecules confirms the successful control of the quantum state between $|1\rangle$ and $|3\rangle$. After the round-trip STIRAP, namely part (2) together with part (3), more than 1.0×10^3 Feshbach molecules are revived and the overall efficiency of more than 64% suggests $\eta > 80\%$.

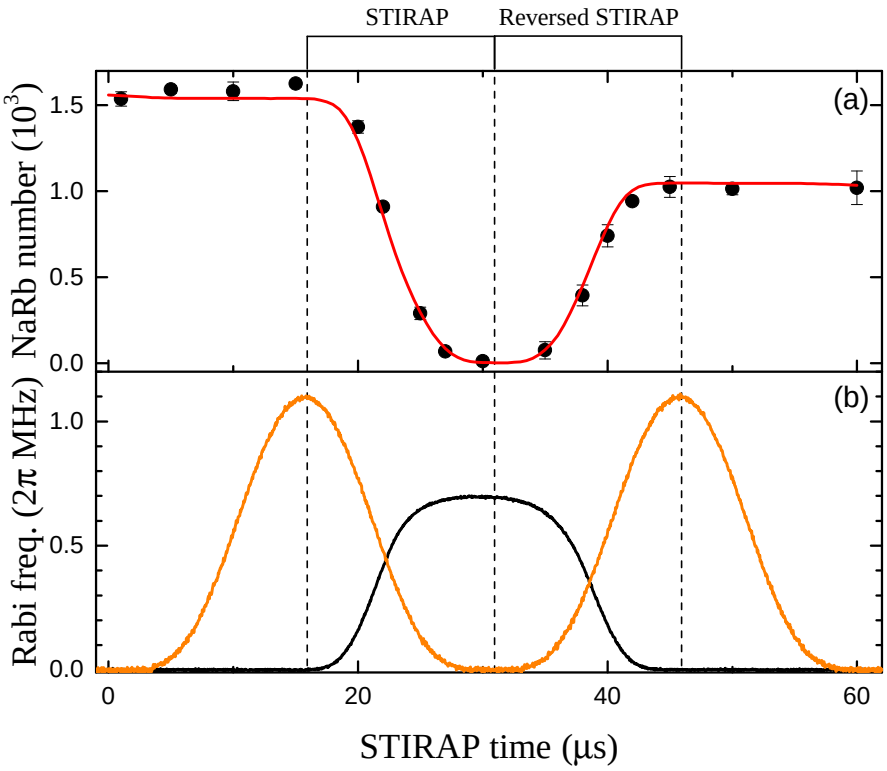

Figure 3.22: The round-trip STIRAP transfer. **a**, Time evolution of the number of Feshbach molecules during round-trip STIRAP. The solid red curve is the simulation result with the master equation where all the parameters are given according to the experimental measurements. The Feshbach molecules are transferred to the absolute ground state after the 15 μs STIRAP sequence and a reversed sequence is immediately applied to transfer the molecules back to the Feshbach state. **b**, The measured pump (black line) and dump (orange line) pulse sequence. The maximum pump (dump) Rabi frequency is 0.7 MHz (1.1 MHz).

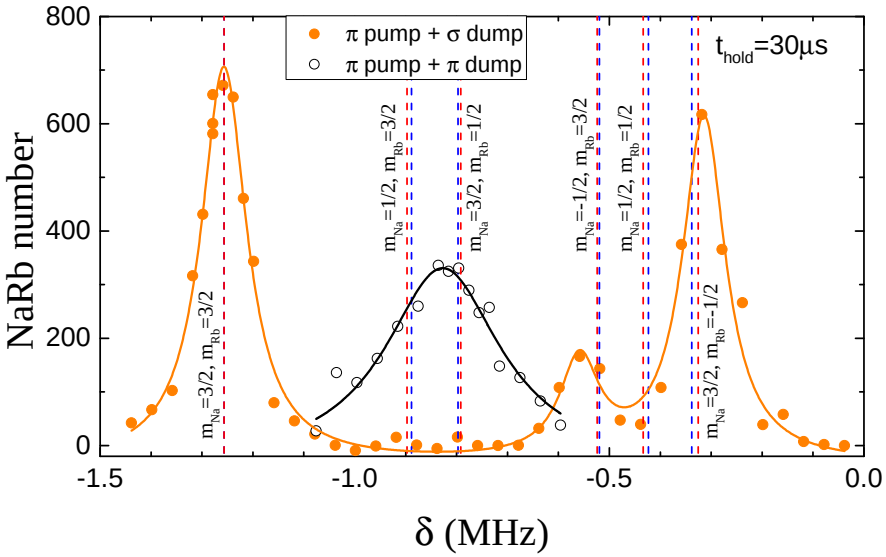

Figure 3.23: The two-photon line shape of STIRAP: The number of Feshbach molecules after a round-trip STIRAP is recorded versus the two-photon detuning. The measurement is done with a time sequence that the system is held for 30 μs between the STIRAP and reversed STIRAP pulse. By changing the polarization of $L2$, $M'' = 1 \sim 3$ are populated. The solid lines are fits to Lorentzian functions. The dashed red and blue vertical lines correspond to the level positions obtained from the dark-resonance spectrum and the theoretical modeling, respectively.

Although we have achieved such a high-efficiency transfer, another question that whether only a single quantum state is populated remains unanswered. In Ref. [187] the authors derived an analytic result for η in case of $\Omega T \gg 1$ from which the two-photon linewidth is estimated to be on the order of $\Omega_{\mathrm{RMS}}/\sqrt{\pi\gamma T}$ ~0.3 MHz. In Fig. 3.23 we show the two-photon line shape of STIRAP by scanning the dump frequency. This set of data was taken with a time sequence that the holding time between the STIRAP pulse and the reversed STIRAP pulse is 30 μs. With π pump + σ dump, both $M'' = 1$ and $M'' = 3$ were accessible. Although there are three possible levels for $M'' = 1$, we only observe two peaks in the line shape and they agree with the previous dark-resonance measurement and the theoretical modeling well. The missing line corresponds to $|m_{\mathrm{Na}} = 1/2, m_{\mathrm{Rb}} = 1/2\rangle$ and we still don't

understand it at all. The fits give the FWHMs of 0.109(7) MHz, 0.093(26) MHz and 0.103(8) MHz for the three peaks from lower to higher frequency. They share almost the same two-photon linewidths but quit different transfer efficiencies especially for the middle one. This may be understood from the changes of Ω_{RMS} and the effective transfer time T, which are hard to analyze. For the two $M'' = 2$ states they are unresolved from the line shape and a one-peak fit gives a FWHM of 0.28(5) MHz.

In short summary, we have achieved a sample of the rovibrational ground-state polar molecules in a single quantum state via STIRAP. The experimental results are well reproduced through a phenomenological master equation.

3.5.2 Characterizing The Permanent Dipole Moment

The dipolar nature of the heteronuclear molecules at their rovibrational ground state can be characterized by measuring the Stark shift of this state in a static electric field. The shift can be understood as the perturbation of the energy of the rovibrational ground state by other rovibration states. From the perturbation theory we know that the contribution of some state is proportional to the inverse of the energy spacing between this state and the rovibrational ground state. To a good approximation we could only consider the rotational structures. So the Hamiltonian reads

$$\begin{aligned} H &= B_v \mathbf{N}^2 - \mathbf{d} \cdot \mathbf{E} \\ &= B_v \mathbf{N}^2 - d_0 E \cos\theta, \end{aligned} \tag{3.18}$$

where d_0 is the permanent dipole moment, E is the electric field strength and θ is the angle between the molecular axis and the $\mathbf{E}$ direction. We can treat the rotations of the linear molecules as the rigid body rotation and the $\cos\theta$ term could only couples states with the same magnetic quantum number. In the basis of $|N, m_N\rangle$ for a $^1\Sigma$ molecule, only $\langle N', m_N| \cos\theta |N, m_N\rangle$ are nonzero. (It is very similar to the spherical Harmonics.) The explicit matrix element reads [188]

$$\begin{aligned} &\langle N', m_N| \cos\theta |N, m_N\rangle \\ &= (-1)^{m_N} \sqrt{(2N'+1)(2N+1)} \begin{pmatrix} N' & 1 & N \\ 0 & 0 & 0 \end{pmatrix} \begin{pmatrix} N' & 1 & N \\ -m_N & 0 & m_N \end{pmatrix}, \end{aligned} \tag{3.19}$$

where $\begin{pmatrix} \cdots \end{pmatrix}$ represent the 3-j symbols. The first 3-j symbol accounts for the coupling along the molecular axis and the second one is the coupling along the

electric field. $\begin{pmatrix} N' & 1 & N \\ 0 & 0 & 0 \end{pmatrix}$ is nonzero only if $N' = N \pm 1$. So for $m_N = 0$ the Hamiltonian is represented by

$$H = \begin{pmatrix} 0 & -\frac{d_0 E}{\sqrt{3}} & 0 & \cdots & 0 \\ -\frac{d_0 E}{\sqrt{3}} & 2B_v & -\frac{2d_0 E}{\sqrt{15}} & \cdots & 0 \\ 0 & -\frac{2d_0 E}{\sqrt{15}} & 6B_v & \cdots & 0 \\ \vdots & \vdots & \vdots & \ddots & \vdots \\ 0 & 0 & 0 & \cdots & B_v N(N+1) \end{pmatrix}, \tag{3.20}$$

where rotational levels up to N are included. We could numerically diagonalize this matrix and the lowest eigenvalue $\epsilon(E; d_0)$ corresponds to the Stark shift of the $|0, 0\rangle$ state. The effective dipole induced by the electric field is defined as $d_e \equiv -d\epsilon(E; d_0)/dE$. To obtain the exact energy shift as well as the effective dipole we need to include infinite rotational levels ($N \to \infty$), which is impossible. For a practical use, $N = 10$ is enough. Besides the rovibrational ground state, the intermediate state $|2\rangle$ with a moderate internuclear distance also experiences a non-negligible Stark shift. However, it is much harder to analyze the Stark shift for our excited state and it is not done yet. The Stark shift of the Feshbach state in an electric field of a few kV/cm is negligible considering its extreme large internuclear distance.

To measure the Stark shift of the rovibrational ground state in a static electric field, we first measure the shift of the excited state ϵ_{pump} by the one-photon spectrum and then locate $|3\rangle$ with the dark-resonance spectrum. It is apparent that $\epsilon(E; d_0) = \epsilon_{pump} - \epsilon_{dump}$ where ϵ_{dump} is the change of the $L2$ photon energy with respect to the zero-field value. Examples are shown in Fig. 3.24**a** where three cases, namely 0 kV/cm, 0.36 kV/cm and 0.54 kV/cm, are presented. In the upper panel the one-photon spectra indicate that the excited state $|2\rangle$ is shifted down by the electric fields and the line shapes are fitted with Lorentzian functions to extract the line centers and linewidths. No obvious broadening or narrowing of the lines is observed in our field range. In the lower panel the dark-resonance spectra are given and similarly Lorentzian functions are used to obtain the line centers and linewidths. A narrowing of the line shapes is observed for the two-photon spectra. Intuitively the extra noise brought by the external electric field would broad the lines, although it is not the case. Possible reason could be the modification of the coupling strengths by the applied field which needs further explorations.

Figure 3.24: Stark spectroscopy for the rovibrational ground state.

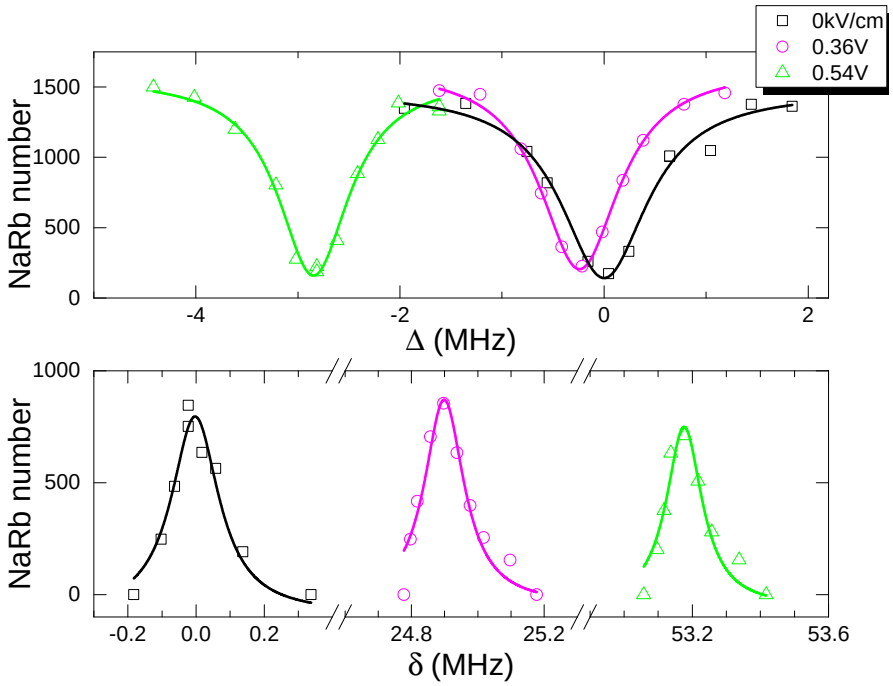

(a) Examples of the one-photon spectra and dark-resonance spectra at a electric field of 0 kV/cm (open black squares), 0.36 kV/cm (open magenta circles) and 0.54 kV/cm (open green triangles).

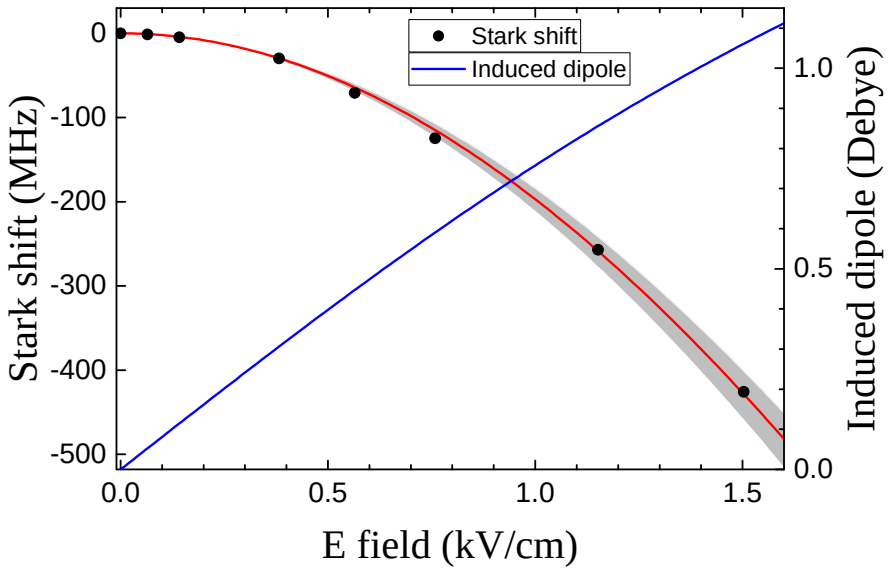

(b) Stark shift of the rovibrational ground state from the spectroscopic measurement. The solid black circles are fitted with the model (red line) described in the main text to extract out the permanent dipole moment. The shade area indicates the uncertainty of of the electric field. Also the induced dipole is shown (blue line).

In Fig. 3.24**b** the Stark shift of the absolute ground state versus the electric field strength is presented. The maximum field we have applied in our measurement is about 1.5 kV/cm and the data points are fitted to the calculated Stark shift counting rotational states up to $N = 10$. This procedure gives a permanent dipole moment of 3.2(1) D for our absolute ground-state $^{23}Na^{Rb}Rb$ molecule which is consistent with previously reported values [189–192]. The uncertainty here comes from the 10% uncertainty of determining the electric fields mentioned in 2.4.2. With the permanent dipole moment in hand we can also calculate the induced dipole moment by the applied electric fields and it is plotted in the same figure as the Stark shift. With our current setup the maximum achievable dipole moment right now is 1.06(4) D.

3.5.3 Measuring The Lifetime of The Sample

Long-lived ultracold samples of polar molecules are predominately preferred for their great potentials in realizing dipolar superfluid systems [81] and high-fidelity gate operations for quantum computing [193]. Especially we are interested in implementing an efficient evaporative cooling in ultracold molecular samples to quantum degeneracy. This requires that the elastic collision rate greatly exceeds the inelastic collision rate, namely the sufficient thermalization among the samples is reached before a significant amount of the molecules is lost due to the inelastic collisions. On the other hand, the study of ultracold collisions itself is also of great interest to us. It was demonstrated with the reactive $^{40}K^{87}Rb$ molecule that the chemical reactions could be controlled via quantum statistics [96], external electric fields [98] and dimensionality [99, 100].

Although our rovibrational ground-state $^{23}Na^{87}Rb$ molecule is chemically stable against the bimolucular exchange reaction, there are still other loss processes which would limit the achievable lifetime. For example, sticky collisions were predicted to make an sample of nonreactive $^{87}Rb^{133}Cs$ molecules with a mean density of $10^{11}cm^{-3}$ only living for a few hundreds of milliseconds [194], which is consistent with the experimental observed lifetime [195]. Such kind of loss mechanism can also be engineered via external electric fields and dimensionality, which would allow us to study ultracold collisions in a controlled manner. For individual systems, the possibilities of exciting the molecules to the dissipative excited states and molecule-

molecule photoassociation [196] by the trapping light can also lead to short-lived samples.

The lifetime of the molecular samples are measured by monitoring the time evolution of the molecular number in our optical dipole trap. As usual, the elementary loss process can be classified according to the number of molecules involved in that: one-body loss, two-body loss, three-body loss, $\cdots$. For a trapped thermal gas, the time evolution of the mean density can be described by the equation reading

$$\frac{d\bar{n}}{dt} = -\bar{n}/\tau - \beta\bar{n}^2 - L_3\bar{n}^3, \tag{3.21}$$

where processes involving more than 3 atoms are neglected and τ, β and L_3 are the one-body loss time constant, two-body loss rate and three-body loss rate, respectively. Assuming constant temperature and a distribution function in Eq. 2.29, the mean density is expressed as $\bar{n} = N\bar{\omega}^3(\frac{M_{\mathrm{NaRb}}}{4\pi k_b T})^{3/2} \equiv \alpha N$. Here N is the molecular number and α is a parameter determined by $\bar{\omega}$ (geometrical mean of three trap angular frequencies), T (temperature) and M_{NaRb} (molecular mass). Substituting this expression into the above equation gives us the following one:

$$\frac{dN}{dt} = -N/\tau - \beta\alpha N^2 - L_3\alpha^2 N^3. \tag{3.22}$$

For us the three-body process is also omitted which would be confirmed later. The solution to this equation reads

$$N(t) = \frac{N_0}{e^{t/\tau}(1 + N_0\alpha\beta\tau) - N_0\alpha\beta\tau}, \tag{3.23}$$

where N_0 is the molecular number at $t = 0$. The data could be fitted to this equation to extract out τ and $\alpha\beta$. Since we are interested in the collision process, i.e. the interaction between molecules, the one-body loss should be avoided as much as possible in real experiments. The determination of β still relies on the determination of the parameter α, namely the temperature and the trap frequencies.

The trap frequencies are determined by calculations based on the last formula in 2.2.6 where the AC polarizability of our rovibrational ground-state molecules is 667.7 au. As a comparison, the polarizability of Feshbach molecules is taken as the sum of atoms to be 909 au. Here au stands for atomic unit. The calculated trap potentials of both the ground-state and Feshbach molecules along the vertical axis in our final FORT are plotted in Fig. 3.25. The trap depths for our molecules at these two different states are indicated in the figure: 4.5 µK and 12.5 µK for them

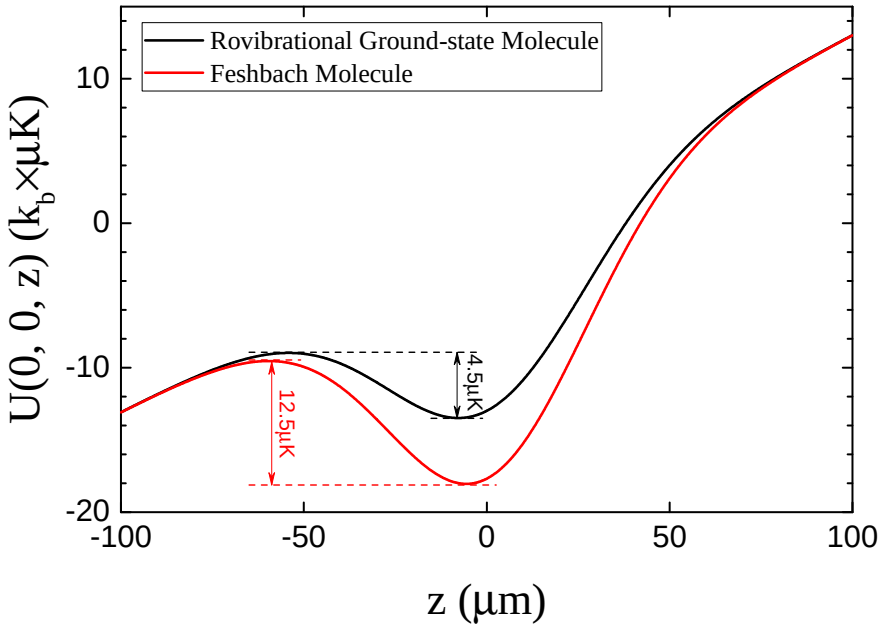

Figure 3.25: The trap potentials for the ground-state (solid black line) and Feshbach-state (solid red line) molecules along the vertical axis: In our final trap, the trap depth for the ground-state molecule is 4.5 µK, nearly 3 times smaller than that for the Feshbach molecule, i.e. 12.5 µK. Also the gravitational sags are different for ^{23}Na^{87}Rb molecules in these two different states and the difference is about 2.2 µm.

respectively. From the figure we can also see that the gravitational sag is different in these two states: the equilibrium position of the ground-state molecule is 2.2 µm lower than that of the Feshbach molecules. Due to these differences, sloshing and breathing motions of the molecular sample are excited after the 15 µs STIRAP which could be seen in our images. However, we cannot clearly identify these motions in our old setup for we cannot reliably image the atoms immediately after the round-trip STIRAP. This is caused by the eddy current after the fast switch-off of the magnetic field. A 20 ms holding is necessary for reliable atomic detections and the motions of the cloud are obscured after this holding due to the different trapping potential for molecules and atoms. Also the measurement of the temperature based on the ballistic expansion also becomes unreliable. However,

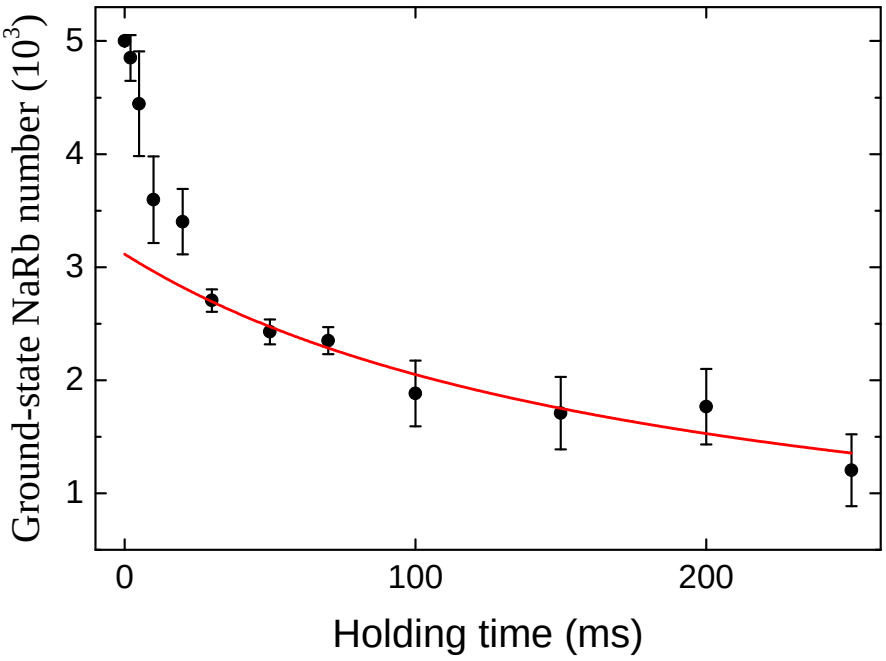

Figure 3.26: The lifetime of the absolute ground-state molecules: The time evolution of the ground state molecule number is plotted. In the final trap, the trap frequencies for the ground-state molecule is $2\pi\times(30,\,156,\,162)$ Hz respectively. Every point corresponds to a three-times repeat and the standard deviation is shown as the error bar. The solid red line is a fit to the data points with more than 50 ms holding (see text for details).

the temperature of the atoms after dissociation is still a good approximation of the temperature of the Feshbach molecules if the dissociation is not too fast [197] and their trapping potential difference is omitted. Ultimately, we have solved the problem of eddy current in our new setup and the final conclusion is drawn based on measurements there. Furthermore we could perform the dissociation at the end of the expansion to reduce the heating from it. Another problem maybe exists in the old setup is that the probability of one-photon excitation of the ground-state molecules is larger due to the broadband nature of our FORT laser, which is changed to a single-frequency laser in the new lab.

The detailed description of the setup and measurement in the new lab may be found in the forthcoming theses of our junior PhD students Mingyang Guo

and Xin Ye. In the final trap, $\bar{\omega} = 2\pi\times91.2\,\mathrm{Hz}$ from both the calculation and the measurement of the sloshing and breathing motions, and typically T =720 nK from the ballistic expansion method. This gives $\alpha = 1.06 \times 10^{7}\,\mathrm{cm}^{-3}$ and a initial mean density of $5.3 \times 10^{10}\,\mathrm{cm}^{-3}$. The time evolution of the molecular number is shown in Fig. 3.26. Due to the sloshing and breathing of the sample, only data points after 50 ms are used to be fitted and here the one-body loss is also neglected. From the fit we could obtain $\beta = 2.5(9) \times 10^{-10}\,\mathrm{cm}^3\cdot\mathrm{s}^{-1}$ (equivalent to a lifetime of about 0.2 s). Actually this loss rate constant should be bound by half of the collision rate constant k_{col} which relates to the collision cross section σ_{col} between two ground-state molecules and the temperature T by $k_{col} = \sigma_{col}\sqrt{8k_bT/\pi M_{\mathrm{NaRb}}}$. The collision cross section between two identical bosons at ultralow temperature is further bound by the unitarity limit of $8\pi/k^2 \sim 4\pi\hbar^2/mk_bT$. Substituting the temperature and other parameters into the rate constant yields $k_{col} \leq 9 \times 10^{-10}$ $\mathrm{cm}^3\cdot\mathrm{s}^{-1}$ and thus our result is very close to the upper bound ($4.5 \times 10^{-10}\,\mathrm{cm}^3\cdot\mathrm{s}^{-1}$) which suggests that every collision leads to loss of two molecules with a large probability.

Such a huge loss is a surprise for our absolute ground-state molecules, which are nonreactive and all occupying the lowest energy state. However, our bosonic ^{23}Na^{87}Rb molecule is not the only case here and a two-body loss constant with the same order for the absolute ground-state bosonic ^{87}Rb^{133}Cs molecule was reported in Ref. [195]. On the other hand, the reported value of this constant for the nonreactive fermionic ^{23}Na^{40}K molecule is smaller by an order of magnitude due to the suppression of s-wave collisions as a sequence of the Pauli principle, which is long but still much shorter than the trap-limited lifetime [198]. The most probable mechanism accounting for this unexpected loss is the aforementioned sticky collision during which long-lived four-body complexes are formed. A large cross section for this process is possible due to the dense density of states of the four-body complex at the colliding energy, hence dense scattering resonances. In Ref. [194] it was shown that the lifetime of the four-body complex is dramatically enhanced by the dense resonances and thus the molecules are invisible after the complexes are formed. By assuming narrower but well-isolated resonances and small mean resonance spacing (far less than the temperature), the sticky rate constant is derived analytically there and the value for us is calculated to be $3.5 \times 10^{-10}\,\mathrm{cm}^3\cdot\mathrm{s}^{-1}$. This is a little larger than our measurement, but still quite reasonable.

3.6 Summary and Outlook

In this chapter, I have described our work on the creation of an ultracold sample of absolute ground-state polar ^{23}Na^{87}Rb molecules beginning with an ultracold mixture of ^{23}Na and ^{87}Rb atoms. The association of atoms into weakly bound molecules discussed in section 3.2 was published in [166]. The spectroscopic study of the excited states near the ^{23}Na($3^2S_{1/2}$)+^{87}Rb($5^2P_{3/2}$) asymptote presented in subsection 3.3.2 formed a publication of [182]. The understanding of the excited states below the ^{23}Na($3^2S_{1/2}$)+^{87}Rb($5^2P_{1/2}$) asymptote in subsection 3.3.1 is on the way and hopefully a new publication would be made focusing on them. We are also preparing another paper concerning the explorations of the mixed levels of the $A^1\Sigma^+$ and $b^3\Pi$ states (subsection 3.3.3), as well as the two-photon spectroscopic study of the $X^1\Sigma^+$ state (section 3.4). The description of the creation and characterization of the absolute ground-state molecules (section 3.5) has already been reported in [199].

Based on all of these previous results, many exciting and important topics are ready to be studied with our ^{23}Na^{87}Rb molecules. Here I want to list a few and discuss them in detail.

3.6.1 Ultracold Collisions Between Absolute Ground-state Molecules

Collisions between quantum particles, i.e. atoms and molecules, are of fundamental importance in determining the properties of quantum gases. For atoms interacting through short-range and isotropic potentials (like van der Walls potential), the physics of collisional dynamics could be captured only by the scattering lengths for bosons or distinguishable particles at the low-energy limit. Collisional resonances, where the scattering lengths could be varied by several orders of magnitude by moderate changes of the external optical or magnetic fields, happen when the collision energy approaches some bound or quasi-bound state energy. However, collisions between particles interacting with long-range or anisotropic potentials could be predominately complex even at the temperature of $0.1 \sim 1\,\mu$K, with which typical current experiments work. For example, chaotic behavior of the scattering resonances has been observed and discussed in collisions between highly magnetic

atoms [88, 200] due to the anisotropic interaction potentials. The resonances are expected to be even much denser for atom-molecule or molecule-molecule collisions concerning the more complex angular momentum couplings, especially for heavier molecules.

Even we assume isotropic interactions, the resonances may still be individually unresolvable from the theoretical point of view, let alone being identified in experiments [194, 201]. A proper method to gain insights into these collisions was developed in Ref. [194, 201], where a statistical description of the collision cross section is used to draw the conclusion that colliding partners have a large possibility to stick together and thus lose from our detected signal. This is called sticky collision. The complexes formed in this manner have finite lifetimes, after which they decay back into the initial colliding particles and thus we could observe the revival of the particle number. Of course there are also possibilities that the complexes decay to some low lying states via collisions with other complexes or molecules and these processes depend on the lifetime of them. Even more bad, the complexes may not be supported by our FORT (blue detuning trap) and they become lost once they are formed. Based on this picture, we could end up with several limit cases of the molecule loss dynamics:

- A pure two-body loss: The loss of the complexes are so fast that no obvious effect of the molecular revival could be seen. We need to mention that the possible quantum Zeno effect is not considered here.
- When the loss of the complexes is not severe, the dynamics would firstly dominate by the complex formation process and then reach some equilibrium state by including the molecular revival.
- The loss of the complexes is in a intermediate level and a quit complex dynamics is observed.

For our data of the loss dynamics are obscured by the trap excitations of the molecular sample, one good solution is to use a magic-wavelength trap in which the polarizabilities of the absolute ground-state molecules and the Feshbach molecules coincide with each other. Unfortunately calculations from our theoretical collaborators suggest that there is no magic wavelength in the far-off-resonance regime. The only thing we can do is to moderately increase the trap power to minimize the effect of trap excitations as well as avoid any heating.

Besides measuring the loss dynamics curve, we could also imagine to directly

observe the revival process if we are lucky to stay at a happy-parameter regime, that's to say the complexes are trapped by our FORT and the collisional loss of them is small. In this case, we could quickly remove the residual ground-state molecules after they are held in the trap for sufficient formation of the complex. Then the molecule number could be monitored to see possible revival dynamics. However, the sticky mechanism is valid only in cases that all the relevant rovibrational states of the complexes are involved during the collision process. This is maybe not the case and other possibilities should also be considered.

One possible mechanism is the collision between the absolute ground-state molecules and the highly excited molecules created during the STIRAP. As I have mentioned in the last section, only about 80% Feshbach molecules are transfered to the absolute ground state and most likely the other 20% molecules occupy many highly excited states. The ground-state molecules can be ejected from the trap by colliding with these excited-state molecules during which energies are released through vibrational quenching of the excited-state molecules. We could gain some insights into this possibility by measuring the loss curves with different STIRAP efficiencies. Another possibility is the excitation of one molecule into excited states or the photoassociation of two molecules into four-body bound states by the trap light. For the former case, the possible excited states are those belonging to the $C^1\Sigma^+$ PES to which the ground-state molecules are excited via a two-photon process. The photoassociation is only possible at short ranges for there are no resonances at long range [196]. In both cases the loss should be sensitive to the frequency of the trap light. So a tunable narrow-linewidth laser is preferred to examine this possibility.

The ultracold collisions would become more interesting when an external electric filed is applied. The sticky cross section was predicted to be greatly enhanced in an electric field and undergoes a ladder behavior as the electric field is increased [194]. This could also be incorporated to test the sticky mechanism. What' s more important is that the external electric field was proposed to be used to stabilize the molecular gases through the short-range shielding mechanisms [100, 202, 203].

3.6.2 Long-lived Ultracold Samples of Polar Molecules

The effort toward producing long-lived ultracold samples of polar molecules is strongly motivated by the various potential applications of those systems as discussed in section 1.2. For our ^{23}Na^{87}Rb molecules, we are able to induce a effective electric dipole moment of 1.06 D in the lab frame, which corresponds to a dipolar length of $\sim$35 000 a_0. To overcome the observed fast loss, several methods are already in hand.

As mentioned in the last paragraph of previous subsection, the short-range shielding mechanisms are expected to suppress the inelastic loss as well as the chemical reaction by several orders of magnitude. The basic idea is to introduce a energy barrier through external fields to prevent two molecules to reach the short-ranges where the inelastic processes happen. In Ref. [202, 203], the authors proposed to work with excited rotational dipolar molecules in a static electric field which would dramatically modify the ratio between the elastic collision rate and the inelastic collision rate. This requires another collisional channel to cross the threshold of the initial collision and typically a large dipole moment as well as a moderate electric field are necessary. The theoretical calculation on ^{23}Na^{87}Rb suggests that at a field of 5 kV/cm the previous ratio can reach $\sim 10^7$, which is very favorite for an efficient evaporative cooling. Another method, demonstrated in Ref. [100] with the reactive fermionic ^{40}K^{87}Rb molecule, incorporates the repulsive dipolar interaction between aligned polar molecules in a quasi-2D trap to prevent them to approach each other. Interestingly, a self-assembled dipolar lattice phase has been proposed in such systems [204], which are potentially suitable for the study of Hubbard models with phonons [205].

To ultimately solve the problem, we can make a molecular insulator in an optical lattice where molecules are well-isolated from each other due to the high tunneling barrier. This also has already been demonstrated with the reactive fermionic ^{40}K^{87}Rb molecule and the lifetime was increased to the trap-limited value (>20 s) in a 3D deep lattice [99]. For our molecules in a simple cubic lattice formed by 1064 nm light, the nearest neighbor DDI strength U_{NN} is $> k_b\times 50$ nK while the recoil energy E_R is about $k_b\times 76$ nK. At a lattice depth of $25E_R \sim k_b\times 1.9$ µK, the tunneling rate is estimated to be $0.001E_R \sim k_b\times 1.9\,\text{nK} \ll U_{NN}$. In the literature [82, 102], the authors extensively studied the insulating ground states as well as many metastable insulating states of the 2D dipolar lattice gas within the extended

Bose-Hubbard model and we are ready to observe these new quantum states.

Chapter 4

Spin Dynamics In Heteronuclear Spin Mixtures and Thermal Spinor Gases

In this chapter, I will change to another absolutely different topic, namely spinor gases. First proposed theoretically in Ref. [108, 109] and realized experimentally in Ref. [107] in 1998, spinor gases are referred to gases with the internal degree of freedom liberated thanks to the developing of FORT. Since then, this field has been one of the hottest one in the ultra-cold scientific community and many fundamental and practical topics have been studied with spinor gases (see discussion in section 1.3). Among them, spin mixing is a process that the atomic population is oscillated among different Zeeman sub-levels of the hyperfine spin F [206]. It is driven by the spin-dependent interaction which is positive (negative) for the antiferromagnetic (ferromagnetic) interaction. At a finite magnetic field, another energy competing with the spin-dependent interaction is the quadratic Zeeman energy. With properly designed initial states, this competition would lead to coherent oscillations of the populations. Furthermore, resonant behavior of the oscillations was predicted in Ref. [207] and experimentally verified with both antiferromagnetic gases (spin-1 ^{23}Na [116, 118] and spin-2 ^{87}Rb [115, 119]) and ferromagnetic

gases (spin-1 ^{87}Rb [117, 119]). In this work I would recall the spin-species spinor gases in section 4.1.

In section 4.2, I would describe our work on the nature extending of the previous study of the coherent spin mixing into a mixture of two spin-1 bosons, i.e. ^{23}Na and ^{87}Rb. By carefully designing the initial state and selecting the external magnetic field, we have found a clear evidence of the coherent magnetization exchange between the ^{23}Na and ^{87}Rb gas, which indicates a coherent dynamics driven by the heteronuclear spin-dependent interactions and this dynamics is observed with a quantum gas mixture for the first time. We have also identified a resonant behavior of it by tuning the external magnetic field, which is similar to the single-species case. Profoundly, another unique knob to control the spin-mixing dynamics in heteronuclear spinor mixtures has been demonstrated in our experiments, namely the species-dependent vector light shift.

We have also studied the coherent spin-mixing dynamics in normal Bose gases of spin-1 and spin-2 ^{87}Rb atoms which is presented in section 4.3. Within the approximation that the external and internal degrees of freedom are decoupled, the equation of motion for the normal spinor gases are the same as that for spinor BECs except for a numerical factor appearing in front of the spin-dependent interactions.

4.1 Introduction to The Single-species Spinor Gases

The physics associated with the single-species spinor Bose gases has been extensively reviewed in Ref. [110,111]. Here I want to focus on the mean-field description of the spin-1 BEC within the so-called single-mode-approximation (SMA), where the G-P equation is utilized to solve the dynamics. The phase diagram with both ferromagnetic and antiferromagnetic interactions are discussed and the solution to the G-P equation is presented and analyzed. The extension of the formalism into a spin-2 BEC is straightforward.

The Hamiltonian for a spin-1 BEC in the second-quantization form reads

$$\begin{aligned} H = &\int d\mathbf{r}\hat{\psi}_k^\dagger(\mathbf{r})[-\frac{\hbar^2}{2m}\nabla^2 + V_{trap}(\mathbf{r}) - pk + qk^2]\hat{\psi}_k(\mathbf{r}) + \\ &\int d\mathbf{r}\hat{\psi}_k^\dagger(\mathbf{r})\hat{\psi}_p^\dagger(\mathbf{r})[\frac{c_0}{2}\delta_{pq}\delta_{kl} + \frac{c_2}{2}\mathbf{F}_{pq}\cdot\mathbf{F}_{kl}]\hat{\psi}_q(\mathbf{r})\hat{\psi}_l(\mathbf{r}). \end{aligned} \tag{4.1}$$

Here V_{trap} is the external trapping potential and $p(q)$ corresponds to the lin-

ear (quadratic) Zeeman energy. $c_0(c_2)$ represents the spin-independent (spin-dependent) interaction parameter, which is related to the scattering length by $c_0 = \frac{4\pi\hbar^2}{3m}(a_0 + 2a_2)$ ($c_2 = \frac{4\pi\hbar^2}{3m}(a_2 - a_0)$). (See Eq. B.3.) $\hat{\psi}_k(\hat{\psi}_k^\dagger)$ is the annihilation (creation) operator for the sub-level k ($k = +1, 0, -1$) and the repeated index implies a summation over all the possible values.. $\mathbf{F}$ is the spin-1 operator whose elements are defined in Eq. 2.61. In the mean field theory the annihilation (creation) operators are replaced by complex order parameters: $\hat{\psi}_k(\hat{\psi}_k^\dagger) \to \psi_k(\psi_k^*)$. The equation of motion for the order parameters reads

$$\begin{aligned} i\hbar\frac{\partial\psi_k}{\partial t} &= \frac{\delta H}{\delta\psi_k^*} \\ &= [-\frac{\hbar^2}{2m}\nabla^2 + V_{trap}(\mathbf{r}) + c_0 n - pk + qk^2]\psi_k + c_2\langle\mathbf{F}\rangle\cdot\mathbf{F}_{kl}\psi_l, \end{aligned} \tag{4.2}$$

where $n = \psi_k^*\psi_k$, is the atomic density and $\langle\mathbf{F}\rangle = \psi_p^*\mathbf{F}_{pq}\psi_q$, is the total spin. The SMA states that different sub-levels share a same static spatial wavefunction: $\psi_k(\mathbf{r}, t) = \phi(\mathbf{r})e^{-i\mu t/\hbar}\xi_k(t)$. The spatial wavefunction satisfies $\mu\phi(\mathbf{r}) = [-\frac{\hbar^2}{2m}\nabla^2 + V_{trap}(\mathbf{r}) + c_0 n]\phi(\mathbf{r})$ and $\xi_k^*\xi_k = 1$. The equation of motion is simplified to be

$$\begin{aligned} i\hbar\dot{\xi}_{\pm1} &= (\mp p + q)\xi_{\pm1} + c_2 n[\xi_0^2\xi_{\mp1}^* + \xi_{\pm1}(|\xi_0|^2 + |\xi_{\pm1}|^2 - |\xi_{\mp1}|^2)], \\ i\hbar\dot{\xi}_0 &= c_2 n[\xi_0(|\xi_{+1}|^2 + |\xi_{-1}|^2) + 2\xi_0^*\xi_{+1}\xi_{-1}]. \end{aligned} \tag{4.3}$$

Based on these equations and the total spin-dependent energy $E = N\{-p(|\xi_{+1}|^2 - |\xi_{-1}|^2) + q(1-|\xi_0|^2) + \frac{c_2\bar{n}}{2}[2\xi_0^2\xi_{+1}^*\xi_{-1}^* + 2\xi_0^{*2}\xi_{+1}\xi_{-1} + 2|\xi_0|^2(1-|\xi_0|^2) + (|\xi_{+1}|^2 - |\xi_{-1}|^2)^2]\}$, we can deduce the ground state and the time evolution of the system with various interaction parameters. ($N = \int|\phi(\mathbf{r})|^2 d\mathbf{r}$, is the total atom number and $\bar{n} = \int|\phi(\mathbf{r})|^4 d\mathbf{r}/N$, is the mean density.)

4.1.1 The Mean-field Ground State of a Spin-1 BEC

The mean-field ground state of a spin-1 BEC can be obtained by minimizing E. It is easy to show that the longitudinal magnetization, $m_0 = |\xi_{+1}|^2 - |\xi_{-1}|^2$, is a constant from Eq. 4.3 and $|\xi_{\pm1}|^2 = \frac{1-\rho_0\pm m_0}{2}$ with $\rho_0 = |\xi_0|^2$. By introducing $m_0 = (1-\rho_0)\cos\alpha$ with $0 \le \alpha \le \pi$, we have written the total spin-dependent energy as

$$\begin{aligned} E/N &= -pm_0 + q(1-\rho_0) + \frac{c_2\bar{n}}{2}[2\rho_0\sqrt{(1-\rho_0)^2 - m_0^2}\cos\theta + 2\rho_0(1-\rho_0) + m_0^2] \\ &= (1-\rho_0)[-p\cos\alpha + q + \frac{c_2\bar{n}}{2}\cos^2\alpha + \frac{c_2\bar{n}}{2}(\sin\alpha^2 + 1 + 2\sin\alpha\cos\theta)\rho_0], \end{aligned} \tag{4.4}$$

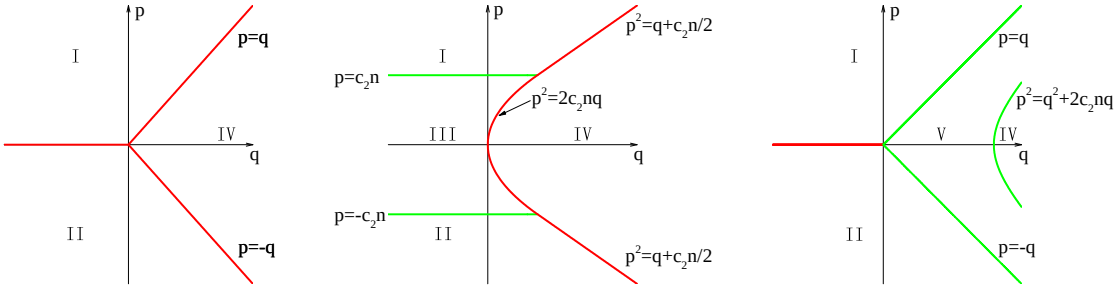

Figure 4.1: The phase diagram of a spin-1 BEC in the (q, p) plane: (a), (b) and (c) are for $c_2 = 0$, $c_2 > 0$ and $c_2 < 0$ respectively. The solid lines are phase boundaries where red (green) ones represent the first-order (second-order) phase transitions. I, II, III, IV and V refer to different phases (see text).

where θ is the argument of $\xi_0^2\xi_{+1}^*\xi_{-1}^*$. The minimization of E depends on the value of c_2:

(1) $c_2 = 0, E = (1-\rho_0)(-p\cos\alpha + q)$.

E is minimum when $\rho_0 = 1$ if $q > |p|$ and $\rho_0 = 0$ if $q < |p|$. The phase diagram in the (q, p) plane is shown in Fig. 4.1 (a).

(2) $c_2 > 0$ (antiferromagnetic interaction) , E is minimized when $\cos\theta = -1$ and $E/N = (1-\rho_0)[-p\cos\alpha + q + \frac{c_2\bar{n}}{2}\cos^2\alpha + \frac{c_2\bar{n}}{2}(1-\sin\alpha)^2\rho_0]$. Since E is a quadratic function of ρ_0 with a negative quadratic coefficient if $\sin\alpha \neq 1$, the minimum is achieved either with $\rho_0 = 1$ or with $\rho_0 = 0$. If $\sin\alpha = 1$, then $\cos\alpha = 0$ and $E = q(1-\rho_0)$. The minimum is also obtained with $\rho_0 = 1$ or 0. So the possible candidates for the minimum of E:

i) $\rho_0 = 0, E_{\min} = \begin{cases} q - \frac{p^2}{2c_2\bar{n}} & |p| \le c_2\bar{n} \text{ and } m_0 = \frac{p}{c_2\bar{n}} \\ q - |p| + c_2\bar{n}/2 & |p| \ge c_2\bar{n} \text{ and } m_0 = \mathrm{sgn}(p) \end{cases}$;

ii) $\rho_0 = 1, E_{\min} = 0$ and $m_0 = 0$.

The phase diagram in this case is shown in Fig. 4.1 (b).

(3) $c_2 < 0$ (ferromagnetic interaction) , E is minimized when $\cos\theta = 1$ and $E/N = (1-\rho_0)[-p\cos\alpha + q + \frac{c_2\bar{n}}{2}\cos^2\alpha + \frac{c_2\bar{n}}{2}(1+\sin\alpha)^2\rho_0]$. The analysis is similar to the case with $c_2 > 0$ except that the minimum is the vertex of the quadratic function

with a positive quadratic coefficient. The possible candidates for the minimum of E:

i) $\rho_0 = 0, E_{\min} = q - |p| + c_2\bar{n}/2$ and $m_0 = \mathrm{sgn}(p)$;

ii) $\rho_0 = 1, E_{\min} = 0$ and $m_0 = 0$;

iii) $\rho_0 = \frac{(q^2-p^2)(-p^2-q^2+2c_2\bar{n}q)}{4c_2\bar{n}q^3}$, $E_{\min} = \frac{(-p^2+q^2+2c_2\bar{n}q)}{8c_2\bar{n}q^2}$ and $m_0 = \frac{p(q+2c_2\bar{n})}{2c_2\bar{n}q}$.

The phase diagram in this case is shown in Fig. 4.1 (c).

	Phase	Order parameter	$E_{\min}$
I	F	$e^{i\beta}(1,0,0)$	$q-p+c_2\bar{n}/2$
II	F	$e^{i\beta}(0,0,1)$	$q+p+c_2\bar{n}/2$
III	AF	$e^{i\beta}(\sqrt{\frac{p+c_2\bar{n}}{2c_2\bar{n}}},0,-\sqrt{\frac{-p+c_2\bar{n}}{2c_2\bar{n}}})$	$q-\frac{p^2}{2c_2\bar{n}}$
IV	P	$e^{i\beta}(0,1,0)$	0
V	BA	$\left(\begin{array}{c}(e^{i\beta}\frac{q+p}{2q}\sqrt{\frac{-p^2+q^2+2c_2\bar{n}q}{2c_2\bar{n}q}} \\ \sqrt{\frac{(q^2-p^2)(-p^2-q^2+2c_2\bar{n}q)}{4c_2\bar{n}q^3}} \\ e^{-i\beta}\frac{q-p}{2q}\sqrt{\frac{-p^2+q^2+2c_2\bar{n}q}{2c_2\bar{n}q}})\end{array}\right)^T$	$\frac{(-p^2+q^2+2c_2\bar{n}q)}{8c_2\bar{n}q^2}$

Table 4.1: Five different phases of a spin-1 BEC: F, AF, P, and BA stand for ferromagnetic, antiferromagnetic, polar, and broken-axisymmetry phases, respectively. β is an arbitrary phase accounting for the $U(1)$ symmetry.

In summary, there are four possible ground states which are listed in Table 4.1. In the ferromagnetic phase, which is denoted as F, all of the spins are parallel (I) or anti-parallel (II) to the magnetic field and gives a maximum $|m_0|$. The antiferromagnetic (AF) phase gives a nonzero m_0 by $p/c_2\bar{n}$ while the polarized spins tend to be anti-parallel to each other. The polar (P) phase gives a zero m_0 and all of the spins are unpolarized. All the previous three phases give $\langle \mathbf{F} \rangle = \bar{n}(0,0,m_0)$, which is along the magnetic field. However, in the last one, known as broken-axisymmetry (BA) phase, the total spin is tilted against the magnetic field and the axisymmetry is broken although the Hamiltonian still preserves the axisymmetry.

4.1.2 The Coherent Spin-mixing Dynamics

The time evolution of the system is determined by equations in Eq. 4.3 where the linear Zeeman term could be gauged out by introducing $\tilde{\xi}_k = \xi_k e^{-ikpt/\hbar}$ in an uniform external field. Furthermore, by introducing $\tilde{\xi}_k = \sqrt{\rho_k}e^{i\theta_k}$ ($0 \leq \rho_k \leq 1$ and θ_k is real) and substituting them into Eq. 4.3, we could obtain two coupled equations for ρ_0 and θ:

$$\begin{aligned}\dot{\rho}_0 &= -\frac{2c_2\bar{n}}{\hbar}\rho_0\sqrt{(1-\rho_0)^2 - m_0^2}\sin\theta, \\ \dot{\theta} &= 2q/\hbar + \frac{2c_2\bar{n}}{\hbar}[2\rho_0 - 1 + \frac{(1-\rho_0)(2\rho_0-1)+m_0^2}{\sqrt{(1-\rho_0)^2-m_0^2}}\cos\theta],\end{aligned} \tag{4.5}$$

where $\theta = 2\theta_0 - \theta_{+1} - \theta_{-1}$, coincides with the θ in previous subsection. ρ_0 and m_0 follow the previous definitions. Since m_0 is conserved, we can omit some constant terms in Eq. 4.4 and rewrite it as $\varepsilon \equiv E/N = q(1-\rho_0) + \frac{c_2\bar{n}}{2}[2\rho_0\sqrt{(1-\rho_0)^2-m_0^2}\cos\theta + 2\rho_0(1-\rho_0)]$. It is easy to show that $\dot{\rho}_0 = \frac{2}{\hbar}\partial_\theta\varepsilon$ and $\dot{\theta} = -\frac{2}{\hbar}\partial_{\rho_0}\varepsilon$, which means the time evolution of the system is along a equal-energy contour in the phase-space of (θ, ρ_0). This aspect was first recognized in Ref. [207]. Generally, ρ_0 experiences a periodic oscillation. Substituting ε into the first equation of Eq. 4.5 we have

$$\begin{aligned}(\dot{\rho}_0)^2 &= \frac{4}{\hbar^2}(A\rho_0^3 + B\rho_0^2 + C\rho_0 + D) \\ &= \frac{4}{\hbar^2}A(\rho_0 - x_1)(\rho_0 - x_2)(\rho_0 - x_3) \\ &\equiv \frac{4}{\hbar^2}f(\rho_0),\end{aligned} \tag{4.6}$$

where

$$A = -2c_2\bar{n}q, B = -(c_2\bar{n}m_0)^2 + 2c_2\bar{n}(2q-\varepsilon) - q^2, C = (q-c_2\bar{n})(q-\varepsilon), D = -(q-\varepsilon)^2.$$

$x_i (i = 1, 2, 3)$ are the roots of $\dot{\rho}_0 = 0$ and $x_1 \leq x_2 \leq x_3$. If $A > 0$, the distribution of x_i is shown by the red curve in Fig. 4.2 for $f(0) \leq 0, f(1) \leq 0$ and $(\dot{\rho}_0)^2 \geq 0$, where $0 \leq x_1 \leq x_2 \leq 1 \leq x_3$. Then we could see that ρ_0 is oscillatory between x_1 and x_2. Similarly, it can be shown that for $A < 0$ ρ_0 is oscillatory between x_2 and x_3.

Resonant behavior is found when $x_2 = x_3 = 1$ ($x_1 = x_2 = 0$) for $A > 0$ ($A < 0$), where the oscillation period is divergent [110, 207]. However, for $A > 0$ this divergent is only possible when $m_0 = 0$, otherwise the period is still finite at the

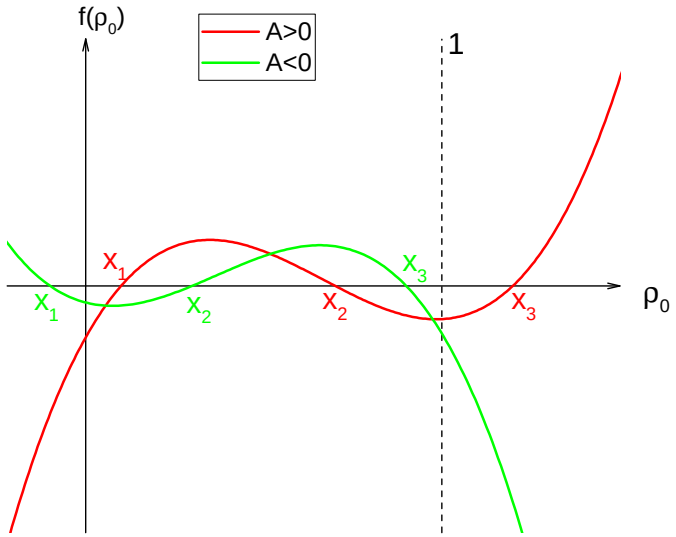

Figure 4.2: The distribution of the roots of $\dot{\rho}_0 = 0$. The red (green) line corresponds to $A > 0$ ($A < 0$). (see text for details.)

resonant point. It also turns out that the critical magnetic field where the resonant behavior happens is $q = -c_2\bar{n}\rho_0(1+\cos\theta)$ $(c_2\bar{n}[1-\rho_0+\sqrt{(1-\rho_0)^2-m_0^2}\cos\theta])$ for $A > 0$ ($A < 0$). Here ρ_0 and θ are the initial values.

Far away from the resonance, Eq. 4.5 could be simplified and two specific regimes are identified [208]. Generally, both the oscillation period and amplitude would decrease when the magnetic field is tuned away from the critical value. For $|q| \ll |c_2\bar{n}|$, the dynamics is dominated by the spin-dependent interaction where the oscillation period reaches a static level with a fixed atomic density. The oscillation amplitude would gradually approach zero as $q \to 0$. This is termed interaction dominated regime in Ref. [208]. On the other hand, the dynamics is dominated by the quadratic Zeeman energy when $|q| \gg |c_2\bar{n}|$. In this case, both the oscillation period and amplitude is proportional to the inverse of $|q|$ and the dynamics is finally suppressed at high enough magnetic fields. This regime is called the quadratic Zeeman regime in Ref. [208].

The coherent spin-mixing dynamics in a spin-1 condensate has been investigated extensively in experiments with ^{23}Na [116] and ^{87}Rb [117, 208] atoms. By comparing the experimental data with the theoretical model, the authors in those references have obtained c_2 for both species. In Ref. [114] c_2 for the spin-1 ^{87}Rb atoms was precisely measured by observing the spin-mixing dynamics between two

atoms confined in a same site of an optical lattice. From those previous studies, we take the value of $\frac{4\pi\hbar^2}{3M_{Na}}2.47a_B$ [116] ($\frac{4\pi\hbar^2}{3M_{Rb}}(-1.07)a_B$ [114]) for ^{23}Na (^{87}Rb) in our experiments. The critical fields in both cases are on the order of 0.2 G with the typical BEC density of $10^{13}\,\mathrm{cm}^{-3}$.

4.1.3 Mean-field Ground States and Coherent Spin-mixing Dynamics of a Spin-2 BEC

The second-quantization form of the Hamiltonian for a spin-2 BEC reads

$$\begin{aligned} H = &\int d\mathbf{r}\hat{\psi}_k^\dagger(\mathbf{r})[-\frac{\hbar^2}{2m}\nabla^2 + V_{trap}(\mathbf{r}) - pk + qk^2]\hat{\psi}_k(\mathbf{r}) + \\ &\int d\mathbf{r}\hat{\psi}_k^\dagger(\mathbf{r})\hat{\psi}_p^\dagger(\mathbf{r})[\frac{c_0}{2}\delta_{pq}\delta_{kl} + \frac{c_2}{2}\mathbf{F}_{pq}\cdot\mathbf{F}_{kl} + \frac{c_4}{2}\frac{(-1)^{p+q}}{5}\delta_{-k,p}\delta_{q,-l}]\hat{\psi}_q(\mathbf{r})\hat{\psi}_l(\mathbf{r}), \end{aligned} \tag{4.7}$$

where c_0, c_2 and c_4 have been defined in Eq. B.5. $\mathbf{F}$ here is the spin operator for the spin-2 object, whose elements are

$$F_x = \begin{pmatrix} 0 & 1 & 0 & 0 & 0 \\ 1 & 0 & \sqrt{\frac{3}{2}} & 0 & 0 \\ 0 & \sqrt{\frac{3}{2}} & 0 & \sqrt{\frac{3}{2}} & 0 \\ 0 & 0 & \sqrt{\frac{3}{2}} & 0 & 1 \\ 0 & 0 & 0 & 1 & 0 \end{pmatrix}, F_y = i\begin{pmatrix} 0 & -1 & 0 & 0 & 0 \\ 1 & 0 & -\sqrt{\frac{3}{2}} & 0 & 0 \\ 0 & \sqrt{\frac{3}{2}} & 0 & -\sqrt{\frac{3}{2}} & 0 \\ 0 & 0 & \sqrt{\frac{3}{2}} & 0 & -1 \\ 0 & 0 & 0 & 1 & 0 \end{pmatrix}, F_z = \begin{pmatrix} 2 & 0 & 0 & 0 & 0 \\ 0 & 1 & 0 & 0 & 0 \\ 0 & 0 & 0 & 0 & 0 \\ 0 & 0 & 0 & -1 & 0 \\ 0 & 0 & 0 & 0 & 2 \end{pmatrix}. \tag{4.8}$$

In the mean-field theory, where the annihilation (creation) operator is replaced by its expectation value $\langle\hat{\psi}_k\rangle = \phi(\mathbf{r})e^{-i\mu t/\hbar}\xi_k$ for $k \in (+2, +1, 0, -1, -2)$, the spin-dependent energy per particle under the SMA is expressed as

$$\varepsilon = -pm_0 + q(4|\xi_{+2}|^2 + |\xi_{+1}|^2 + |\xi_{-1}|^2 + 4|\xi_{+2}|^2) + \frac{c_2\bar{n}}{2}|\langle\mathbf{F}\rangle|^2 + \frac{c_4\bar{n}}{2}|\langle S\rangle|^2, \tag{4.9}$$

where $\langle\mathbf{F}\rangle = \boldsymbol{\xi}^\dagger\mathbf{F}\boldsymbol{\xi}$ with $\boldsymbol{\xi} = (\xi_{+2}, \xi_{+1}, \xi_0, \xi_{-1}, \xi_{-2})^T$ is the spin expectation value, $\langle S\rangle = \frac{2\xi_{+2}\xi_{-2} - 2\xi_{+1}\xi_{-1} + \xi_0^2}{\sqrt{5}}$ is the spin-singlet pair expectation value, and $m_0 = 2|\xi_{+2}|^2 + |\xi_{+1}|^2 - |\xi_{-1}|^2 - 2|\xi_{-2}|^2$ is the magnetization. The equation of motion for ξ_k is given by $\dot{\xi}_k = \delta\varepsilon/\delta\xi_k^*$.

Similar to that in a spin-1 BEC, the mean-field ground state of a spin-2 BEC could also be obtained by minimizing the spin-dependent energy per particle in

Eq. 4.9. However, the situation is much more complex here. Three possible phases were predicted at a zero magnetic field depending on the value of c_2 and c_4 in Ref. [209], namely ferromagnetic phase for $c_2 < 0$ and $c_4 > 0$, nematic phase for $c_2 > 0$ and $c_4 < 0$, and cyclic phase for $c_2 > 0$ and $c_4 > 0$. When both parameters are negative the competition between the ferromagnetic phase and the nematic phase resulting into a phase boundary $c_4 = 20c_2$. At a finite magnetic filed, the direct minimization of the energy is so complicated that it is unpractical. Another method considering the stationary solutions to the dynamical equation was provided and reviewed in Ref. [110], which is out of the scope here.

The coherent spin-mixing dynamics has also been studied experimentally with a ^{87}Rb spin-2 BEC in an uniform magnetic field [115]. Although the coupled dynamical equations are quite hard to solve, it turns out that $c_4 \ll c_2$ in a ^{87}Rb spin-2 BEC [114] and some simplified solutions could be obtained with a special initial state [115]. Nevertheless, we use a numerical method to solve the dynamics in this work presented in section 4.3.

4.2 Observation of Coherent Spin-mixing Dynamics in an Ultracold Mixture of Two Spin-1 Bosons

In the section, I would describe the first experimental study of a heteronuclear spinor system in our group. Specifically, we have investigated the coherent spin-mixing process between two different spin-1 atoms, which turns out to be driven by the heteronuclear spin-exchange interactions.

4.2.1 Theory

The Hamiltonian we consider here in the second-quantization form reads

$$H = H_1 + H_2 + H_{12}, \tag{4.10}$$

where

$$H_i = \int d\vec{r}\hat{\psi}^\dagger_{i_k}(\vec{r})[-\frac{\hbar^2}{2m_i}\vec{\nabla}^2 + V^i_{trap}(\vec{r}) - p_i k + q_i k^2]\hat{\psi}_{i_k}(\vec{r}) + \int d\vec{r}\hat{\psi}^\dagger_{i_k}(\vec{r})\hat{\psi}^\dagger_{i_p}(\vec{r})[\frac{c_{0i}}{2}\delta_{pq}\delta_{kl} + \frac{c_{2i}}{2}\vec{\mathbf{F}}_{pq}\cdot\vec{\mathbf{F}}_{kl}]\hat{\psi}_{i_q}(\vec{r})\hat{\psi}_{i_l}(\vec{r}), \tag{4.11}$$

and

$$H_{12} = \int d\mathbf{r}\hat{\psi}^\dagger_{1_k}(\mathbf{r})\hat{\psi}^\dagger_{2_p}(\mathbf{r})[\frac{\alpha}{2}\delta_{pq}\delta_{kl} + \frac{\beta}{2}\vec{\mathbf{F}}_{pq}\cdot\vec{\mathbf{F}}_{kl} + \frac{\gamma}{2}\frac{(-1)^{p+q}}{3}\delta_{k,-p}\delta_{-q,l}]\hat{\psi}_{2_q}(\mathbf{r})\hat{\psi}_{1_l}(\mathbf{r}). \tag{4.12}$$

Here 1 (2) labels Na (Rb) and the interaction coefficients are defined in Eqs. B.3 and B.4. H_i includes the single-particle Hamiltonian as well as the intra-species interactions for $i = 1$ or 2 and H_{12} represents the interspecies interactions.

If both species are nearly pure condensates, the above Hamiltonian can be treated using the SMA in the mean-field level to simplify the problem, as done in Ref. [130]. However, the double condensates of ^{23}Na and ^{87}Rb are immiscible at the background scattering lengths [42]. To increase the spatial overlap of the two clouds, which turns out to be necessary to clearly observe the interspecies spin mixing, we have utilized a mixture of a ^{23}Na condensate and a ultracold ^{87}Rb thermal gas in our experiments.

Although the ^{23}Na condensate can still be described by a order parameter, the ^{87}Rb thermal gas should be treated in another way. Following Refs. [118, 210], we use a Boltzmann transport equation to describe the thermal gas. The elements of Wigner density matrix $\mathbf{G}$ are defined as

$$g_{ab}(\vec{r},\vec{p},t) = \int d\vec{r'}e^{-i\vec{p}\cdot\vec{r'}/\hbar}\langle\hat{\psi}^\dagger_{2_a}(\vec{r}+\vec{r'}/2)\hat{\psi}_{2_b}(\vec{r}-\vec{r'}/2)\rangle_t. \tag{4.13}$$

From the moment of $\mathbf{G}$ we can obtain the atomic density by $n^{(2)}_{ab}(\vec{r},t) = \frac{1}{(2\pi\hbar)^3}\int d\vec{p}g_{ab}(\vec{r},\vec{p},t)$. The general Boltzmann equation for $\mathbf{G}$ reads

$$\frac{\partial}{\partial t}\mathbf{G} + \frac{\vec{p}}{m_2}\cdot\vec{\nabla}_{\vec{r}}\mathbf{G} = i[\mathbf{M},\mathbf{G}] + \frac{1}{2}\{\vec{\nabla}_{\vec{r}}\mathbf{M},\vec{\nabla}_{\vec{p}}\mathbf{G}\} + \mathbf{I}_c, \tag{4.14}$$

where $\mathbf{M}$ is the interaction potential, whose expression is $\mathbf{M} = -p_2\mathbf{F}_z + q_2\mathbf{F}_z^2 + [V^2_{trap} + c_{02}\mathrm{Tr}(\mathbf{n}^{(2)}) + \frac{\alpha}{2}\mathrm{Tr}(\mathbf{n}^{(1)})]\mathbf{1} + c_{02}\mathbf{n}^{(2)} + c_{22}(\vec{\mathbf{F}}\mathbf{n}^{(2)}\cdot\vec{\mathbf{F}} + \mathrm{Tr}(\vec{\mathbf{F}}\mathbf{n}^{(2)})\cdot\vec{\mathbf{F}}) + \frac{\beta}{2}\vec{\mathbf{F}}\mathbf{n}^{(1)}\cdot\vec{\mathbf{F}} + \frac{\gamma}{2}\mathbf{U}^{(1)}$, and $\mathbf{I}_c$ is the collisional integral which is neglected in our treatment. (See the derivation and discussion in Appendix.) Here $n^{(1)}_{ab} = \langle\hat{\psi}^\dagger_{1_a}(\vec{r})\hat{\psi}_{1_b}(\vec{r})\rangle_t$ and $U^{(1)}_{ab} = \frac{(-1)^{a+b}}{3}n^{(1)}_{(-a)(-b)}$.

The Heisenberg equation of motion for the condensate reads

$$\begin{aligned} i\hbar\frac{\partial\hat{\psi}_{1_a}}{\partial t} =& -[H,\hat{\psi}_{1_a}] \\ =&[-\frac{\hbar^2}{2m_1}\vec{\nabla}^2+V^i_{trap}(\vec{r})-p_ik+q_ik^2+c_{01}\mathrm{Tr}(\mathbf{n}^{(1)})]\hat{\psi}_{1_a}+c_{21}\langle\vec{\mathbf{F}}\rangle^{(1)}\cdot(\vec{\mathbf{F}}\hat{\psi}_1)_a \\ &+[\frac{\alpha}{2}\mathrm{Tr}(\mathbf{n}^{(2)})+\frac{\beta}{2}\mathrm{Tr}(\vec{\mathbf{F}}\mathbf{n}^{(2)})\cdot\vec{\mathbf{F}}]\hat{\psi}_{1_a}+(\mathbf{U}^{(2)}\hat{\psi}_1)_a, \end{aligned} \tag{4.15}$$

where $\mathbf{n}^{(2)}$ and $\mathbf{U}^{(2)}$ have the same definition as $\mathbf{n}^{(1)}$ and $\mathbf{U}^{(1)}$ with the replacement of ^{23}Na by ^{87}Rb and $\hat{\psi}_1=(\hat{\psi}_{1_{+1}},\hat{\psi}_{1_0},\hat{\psi}_{1_{-1}})^T$.

Starting from Eqs. 4.14 and 4.15, we use the SMA for the condensate in the mean-field limit and a SMA ansatz for the thermal gas to separate the spin dynamics from the spatial degree of freedom: $\hat{\psi}_{1_i}\rightarrow\phi_1(\vec{r})e^{-i\mu_1t/\hbar}\xi_i(t)$ and $g_{ab}(\vec{r},\vec{p},t)=\tilde{g}(\vec{r},\vec{p})\sigma_{ab}(t)$, where $\tilde{g}(\vec{r},\vec{p})$ is a Maxwell distribution of the thermal gas in the harmonic trap. Thus we have $n^{(1)}_{ab}(\vec{r},t)=|\phi(\vec{r})|^2\xi^*_a\xi_b\equiv|\phi(\vec{r})|^2\boldsymbol{\tau}_{ab}(t)$ and $n^{(2)}_{ab}(\vec{r},t)=\frac{1}{(2\pi\hbar)^3}\int d\vec{p}\tilde{g}(\vec{r},\vec{p})\times\sigma_{ab}(t)$ (see section 4.3 for the ansatz of $g_{ab}(\vec{r},\vec{p},t)$). Substituting these expressions into the above equations we could obtain

$$\frac{\partial}{\partial t}\boldsymbol{\sigma}=i[\tilde{\mathbf{M}}_{TG},\boldsymbol{\sigma}], \tag{4.16}$$

$$\frac{\partial}{\partial t}\boldsymbol{\tau}=i[\tilde{\mathbf{M}}_{BEC},\boldsymbol{\tau}], \tag{4.17}$$

where $\tilde{\mathbf{M}}_{TG}=-p_2\mathbf{F}_z+q_2\mathbf{F}_z^2+c_{22}\bar{n}^{(2)}(\vec{\mathbf{F}}\boldsymbol{\sigma}\cdot\vec{\mathbf{F}}+\mathrm{Tr}(\vec{\mathbf{F}}\boldsymbol{\sigma})\cdot\vec{\mathbf{F}})+\frac{\beta}{2}\bar{n}^{(12)}\sqrt{\frac{N_1}{N_2}}\vec{\mathbf{F}}\boldsymbol{\tau}\cdot\vec{\mathbf{F}}+\frac{\gamma}{2}\bar{n}^{(12)}\sqrt{\frac{N_1}{N_2}}\mathbf{U}^{(1)}_\xi$ and $\tilde{\mathbf{M}}_{BEC}=-p_1\mathbf{F}_z+q_1\mathbf{F}_z^2+c_{21}\bar{n}^{(1)}\mathrm{Tr}(\vec{\mathbf{F}}\boldsymbol{\sigma})\cdot\vec{\mathbf{F}}+\frac{\beta}{2}\bar{n}^{(12)}\sqrt{\frac{N_2}{N_1}}\vec{\mathbf{F}}\boldsymbol{\sigma}\cdot\vec{\mathbf{F}}+\frac{\gamma}{2}\bar{n}^{(12)}\sqrt{\frac{N_2}{N_1}}\mathbf{U}^{(2)}_\sigma$. Here $N_i=\int d\vec{r}\mathrm{Tr}(\mathbf{n}^{(i)})$, $\bar{n}^{(i)}=\int d\vec{r}\mathrm{Tr}(\mathbf{n}^{(i)})^2/N_i$, and $\bar{n}^{(12)}=\int d\vec{r}\mathrm{Tr}(\mathbf{n}^{(1)})\mathrm{Tr}(\mathbf{n}^{(2)})/\sqrt{N_1N_2}$. The details of the derivation could be found in the Appendix. Based on these two sets of equations, we could numerically solve the dynamics.

4.2.2 Unique Features of The Spin-mixing Dynamics in The Spin-1 Mixtures

There are several unique features in our system I want to highlight here.

Obviously, one profound feature of the spinor mixtures compared to the single-species spin-1 gases is the additional two-body scattering channel with the total spin 1. Considering the elementary scattering processes in the single-species

Process	Interaction Energy	ΔE_Z
$2\left\|0_{\mathrm{Na}}\right\rangle \leftrightarrow \left\|+1_{\mathrm{Na}}\right\rangle + \left\|-1_{\mathrm{Na}}\right\rangle$	$c_{21}\bar{n}^{(1)}$	$2q_1$
$2\left\|0_{\mathrm{Rb}}\right\rangle \leftrightarrow \left\|+1_{\mathrm{Rb}}\right\rangle + \left\|-1_{\mathrm{Rb}}\right\rangle$	$2c_{22}\bar{n}^{(1)}$	$2q_2$
$\left\|0_{\mathrm{Na}}\right\rangle + \left\|-1_{\mathrm{Rb}}\right\rangle \leftrightarrow \left\|-1_{\mathrm{Na}}\right\rangle + \left\|0_{\mathrm{Rb}}\right\rangle$	$\frac{\beta}{2}\bar{n}^{(12)}$	$p_1 - p_2 + q_1 - q_2$
$\left\|0_{\mathrm{Na}}\right\rangle + \left\|+1_{\mathrm{Rb}}\right\rangle \leftrightarrow \left\|+1_{\mathrm{Na}}\right\rangle + \left\|0_{\mathrm{Rb}}\right\rangle$	$\frac{\beta}{2}\bar{n}^{(12)}$	$-p_1 + p_1 + q_1 - q_2$
$\left\|-1_{\mathrm{Na}}\right\rangle + \left\|+1_{\mathrm{Rb}}\right\rangle \leftrightarrow \left\|+1_{\mathrm{Na}}\right\rangle + \left\|-1_{\mathrm{Rb}}\right\rangle$	$\frac{\gamma}{6}\bar{n}^{(12)}$	$2(-p_1 + p_2)$
$\left\|0_{\mathrm{Na}}\right\rangle + \left\|0_{\mathrm{Rb}}\right\rangle \leftrightarrow \left\|-1_{\mathrm{Na}}\right\rangle + \left\|+1_{\mathrm{Rb}}\right\rangle$	$\frac{\beta+\gamma/3}{2}\bar{n}^{(12)}$	$p_1 - p_2 + q_1 + q_2$
$\left\|0_{\mathrm{Na}}\right\rangle + \left\|0_{\mathrm{Rb}}\right\rangle \leftrightarrow \left\|+1_{\mathrm{Na}}\right\rangle + \left\|-1_{\mathrm{Rb}}\right\rangle$	$\frac{\beta+\gamma/3}{2}\bar{n}^{(12)}$	$-p_1 + p_2 + q_1 + q_2$

Table 4.2: All the possible elementary scattering processes: two homonuclear ones and five heteronuclear ones. The corresponding spin-dependent interaction energies and the changes of the Zeeman energies are also included.

case, only $2\left|0\right\rangle \leftrightarrow \left|-1\right\rangle + \left|1\right\rangle$ are relevant, where $\left|m\right\rangle$ represent the state with the hyperfine spin 1 and magnetic quantum number m ($m = +1, 0, -1$). While in the spinor mixtures, more relevant processes can be driven, like $\left|m^{(1)}, m^{(2)}\right\rangle \leftrightarrow \left|m'^{(1)}, m'^{(2)}\right\rangle$ ($m^{(1)} \neq m^{(2)}, m'^{(1)} \neq m'^{(2)}$), where $m^{(1)} + m^{(2)} = m'^{(1)} + m'^{(2)}$ to conserve the axisymmetry, . Here $m^{(1)}$ ($m^{(2)}$) is the projection of the corresponding hyperfine spin along the magnetic field. As a result, another γ term describing the singlet-pairing processes appears in the spin-dependent interaction Hamiltonian. Also we can easily identify that $\left|+1, -1\right\rangle \leftrightarrow \left|-1, +1\right\rangle$ is only driven by this term, which may be used to measure the value of γ if we can isolate that process. In our system, the values of (α, β, γ) are calculated to be $\frac{4\pi\hbar^2 a_B}{2\mu} \times (78.9, -2.5, 0.06)$. Since $\gamma \ll \beta$, the former would be neglected in our discuss from now on but we keep it in our calculation.

Another important aspect of the spin-1 mixtures is the Zeeman energies, which compete with the spin-dependent interaction energies giving rise to rich spin-mixing dynamics. In the single-species spinor gases, the linear Zeeman term could be gauged out due to the conservation of the magnetization and only the quadratic

Zeeman term is important. However, in our spin-1 mixtures, both the linear and quadratic Zeeman energies are preserved since only the total magnetization is conserved. More profoundly, this feature can be utilized to isolate the heteronuclear spin-mixing processes from the homonuclear ones. To see this point clearly, I list all the possible elementary scattering processes in Table 4.2. There are totally two homonuclear spin-mixing processes and five heteronuclear ones. The corresponding spin-dependent interaction energies and the changes of the Zeeman energies (ΔE_Z) are also shown. To observe significant amplitudes of the spin-mixing processes, the spin-dependent interaction energies should be comparable with ΔE_Z, where the former are typically on the order of $h\times$Hz. ΔE_Z versus the magnetic field (B) are plotted in Fig. 4.3a. At the low fields (B <0.5 G), all the processes are strongly mixed and we expect to observe very complex dynamics. When the magnetic field are gradually increased to more than 1 G, all of the processes are suppressed due to the large ΔE_Z except two heteronuclear processes: $|0_{\rm Na}\rangle + |-1_{\rm Rb}\rangle \leftrightarrow |-1_{\rm Na}\rangle + |0_{\rm Rb}\rangle$ and $|0_{\rm Na}\rangle + |0_{\rm Rb}\rangle \leftrightarrow |-1_{\rm Na}\rangle + |+1_{\rm Rb}\rangle$. A zero-crossing of ΔE_Z located around 1.691 G (0.99 G) is identified and marked (pink circle) in the figure for the former (later) process. These two points give us the possibility to isolate the heteronuclear processes and simplify the dynamics.

The last interesting feature is the possibility of controlling the heteronuclear spin mixing with the species-dependent vector light shifts [141]. The quantum control of spinor dynamics using microwaves has been successfully demonstrated with single-species gases [211, 212] and this powerful technique has many applications, such as exploring the spin fluctuations [213], quenching the system through the quantum phase transition point [214], and studying the phase diagram [215]. Optical method has also been proposed for the single-species spinor gases by utilizing the tensor light shifts [216]. Since all of these methods deal with the quadratic Zeeman energy q, typically large Rabi frequencies induced by the microwave or optical fields are necessary to provide enough shifts of q, which may short the lifetimes of the trapped gases. As a comparison, we can play with the species-dependent linear Zeeman energies in a spin-1 mixture and thus it is much easier to be implemented in experiments. Actually a simple tuning of the polarizability of the trapping light is afforded to induce significant changes of the vector light shifts, which can be regarded as being induced by a effective magnetic field along the real external field direction. In next subsection, we would show that this effect is much more profound for ^{87}Rb by a factor of two orders of magnitude. An example is shown in Fig.

4.3b, where the tunability of ΔE_Z for the process $|0_{\mathrm{Na}}\rangle + |-1_{\mathrm{Rb}}\rangle \leftrightarrow |-1_{\mathrm{Na}}\rangle + |0_{\mathrm{Rb}}\rangle$ by the effective field is demonstrated. In the figure B_{eff} is only for ^{87}Rb, which can change the position of the zero-crossing. It can be pushed from the original position (1.691 G) to a either higher or lower field. On the lower-field side, it even vanishes when $B_{eff} < -0.21\,\mathrm{mG}$.

Figure 4.3: The changes of the Zeeman energies (ΔE_Z) associated with the elementary scattering processes versus the magnetic field (B) as well as the influence of the effective field (B_{eff}).

(a) ΔE_Z versus B. The ^{23}Na and ^{87}Rb states are indicated with the orange and magenta color, respectively. Totally 7 different curves are included, where 2 of them are for the homonuclear spin-mixing processes (dashed lines) and the others are for the heteroculear case (solid lines). Two zero-crossings are marked using pink circles.

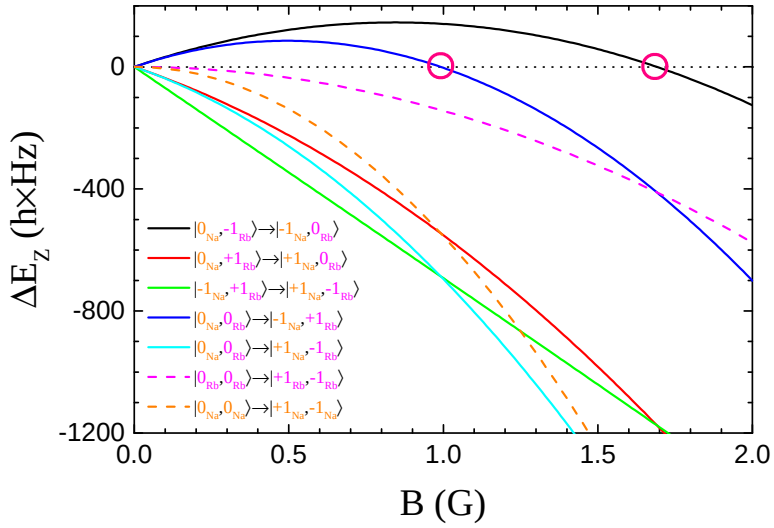

(b) The influence of B_{eff} on ΔE_Z of the process $|0_{\rm Na}\rangle + |-1_{\rm Rb}\rangle \leftrightarrow |-1_{\rm Na}\rangle + |0_{\rm Rb}\rangle$. B_{eff} is on the order of 0.1 mG. See text for details.

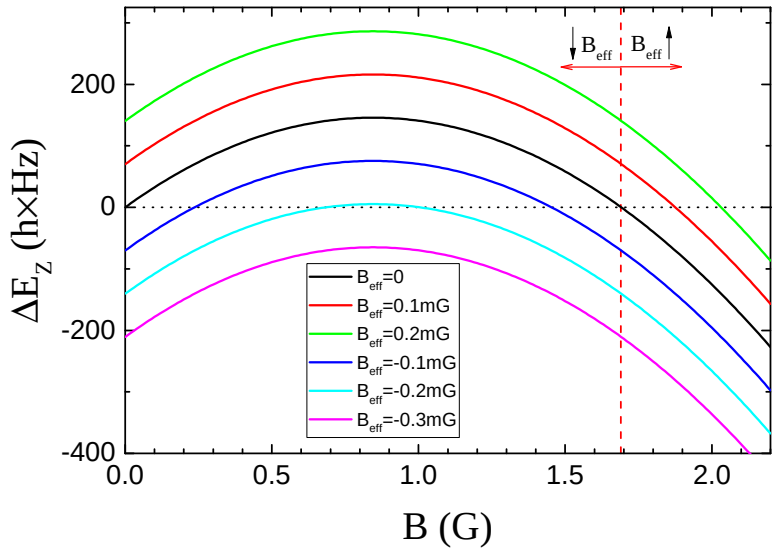

4.2.3 Experimental Observations

Based on above considerations, it is promising to cleanly observe the process $|0_{\mathrm{Na}}\rangle + |-1_{\mathrm{Rb}}\rangle \leftrightarrow |-1_{\mathrm{Na}}\rangle + |0_{\mathrm{Rb}}\rangle$ around 1.691 G, where other processes are suppressed. What' s more, we could control this process via the vector light shifts.

A Simplified Model

Before we discuss the experimental details, let me introduce simplified equations for the dynamics where only the above process happens. The spin-dependent Hamiltonian in this case reads

$$\begin{aligned} H = \int d\vec{r}\{&\hat{\psi}^\dagger_{1_{-1}}(\vec{r})(p_1+q_1)\hat{\psi}_{1_{-1}}(\vec{r}) + \hat{\psi}^\dagger_{2_{-1}}(\vec{r})(p_2+q_2)\hat{\psi}_{2_{-1}}(\vec{r}) \\ &+ \frac{\beta}{2}[\hat{\psi}^\dagger_{1_0}(\vec{r})\hat{\psi}^\dagger_{2_{-1}}(\vec{r})\hat{\psi}_{2_0}(\vec{r})\hat{\psi}_{1_{-1}}(\vec{r}) + \hat{\psi}^\dagger_{1_{-1}}(\vec{r})\hat{\psi}^\dagger_{2_0}(\vec{r})\hat{\psi}_{2_{-1}}(\vec{r})\hat{\psi}_{1_0}(\vec{r})]\}. \end{aligned} \tag{4.18}$$

The Heisenberg equation of motion reads

$$i\hbar\frac{\partial}{\partial t}\hat{\psi}_{1_0} = \frac{\beta}{2}\hat{\psi}^\dagger_{2_{-1}}\hat{\psi}_{2_0}\hat{\psi}_{1_{-1}}; \tag{4.19}$$

$$i\hbar\frac{\partial}{\partial t}\hat{\psi}_{1_{-1}} = (p_1+q_1)\hat{\psi}_{1_{-1}} + \frac{\beta}{2}\hat{\psi}^\dagger_{2_0}\hat{\psi}_{2_{-1}}\hat{\psi}_{1_0}; \tag{4.20}$$

$$i\hbar\frac{\partial}{\partial t}\hat{\psi}_{2_0} = \frac{\beta}{2}\hat{\psi}^\dagger_{1_{-1}}\hat{\psi}_{2_{-1}}\hat{\psi}_{1_0}; \tag{4.21}$$

$$i\hbar\frac{\partial}{\partial t}\hat{\psi}_{2_{-1}} = (p_2+q_2)\hat{\psi}_{2_{-1}} + \frac{\beta}{2}\hat{\psi}^\dagger_{1_0}\hat{\psi}_{2_0}\hat{\psi}_{1_{-1}}. \tag{4.22}$$

Of course we could employ the Boltzmann transport equation for the thermal gas and the G-P equation for the BEC to obtain the coupled differential equations. However, it is equivalent to replace the annihilation and creation operators with their means with the SMA which would give

$$\begin{aligned} i\hbar\dot{\xi}_0 &= \frac{\beta\bar{n}^{(12)}}{2}\sqrt{N_2/N_1}\eta^*_{-1}\eta_0\xi_{-1}, \\ i\hbar\dot{\xi}_{-1} &= (p_1+q_1)\xi_{-1} + \frac{\beta\bar{n}^{(12)}}{2}\sqrt{N_2/N_1}\eta^*_0\eta_{-1}\xi_0, \\ i\hbar\dot{\eta}_0 &= \frac{\beta\bar{n}^{(12)}}{2}\sqrt{N_1/N_2}\xi^*_{-1}\xi_0\eta_{-1}, \\ i\hbar\dot{\eta}_{-1} &= (p_2+q_2)\eta_{-1} + \frac{\beta\bar{n}^{(12)}}{2}\sqrt{N_1/N_2}\xi^*_0\xi_{-1}\eta_0, \end{aligned} \tag{4.23}$$

where N_1 is the atom number and $|\xi_0|^2 + |\xi_{-1}|^2 = 1$ for ^{23}Na, and N_2 is also the atom number and $|\eta_0|^2 + |\eta_{-1}|^2 = 1$ for ^{87}Rb. Introducing $\xi_0 = \sqrt{\rho_1}e^{i\theta_0}, \xi_{-1} =$

$\sqrt{1-\rho_1}e^{i\theta_{-1}}, \eta_0 = \sqrt{\rho_2}e^{i\alpha_0}, \eta_{-1} = \sqrt{1-\rho_2}e^{i\alpha_{-1}}$, and $\theta = \alpha_0 - \alpha_{-1} - \theta_0 + \theta_{-1}$, we could obtain

$$\begin{aligned} N_1\dot{\rho_1} = -N_2\dot{\rho_2} &= \frac{\beta\bar{n}^{(12)}\sqrt{N_1N_2}}{\hbar}\sqrt{\rho_1(1-\rho_1)\rho_2(1-\rho_2)}\sin\theta, \\ \dot{\theta} &= \frac{p_2 - p_1 + q_2 - q_1}{\hbar} + \frac{\beta\bar{n}^{(12)}}{2\hbar}\frac{N_1\rho_1(1-\rho_1)(2\rho_2-1) - N_2\rho_2(1-\rho_2)(2\rho_1-1)}{\sqrt{N_1N_2\rho_1(1-\rho_1)\rho_2(1-\rho_2)}}\cos\theta. \end{aligned} \tag{4.24}$$

So the quantity $m = N_1\rho_1 + N_2\rho_2$ is conserved due to the conservation of the total magnetization $(N_1 + N_2 - m)$. Then by introducing $\rho = N_1\rho_1 - N_2\rho_2$ we could rewrite the equations as

$$\begin{aligned} \dot{\rho} =& \frac{\beta\bar{n}^{(12)}}{2\hbar\sqrt{N_1N_2}}\sqrt{(m^2-\rho^2)(2N_1-\rho-m)(2N_2+\rho-m)}\sin\theta, \\ \dot{\theta} =& \frac{p_2 - p_1 + q_2 - q_1}{\hbar} + \\ & \frac{\beta\bar{n}^{(12)}}{2\hbar\sqrt{N_1N_2}}\frac{(\rho+m)(2N_1-\rho-m)(m-\rho-N_2) - (m-\rho)(2N_2-m+\rho)(\rho+m-N_1)}{\sqrt{(m^2-\rho^2)(2N_1-\rho-m)(2N_2+\rho-m)}}\cos\theta. \end{aligned} \tag{4.25}$$

These two coupled equations is quite similar to those in Eq. 4.5 and following the treatment there we could conclude that ρ oscillates periodically and a resonance of the oscillation may be observed. Actually analytic solutions for ρ could be obtained using the elliptic integral [207]. However, here the involved Zeeman energy $p_2-p_1+q_2-q_1$ could be either positive or negative and we expect to have two resonances where the oscillation period and amplitude have local maximums [116].

The Initial State and Interaction Parameters

It is idea that we could prepare a initial state like $(\sqrt{1-\rho_0}, \sqrt{\rho_0}e^{i\theta_0}, 0)$ $(0 < \rho_0 < 1)$ for both species, where the state is represented by the spin configuration. However, it is impossible to do this with a simple spin rotation described in the subsection 2.5.2. Our scheme is to keep the population of $m_f = +1$ as small as possible: Rotate the spin starting from $(0, 0, 1)$ $(|f = 1, m_f = -1\rangle)$ by a RF pulse with the pulse area of $\pi/3$ to $(-1/4, -i\sqrt{6}/4, 3/4)$. This gives the initial conditions for $\boldsymbol{\sigma}$ and $\boldsymbol{\tau}$:

$$\boldsymbol{\sigma}(0) = \boldsymbol{\tau}(0) = \begin{pmatrix} 1/16 & i\sqrt{6}/16 & -3/16 \\ -i\sqrt{6}/16 & 3/8 & i3\sqrt{6}/16 \\ -3/16 & -i3\sqrt{6}/16 & 9/16 \end{pmatrix}. \tag{4.26}$$

Also the initial conditions of Eq. 4.25 are given to be $\rho(0) = \frac{3}{8}(N_1 - N_2), m = \frac{3}{8}(N_1 + N_2)$, and $\theta = 0$ respectively.

Typically we have $N_1 = 1.0 \times 10^5$ and $N_1 = 6.3 \times 10^4$. In the final trap, the measured trap frequencies for ^{23}Na and ^{87}Rb are $2\pi \times (98, 190, 168)$ Hz and $2\pi \times (110, 215, 190)$ Hz respectively. The temperature of the ^{87}Rb thermal gas is measured to be $\sim$100 nK above its BEC transition temperature. We assume a Thomas-Fermi distribution for the ^{23}Na condensate and a Gaussian distribution for the ^{87}Rb thermal gas. The mean densities are calculated to be $\bar{n}^{(1)} = 5.9 \times 10^{13}$ cm^{-3} and $\bar{n}^{(2)} = 6.5 \times 10^{12}$ cm^{-3}. Taking the gravitational sag of the two atomic clouds into consideration, we have also determined the density overlap $\bar{n}^{(12)}$ to be 1.2×10^{13} cm^{-3}. Then $c_{21}\bar{n}^{(1)} = h\times 14.19$ Hz, $c_{22}\bar{n}^{(2)} = -h\times 0.18$ Hz, $\beta\bar{n}^{(12)} = -h\times 5.54$ Hz, and $\gamma\bar{n}^{(12)} = h\times 0.13$ Hz.

Coherent Heteronuclear Spin-mixing Dynamics

By varying the holding time in our FORT with the above initial states and detecting the spin populations with a species-dependent Stern-Gerlach experiment, we could obtain the time evolution of the spin populations. An example at a magnetic field of 1.9 G is given in Fig. 4.4, where nearly three periods of oscillation are shown. Every point in the figure is an average of three measurements. We could clearly see that the fractional population, $N_{i_{m_f}}/N_i$ $(i = 1, 2)$, periodically oscillates between $m_f = -1$ and $m_f = 0$ sub-levels for both species. The population of $m_f = +1$ keeps almost constant during the evolution. We also show the time evolution of the fractional magnetizations defined as $(N_{i_{+1}} - N_{i_{-1}})/N_i$ $(i = 1, 2)$, where out-of-phase oscillations are observed. From the data we could say we have observed coherent heteronuclear spin-mixing dynamics. The conservation of the total fractional magnetization $(N_{1_{+1}} + N_{2_{+1}} - N_{1_{-1}} - N_{2_{-1}})/(N_1 + N_2)$ is shown on the bottom of Fig. 4.4, where the small fluctuation on the order of 0.01 is due to the uncertainty of our preparation of the initial states.

We have systematically measured this dynamics with magnetic fields ranging from 1.0 G to 2.1 G, where the corresponding ΔE_Z $(p_2 - p_1 + q_2 - q_1)$ varies from $h\times 140.85$ Hz to $-h\times 174.28$ Hz monotonically. Close to the lower bound, other two processes may be involved due to the small ΔE_z, namely $2\,|0_{\rm Rb}\rangle \leftrightarrow |+1_{\rm Rb}\rangle + |-1_{\rm Rb}\rangle$ and $|0_{\rm Na}\rangle + |0_{\rm Rb}\rangle \leftrightarrow |-1_{\rm Na}\rangle + |+1_{\rm Rb}\rangle$. However, the oscillation amplitudes would be limited by the relative large ΔE_z and the small ^{87}Rb $m_f = +1$ population for the

former process. In the latter case, the oscillation periods would be large compared to those of the interested process and also their amplitudes are limited by the small ^{87}Rb $m_f = +1$ population. On the other hand, the dynamics is expected to agree more with the simplified model described in Eq. 4.25 when we are close to the upper bound. The experimental results as well as the theoretical calculations of the magnetic-field dependence of the dynamics are shown in Fig. 4.5.

The spin population oscillations at three different magnetic fields, 1.5 G,1.7 G, and 1.9 G, are compared in Fig. 4.5**a**. Near the zero-crossing, both the oscillation period and amplitude become larger than those at fields away from the zero-crossing. We also note that the initial phase of the oscillation is changed by π when the magnetic field crosses some critical point. We could understand it from the simplified model in Eq. 4.25, where the initial phase of the oscillation of the population of the ^{23}Na $m_f = 0$ state or the ^{87}Rb $m_f = -1$ state is same as that of ρ. Since $\beta < 0$, the initial phase is solely determined by $\sin[\theta(\Delta t)]$ ($\Delta t \ll 1$), hence $\frac{p_2-p_1+q_2-q_1}{\hbar} + \frac{\beta\bar{n}^{(12)}}{2\hbar\sqrt{N_1N_2}} \frac{(\rho(0)+m)(2N_1-\rho(0)-m)(m-\rho(0)-N_2)-(m-\rho(0))(2N_2-m+\rho(0))(\rho(0)+m-N_1)}{\sqrt{(m^2-\rho(0)^2)(2N_1-\rho(0)-m)(2N_2+\rho(0)-m)}}$. This quantity would change sign at some critical field, 1.692 G in our case. For real experiments the critical field is at ∼1.655 G. Significant damping of the oscillation is observed at all fields. So the data is fitted with a damped sinusoidal function to extract the oscillation period and amplitude, as well as the damping time constant, of which we don't have any good understanding now.

In Figs. 4.5**b** and 4.5**c**, we summarize the oscillation period and amplitude at different magnetic fields respectively. Also we show the simulation results of the full and simplified many-body model. We have identified one peak for the oscillation period at ∼1.65 G, near which the time evolution curve becomes non-sinusoidal. For the oscillation amplitude, the data suggests two local maximums and one local minimum in between them. We could recover these features qualitatively from our simplified model. However, the quantitative deviations become severe near the zero-crossing. Specifically, it looks like that those maximum and minimum positions are shifted left in the real experiments. This could be captured partly within our full many-body model, where the divergence of the oscillation period at the resonance in the simplified model disappears. A small kink of the oscillation period appears on the right side of the resonance in both models, which is hard to be confirmed in experiments. The two-peak feature of the oscillation amplitude is consistent between both models and the experiment, while the experimental data lies higher than the theoretical curves.

Figure 4.4: Coherent heteronuclear spin-mixing dynamics at 1.9 G. The top two figures show the fractional spin populations (left) and fraction magnetization (right) oscillations of ^{87}Rb. Open orange squares, open red circles, and open olive triangles are for m_f =-1, 0, and +1, respectively. The middle two figures are for ^{23}Na and the shape code is similar as the top figures. The bottom figure shows the total fractional magnetization. The solid curves are for eye guiding and the error bars are from statistics of three measurements.

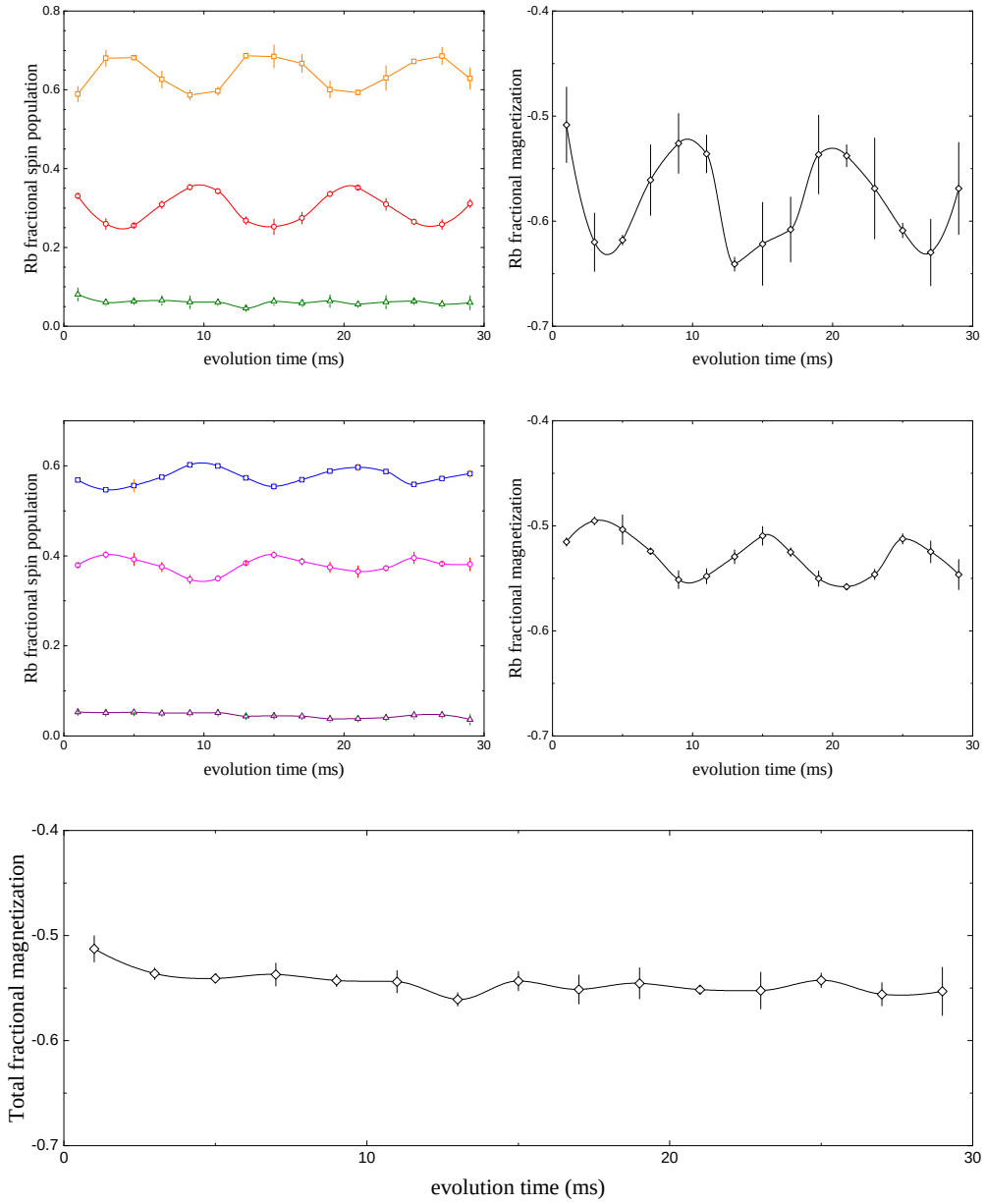

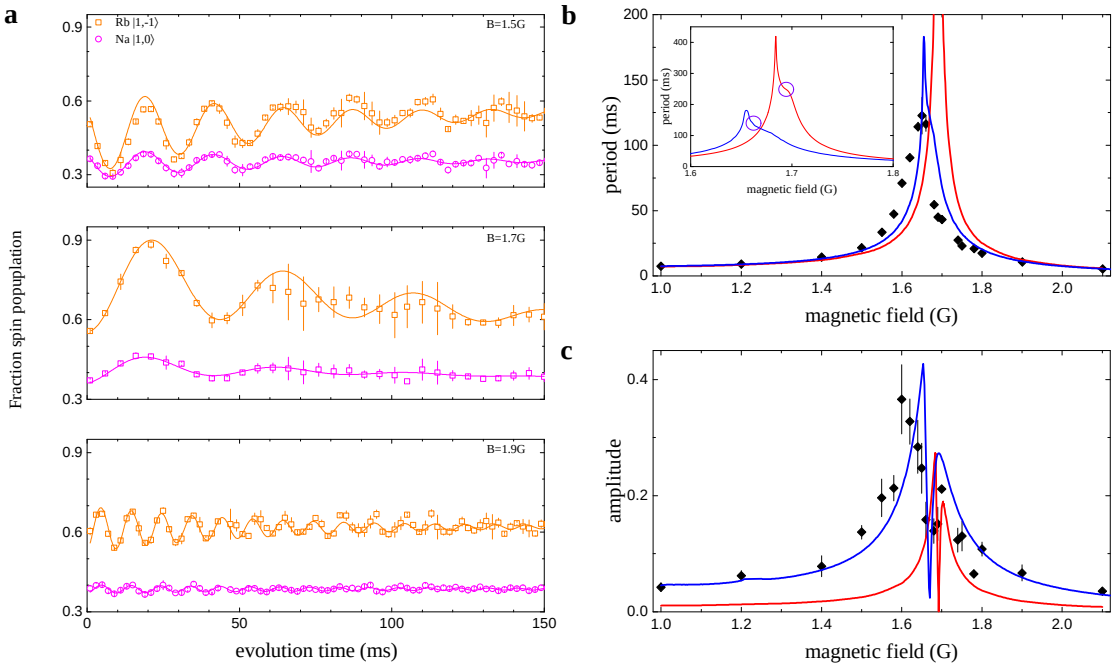

Figure 4.5: The magnetic-field dependence of the coherent heteronuclear spin-mixing dynamics. **a**, The time evolution of the fractional spin populations of the ^{87}Rb $m_f = -1$ state (open orange circles) and the ^{23}Na $m_f = 0$ state (open magenta squares) at magnetic fields of 1.5 G, 1.7 G and 1.9 G. The solid curves are fits to a damped sinusoidal function and the error bars are from statistics of several experimental shots. **b** and **c**, The oscillation period and amplitude versus the magnetic field (black rhombuses). Solid blue (red) curve is the simulation result based on the full (simplified) many-body equations and the error bars are from the fitting uncertainties. A kink appears for the oscillation period in both models which are indicated by violet circles.

4.2.4 Vector-light-shift Control of The Dynamics

The light shift of the atomic state $|f, m_f\rangle$ in an optical electric field $E(\vec{r}) = \hat{\epsilon}E_+(\vec{r})e^{-i\omega t} + c.c.$ can be expresses as [140]

$$U(f, m_f; \omega) = -\alpha_0(f;\omega)|E_+|^2 - \alpha_1(f;\omega)(i\vec{E}_- \times \vec{E}_+)_z \frac{m_f}{f} + \alpha_2(f;\omega)\frac{3|E_{+_z}|^2 - |E_+|^2}{2}\frac{3m_f^2 - f(f+1)}{f(2f-1)}, \tag{4.27}$$

where $\hat{\epsilon}$ is the unit polarization vector and $\vec{E}_{+(-)} = \hat{\epsilon}E_{+(-)}$. The magnetic field is along the z direction. α_0, α_1, and α_2 are called scalar, vector, and tensor polarizability respectively. The expressions for them are

$$\begin{aligned}
\alpha_0(f;\omega) &= \sum_{f'} \frac{2\omega_{f'f}\left|\langle f|\,\vec{d}\,|f'\rangle\right|^2}{3\hbar(\omega_{f'f}^2 - \omega^2)} \\
&\approx \sum_{J'} \frac{2\omega_{J'J}\left|\langle J|\,\vec{d}\,|J'\rangle\right|^2}{3\hbar(\omega_{J'J}^2 - \omega^2)}, \\
\alpha_1(f;\omega) &= \sum_{f'} (-1)^{f+f'+1}\sqrt{\frac{6f(2f+1)}{f+1}}\begin{Bmatrix} 1 & 1 & 1 \\ f & f & f' \end{Bmatrix}\frac{\omega_{f'f}\left|\langle f|\,\vec{d}\,|f'\rangle\right|^2}{\hbar(\omega_{f'f}^2 - \omega^2)} \\
&\approx \sum_{J'} (-1)^{-2J-J'-f-I+1}\sqrt{\frac{6f(2f+1)}{f+1}}(2J+1)\begin{Bmatrix} 1 & 1 & 1 \\ J & J & J' \end{Bmatrix}\begin{Bmatrix} J & J & 1 \\ f & f & I \end{Bmatrix}\frac{\omega_{J'J}\left|\langle J|\,\vec{d}\,|J'\rangle\right|^2}{\hbar(\omega_{J'J}^2 - \omega^2)}, \\
\alpha_2(f;\omega) &= \sum_{J'} (-1)^{f+f'}\sqrt{\frac{40f(2f+1)(2f-1)}{3(f+1)(2f+3)}}\begin{Bmatrix} 1 & 1 & 2 \\ f & f & f' \end{Bmatrix}\frac{\omega_{f'f}\left|\langle f|\,\vec{d}\,|f'\rangle\right|^2}{\hbar(\omega_{f'f}^2 - \omega^2)} \\
&\approx \sum_{J'} (-1)^{-2J-J'-f-I}\sqrt{\frac{40f(2f+1)(2f-1)}{3(f+1)(2f+3)}}(2J+1)\begin{Bmatrix} 1 & 1 & 2 \\ J & J & J' \end{Bmatrix}\begin{Bmatrix} J & J & 2 \\ f & f & I \end{Bmatrix} \\
&\quad \times \frac{\omega_{J'J}\left|\langle J|\,\vec{d}\,|J'\rangle\right|^2}{\hbar(\omega_{J'J}^2 - \omega^2)}.
\end{aligned} \tag{4.28}$$

Here $\begin{Bmatrix} \cdots \end{Bmatrix}$ is the Wigner $6-j$ symbol. The approximation results are obtained for large detuning case, which coincides with our case of ^{23}Na and ^{87}Rb atoms in the 1064 nm optical dipole trap. We only consider the D-lines for the above summation and the non-scalar light shifts of ^{23}Na atoms are neglected due to their much larger detuning. The exact values are $\alpha_1^{\mathrm{Rb}}(1;\omega) = -1.25 \times 10^{-40}\,\mathrm{C}\cdot\mathrm{m}^2/\mathrm{V}$ and $\alpha_1^{\mathrm{Na}}(1;\omega) = -1.19 \times 10^{-42}\,\mathrm{C}\cdot\mathrm{m}^2/\mathrm{V} \ll \alpha_1^{\mathrm{Rb}}(1;\omega)$.

Let's omit the tensor part from now on. Generally, $\hat{\epsilon} = \begin{pmatrix} \cos\theta \\ \sin\theta e^{i\gamma} \end{pmatrix}$ using the Jones vector. $\gamma = 0$ is corresponding to the linearly polarized light. $\theta = \pi/4$ and $\gamma = \pm\pi/2$ are for the $\sigma^{\pm}$ light. We have $i\vec{E}_- \times \vec{E}_+ = -|E_+|^2 \sin 2\theta \sin\gamma \hat{k}$ where $\hat{k}$ is the unit vector along the propagating direction. With our trapping light propagating in the horizontal plane, the vector light shift is always zero in a vertical magnetic field. Only when the polarization contains circular part and the magnetic field is set in the horizontal plane, the vector light shift is nonzero. In our experiments, we have inserted a quarter wave-plate into one of the beam paths of our crossed optical trap to control the polarization of it. The direction of the magnetic field is changed from the vertical axis to the horizontal plane along the imaging path. So the angle ϕ between the light propagating direction and z axis is 30.5°. The vector light shift reads $\alpha_1^{\mathrm{Rb}}(1;\omega) \sin 2\theta \sin\gamma \cos\phi |E_+|^2 m_f/f$. In our setup, we have $\gamma = \pi/2$ and θ is controlled by the wave-plate. This vector light shift is effectively a linear Zeeman energy corresponding to a effective magnetic field $B_{\mathrm{ac}} = \frac{\alpha_1^{\mathrm{Rb}}(1;\omega) \sin 2\theta \cos\phi |E_+|^2}{f g_f \mu_B}$.

The experimental results are shown in Fig. 4.6, where we have demonstrated the controllability with effective magnetic fields (B_{ac}) of $-0.32\,\mathrm{mG}$, $-0.16\,\mathrm{mG}$, $-0.08\,\mathrm{mG}$, $0\,\mathrm{mG}$, $0.16\,\mathrm{mG}$, and $0.32\,\mathrm{mG}$. As we have seen in the subsection 4.2.2, the zero-crossing of ΔE_Z is pushed to the higher (lower) field side with positive (negative) B_{ac}. It eventually vanishes for $B_{\mathrm{ac}} < -0.21\,\mathrm{mG}$. This feature is recalled in Fig. 4.6**a** where five out of our six B_{ac} still have zero-crossings (dashed vertical lines) and $\Delta E_Z \leq -\hbar \times 79\,\mathrm{Hz}$ for $B_{\mathrm{ac}} = -0.32\,\mathrm{mG}$. So the resonant feature of the oscillation period vanishes in this case and the system behaves like a off-resonantly driven two-level model: $T \approx h/|\Delta E_Z|$ and only a wide peak appears. With other five B_{ac}, we still have narrower peaks and the peak positions are changed according to the positions of the zero-crossing.

4.2.5 Summary

In summary, we have observed the heteronuclear spin-mixing dynamics for the first time and the magnetic-field dependence of one such process has also been investigated. One-peak structure and two-peak structure are identified in the oscillation period and amplitude, respectively. They are compared with a many-body theory as well as a simplified model and we have found good agreements

qualitatively and partially quantitatively. We also demonstrated a new tool to control the dynamics in spinor gases, namely the vector light shift. This work has been published in [120] where I was the second author. I mainly contributed to the data collection and analysis and the effect of the vector light shift was also suggested by me.

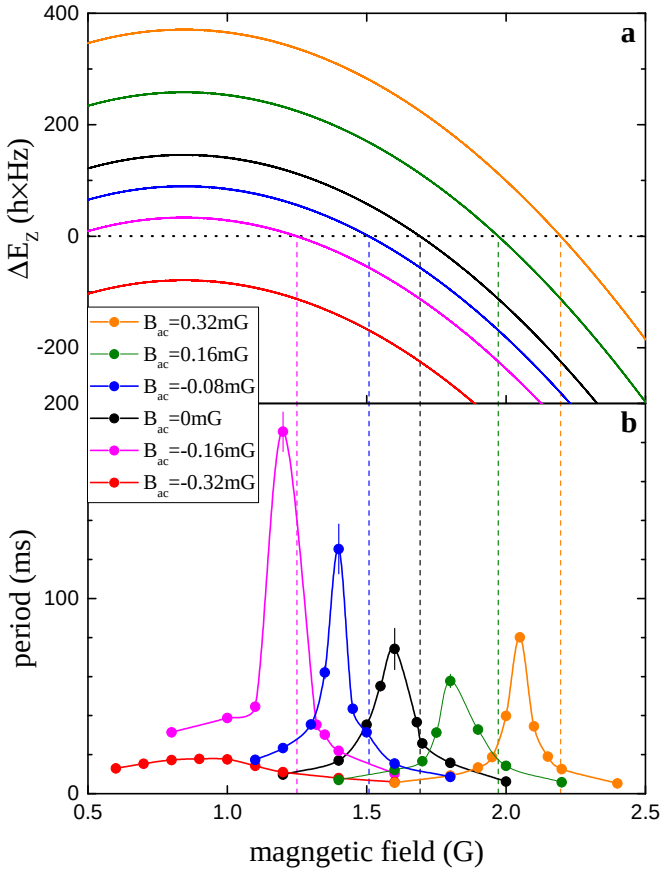

Figure 4.6: The quantum control of the heteronuclear spin-mixing dynamics with the species-dependent vector light shifts. **a**, We recall the tuning of ΔE_Z with $B_{\mathbf{ac}}$ of $-0.32\,\mathrm{mG}$ (solid red curve), $-0.16\,\mathrm{mG}$ (solid magenta curve), $-0.08\,\mathrm{mG}$ (solid blue curve), $0\,\mathrm{mG}$ (solid black curve), $0.16\,\mathrm{mG}$ (solid olive curve), and $0.32\,\mathrm{mG}$ (solid orange curve). The zero-crossings are indicated by vertical dashed lines. **b**, The tuning of magnetic-dependence of the oscillation period with B_{ac}. The solid curves are guiding for eye.

4.3 Thermal Spinor Gases of ^{87}Rb

In this section, I would like to present our study of normal spinor gases, also focusing on the coherent spin-mixing dynamics. Specifically, we have systematically studied the magnetic-field dependence of the coherent spin-mixing dynamics of the ^{87}Rb spin-1 and spin-2 normal gases. In both cases we have identified a resonance where the spin-dependent interaction energy is comparable with the quadratic Zeeman energy. To understand the dynamics a Boltzmann transport equation is used and we find good agreements between the experiment and the theory.

4.3.1 Theory For The Normal Spinor Gases

As we have done in the previous section, a Boltzmann transport equation is needed to describe the normal spinor gases. Let' s recall the general equation in Eq. 4.14:

$$\frac{\partial}{\partial t}\mathbf{G} + \frac{\vec{p}}{m}\cdot\vec{\nabla}_{\vec{r}}\mathbf{G} = i[\mathbf{M},\mathbf{G}] + \frac{1}{2}\{\vec{\nabla}_{\vec{r}}\mathbf{M},\vec{\nabla}_{\vec{p}}\mathbf{G}\} + \mathbf{I}_c, \tag{4.29}$$

where similarly $\mathbf{G}$ is the Wigner density matrix and $\mathbf{I}_c$ is the collisional integral. The interaction potential, $\mathbf{M}$, reads $q\mathbf{F}_z^2 + [V_{trap} + c_0\mathrm{Tr}(\mathbf{n})]\mathbf{1} + c_0\mathbf{n} + c_2[\vec{\mathbf{F}}\mathbf{n}\cdot\vec{\mathbf{F}} + \mathrm{Tr}(\vec{\mathbf{F}}\mathbf{n})\cdot\vec{\mathbf{F}}] + 2c_4\mathbf{U}$. Here q term is the quadratic Zeeman energy, V_{trap} is the trapping potential, $\mathbf{n}$ is the matrix of the atomic density, and c_0, c_2 and c_4 are the spin-independent interaction coefficient, the spin-exchange interaction coefficient and the singlet-pairing coefficient. The factor of 2 appears in front of the singlet-pairing term is due to the equal contribution from the Hartree and Fock terms. For spin-1 gases, this term vanishes with $c_4 = 0$.

The idea of SMA, decoupling the spins from the external motions, can be generalized to the normal spinor gases under proper experimental conditions. In the case of a condensate, the SMA requires that the condensate size is much smaller than the spin healing length $2\pi\hbar/\sqrt{2m|c_2|n}$ as well as the magnetic healing length $2\pi\hbar/\sqrt{2m|q|n}$. In the normal gases, if the spatial motion of atoms is much faster than the internal dynamics, namely $\omega_{x,y,z} \gg c_2 n$ and q, we could remove the external motion by averaging the Wigner density matrix over the trap oscillation. In this case, we could make the ansatz

$$g_{ab}(\vec{r},\vec{p},t) = \exp\left\{-\frac{\vec{p}^2/2m + V_{trap}(\vec{r})}{k_bT}\right\}\sigma_{ab}(t)/Z,$$

where Z is chosen such that $\mathrm{Tr}(\boldsymbol{\sigma}) = 1$ and $\int d\vec{p}d\vec{r}\mathrm{Tr}[\mathbf{G}(\vec{r},\vec{p},t)]/(2\pi\hbar)^3 = N$. Here T is the temperature and N is the total atom number. The matrix of the atomic density is reduced to $n_{ab}(\vec{r},t) = (\frac{mk_bT}{2\pi\hbar^2})^{3/2}\exp\Big\{-\frac{V_{trap}(\vec{r})}{k_bT}\Big\}\sigma_{ab}(t)/Z$. Substituting this ansatz into the transport equation we have

$$\dot{\boldsymbol{\sigma}} = i[\mathbf{M},\boldsymbol{\sigma}] = i[\tilde{\mathbf{M}},\boldsymbol{\sigma}], \tag{4.30}$$

where $\tilde{\mathbf{M}} = q\mathbf{F}_z^2 + c_2\bar{n}[\vec{\mathbf{F}}\boldsymbol{\sigma}\cdot\vec{\mathbf{F}} + \mathrm{Tr}(\vec{\mathbf{F}}\boldsymbol{\sigma})\cdot\vec{\mathbf{F}}] + 2c_4\bar{n}\mathbf{U}_\sigma$ with $\bar{n} = \int d\vec{r}\mathrm{Tr}(\mathbf{n})^2/N$.

In the spin-1 case, it is easy to explicitly show that $\vec{\mathbf{F}}\mathbf{A}\cdot\vec{\mathbf{F}} - \mathrm{Tr}(\vec{\mathbf{F}}\mathbf{A})\cdot\vec{\mathbf{F}} = \mathrm{Tr}(\mathbf{A}) - \mathbf{A}$ for any 3×3 matrix $\mathbf{A}$. So we have $[\vec{\mathbf{F}}\boldsymbol{\sigma}\cdot\vec{\mathbf{F}},\boldsymbol{\sigma}] = [\mathrm{Tr}(\vec{\mathbf{F}}\boldsymbol{\sigma})\cdot\vec{\mathbf{F}},\boldsymbol{\sigma}]$ and $\tilde{\mathbf{M}} = q\mathbf{F}_z^2 + 2c_2\bar{n}\mathrm{Tr}(\vec{\mathbf{F}}\boldsymbol{\sigma})\cdot\vec{\mathbf{F}}$. This would give rise to the coincidence of the equation of motion for normal gases and condensates except for the factor of 2 appearing in front of the spin-dependent interaction term in the former case. In Ref. [118], this has been experimentally verified with a ^{23}Na spin-1 normal gas. Here we could provide further experimental evidence by exploring the ^{87}Rb spin-1 normal gas.

In the spin-2 case, we don't have $\vec{\mathbf{F}}\mathbf{A}\cdot\vec{\mathbf{F}} - \mathrm{Tr}(\vec{\mathbf{F}}\mathbf{A})\cdot\vec{\mathbf{F}} = \mathrm{Tr}(\mathbf{A}) - \mathbf{A}$ in general. However, if $A_{ab} = B_aC_b$ where $\vec{B}$ and $\vec{C}$ are vectors, we still have $[\vec{\mathbf{F}}\mathbf{A}\cdot\vec{\mathbf{F}},\mathbf{A}] = [\mathrm{Tr}(\vec{\mathbf{F}}\mathbf{A})\cdot\vec{\mathbf{F}},\mathbf{A}]$. In our case, the spin matrix $\boldsymbol{\sigma}$ could be written as $\boldsymbol{\sigma} = \xi\xi^\dagger$ where ξ is the atomic spin state and thus $[\vec{\mathbf{F}}\boldsymbol{\sigma}\cdot\vec{\mathbf{F}},\boldsymbol{\sigma}] = [\mathrm{Tr}(\vec{\mathbf{F}}\boldsymbol{\sigma})\cdot\vec{\mathbf{F}},\boldsymbol{\sigma}]$. We arrive at the same conclusion as that in the spin-1 case. Experimentally we have confirmed the factor of 2 directly in the spin-2 case by measuring the relation between the oscillation amplitude and the atomic density in the regime of dominated quadratic Zeeman energy.

4.3.2 Experimental Observations

Experimental Procedures and Initial Conditions

We start with pure thermal gases of $|f=1,m_f=-1\rangle$ atoms with a total atom number of $3.0(3)\times10^5$. The measured final trap frequencies are $(\omega_x,\omega_y,\omega_z) = 2\pi\times(150,172,75)\,\mathrm{Hz}$ and the temperature is just $\sim$50 nK above the BEC transition. Thus the typical atomic mean density $\bar{n} = 3.0\times10^{13}\,\mathrm{cm}^{-3}$.

To investigate the spin-1 case, we initialize the spin dynamics by directly applying a resonant RF $\pi/2$-pulse to transfer the sample to the fully transversely magnetized initial state $\xi = (\frac{1}{2},\frac{1}{\sqrt{2}},\frac{1}{2})^T$. Here $\xi_i = \sqrt{\rho_i}\exp\{i\theta_i\}$ with ρ_i and θ_i as

the fractional populations and phase in hyperfine spin i ($i = +1, 0, -1$). So the initial spin density matrix reads

$$\boldsymbol{\sigma}(0) = \begin{pmatrix} 1/4 & \sqrt{2}/4 & 1/4 \\ \sqrt{2}/4 & 1/2 & \sqrt{2}/4 \\ 1/4 & \sqrt{2}/4 & 1/4 \end{pmatrix}.$$

The fractional magnetization is defined as $m_0 = \rho_{+1} - \rho_{-1}$ which is conserved during the time evolution.

To study the spin-mixing dynamics in the spin-2 case, we first transfer the atoms to the $|2, -2\rangle$ hyperfine state with a microwave rapid adiabatic passage at a magnetic field of 1.3 G with a near-unity efficiency. The magnetic field is then ramped adiabatically to some desired value before a fully transversely magnetized initial state $\xi = (\frac{1}{4}, \frac{1}{2}, \frac{\sqrt{6}}{4}, \frac{1}{2}, \frac{1}{4})^T$ is prepared with a RF $\pi/2$-pulse pulse and the corresponding initial spin density matrix is

$$\boldsymbol{\sigma}(0) = \begin{pmatrix} 1/16 & 1/8 & \sqrt{6}/16 & 1/8 & 1/16 \\ 1/8 & 1/4 & \sqrt{6}/8 & 1/4 & 1/8 \\ \sqrt{6}/16 & \sqrt{6}/8 & 3/8 & \sqrt{6}/8 & \sqrt{6}/16 \\ 1/8 & 1/4 & \sqrt{6}/8 & 1/4 & 1/8 \\ 1/16 & 1/8 & \sqrt{6}/16 & 1/8 & 1/16 \end{pmatrix}.$$

The magnetization is defined as $m_0 = 2\rho_{+2} + \rho_{+1} - \rho_{-1} - 2\rho_{-2}$ in this case.

After the initialization of the spin state, we hold it in our FORT for a range of time to let the system evolve and then we image the atoms with the spin-sensitive absorption imaging after a ballistic expansion of 12 ms. The fraction spin populations are extracted from the image with $\rho_i = N_i/N$.

Spin-1 Case

In the spin-1 case, we have systematically studied the coherent spin-mixing dynamics at magnetic fields ranging from 0.1 G to 0.3 G. The quadratic Zeeman energy q scales as $h \times 72B^2\,\mathrm{Hz/G^2}$ ($h\times 0.72\,\mathrm{Hz}\sim 6.48\,\mathrm{Hz}$). On the other hand, $2c_2\bar{n} = -h\times 1.45\,\mathrm{Hz}$ with our typical density.

Generally we observe long-lived coherent oscillations of the fractional population at all magnetic fields. As examples, in Figs. 4.7 (a) and (b), we show the time evolution of ρ_0 at 0.1 G and 0.18 G respectively. Clearly, the dependence of the

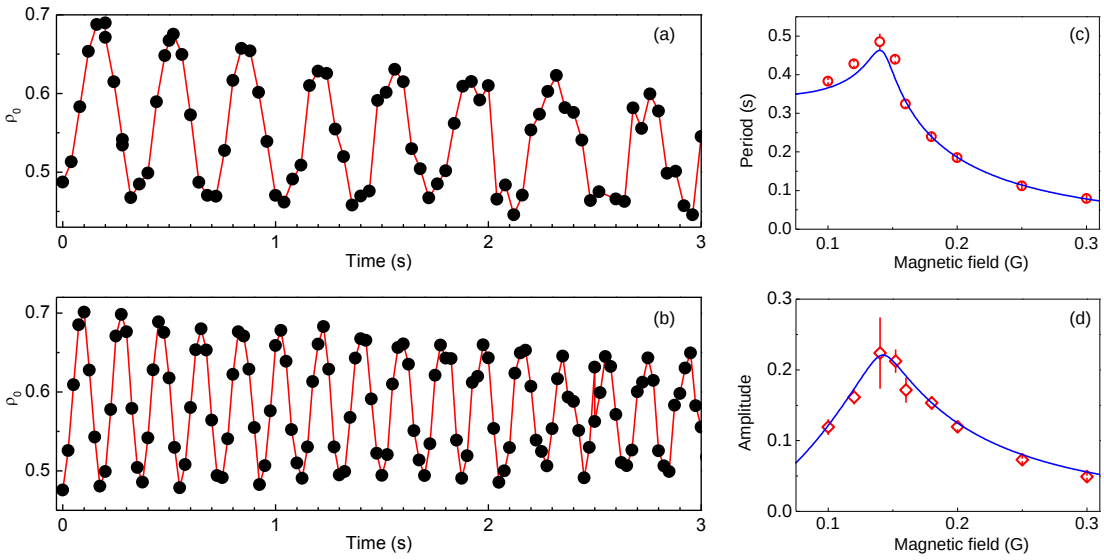

Figure 4.7: The coherent spin-mixing dynamics in a ^{87}Rb thermal spin-1 gas and its magnetic-field dependence.

spin-mixing dynamics on the magnetic field is demonstrated. Since the equation of motion here is almost same as that in the condensate, we could understand our observation with Eq. 4.5 where c_2 is replaced by $2c_2$. At low fields of the interaction dominated regime ($q \ll 2|c_2\bar{n}|$), the oscillation period is intrinsically determined by $2c_2\bar{n}$ and this is the case in Fig. 4.7 (a). On the other hand, the oscillation period is proportional to $1/q$ in the quadratic Zeeman regime where $q \gg |2c_2\bar{n}|$, as shown in Fig. 4.7 (b). In both cases, the oscillation lasts for more than 5 s, although only data in first 3 s is presented here. The oscillation becomes non-periodic severely for data beyond 3 s, maybe due to the significant loss of the atom number. We fit our data to a damped sinusoidal function to extract the oscillation period and amplitude.

The oscillation period and amplitude at all our magnetic fields are collected and summarized in Figs. 4.7 (c) and (d) respectively. With our initial state ($\rho_0(0) = 0.5, \theta(0) = 0$ in Eq. 4.5), the critical value of q is $-2c_2\bar{n}$ that is irrelevant with m_0. This gives $B_c \sim$1.42 G, which is confirmed by the maximum observed oscillation period and amplitude. However, the divergence of the resonant period is removed here due to the finite m_0 of our initial state. Our data is also compared with the theoretical result (solid blue curves) in the figure, where excellent agreements could be found for both the period and amplitude. The solid curves are fits Eq.

4.30 with c_2 as the only fitting parameter, where the mean density is from our measurement and $m_0 = 0.06(2)$ due to the imperfect RF $\pi/2-$pulse. We obtain $c_2 = \frac{4\pi\hbar^2}{3m}(-1.00 \pm 0.12)a_B$, which is consistent with previous values [114, 117].

Spin-2 Case

We can have more spin-mixing channels in a spin-2 gas, which give rise to two spin-dependent interaction parameters c_2 and c_4. In a ^{87}Rb gas, $c_2 > 0, c_4 < 0$ and $c_2 \gg |c_4|$ [114,115]. With our typical density, $2c_2\bar{n} = h\times 4.6\,\mathrm{Hz}$ and $q = -h\times 72B^2$ Hz/G^2. Although generally there are no analytic solutions to the equation of motion in this case, we could numerically integrate the equations to simulate the dynamics. Another feature is that the lifetime of a ^{87}Rb spin-2 gas in our setup is limited to 0.5 s by the spin-relaxation processes [217]. We note that the time scale for the spin-mixing dynamics ($\hbar/2c_2\bar{n} \sim$30 ms) is much shorter than the lifetime, which makes our theoretical model still working. Similarly, we have carried our the measurements at magnetic fields ranging from 1.0 G to 0.6 G and we present the results in Fig. 4.8.

In Fig. 4.8 (a) and Fig. 4.8 (b) we show the time evolution of all the fractional spin population within 100 ms at 0.1 G and 0.45 G respectively. Since $c_2 \gg |c_4|$, we could omit the latter term with our initial state in discussions here. The problem becomes almost the same as that in the spin-1 case qualitatively. The quadratic Zeeman term favors the ferromagnetic state for $q < 0$, while the c_2 term favors the polar state for $c_2 > 0$. The competition between these two energies lead to a resonant behavior at some critical magnetic field. Actually previous studies in Refs. [115, 218] on the ^{87}Rb spin-2 BEC with the same initial sate as ours have given approximated analytic results in two limiting cases: the mean field regime with $|q| \ll 2c_2\bar{n}$ and the quadratic Zeeman regime with $|q| \gg 2c_2\bar{n}$. In the low field regime, only the process $2\,|2,0\rangle \leftrightarrow |2,+2\rangle + |2,-2\rangle$ happens and the populations in $|2,\pm1\rangle$ are not changed. The oscillation period is predominately fixed by the spin-dependent interaction which the amplitude is proportional to q. This is the case shown in Fig. 4.8 (a). At high magnetic fields, the dynamics are dominated by the quadratic Zeeman energy, where the oscillation period is set by q. and the amplitude is proportional to $c_2\bar{n}$. The dynamics in Fig. 4.8 (b) is an example in this case.

The systematic oscillation period and amplitude of ρ_0 are presented in Fig. 4.8

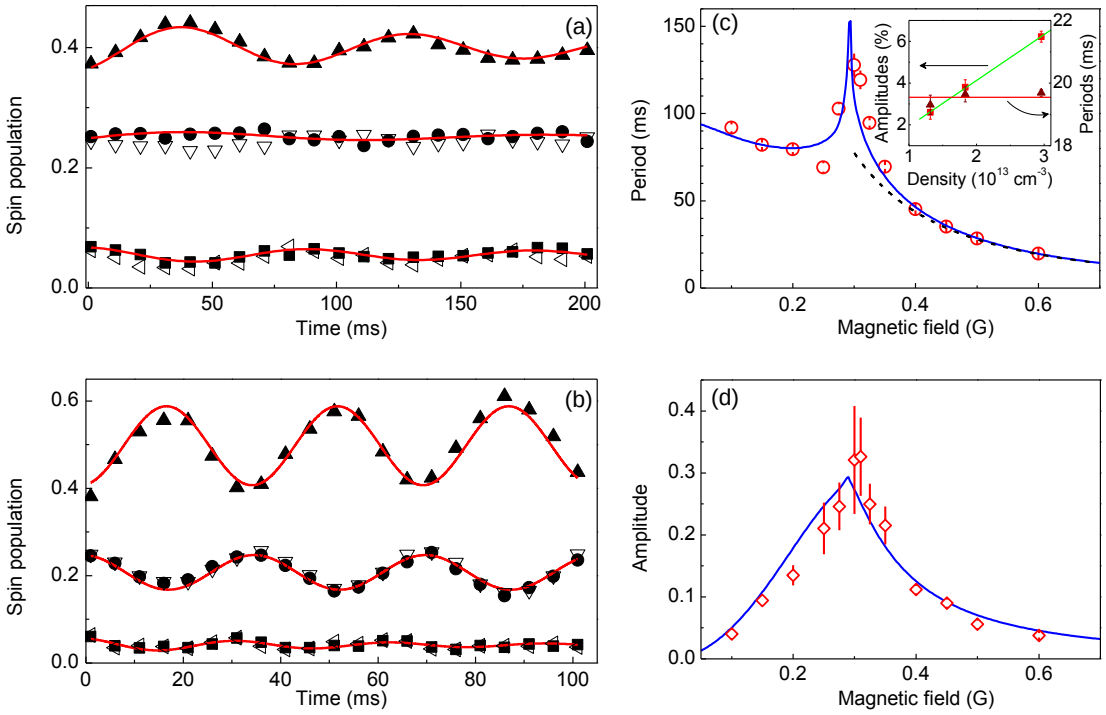

Figure 4.8: The coherent spin-mixing dynamics in a ^{87}Rb thermal spin-2 gas and its magnetic-field dependence.

(c) and Fig. 4.8 (d), respectively. It is clear that a magnetic resonance at $\sim$0.3 G could be identified where both the oscillation period and amplitude reach their maximums. The numerical result without free-parameters is also shown in the figure with the solid blue curves. Good agreements between the experiment and the theory is clearly seen.

Based on the analytic result at high magnetic fields, we could directly verify the factor-of-2 thermal enhancement of the spin-dependent interaction energy. In this regime, the expression for the time evolution of ρ_0 in a condensate reads [115]

$$\rho_0(t) = \frac{3}{8}\{1 - \frac{c_2 n}{2q}[2\cos(2qt) - 2 + \frac{\cos(4qt) - 1}{2}]\}.$$

Since the amplitude of $\cos(2qt)$ term is 4 times that of $\cos(4qt)$ term, we focus on the former term. At a magnetic field of 0.6 G, $|q| = h\times 25.92\,\text{Hz} \gg c_2\bar{n}$ which gives rise to a oscillation period of 19.3 ms. The oscillation amplitude is proportional to $\bar{n}$ with a slope of $3c_2/8|q|$. By measuring the relation between the oscillation amplitude and the mean density, we could obtain the value of c_2 from a linear fit. The result is shown in the set of Fig. 4.8 (c), where we have tuned the

mean atomic density from $1.3 \times 10^{13}\,\mathrm{cm}^{-3}$ to $2.9 \times 10^{13}\,\mathrm{cm}^{-3}$. We could observe that the period keeps nearly a constant while the amplitude scales linearly with the mean density and the best fit gives a slope of $0.022(2.5)/10^{13}\,\mathrm{cm}^3$ and thus $c_2 = \frac{4\pi\hbar^2}{7m}(13.78 \pm 1.57)a_B$. With the best known value of $a_4 - a_2 \approx 6.95a_B$ [114] we get a enhancement factor of 2.0(2.3).

Summary

In short summary, we have experimentally studied the coherent spin-mixing dynamics in a thermal spin-1 and spin-2 gas. We have observed a magnetic resonance for the spin population oscillation in each case. To understand them, a previously developed Boltzmann transport equation is generalized to our cases. Importantly, we have experimentally verified the profound feature in a thermal spinor gas, namely the factor-of-2 enhancement of the spin-dependent interaction energy. These results have been published in Ref. [119] where I was the second author. I mainly contributed to taking and analyzing the data, helping the numerical simulation, and discussing the results.

Appendix A

Appendix for The Molecular Part

A.1 Dipole-Dipole Interaction

As shown in Fig. A.1, the energy associated with two interacting identical dipoles reads

$$U_{dd}(\mathbf{r}) = \frac{C_{dd}}{4\pi}\frac{(\hat{\mathbf{r}}_1 \cdot \hat{\mathbf{r}}_2)R^2 - 3(\hat{\mathbf{r}}_1 \cdot \mathbf{R})(\hat{\mathbf{r}}_2 \cdot \mathbf{R})}{R^5}, \tag{A.1}$$

where $\hat{\mathbf{r}}_1, \hat{\mathbf{r}}_2$, and $\mathbf{R}$ are explained in the figure and C_{dd} is the couping constant. C_{dd} is $\mu_0\mu^2$ (μ_0 is the permeability of vacuum) for magnetic dipoles and μ^2/ε_0 (ε_0 is the permittivity of vacuum) for electric dipoles. The dipolar length, the corresponding length scale of the DDI, is defined as $a_{dd} = \frac{C_{dd}m}{4\pi\hbar^2}$ where m is the mass.

The anisotropic nature of DDI is apparent from Eq. A.1. On the other hand, the potential $V(R) \propto 1/R^n$ is long-range only when the integral $\int V(R)d^3R$ diverges, which strongly depends on the dimensionality. Here R is the inter-particle distance and n is a positive integer. So the DDI is long-range in 3D or quasi-2D but effectively short-range in 2D or 1D.

The collision in 3D between two dipoles could be dramatically different from that between two simple atoms. The phase shifts δ_l for different partial waves in

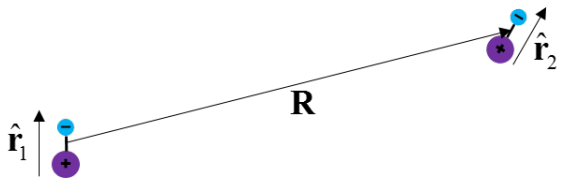

Figure A.1: The interaction between two dipoles. $\hat{\mathbf{r}}_i$ is the unit vector along the direction of dipole i ($i = 1, 2$) and $\mathbf{R}$ is the relative position vector between them.

the low energy limit obey the following threshold law [219]:

$$\left.\begin{aligned} \lim_{k\to 0} k^{2l+1} \cot \delta_l &= -\frac{1}{A_l} \quad \text{if } 2l < n-3, \\ \lim_{k\to 0} k^{n-2} \cot \delta_l &= \text{const} \quad \text{if } 2l \geq n-3, \end{aligned}\right\} \tag{A.2}$$

where A_l is a l-dependent constant and k is the entrance wave vector. With the van der Waals interaction ($n = 6$), the dominated contribution comes from the $l = 0$ (s-wave) while δ_l approach zero as fast as k^3 for $l = 1$ and k^4 for $l \geq 2$. With the DDI ($n = 3$), the contributions of all the partial waves are proportional to k and all the partial waves are coupled by the DDI.

In Table A.1, we list the dipolar lengths a_{dd} achieved with various atoms and molecules which can be compared to the contact interactions. For bosons or distinguishable particles, the contact interaction is s-wave where the scattering length is typically on the order of $100a_0$. For fermions, the p-wave interaction is negligible. From this table we can see that dominate DDIs could be easily achieved with UPMs while they are comparable with the contact interactions in magnetic atoms.

particles	Permanent dipole moment	Induced dipole moment	a_{dd}
^{87}Rb	1 μ_B	-	$2a_0$
^{52}Cr	6 μ_B	-	$45a_0$
^{162}Dy	10 μ_B	-	$393a_0$
^{40}K^{87}Rb [220]	0.57D	0.22D	$1700a_0$
^{87}Rb^{133}Cs [195, 221]	1.23D	0.36D	$8000a_0$
^{23}Na^{40}K [198]	2.72D	0.8D	$11400a_0$
^{23}Na^{87}Rb (Our work [199])	3.2D	1.06D	$34900a_0$

Table A.1: DDI with several atoms and molecules. Compared with the contact interactions between magnetic atoms , the DDIs are smaller, or at most on the same order.

Appendix B

Appendix for The Spinor Part

B.1 The Interaction Hamiltonian

If the internal degree of freedom are decoupled from the external degree of freedom, collisions between two alkali atoms with hyperfine spins $\mathbf{f}_1$ and $\mathbf{f}_2$ conserve the total spin $\mathbf{F} = \mathbf{f}_1 + \mathbf{f}_2$. Thus the interaction Hamiltonian can be divided into different total spin channel:

$$\begin{aligned}\hat{V}(\mathbf{r}) &= \sum_{F=|f_1-f_2|}^{f_1+f_2} \kappa_F V_F(\mathbf{r}) \hat{P}_F \\ &= \frac{4\pi\hbar^2}{\mu} \sum_{F=|f_1-f_2|}^{f_1+f_2} \kappa_F a_F \delta(\mathbf{r}) \hat{P}_F.\end{aligned} \tag{B.1}$$

Here a_F is the s-wave scattering length of the total spin-F channel and μ is the reduced mass. $\hat{P}_F$ is the projection operator and we have the completeness relation $\hat{1} = \sum_F \hat{P}_F$. κ_F are prefactors accounting for the statistical nature of the colliding pairs. If they are identical particles ($\mathbf{f}_1$=$\mathbf{f}_2$=$\mathbf{f}$), the permutation symmetry requires that the total wavefunction is changed by a factor of $(-1)^{2f}$. On the other hand, the factor for the spin part of the wavefunction is $(-1)^{F+2f}$ and that for the spatial part is $(-1)^l$, where $\mathbf{l}$ is their relative orbital angular momentum. So to be consistence $F + l$ should be even, no matter the identical atoms are bosons or fermions. In the low energy limit, only $l = 0$ ($l = 1$) happens for bosons (fermions) and even (odd) F are allowed.

In general, we can derive a useful relation from the composition law of the angular momentum $\mathbf{f}_1 \cdot \mathbf{f}_2 = \frac{1}{2}((\mathbf{f}_1 + \mathbf{f}_2)^2 - \mathbf{f}_1^2 - \mathbf{f}_1^2)$. By operating this law to the above completeness relation we can get

$$\mathbf{f}_1 \cdot \mathbf{f}_2 = \frac{1}{2} \sum_{F=|f_1-f_2|}^{f_1+f_2} [F(F+1) - f_1(f_1+1) - f_2(f_2+1)]\hat{P}_F. \tag{B.2}$$

For the single-species spin-1 gases, only $F = 0$ and 2 are allowed and Eq. B.2 becomes $\mathbf{f}_1 \cdot \mathbf{f}_2 = \hat{P}_2 - 2\hat{P}_0$. Together with $\hat{1} = \hat{P}_0 + \hat{P}_0$ we have $\hat{P}_0 = (\hat{1} - \mathbf{f}_1 \cdot \mathbf{f}_2)/3$ and $\hat{P}_2 = (2\hat{1} + \mathbf{f}_1 \cdot \mathbf{f}_2)/3$. Substituting these two into the interaction Hamiltonian we obtain

$$\hat{V}(\mathbf{r}) = \delta(\mathbf{r})\frac{4\pi\hbar^2}{\mu}(\frac{a_0 + 2a_2}{3}\hat{1} + \frac{a_2 - a_0}{3}\mathbf{f}_1 \cdot \mathbf{f}_2). \tag{B.3}$$

The first term has nothing to do with the spin and thus it is called spin-independent interaction with the parameter $c_0 = \frac{4\pi\hbar^2}{\mu}\frac{a_0+2a_2}{3}$. The spin-depend interaction is corresponding to the second term with the interaction parameter $c_2 = \frac{4\pi\hbar^2}{\mu}\frac{a_2-a_0}{3}$. However, for collision between two heteronuclear spin-1 bosons, $F = 0, 1, 2$ channels are all allowed and Eq. B.2 reads $\mathbf{f}_1 \cdot \mathbf{f}_2 = \hat{P}_2 - \hat{P}_1 - 2\hat{P}_0$. The interaction Hamiltonian is rewritten as

$$\hat{V}(\mathbf{r}) = \delta(\mathbf{r})(\frac{\alpha}{2}\hat{1} + \frac{\beta}{2}\mathbf{f}_1 \cdot \mathbf{f}_2 + \frac{\gamma}{2}\hat{P}_0), \tag{B.4}$$

where $\alpha = \frac{2\pi\hbar^2}{\mu}(a_1 + a_2)$, $\beta = \frac{2\pi\hbar^2}{\mu}(a_2 - a_1)$, and $\gamma = \frac{2\pi\hbar^2}{\mu}(2a_0 - 3a_1 + a_2)$. For a single-species spin-2 gas, following the same procedure we can rewrite the interaction Hamiltonian as

$$\hat{V}(\mathbf{r}) = \delta(\mathbf{r})(c_0\hat{1} + c_2\mathbf{f}_1 \cdot \mathbf{f}_2 + c_4\hat{P}_0), \tag{B.5}$$

where $c_0 = \frac{4\pi\hbar^2}{\mu}\frac{4a_2+3a_4}{7}$, $c_2 = \frac{4\pi\hbar^2}{\mu}\frac{a_4-a_2}{7}$, and $c_4 = \frac{4\pi\hbar^2}{\mu}\frac{7a_0-10a_2+3a_4}{7}$ are interaction coefficients of the spin-independent, spin-exchange, and spin-singlet pairing terms, respectively.

Bibliography

[1] M. H. Anderson, J. R. Ensher, M. R. Matthews, C. E. Wieman, and E. A. Cornell. Observation of Bose-Einstein Condensation in a Dilute Atomic Vapor. *Science*, 269(5221):198–201, 1995. http://science.sciencemag.org/content/269/5221/198.

[2] K. B. Davis, M. O. Mewes, M. R. Andrews, N. J. van Druten, D. S. Durfee, D. M. Kurn, and W. Ketterle. Bose-Einstein Condensation in a Gas of Sodium Atoms. *Phys. Rev. Lett.*, 75:3969–3973, Nov 1995. http://link.aps.org/doi/10.1103/PhysRevLett.75.3969.

[3] C. C. Bradley, C. A. Sackett, J. J. Tollett, and R. G. Hulet. Evidence of Bose-Einstein Condensation in an Atomic Gas with Attractive Interactions. *Phys. Rev. Lett.*, 75:1687–1690, Aug 1995. http://link.aps.org/doi/10.1103/PhysRevLett.75.1687.

[4] Maciej Lewenstein, Anna Sanpera, Veronica Ahufinger, Bogdan Damski, Aditi Sen(De), and Ujjwal Sen. Ultracold atomic gases in optical lattices: mimicking condensed matter physics and beyond. *Advances in Physics*, 56(2):243–379, 2007. http://dx.doi.org/10.1080/00018730701223200.

[5] Erez Zohar, J Ignacio Cirac, and Benni Reznik. Quantum simulations of lattice gauge theories using ultracold atoms in optical lattices. *Reports on Progress in Physics*, 79(1):014401, 2016. http://stacks.iop.org/0034-4885/79/i=1/a=014401.

[6] HUI ZHAI. SPIN-ORBIT COUPLED QUANTUM GASES. *International Journal of Modern Physics B*, 26(01):1230001, 2012. http://www.worldscientific.com/doi/abs/10.1142/S0217979212300010.

[7] Victor Galitski and Ian B Spielman. Spin-orbit coupling in quantum gases. *Nature*, 494(7435):49–54, 2013. http://dx.doi.org/10.1038/nature11841.

[8] Hui Zhai. Degenerate quantum gases with spin–orbit coupling: a review. *Reports on Progress in Physics*, 78(2):026001, 2015. http://stacks.iop.org/0034-4885/78/i=2/a=026001.

[9] Markus Greiner, Olaf Mandel, Tilman Esslinger, Theodor W. Hansch, and Immanuel Bloch. Quantum phase transition from a superfluid to a Mott insulator in a gas of ultracold atoms. *Nature*, 415(6867):39–44, 2002. http://dx.doi.org/10.1038/415039a.

[10] D. Jaksch and P. Zoller. The cold atom hubbard toolbox. *Annals of Physics*, 315(1):52 – 79, 2005. Special Issue. http://www.sciencedirect.com/science/article/pii/S0003491604001782.

[11] Tilman Esslinger. Fermi-Hubbard Physics with Atoms in an Optical Lattice. *Annual Review of Condensed Matter Physics*, 1(1):129–152, 2010. http://dx.doi.org/10.1146/annurev-conmatphys-070909-104059.

[12] Gregor Jotzu, Michael Messer, Rémi Desbuquois, Martin Lebrat, Thomas Uehlinger, Daniel Greif, and Tilman Esslinger. Experimental realization of the topological haldane model with ultracold fermions. *Nature*, 515(7526):237–240, 2014. http://dx.doi.org/10.1038/nature13915.

[13] Quentin Baudouin, William Guerin, and Robin Kaiser. Cold and hot atomic vapors: a testbed for astrophysics? In *Annual Review of Cold Atoms and Molecules, Volume 2*, page 251. World Scientific, 2014. https://hal.archives-ouvertes.fr/hal-00968233.

[14] Jiahao Huang, Shuyuan Wu, Honghua Zhong, and Chaohong Lee. *Quantum metrology with cold atoms*, chapter 7, pages 365–415. http://www.worldscientific.com/doi/abs/10.1142/9789814590174_0007.

[15] G Rosi, F Sorrentino, L Cacciapuoti, M Prevedelli, and GM Tino. Precision measurement of the newtonian gravitational constant using cold atoms. *arXiv preprint arXiv:1412.7954*, 2014. http://dx.doi.org/10.1038/nature13433.

[16] Rym Bouchendira, Pierre Cladé, Saïda Guellati-Khélifa, Fran çois Nez, and Fran çois Biraben. New Determination of the Fine Structure Constant and Test of the Quantum Electrodynamics. *Phys. Rev. Lett.*, 106:080801, Feb 2011. http://link.aps.org/doi/10.1103/PhysRevLett.106.080801.

[17] Herman Feshbach. Unified theory of nuclear reactions. *Annals of Physics*, 5(4):357 – 390, 1958. http://www.sciencedirect.com/science/article/pii/0003491658900071.

[18] Herman Feshbach. A unified theory of nuclear reactions. II. *Annals of Physics*, 19(2):287 – 313, 1962. http://www.sciencedirect.com/science/article/pii/000349166290221X.

[19] U. Fano. Effects of Configuration Interaction on Intensities and Phase Shifts. *Phys. Rev.*, 124:1866–1878, Dec 1961. http://link.aps.org/doi/10.1103/PhysRev.124.1866.

[20] Cheng Chin, Rudolf Grimm, Paul Julienne, and Eite Tiesinga. Feshbach resonances in ultracold gases. *Rev. Mod. Phys.*, 82:1225–1286, Apr 2010. http://link.aps.org/doi/10.1103/RevModPhys.82.1225.

[21] P.S. Jessen and I.H. Deutsch. Optical lattices. volume 37 of *Advances In Atomic, Molecular, and Optical Physics*, pages 95 – 138. Academic Press, 1996. http://www.sciencedirect.com/science/article/pii/S1049250X08600993.

[22] Immanuel Bloch. Ultracold quantum gases in optical lattices. *Nature Physics*, 1(1):23–30, 2005. http://dx.doi.org/10.1038/nphys138.

[23] Gavin K. Brennen, Carlton M. Caves, Poul S. Jessen, and Ivan H. Deutsch. Quantum Logic Gates in Optical Lattices. *Phys. Rev. Lett.*, 82:1060–1063, Feb 1999. http://link.aps.org/doi/10.1103/PhysRevLett.82.1060.

[24] Jiannis K. Pachos and Peter L. Knight. Quantum Computation with a One-Dimensional Optical Lattice. *Phys. Rev. Lett.*, 91:107902, Sep 2003. http://link.aps.org/doi/10.1103/PhysRevLett.91.107902.

[25] T. Calarco, U. Dorner, P. S. Julienne, C. J. Williams, and P. Zoller. Quantum computations with atoms in optical lattices: Marker qubits and molecular

interactions. *Phys. Rev. A*, 70:012306, Jul 2004. http://link.aps.org/doi/10.1103/PhysRevA.70.012306.

[26] J Ignacio Cirac and Peter Zoller. New frontiers in quantum information with atoms and ions. *Physics Today*, 57(3):38–45, 2004. http://scitation.aip.org/content/aip/magazine/physicstoday/article/57/3/10.1063/1.1712500.

[27] David M Larsen. Binary mixtures of dilute bose gases with repulsive interactions at low temperature. *Annals of Physics*, 24:89 – 101, 1963. http://www.sciencedirect.com/science/article/pii/0003491663900666.

[28] W. B. Colson and Alexander L. Fetter. Mixtures of bose liquids at finite temperature. *Journal of Low Temperature Physics*, 33(3):231–242. http://dx.doi.org/10.1007/BF00114996.

[29] Juha Tuoriniemi, Juha Martikainen, Elias Pentti, Alexander Sebedash, Sergey Boldarev, and George Pickett. Towards Superfluidity of 3He Diluted by 4He. *Journal of Low Temperature Physics*, 129(5):531–545. http://dx.doi.org/10.1023/A:1021468614550.

[30] C. J. Myatt, E. A. Burt, R. W. Ghrist, E. A. Cornell, and C. E. Wieman. Production of Two Overlapping Bose-Einstein Condensates by Sympathetic Cooling. *Phys. Rev. Lett.*, 78:586–589, Jan 1997. http://link.aps.org/doi/10.1103/PhysRevLett.78.586.

[31] B. DeMarco and D. S. Jin. Onset of Fermi Degeneracy in a Trapped Atomic Gas. *Science*, 285(5434):1703–1706, 1999. http://science.sciencemag.org/content/285/5434/1703.

[32] M. Taglieber, A.-C. Voigt, T. Aoki, T. W. Hänsch, and K. Dieckmann. Quantum Degenerate Two-Species Fermi-Fermi Mixture Coexisting with a Bose-Einstein Condensate. *Phys. Rev. Lett.*, 100:010401, Jan 2008. http://link.aps.org/doi/10.1103/PhysRevLett.100.010401.

[33] Andrew G. Truscott, Kevin E. Strecker, William I. McAlexander, Guthrie B. Partridge, and Randall G. Hulet. Observation of Fermi Pressure in a Gas of Trapped Atoms. *Science*, 291(5513):2570–2572, 2001. http://science.sciencemag.org/content/291/5513/2570.

[34] F. Schreck, L. Khaykovich, K. L. Corwin, G. Ferrari, T. Bourdel, J. Cubizolles, and C. Salomon. Quasipure Bose-Einstein Condensate Immersed in a Fermi Sea. *Phys. Rev. Lett.*, 87:080403, Aug 2001. http://link.aps.org/doi/10.1103/PhysRevLett.87.080403.

[35] Z. Hadzibabic, C. A. Stan, K. Dieckmann, S. Gupta, M. W. Zwierlein, A. Görlitz, and W. Ketterle. Two-Species Mixture of Quantum Degenerate Bose and Fermi Gases. *Phys. Rev. Lett.*, 88:160401, Apr 2002. http://link.aps.org/doi/10.1103/PhysRevLett.88.160401.

[36] G. Roati, F. Riboli, G. Modugno, and M. Inguscio. Fermi-Bose Quantum Degenerate ^{40}K-^{87}Rb Mixture with Attractive Interaction. *Phys. Rev. Lett.*, 89:150403, Sep 2002. http://link.aps.org/doi/10.1103/PhysRevLett.89.150403.

[37] G. Modugno, M. Modugno, F. Riboli, G. Roati, and M. Inguscio. Two Atomic Species Superfluid. *Phys. Rev. Lett.*, 89:190404, Oct 2002. http://link.aps.org/doi/10.1103/PhysRevLett.89.190404.

[38] G. Thalhammer, G. Barontini, L. De Sarlo, J. Catani, F. Minardi, and M. Inguscio. Double Species Bose-Einstein Condensate with Tunable Interspecies Interactions. *Phys. Rev. Lett.*, 100:210402, May 2008. http://link.aps.org/doi/10.1103/PhysRevLett.100.210402.

[39] S. B. Papp, J. M. Pino, and C. E. Wieman. Tunable Miscibility in a Dual-Species Bose-Einstein Condensate. *Phys. Rev. Lett.*, 101:040402, Jul 2008. http://link.aps.org/doi/10.1103/PhysRevLett.101.040402.

[40] Lercher, A.D., Takekoshi, T., Debatin, M., Schuster, B., Rameshan, R., Ferlaino, F., Grimm, R., and Nägerl, H.-C. Production of a dual-species Bose-Einstein condensate of Rb and Cs atoms. *Eur. Phys. J. D*, 65(1), 2011. http://dx.doi.org/10.1140/epjd/e2011-20015-6.

[41] D. J. McCarron, H. W. Cho, D. L. Jenkin, M. P. Köppinger, and S. L. Cornish. Dual-species Bose-Einstein condensate of ^{87}Rb and ^{133}Cs. *Phys. Rev. A*, 84:011603, Jul 2011. http://link.aps.org/doi/10.1103/PhysRevA.84.011603.

[42] Fudong Wang, Xiaoke Li, Dezhi Xiong, and Dajun Wang. A double species 23 Na and 87 Rb Bose–Einstein condensate with tunable miscibility via an interspecies Feshbach resonance. *Journal of Physics B: Atomic, Molecular and Optical Physics*, 49(1):015302, 2016. http://stacks.iop.org/0953-4075/49/i=1/a=015302.

[43] C. A. Regal, M. Greiner, and D. S. Jin. Observation of Resonance Condensation of Fermionic Atom Pairs. *Phys. Rev. Lett.*, 92:040403, Jan 2004. http://link.aps.org/doi/10.1103/PhysRevLett.92.040403.

[44] M. W. Zwierlein, C. A. Stan, C. H. Schunck, S. M. F. Raupach, A. J. Kerman, and W. Ketterle. Condensation of Pairs of Fermionic Atoms near a Feshbach Resonance. *Phys. Rev. Lett.*, 92:120403, Mar 2004. http://link.aps.org/doi/10.1103/PhysRevLett.92.120403.

[45] T. Bourdel, L. Khaykovich, J. Cubizolles, J. Zhang, F. Chevy, M. Teichmann, L. Tarruell, S. J. J. M. F. Kokkelmans, and C. Salomon. Experimental Study of the BEC-BCS Crossover Region in Lithium 6. *Phys. Rev. Lett.*, 93:050401, Jul 2004. http://link.aps.org/doi/10.1103/PhysRevLett.93.050401.

[46] C. Chin, M. Bartenstein, A. Altmeyer, S. Riedl, S. Jochim, J. Hecker Denschlag, and R. Grimm. Observation of the Pairing Gap in a Strongly Interacting Fermi Gas. *Science*, 305(5687):1128–1130, 2004. http://science.sciencemag.org/content/305/5687/1128.

[47] G. B. Partridge, K. E. Strecker, R. I. Kamar, M. W. Jack, and R. G. Hulet. Molecular Probe of Pairing in the BEC-BCS Crossover. *Phys. Rev. Lett.*, 95:020404, Jul 2005. http://link.aps.org/doi/10.1103/PhysRevLett.95.020404.

[48] Chih-Chun Chien, Qijin Chen, Yan He, and K. Levin. Superfluid Phase Diagrams of Trapped Fermi Gases with Population Imbalance. *Phys. Rev. Lett.*, 98:110404, Mar 2007. http://link.aps.org/doi/10.1103/PhysRevLett.98.110404.

[49] Peter Fulde and Richard A. Ferrell. Superconductivity in a Strong Spin-Exchange Field. *Phys. Rev.*, 135:A550–A563, Aug 1964. http://link.aps.org/doi/10.1103/PhysRev.135.A550.

[50] A.I. Larkin and Yu.N. Ovchinnikov. Inhomogeneous State of Superconductors. *Sov.Phys.JETP*, 20:762, 1965.

[51] Roberto Casalbuoni and Giuseppe Nardulli. Inhomogeneous superconductivity in condensed matter and QCD. *Rev. Mod. Phys.*, 76:263–320, Feb 2004. http://link.aps.org/doi/10.1103/RevModPhys.76.263.

[52] M. J. Bijlsma, B. A. Heringa, and H. T. C. Stoof. Phonon exchange in dilute Fermi-Bose mixtures: Tailoring the Fermi-Fermi interaction. *Phys. Rev. A*, 61:053601, Apr 2000. http://link.aps.org/doi/10.1103/PhysRevA.61.053601.

[53] Klaus Mølmer. Bose Condensates and Fermi Gases at Zero Temperature. *Phys. Rev. Lett.*, 80:1804–1807, Mar 1998. http://link.aps.org/doi/10.1103/PhysRevLett.80.1804.

[54] Rina Kanamoto and Makoto Tsubota. Phase Separation of a Fast Rotating Boson-Fermion Mixture in the Lowest-Landau-Level Regime. *Phys. Rev. Lett.*, 96:200405, May 2006. http://link.aps.org/doi/10.1103/PhysRevLett.96.200405.

[55] Cristoph Kohstall, Mattheo Zaccanti, Matthias Jag, Andreas Trenkwalder, Pietro Massignan, Georg M Bruun, Florian Schreck, and Rudolf Grimm. Metastability and coherence of repulsive polarons in a strongly interacting fermi mixture. *Nature*, 485(7400):615–618, 2012. http://dx.doi.org/10.1038/nature11065.

[56] Ming-Guang Hu, Michael J. Van de Graaff, Dhruv Kedar, John P. Corson, Eric A. Cornell, and Deborah S. Jin. Bose polarons in the strongly interacting regime. *preprint*, arXiv:1605.00729[**cond-mat.quant-gas**]. http://arxiv.org/abs/1605.00729.

[57] H. P. Büchler and G. Blatter. Supersolid versus Phase Separation in Atomic Bose-Fermi Mixtures. *Phys. Rev. Lett.*, 91:130404, Sep 2003. http://link.aps.org/doi/10.1103/PhysRevLett.91.130404.

[58] F. Hébert, G. G. Batrouni, X. Roy, and V. G. Rousseau. Supersolids in one-dimensional Bose-Fermi mixtures. *Phys. Rev. B*, 78:184505, Nov 2008. http://link.aps.org/doi/10.1103/PhysRevB.78.184505.

[59] I. Titvinidze, M. Snoek, and W. Hofstetter. Supersolid Bose-Fermi Mixtures in Optical Lattices. *Phys. Rev. Lett.*, 100:100401, Mar 2008. http://link.aps.org/doi/10.1103/PhysRevLett.100.100401.

[60] Zhi-Fang Xu, Xiaopeng Li, Peter Zoller, and W. Vincent Liu. Spontaneous Quantum Hall Effect in an Atomic Spinor Bose-Fermi Mixture. *Phys. Rev. Lett.*, 114:125303, Mar 2015. http://link.aps.org/doi/10.1103/PhysRevLett.114.125303.

[61] Nguyen Thanh Phuc, Gen Tatara, Yuki Kawaguchi, and Masahito Ueda. Controlling and probing non-abelian emergent gauge potentials in spinor Bose-Fermi mixtures. *Nat. Commun.*, 6:8135, Sep 2015. http://dx.doi.org/10.1038/ncomms9135.

[62] Tin-Lun Ho and V. B. Shenoy. Binary Mixtures of Bose Condensates of Alkali Atoms. *Phys. Rev. Lett.*, 77:3276–3279, Oct 1996. http://link.aps.org/doi/10.1103/PhysRevLett.77.3276.

[63] H. Pu and N. P. Bigelow. Properties of Two-Species Bose Condensates. *Phys. Rev. Lett.*, 80:1130–1133, Feb 1998. http://link.aps.org/doi/10.1103/PhysRevLett.80.1130.

[64] Johannes Hofmann, Stefan S. Natu, and S. Das Sarma. Coarsening Dynamics of Binary Bose Condensates. *Phys. Rev. Lett.*, 113:095702, Aug 2014. http://link.aps.org/doi/10.1103/PhysRevLett.113.095702.

[65] Jacopo Sabbatini, Wojciech H Zurek, and Matthew J Davis. Causality and defect formation in the dynamics of an engineered quantum phase transition in a coupled binary Bose–Einstein condensate. *New Journal of Physics*, 14(9):095030, 2012. http://stacks.iop.org/1367-2630/14/i=9/a=095030.

[66] I.-K. Liu, R. W. Pattinson, T. P. Billam, S. A. Gardiner, S. L. Cornish, T.-M. Huang, W.-W. Lin, S.-C. Gou, N. G. Parker, and N. P. Proukakis. Stochastic growth dynamics and composite defects in quenched immiscible binary condensates. *Phys. Rev. A*, 93:023628, Feb 2016. http://link.aps.org/doi/10.1103/PhysRevA.93.023628.

[67] Jacopo Sabbatini, Wojciech H. Zurek, and Matthew J. Davis. Phase Separation and Pattern Formation in a Binary Bose-Einstein Condensate. *Phys. Rev. Lett.*, 107:230402, Nov 2011. http://link.aps.org/doi/10.1103/PhysRevLett.107.230402.

[68] Satoshi Tojo, Yoshihisa Taguchi, Yuta Masuyama, Taro Hayashi, Hiroki Saito, and Takuya Hirano. Controlling phase separation of binary Bose-Einstein condensates via mixed-spin-channel Feshbach resonance. *Phys. Rev. A*, 82:033609, Sep 2010. http://link.aps.org/doi/10.1103/PhysRevA.82.033609.

[69] E. Nicklas, M. Karl, M. Höfer, A. Johnson, W. Muessel, H. Strobel, J. Tomkovič, T. Gasenzer, and M. K. Oberthaler. Observation of Scaling in the Dynamics of a Strongly Quenched Quantum Gas. *Phys. Rev. Lett.*, 115:245301, Dec 2015. http://link.aps.org/doi/10.1103/PhysRevLett.115.245301.

[70] D. Gordon and C. M. Savage. Excitation spectrum and instability of a two-species Bose-Einstein condensate. *Phys. Rev. A*, 58:1440–1444, Aug 1998. http://link.aps.org/doi/10.1103/PhysRevA.58.1440.

[71] Kenichi Kasamatsu, Makoto Tsubota, and Masahito Ueda. Quadrupole and scissors modes and nonlinear mode coupling in trapped two-component Bose-Einstein condensates. *Phys. Rev. A*, 69:043621, Apr 2004. http://link.aps.org/doi/10.1103/PhysRevA.69.043621.

[72] D. Kobyakov, A. Bezett, E. Lundh, M. Marklund, and V. Bychkov. Turbulence in binary Bose-Einstein condensates generated by highly nonlinear Rayleigh-Taylor and Kelvin-Helmholtz instabilities. *Phys. Rev. A*, 89:013631, Jan 2014. http://link.aps.org/doi/10.1103/PhysRevA.89.013631.

[73] Nils B. Jϕrgensen, Lars Wacker, Kristoffer T. Skalmstang, Meera M. Parish, Jesper Levinsen, Rasmus S. Christensen, Georg M. Bruun, and Jan J. Arlt. Observation of attractive and repulsive polarons in a bose-einstein condensate. *preprint*, arXiv:1604.07883[**cond-mat.quant-gas**]. http://arxiv.org/abs/1604.07883.

[74] Yu Shi and Qian Niu. Bose-Einstein Condensation with an Entangled Order Parameter. *Phys. Rev. Lett.*, 96:140401, Apr 2006. http://link.aps.org/doi/10.1103/PhysRevLett.96.140401.

[75] Fei Zhan, Jacopo Sabbatini, Matthew J. Davis, and Ian P. McCulloch. Miscible-immiscible quantum phase transition in coupled two-component Bose-Einstein condensates in one-dimensional optical lattices. *Phys. Rev. A*, 90:023630, Aug 2014. http://link.aps.org/doi/10.1103/PhysRevA.90.023630.

[76] L. Barbiero, M. Abad, and A. Recati. Magnetic phase transition in coherently coupled Bose gases in optical lattices. *Phys. Rev. A*, 93:033645, Mar 2016. http://link.aps.org/doi/10.1103/PhysRevA.93.033645.

[77] Olaf Mandel, Markus Greiner, Artur Widera, Tim Rom, Theodor W. Hansch, and Immanuel Bloch. Controlled collisions for multi-particle entanglement of optically trapped atoms. *Nature*, 425(6961):937–940, 2003. http://dx.doi.org/10.1038/nature02008.

[78] M. Rodríguez, S. R. Clark, and D. Jaksch. Adiabatic melting of two-component Mott-insulator states. *Phys. Rev. A*, 77:043613, Apr 2008. http://link.aps.org/doi/10.1103/PhysRevA.77.043613.

[79] S. Trotzky, P. Cheinet, S. Fölling, M. Feld, U. Schnorrberger, A. M. Rey, A. Polkovnikov, E. A. Demler, M. D. Lukin, and I. Bloch. Time-Resolved Observation and Control of Superexchange Interactions with Ultracold Atoms in Optical Lattices. *Science*, 319(5861):295–299, 2008. http://science.sciencemag.org/content/319/5861/295.

[80] David M. Weld, Patrick Medley, Hirokazu Miyake, David Hucul, David E. Pritchard, and Wolfgang Ketterle. Spin Gradient Thermometry for Ultracold Atoms in Optical Lattices. *Phys. Rev. Lett.*, 103:245301, Dec 2009. http://link.aps.org/doi/10.1103/PhysRevLett.103.245301.

[81] T. Lahaye, C. Menotti, L. Santos, M. Lewenstein, and T. Pfau. The physics of dipolar bosonic quantum gases. *Reports on Progress in Physics*, 72(12):126401, 2009. http://stacks.iop.org/0034-4885/72/i=12/a=126401.

[82] C Trefzger, C Menotti, B Capogrosso-Sansone, and M Lewenstein. Ultracold dipolar gases in optical lattices. *Journal of Physics B: Atomic, Molecular and Optical Physics*, 44(19):193001, 2011. http://stacks.iop.org/0953-4075/44/i=19/a=193001.

[83] M. A. Baranov, M. Dalmonte, G. Pupillo, and P. Zoller. Condensed Matter Theory of Dipolar Quantum Gases. *Chemical Reviews*, 112(9):5012–5061, 2012. http://dx.doi.org/10.1021/cr2003568.

[84] J. Stuhler, A. Griesmaier, T. Koch, M. Fattori, T. Pfau, S. Giovanazzi, P. Pedri, and L. Santos. Observation of Dipole-Dipole Interaction in a Degenerate Quantum Gas. *Phys. Rev. Lett.*, 95:150406, Oct 2005. http://link.aps.org/doi/10.1103/PhysRevLett.95.150406.

[85] S. Müller, J. Billy, E. A. L. Henn, H. Kadau, A. Griesmaier, M. Jona-Lasinio, L. Santos, and T. Pfau. Stability of a dipolar Bose-Einstein condensate in a one-dimensional lattice. *Phys. Rev. A*, 84:053601, Nov 2011. http://link.aps.org/doi/10.1103/PhysRevA.84.053601.

[86] K. Aikawa, S. Baier, A. Frisch, M. Mark, C. Ravensbergen, and F. Ferlaino. Observation of Fermi surface deformation in a dipolar quantum gas. *Science*, 345(6203):1484–1487, 2014. http://science.sciencemag.org/content/345/6203/1484.

[87] A. de Paz, A. Sharma, A. Chotia, E. Maréchal, J. H. Huckans, P. Pedri, L. Santos, O. Gorceix, L. Vernac, and B. Laburthe-Tolra. Nonequilibrium Quantum Magnetism in a Dipolar Lattice Gas. *Phys. Rev. Lett.*, 111:185305, Oct 2013. http://link.aps.org/doi/10.1103/PhysRevLett.111.185305.

[88] Albert Frisch, Michael Mark, Kiyotaka Aikawa, Francesca Ferlaino, John L. Bohn, Constantinos Makrides, Alexander Petrov, and Svetlana Kotochigova. Quantum chaos in ultracold collisions of gas-phase erbium atoms. *Nature*, 507(7493):475–479, 2014. http://dx.doi.org/10.1038/nature13137.

[89] W. R. Anderson, J. R. Veale, and T. F. Gallagher. Resonant Dipole-Dipole Energy Transfer in a Nearly Frozen Rydberg Gas. *Phys. Rev. Lett.*, 80:249–252, Jan 1998. http://link.aps.org/doi/10.1103/PhysRevLett.80.249.

[90] I. Mourachko, D. Comparat, F. de Tomasi, A. Fioretti, P. Nosbaum, V. M. Akulin, and P. Pillet. Many-Body Effects in a Frozen Rydberg Gas. *Phys. Rev. Lett.*, 80:253–256, Jan 1998. http://link.aps.org/doi/10.1103/PhysRevLett.80.253.

[91] Alpha Gaetan, Yevhen Miroshnychenko, Tatjana Wilk, Amodsen Chotia, Matthieu Viteau, Daniel Comparat, Pierre Pillet, Antoine Browaeys, and Philippe Grangier. Observation of collective excitation of two individual atoms in the rydberg blockade regime. *Nat Phys*, 5(2):115–118, 2009. http://dx.doi.org/10.1038/nphys1183.

[92] L. Isenhower, E. Urban, X. L. Zhang, A. T. Gill, T. Henage, T. A. Johnson, T. G. Walker, and M. Saffman. Demonstration of a Neutral Atom Controlled-NOT Quantum Gate. *Phys. Rev. Lett.*, 104:010503, Jan 2010. http://link.aps.org/doi/10.1103/PhysRevLett.104.010503.

[93] M. Robert-de Saint-Vincent, C. S. Hofmann, H. Schempp, G. Günter, S. Whitlock, and M. Weidemüller. Spontaneous Avalanche Ionization of a Strongly Blockaded Rydberg Gas. *Phys. Rev. Lett.*, 110:045004, Jan 2013. http://link.aps.org/doi/10.1103/PhysRevLett.110.045004.

[94] Lincoln D Carr, David DeMille, Roman V Krems, and Jun Ye. Cold and ultracold molecules: science, technology and applications. *New Journal of Physics*, 11(5):055049, 2009. http://stacks.iop.org/1367-2630/11/i=5/a=055049.

[95] M. G. Moore and A. Vardi. Bose-Enhanced Chemistry: Amplification of Selectivity in the Dissociation of Molecular Bose-Einstein Condensates. *Phys. Rev. Lett.*, 88:160402, Apr 2002. http://link.aps.org/doi/10.1103/PhysRevLett.88.160402.

[96] S. Ospelkaus, K.-K. Ni, D. Wang, M. H. G. de Miranda, B. Neyenhuis, G. Quéméner, P. S. Julienne, J. L. Bohn, D. S. Jin, and J. Ye. Quantum-State Controlled Chemical Reactions of Ultracold Potassium-Rubidium Molecules. *Science*, 327(5967):853–857, 2010. http://science.sciencemag.org/content/327/5967/853.

[97] R. V. Krems. Cold controlled chemistry. *Phys. Chem. Chem. Phys.*, 10:4079–4092, 2008. http://dx.doi.org/10.1039/B802322K.

[98] K-K Ni, S Ospelkaus, D Wang, G Quéméner, B Neyenhuis, MHG De Miranda, JL Bohn, J Ye, and DS Jin. Dipolar collisions of polar molecules in the quantum regime. *Nature*, 464(7293):1324–1328, 2010. http://dx.doi.org/10.1038/nature08953.

[99] Amodsen Chotia, Brian Neyenhuis, Steven A. Moses, Bo Yan, Jacob P. Covey, Michael Foss-Feig, Ana Maria Rey, Deborah S. Jin, and Jun Ye. Long-Lived Dipolar Molecules and Feshbach Molecules in a 3D Optical Lattice. *Phys. Rev. Lett.*, 108:080405, Feb 2012. http://link.aps.org/doi/10.1103/PhysRevLett.108.080405.

[100] M. H. G. De Miranda, A. Chotia, B. Neyenhuis, D. Wang, G. Quéméner, S. Ospelkaus, J. L. Bohn, J. Ye, and D. S. Jin. Controlling the quantum stereodynamics of ultracold bimolecular reactions. *Nature Physics*, 7(6):502–507, 2011. http://dx.doi.org/10.1038/nphys1939.

[101] V. V. Flambaum and M. G. Kozlov. Enhanced Sensitivity to the Time Variation of the Fine-Structure Constant and m_p/m_e in Diatomic Molecules. *Phys. Rev. Lett.*, 99:150801, Oct 2007. http://link.aps.org/doi/10.1103/PhysRevLett.99.150801.

[102] K. Góral, L. Santos, and M. Lewenstein. Quantum Phases of Dipolar Bosons in Optical Lattices. *Phys. Rev. Lett.*, 88:170406, Apr 2002. http://link.aps.org/doi/10.1103/PhysRevLett.88.170406.

[103] M L Wall and L D Carr. Emergent timescales in entangled quantum dynamics of ultracold molecules in optical lattices. *New Journal of Physics*, 11(5):055027, 2009. http://stacks.iop.org/1367-2630/11/i=5/a=055027.

[104] B. T. Matthias, H. Suhl, and E. Corenzwit. Spin Exchange in Superconductors. *Phys. Rev. Lett.*, 1:92–94, Aug 1958. http://link.aps.org/doi/10.1103/PhysRevLett.1.92.

[105] Patrick A. Lee, Naoto Nagaosa, and Xiao-Gang Wen. Doping a Mott insulator: Physics of high-temperature superconductivity. *Rev. Mod. Phys.*, 78:17–85, Jan 2006. http://link.aps.org/doi/10.1103/RevModPhys.78.17.

[106] Pengcheng Dai. Antiferromagnetic order and spin dynamics in iron-based superconductors. *Rev. Mod. Phys.*, 87:855–896, Aug 2015. http://link.aps.org/doi/10.1103/RevModPhys.87.855.

[107] J Stenger, S Inouye, DM Stamper-Kurn, H-J Miesner, AP Chikkatur, and W Ketterle. Spin domains in ground-state bose–einstein condensates. *Nature*, 396(6709):345–348, 1998. http://dx.doi.org/10.1038/24567.

[108] Tin-Lun Ho. Spinor Bose Condensates in Optical Traps. *Phys. Rev. Lett.*, 81:742–745, Jul 1998. http://link.aps.org/doi/10.1103/PhysRevLett.81.742.

[109] Tetsuo Ohmi and Kazushige Machida. Bose-Einstein Condensation with Internal Degrees of Freedom in Alkali Atom Gases. *Journal of the Physical Society of Japan*, 67(6):1822–1825, 1998. http://dx.doi.org/10.1143/JPSJ.67.1822.

[110] Yuki Kawaguchi and Masahito Ueda. Spinor Bose–Einstein condensates. *Physics Reports*, 520(5):253 – 381, 2012. http://www.sciencedirect.com/science/article/pii/S0370157312002098,.

[111] Dan M. Stamper-Kurn and Masahito Ueda. Spinor Bose gases: Symmetries, magnetism, and quantum dynamics. *Rev. Mod. Phys.*, 85:1191–1244, Jul 2013. http://link.aps.org/doi/10.1103/RevModPhys.85.1191.

[112] Jasper S Krauser, Jannes Heinze, Nick Fläschner, Sören Götze, Ole Jürgensen, Dirk-Sören Lühmann, Christoph Becker, and Klaus Sengstock. Coherent multi-flavour spin dynamics in a fermionic quantum gas. *Nature Physics*, 8(11):813–818, 2012. http://dx.doi.org/10.1038/nphys2409.

[113] M.-S. Chang, C. D. Hamley, M. D. Barrett, J. A. Sauer, K. M. Fortier, W. Zhang, L. You, and M. S. Chapman. Observation of Spinor Dynamics in Optically Trapped ^{87}Rb Bose-Einstein Condensates. *Phys. Rev. Lett.*, 92:140403, Apr 2004. http://link.aps.org/doi/10.1103/PhysRevLett.92.140403.

[114] Artur Widera, Fabrice Gerbier, Simon Fölling, Tatjana Gericke, Olaf Mandel, and Immanuel Bloch. Precision measurement of spin-dependent inter-

action strengths for spin-1 and spin-2 87 Rb atoms. *New Journal of Physics*, 8(8):152, 2006. http://stacks.iop.org/1367-2630/8/i=8/a=152.

[115] J. Kronjäger, C. Becker, P. Navez, K. Bongs, and K. Sengstock. Magnetically Tuned Spin Dynamics Resonance. *Phys. Rev. Lett.*, 97:110404, Sep 2006. http://link.aps.org/doi/10.1103/PhysRevLett.97.110404.

[116] A. T. Black, E. Gomez, L. D. Turner, S. Jung, and P. D. Lett. Spinor Dynamics in an Antiferromagnetic Spin-1 Condensate. *Phys. Rev. Lett.*, 99:070403, Aug 2007. http://link.aps.org/doi/10.1103/PhysRevLett.99.070403.

[117] Ming-Shien Chang, Qishu Qin, Wenxian Zhang, Li You, and Michael S Chapman. Coherent spinor dynamics in a spin-1 bose condensate. *Nature physics*, 1(2):111–116, 2005. http://dx.doi.org/10.1038/nphys153.

[118] H. K. Pechkis, J. P. Wrubel, A. Schwettmann, P. F. Griffin, R. Barnett, E. Tiesinga, and P. D. Lett. Spinor Dynamics in an Antiferromagnetic Spin-1 Thermal Bose Gas. *Phys. Rev. Lett.*, 111:025301, Jul 2013. http://link.aps.org/doi/10.1103/PhysRevLett.111.025301.

[119] Xiaodong He, Bing Zhu, Xiaoke Li, Fudong Wang, Zhi-Fang Xu, and Dajun Wang. Coherent spin-mixing dynamics in thermal ^{87}Rb spin-1 and spin-2 gases. *Phys. Rev. A*, 91:033635, Mar 2015. http://link.aps.org/doi/10.1103/PhysRevA.91.033635.

[120] Xiaoke Li, Bing Zhu, Xiaodong He, Fudong Wang, Mingyang Guo, Zhi-Fang Xu, Shizhong Zhang, and Dajun Wang. Coherent Heteronuclear Spin Dynamics in an Ultracold Spinor Mixture. *Phys. Rev. Lett.*, 114:255301, Jun 2015. http://link.aps.org/doi/10.1103/PhysRevLett.114.255301.

[121] LE Sadler, JM Higbie, SR Leslie, M Vengalattore, and DM Stamper-Kurn. Spontaneous symmetry breaking in a quenched ferromagnetic spinor bose–einstein condensate. *Nature*, 443(7109):312–315, 2006. http://dx.doi.org/10.1038/nature05094.

[122] CS Gerving, TM Hoang, BJ Land, M Anquez, CD Hamley, and MS Chapman. Non-equilibrium dynamics of an unstable quantum pendulum explored

in a spin-1 bose-einstein condensate. *Nature communications*, 3:1169, 2012. http://dx.doi.org/10.1038/ncomms2179.

[123] Chris D Hamley, CS Gerving, TM Hoang, EM Bookjans, and Michael S Chapman. Spin-nematic squeezed vacuum in a quantum gas. *Nature Physics*, 8(4):305–308, 2012. http://dx.doi.org/10.1038/nphys2245.

[124] Christian Gross. Spin squeezing, entanglement and quantum metrology with bose–einstein condensates. *Journal of Physics B: Atomic, Molecular and Optical Physics*, 45(10):103001, 2012. http://stacks.iop.org/0953-4075/45/i=10/a=103001.

[125] M. Anquez, B. A. Robbins, H. M Bharath, M. Boguslawski, T. M. Hoang, and M. S. Chapman. Quantum Kibble-Zurek Mechanism in a Spin-1 Bose-Einstein Condensate. *Phys. Rev. Lett.*, 116:155301, Apr 2016. http://link.aps.org/doi/10.1103/PhysRevLett.116.155301.

[126] Z. F. Xu, Yunbo Zhang, and L. You. Binary mixture of spinor atomic Bose-Einstein condensates. *Phys. Rev. A*, 79:023613, Feb 2009. http://link.aps.org/doi/10.1103/PhysRevA.79.023613.

[127] Z. F. Xu, J. W. Mei, R. Lü, and L. You. Spontaneously axisymmetry-breaking phase in a binary mixture of spinor Bose-Einstein condensates. *Phys. Rev. A*, 82:053626, Nov 2010. http://link.aps.org/doi/10.1103/PhysRevA.82.053626.

[128] Yu Shi. Ground states of a mixture of two species of spinor Bose gases with interspecies spin exchange. *Phys. Rev. A*, 82:023603, Aug 2010. http://link.aps.org/doi/10.1103/PhysRevA.82.023603.

[129] Z. F. Xu, Jie Zhang, Yunbo Zhang, and L. You. Quantum states of a binary mixture of spinor Bose-Einstein condensates. *Phys. Rev. A*, 81:033603, Mar 2010. http://link.aps.org/doi/10.1103/PhysRevA.81.033603.

[130] Z. F. Xu, D. J. Wang, and L. You. Quantum spin mixing in a binary mixture of spin-1 atomic condensates. *Phys. Rev. A*, 86:013632, Jul 2012. http://link.aps.org/doi/10.1103/PhysRevA.86.013632.

[131] Takeshi Fukuhara, Adrian Kantian, Manuel Endres, Marc Cheneau, Peter Schauß, Sebastian Hild, David Bellem, Ulrich Schollwöck, Thierry Giamarchi, Christian Gross, et al. Quantum dynamics of a mobile spin impurity. *Nature Physics*, 9(4):235–241, 2013. http://dx.doi.org/10.1038/nphys2561.

[132] H. J. Lewandowski, D. M. Harber, D. L. Whitaker, and E. A. Cornell. Simplified system for creating a Bose–Einstein Condensate. *Journal of Low Temperature Physics*, 132(5):309–367. http://dx.doi.org/10.1023/A:1024800600621.

[133] A. Gozzini, F. Mango, J. H. Xu, G. Alzetta, F. Maccarrone, and R. A. Bernheim. Light-induced ejection of alkali atoms in polysiloxane coated cells. *Il Nuovo Cimento D*, 15(5):709–722. http://dx.doi.org/10.1007/BF02482437.

[134] C. Klempt, T. van Zoest, T. Henninger, O. Topic, E. Rasel, W. Ertmer, and J. Arlt. Ultraviolet light-induced atom desorption for large rubidium and potassium magneto-optical traps. *Phys. Rev. A*, 73:013410, Jan 2006. http://link.aps.org/doi/10.1103/PhysRevA.73.013410.

[135] Daniel A Steck. Rubidium 87 D line data, 2010. http://steck.us/alkalidata/cesiumnumbers.pdf.

[136] Daniel A Steck. Sodium D line data, 2010. http://steck.us/alkalidata/sodiumnumbers.pdf.

[137] Hendrik Antoon Lorentz. *The theory of electrons and its applications to the phenomena of light and radiant heat*, volume 29. BG Teubner, 1916.

[138] Christopher J Foot. *Atomic physics*. OUP Oxford, 2004.

[139] J. P. Gordon and A. Ashkin. Motion of atoms in a radiation trap. *Phys. Rev. A*, 21:1606–1617, May 1980. http://link.aps.org/doi/10.1103/PhysRevA.21.1606.

[140] Daniel A Steck. Quantum and atom optics. 2007. http://atomoptics-nas.uoregon.edu/~dsteck/teaching/quantum-optics/quantum-optics-notes.pdf.

[141] Rudolf Grimm, Matthias Weidemüller, and Yurii B. Ovchinnikov. Optical dipole traps for neutral atoms. volume 42 of *Advances In Atomic, Molecular, and Optical Physics*, pages 95 – 170. Academic Press, 2000. http://www.sciencedirect.com/science/article/pii/S1049250X0860186X.

[142] Alexander L. Gaunt, Tobias F. Schmidutz, Igor Gotlibovych, Robert P. Smith, and Zoran Hadzibabic. Bose-einstein condensation of atoms in a uniform potential. *Phys. Rev. Lett.*, 110:200406, May 2013. http://link.aps.org/doi/10.1103/PhysRevLett.110.200406.

[143] Xiaoke Li. *Coherent heteronuclear spin dynamics in an ultracold spinor mixture*. PhD thesis, The Chinese University of Hong Kong, 2015.

[144] C. J. Hawthorn, K. P. Weber, and R. E. Scholten. Littrow configuration tunable external cavity diode laser with fixed direction output beam. *Review of Scientific Instruments*, 72(12):4477–4479, 2001. http://scitation.aip.org/content/aip/journal/rsi/72/12/10.1063/1.1419217.

[145] Christopher J Pethick and Henrik Smith. *Bose-Einstein condensation in dilute gases*. Cambridge university press, 2002.

[146] Eugene P Gross. Structure of a quantized vortex in boson systems. *Il Nuovo Cimento (1955-1965)*, 20(3):454–477, 1961.

[147] LP Pitaevskii. Vortex lines in an imperfect bose gas. *Sov. Phys. JETP*, 13(2):451–454, 1961.

[148] P. A. Ruprecht, M. J. Holland, K. Burnett, and Mark Edwards. Time-dependent solution of the nonlinear Schrödinger equation for Bose-condensed trapped neutral atoms. *Phys. Rev. A*, 51:4704–4711, Jun 1995. http://link.aps.org/doi/10.1103/PhysRevA.51.4704.

[149] C. C. Bradley, C. A. Sackett, and R. G. Hulet. Bose-Einstein Condensation of Lithium: Observation of Limited Condensate Number. *Phys. Rev. Lett.*, 78:985–989, Feb 1997. http://link.aps.org/doi/10.1103/PhysRevLett.78.985.

[150] J. L. Roberts, N. R. Claussen, S. L. Cornish, E. A. Donley, E. A. Cornell, and C. E. Wieman. Controlled Collapse of a Bose-Einstein Condensate. *Phys.*

Rev. Lett., 86:4211–4214, May 2001. http://link.aps.org/doi/10.1103/PhysRevLett.86.4211.

[151] Murray D Barrett. *A QUEST for BEC: An all optical alternative*. PhD thesis, Georgia Institute of Technology, 2002.

[152] G Reinaudi, T Lahaye, Z Wang, and D Guéry-Odelin. Strong saturation absorption imaging of dense clouds of ultracold atoms. *Optics Letters*, 32(21):3143–3145, 2007. http://ol.osa.org/abstract.cfm?URI=ol-32-21-3143.

[153] Woo Jin Kwon, Jae-yoon Choi, and Yong-il Shin. Calibration of saturation absorption imaging of ultracold atom clouds. *Journal of the Korean Physical Society*, 61(12):1970–1974, 2012.

[154] G. Breit and I. I. Rabi. Measurement of Nuclear Spin. *Phys. Rev.*, 38:2082–2083, Dec 1931. http://link.aps.org/doi/10.1103/PhysRev.38.2082.2.

[155] S-Q. Shang, B. Sheehy, P. van der Straten, and H. Metcalf. Velocity-selective magnetic-resonance laser cooling. *Phys. Rev. Lett.*, 65:317–320, Jul 1990. http://link.aps.org/doi/10.1103/PhysRevLett.65.317.

[156] Kang-Kuen Ni. *A quantum gas of polar molecules*. PhD thesis, Citeseer, 2009.

[157] T. H. Bergeman, Patrick McNicholl, Jan Kycia, Harold Metcalf, and N. L. Balazs. Quantized motion of atoms in a quadrupole magnetostatic trap. *J. Opt. Soc. Am. B*, 6(11):2249–2256, Nov 1989. http://josab.osa.org/abstract.cfm?URI=josab-6-11-2249.

[158] Jun Chen. Optical dipole traps for optimized preparation of ultracold atomic mixtures. Master's thesis, The Chinese University of Hong Kong, 2014.

[159] Fudong Wang, Dezhi Xiong, Xiaoke Li, Dajun Wang, and Eberhard Tiemann. Observation of Feshbach resonances between ultracold Na and Rb atoms. *Phys. Rev. A*, 87:050702, May 2013. http://link.aps.org/doi/10.1103/PhysRevA.87.050702.

[160] Piotr S. Żuchowski and Jeremy M. Hutson. Reactions of ultracold alkali-metal dimers. *Phys. Rev. A*, 81:060703, Jun 2010. http://link.aps.org/doi/10.1103/PhysRevA.81.060703.

[161] A. Pashov, O. Docenko, M. Tamanis, R. Ferber, H. Knöckel, and E. Tiemann. Potentials for modeling cold collisions between na (3s) and rb (5s) atoms. *Phys. Rev. A*, 72:062505, Dec 2005. http://link.aps.org/doi/10.1103/PhysRevA.72.062505.

[162] O. Docenko, M. Tamanis, R. Ferber, E. A. Pazyuk, A. Zaitsevskii, A. V. Stolyarov, A. Pashov, H. Knöckel, and E. Tiemann. Deperturbation treatment of the $A\,^1\Sigma^+ \breve{} b\,^3\Pi$ complex of NaRb and prospects for ultracold molecule formation in $X\,^1\Sigma^+(v = 0; J = 0)$. *Phys. Rev. A*, 75:042503, Apr 2007. http://link.aps.org/doi/10.1103/PhysRevA.75.042503.

[163] You Chang Wang, Kensuke Matsubara, and Hajime Katô. Perturbation analysis of the $B^1\Pi$ state of $^{23}Na^{85}Rb$ molecule. *The Journal of Chemical Physics*, 97(2):811–817, 1992. http://scitation.aip.org/content/aip/journal/jcp/97/2/10.1063/1.463183.

[164] A. Pashov, W. Jastrzebski, P. Kortyka, and P. Kowalczyk. Experimental long range potential of the $b\,^3\Pi\,1$ state in narb. *The Journal of Chemical Physics*, 124(20), 2006. http://scitation.aip.org/content/aip/journal/jcp/124/20/10.1063/1.2198199.

[165] Max Born and Robert Oppenheimer. Zur quantentheorie der molekeln. *Annalen der Physik*, 389(20):457–484, 1927.

[166] Fudong Wang, Xiaodong He, Xiaoke Li, Bing Zhu, Jun Chen, and Dajun Wang. Formation of ultracold narb feshbach molecules. *New Journal of Physics*, 17(3):035003, 2015. http://stacks.iop.org/1367-2630/17/i=3/a=035003.

[167] S. T. Thompson, E. Hodby, and C. E. Wieman. Ultracold Molecule Production via a Resonant Oscillating Magnetic Field. *Phys. Rev. Lett.*, 95:190404, Nov 2005. http://link.aps.org/doi/10.1103/PhysRevLett.95.190404.

[168] A. D. Lange, K. Pilch, A. Prantner, F. Ferlaino, B. Engeser, H.-C. Nägerl, R. Grimm, and C. Chin. Determination of atomic scattering lengths

from measurements of molecular binding energies near Feshbach resonances. *Phys. Rev. A*, 79:013622, Jan 2009. http://link.aps.org/doi/10.1103/PhysRevA.79.013622.

[169] Kevin M. Jones, Eite Tiesinga, Paul D. Lett, and Paul S. Julienne. Ultracold photoassociation spectroscopy: Long-range molecules and atomic scattering. *Rev. Mod. Phys.*, 78:483–535, May 2006. http://link.aps.org/doi/10.1103/RevModPhys.78.483.

[170] Robert J. LeRoy and Richard B. Bernstein. Dissociation energy and longrange potential of diatomic molecules from vibrational spacings of higher levels. *The Journal of Chemical Physics*, 52(8):3869–3879, 1970. http://scitation.aip.org/content/aip/journal/jcp/52/8/10.1063/1.1673585.

[171] W.C. Stwalley. The dissociation energy of the hydrogen molecule using long-range forces. *Chemical Physics Letters*, 6(3):241 – 244, 1970. http://www.sciencedirect.com/science/article/pii/0009261470802305.

[172] Marlan O Scully and M Suhail Zubairy. *Quantum optics*. Cambridge university press, 1997.

[173] N. V. Vitanov and S. Stenholm. Population transfer via a decaying state. *Phys. Rev. A*, 56:1463–1471, Aug 1997. http://link.aps.org/doi/10.1103/PhysRevA.56.1463.

[174] A. Orbán, R. Vexiau, O. Krieglsteiner, H.-C. Nägerl, O. Dulieu, A. Crubellier, and N. Bouloufa-Maafa. Model for the hyperfine structure of electronically excited KCs molecules. *Phys. Rev. A*, 92:032510, Sep 2015. http://link.aps.org/doi/10.1103/PhysRevA.92.032510.

[175] B. C. Young, F. C. Cruz, W. M. Itano, and J. C. Bergquist. Visible Lasers with Subhertz Linewidths. *Phys. Rev. Lett.*, 82:3799–3802, May 1999. http://link.aps.org/doi/10.1103/PhysRevLett.82.3799.

[176] Miao Zhu and John L. Hall. Stabilization of optical phase/frequency of a laser system: application to a commercial dye laser with an external stabilizer. *J. Opt. Soc. Am. B*, 10(5):802–816, May 1993. http://josab.osa.org/abstract.cfm?URI=josab-10-5-802.

[177] T Bergeman, J Qi, D Wang, Y Huang, H K Pechkis, E E Eyler, P L Gould, W C Stwalley, R A Cline, J D Miller, and D J Heinzen. Photoassociation of 85 rb atoms into 0 u + states near the 5s+5p atomic limits. *Journal of Physics B: Atomic, Molecular and Optical Physics*, 39(19):S813, 2006. http://stacks.iop.org/0953-4075/39/i=19/a=S01.

[178] M. Marinescu and H. R. Sadeghpour. Long-range potentials for two-species alkali-metal atoms. *Phys. Rev. A*, 59:390–404, Jan 1999. http://link.aps.org/doi/10.1103/PhysRevA.59.390.

[179] Béatrice Bussery, Yamina Achkar, and Monique Aubert-Frécon. Long-range molecular states dissociating to the three or four lowest asymptotes for the ten heteronuclear diatomic alkali molecules. *Chemical Physics*, 116(3):319 – 338, 1987. http://www.sciencedirect.com/science/article/pii/0301010487802021.

[180] M. Aubert-Frécon, G. Hadinger, S. Magnier, and S. Rousseau. Analytical Formulas for Long-Range Energies of the 16 $\Omega_{g,u}^{(+/-)}$ States of Alkali Dimers Dissociating into M(ns) + M(np^2P_J). *Journal of Molecular Spectroscopy*, 188(2):182 – 189, 1998. http://www.sciencedirect.com/science/article/pii/S002228529797510X.

[181] Daniel Comparat. Improved leroy–bernstein near-dissociation expansion formula, and prospect for photoassociation spectroscopy. *The Journal of Chemical Physics*, 120(3):1318–1329, 2004. http://scitation.aip.org/content/aip/journal/jcp/120/3/10.1063/1.1626539.

[182] Bing Zhu, Xiaoke Li, Xiaodong He, Mingyang Guo, Fudong Wang, Romain Vexiau, Nadia Bouloufa-Maafa, Olivier Dulieu, and Dajun Wang. Long-range states of the NaRb molecule near the $\mathrm{Na}(3^2S_{1/2}) + \mathrm{Rb}(5^2P_{3/2})$ asymptote. *Phys. Rev. A*, 93:012508, Jan 2016. http://link.aps.org/doi/10.1103/PhysRevA.93.012508.

[183] Markus Debatin, Tetsu Takekoshi, Raffael Rameshan, Lukas Reichsollner, Francesca Ferlaino, Rudolf Grimm, Romain Vexiau, Nadia Bouloufa, Olivier Dulieu, and Hanns-Christoph Nagerl. Molecular spectroscopy for ground-state transfer of ultracold rbcs molecules. *Phys. Chem. Chem. Phys.*, 13:18926–18935, 2011. http://dx.doi.org/10.1039/C1CP21769K.

[184] J. Aldegunde, Ben A. Rivington, Piotr S. Żuchowski, and Jeremy M. Hutson. Hyperfine energy levels of alkali-metal dimers: Ground-state polar molecules in electric and magnetic fields. *Phys. Rev. A*, 78:033434, Sep 2008. http://link.aps.org/doi/10.1103/PhysRevA.78.033434.

[185] Nikolay V Vitanov, Andon A Rangelov, Bruce W Shore, and Klaas Bergmann. Stimulated raman adiabatic passage in physics, chemistry and beyond. *arXiv preprint arXiv:1605.00224*, 2016.

[186] M. Scala, B. Militello, A. Messina, and N. V. Vitanov. Stimulated Raman adiabatic passage in an open quantum system: Master equation approach. *Phys. Rev. A*, 81:053847, May 2010. http://link.aps.org/doi/10.1103/PhysRevA.81.053847.

[187] L. P. Yatsenko, V. I. Romanenko, B. W. Shore, and K. Bergmann. Stimulated Raman adiabatic passage with partially coherent laser fields. *Phys. Rev. A*, 65:043409, Apr 2002. http://link.aps.org/doi/10.1103/PhysRevA.65.043409.

[188] John M Brown and Alan Carrington. *Rotational spectroscopy of diatomic molecules*. Cambridge University Press, 2003.

[189] Paul J. Dagdigian and Lennard Wharton. Molecular beam electric deflection and resonance spectroscopy of the heteronuclear alkali dimers: 39K7Li, Rb7Li, 39K23Na, Rb23Na, and 133Cs23Na. *The Journal of Chemical Physics*, 57(4), 1972.

[190] G. Igel-Mann, U. Wedig, P. Fuentealba, and H. Stoll. Ground-state properties of alkali dimers XY (X, Y=Li to Cs). *The Journal of Chemical Physics*, 84(9):5007–5012, 1986. http://scitation.aip.org/content/aip/journal/jcp/84/9/10.1063/1.450649.

[191] V. Tarnovsky, M. Bunimovicz, L. Vušković, B. Stumpf, and B. Bederson. Measurements of the dc electric dipole polarizabilities of the alkali dimer molecules, homonuclear and heteronuclear. *The Journal of Chemical Physics*, 98(5):3894–3904, 1993. http://scitation.aip.org/content/aip/journal/jcp/98/5/10.1063/1.464017.

[192] M. Aymar and O. Dulieu. Calculation of accurate permanent dipole moments of the lowest $\Sigma+1,3$ states of heteronuclear alkali dimers using extended basis sets. *The Journal of Chemical Physics*, 122(20), 2005. http://scitation.aip.org/content/aip/journal/jcp/122/20/10.1063/1.1903944.

[193] D. DeMille. Quantum Computation with Trapped Polar Molecules. *Phys. Rev. Lett.*, 88:067901, Jan 2002. http://link.aps.org/doi/10.1103/PhysRevLett.88.067901.

[194] Michael Mayle, Goulven Quéméner, Brandon P. Ruzic, and John L. Bohn. Scattering of ultracold molecules in the highly resonant regime. *Phys. Rev. A*, 87:012709, Jan 2013. http://link.aps.org/doi/10.1103/PhysRevA.87.012709.

[195] Tetsu Takekoshi, Lukas Reichsöllner, Andreas Schindewolf, Jeremy M. Hutson, C. Ruth Le Sueur, Olivier Dulieu, Francesca Ferlaino, Rudolf Grimm, and Hanns-Christoph Nägerl. Ultracold Dense Samples of Dipolar RbCs Molecules in the Rovibrational and Hyperfine Ground State. *Phys. Rev. Lett.*, 113:205301, Nov 2014. http://link.aps.org/doi/10.1103/PhysRevLett.113.205301.

[196] M. Lepers, R. Vexiau, M. Aymar, N. Bouloufa-Maafa, and O. Dulieu. Long-range interactions between polar alkali-metal diatoms in external electric fields. *Phys. Rev. A*, 88:032709, Sep 2013. http://link.aps.org/doi/10.1103/PhysRevA.88.032709.

[197] T. Mukaiyama, J. R. Abo-Shaeer, K. Xu, J. K. Chin, and W. Ketterle. Dissociation and Decay of Ultracold Sodium Molecules. *Phys. Rev. Lett.*, 92:180402, May 2004. http://link.aps.org/doi/10.1103/PhysRevLett.92.180402.

[198] Jee Woo Park, Sebastian A. Will, and Martin W. Zwierlein. Ultracold Dipolar Gas of Fermionic $^{23}Na^{40}K$ Molecules in Their Absolute Ground State. *Phys. Rev. Lett.*, 114:205302, May 2015. http://link.aps.org/doi/10.1103/PhysRevLett.114.205302.

[199] Mingyang Guo, Bing Zhu, Bo Lu, Xin Ye, Fudong Wang, Romain Vexiau, Nadia Bouloufa-Maafa, Goulven Quéméner, Olivier Dulieu, and Dajun

Wang. Creation of an Ultracold Gas of Ground-State Dipolar $^{23}Na^{87}Rb$ Molecules. *Phys. Rev. Lett.*, 116:205303, May 2016. http://link.aps.org/doi/10.1103/PhysRevLett.116.205303.

[200] T. Maier, H. Kadau, M. Schmitt, M. Wenzel, I. Ferrier-Barbut, T. Pfau, A. Frisch, S. Baier, K. Aikawa, L. Chomaz, M. J. Mark, F. Ferlaino, C. Makrides, E. Tiesinga, A. Petrov, and S. Kotochigova. Emergence of Chaotic Scattering in Ultracold Er and Dy. *Phys. Rev. X*, 5:041029, Nov 2015. http://link.aps.org/doi/10.1103/PhysRevX.5.041029.

[201] Michael Mayle, Brandon P. Ruzic, and John L. Bohn. Statistical aspects of ultracold resonant scattering. *Phys. Rev. A*, 85:062712, Jun 2012. http://link.aps.org/doi/10.1103/PhysRevA.85.062712.

[202] Alexander V. Avdeenkov, Masatoshi Kajita, and John L. Bohn. Suppression of inelastic collisions of polar $^1\Sigma$ state molecules in an electrostatic field. *Phys. Rev. A*, 73:022707, Feb 2006. http://link.aps.org/doi/10.1103/PhysRevA.73.022707.

[203] Gaoren Wang and Goulven Quéméner. Tuning ultracold collisions of excited rotational dipolar molecules. *New Journal of Physics*, 17(3):035015, 2015. http://stacks.iop.org/1367-2630/17/i=3/a=035015.

[204] H. P. Büchler, E. Demler, M. Lukin, A. Micheli, N. Prokof'ev, G. Pupillo, and P. Zoller. Strongly Correlated 2D Quantum Phases with Cold Polar Molecules: Controlling the Shape of the Interaction Potential. *Phys. Rev. Lett.*, 98:060404, Feb 2007. http://link.aps.org/doi/10.1103/PhysRevLett.98.060404.

[205] G. Pupillo, A. Griessner, A. Micheli, M. Ortner, D.-W. Wang, and P. Zoller. Cold Atoms and Molecules in Self-Assembled Dipolar Lattices. *Phys. Rev. Lett.*, 100:050402, Feb 2008. http://link.aps.org/doi/10.1103/PhysRevLett.100.050402.

[206] C. K. Law, H. Pu, and N. P. Bigelow. Quantum Spins Mixing in Spinor Bose-Einstein Condensates. *Phys. Rev. Lett.*, 81:5257–5261, Dec 1998. http://link.aps.org/doi/10.1103/PhysRevLett.81.5257.

[207] Wenxian Zhang, D. L. Zhou, M.-S. Chang, M. S. Chapman, and L. You. Coherent spin mixing dynamics in a spin-1 atomic condensate. *Phys. Rev. A*, 72:013602, Jul 2005. http://link.aps.org/doi/10.1103/PhysRevA.72.013602.

[208] J. Kronjäger, C. Becker, M. Brinkmann, R. Walser, P. Navez, K. Bongs, and K. Sengstock. Evolution of a spinor condensate: Coherent dynamics, dephasing, and revivals. *Phys. Rev. A*, 72:063619, Dec 2005. http://link.aps.org/doi/10.1103/PhysRevA.72.063619.

[209] C. V. Ciobanu, S.-K. Yip, and Tin-Lun Ho. Phase diagrams of $F = 2$ spinor Bose-Einstein condensates. *Phys. Rev. A*, 61:033607, Feb 2000. http://link.aps.org/doi/10.1103/PhysRevA.61.033607.

[210] Stefan S. Natu and Erich J. Mueller. Spin waves in a spin-1 normal Bose gas. *Phys. Rev. A*, 81:053617, May 2010. http://link.aps.org/doi/10.1103/PhysRevA.81.053617.

[211] Fabrice Gerbier, Artur Widera, Simon Fölling, Olaf Mandel, and Immanuel Bloch. Resonant control of spin dynamics in ultracold quantum gases by microwave dressing. *Phys. Rev. A*, 73:041602, Apr 2006. http://link.aps.org/doi/10.1103/PhysRevA.73.041602.

[212] L. Zhao, J. Jiang, T. Tang, M. Webb, and Y. Liu. Dynamics in spinor condensates tuned by a microwave dressing field. *Phys. Rev. A*, 89:023608, Feb 2014. http://link.aps.org/doi/10.1103/PhysRevA.89.023608.

[213] S. R. Leslie, J. Guzman, M. Vengalattore, Jay D. Sau, Marvin L. Cohen, and D. M. Stamper-Kurn. Amplification of fluctuations in a spinor Bose-Einstein condensate. *Phys. Rev. A*, 79:043631, Apr 2009. http://link.aps.org/doi/10.1103/PhysRevA.79.043631.

[214] E. M. Bookjans, A. Vinit, and C. Raman. Quantum Phase Transition in an Antiferromagnetic Spinor Bose-Einstein Condensate. *Phys. Rev. Lett.*, 107:195306, Nov 2011. http://link.aps.org/doi/10.1103/PhysRevLett.107.195306.

[215] J. Jiang, L. Zhao, M. Webb, and Y. Liu. Mapping the phase diagram of spinor condensates via adiabatic quantum phase transitions. *Phys. Rev. A*,

90:023610, Aug 2014. http://link.aps.org/doi/10.1103/PhysRevA.90.023610.

[216] L. Santos, M. Fattori, J. Stuhler, and T. Pfau. Spinor condensates with a laser-induced quadratic Zeeman effect. *Phys. Rev. A*, 75:053606, May 2007. http://link.aps.org/doi/10.1103/PhysRevA.75.053606.

[217] H. Schmaljohann, M. Erhard, J. Kronjäger, M. Kottke, S. van Staa, L. Cacciapuoti, J. J. Arlt, K. Bongs, and K. Sengstock. Dynamics of $F = 2$ Spinor Bose-Einstein Condensates. *Phys. Rev. Lett.*, 92:040402, Jan 2004. http://link.aps.org/doi/10.1103/PhysRevLett.92.040402.

[218] J. Kronjäger, C. Becker, P. Navez, K. Bongs, and K. Sengstock. Erratum: Magnetically Tuned Spin Dynamics Resonance [Phys. Rev. Lett. **97** , 110404 (2006)]. *Phys. Rev. Lett.*, 100:189901, May 2008. http://link.aps.org/doi/10.1103/PhysRevLett.100.189901.

[219] Mott N. F. and H. S. W. Massey. *The Theory of Atomic Collisions*. Clarendon Press, third edition, 1965.

[220] K.-K. Ni, S. Ospelkaus, M. H. G. de Miranda, A. Pe'er, B. Neyenhuis, J. J. Zirbel, S. Kotochigova, P. S. Julienne, D. S. Jin, and J. Ye. A High Phase-Space-Density Gas of Polar Molecules. *Science*, 322(5899):231–235, 2008. http://science.sciencemag.org/content/322/5899/231.

[221] Peter K. Molony, Philip D. Gregory, Zhonghua Ji, Bo Lu, Michael P. Köppinger, C. Ruth Le Sueur, Caroline L. Blackley, Jeremy M. Hutson, and Simon L. Cornish. Creation of Ultracold $^{87}Rb^{133}Cs$ Molecules in the Rovibrational Ground State. *Phys. Rev. Lett.*, 113:255301, Dec 2014. http://link.aps.org/doi/10.1103/PhysRevLett.113.255301.